

Structural Modification for Chatter Avoidance in High Speed Milling



A thesis submitted to The University of Sheffield
for the degree of Doctor of Engineering in The Faculty of Engineering

by

Thomas Joseph Gibbons

Department of Mechanical Engineering
University of Sheffield
June 2017

Acknowledgements

Firstly, I would like to express my gratitude to The Boeing Company for their generous financial support over the past four years; in particular, to Leon Xu, James Castle, and Chris Tyler, without whom none of this would have been possible.

I would also like to thank Neil Sims for his excellent supervision throughout my EngD, for his constant guidance and encouragement, and for taking the time to explain some (very basic) engineering concepts to a confused mathematician.

I must also thank my AMRC supervisor Erdem Öztürk, for initially accepting me into the world of machining dynamics all those years ago, and for his relentless enthusiasm and knowledge during my time with the AMRC.

My endless appreciation goes to Leon Xu for instigating the project, his kind assistance on my trip to Seattle, and those many early morning conference calls.

To all members of the IDC in machining science, I am sincerely grateful for your friendship and support over the past four years. In particular, thank you to those who took me to the pub when all hope of finishing was lost. Not to forget Andrea and Clare and their first-rate management.

Finally, to my friends and family for putting up with my constant moaning, long may it continue!

Abstract

High speed machining operations, such as milling, are widely used in many industries including the aerospace sector. Elevated manufacturing costs coupled with ever more complex geometry components have led to the need to cut deeper and faster than ever; the dynamics of the structures involved, however, greatly restrict these boundaries. As speed and depth of cut are increased, self-excited vibrations, known as chatter, can occur due to the dynamic interaction between the tool tip and the workpiece. This has undesirable consequences such as poor surface finish, rapid tool and machine wear, and high noise levels, all of which lead to a reduction in production rates and an increase in production costs. Efforts to reduce and control chatter are therefore of great importance to industrial engineers.

Selection and design of appropriate cutting tools, in an attempt to minimize the occurrence of chatter, are well established methods in the manufacturing industry; however, the choice of tool (type, diameter, length) is often restricted by the required operation, and since the spindle is set by the machine itself, the only other variable component in the machining structure is the tool holder. Little research has been carried out on the dynamics of the tool holder, despite it being a much simpler structure. This thesis shows that the geometry of the tool holder has a significant effect on the dynamics at the tool tip (source of chatter). Therefore the overall focus of this work is to show how the geometry of the tool holder may be utilised to control the speed and depth at which chatter occurs.

Structural modification theory allows for models of smaller, simpler structures to be combined to predict the dynamics of larger, more complex structures. One

of its main advantages is that experimental models may be combined with numerical models, allowing for experimental structures to be optimised numerically. Structural modification theory is applied to the problem of tool holder dynamics and chatter control. Inverse structural modification is used to optimise the tool holder geometry in terms of tool tip dynamics and, in-turn, the onset of chatter. A prototype tuneable tool holder prototype is designed and tested for use with this structural modification model.

In addition to the focus on machining, it will be shown that spatial incompleteness is, perhaps, the largest draw-back with structural modification methods. For structural modification to give accurate results, a full spatial model, including rotational degrees of freedom is needed. Since direct measurement of such information requires specialist equipment, often not available to industry, numerical methods such as the finite difference technique have been developed to synthesise rotational data from translational measurements. As with any numerical method the accuracy of the finite difference technique relies on the correct spacing, however, there is currently no method to select an optimum spacing. An error analysis of the finite difference technique with non-exact data is carried out for application to rotational degree of freedom synthesis.

Contents

1	Introduction	2
1.1	Motivation and objectives	3
1.2	Outline of chapters	5
2	Literature Review	8
2.1	Chatter prediction	8
2.2	Chatter avoidance	9
2.3	Dynamic substructuring	12
2.3.1	Categorisation	13
2.3.2	Limitations of dynamic substructuring	15
2.3.3	Spatial incompleteness	17
2.4	Receptance coupling substructure analysis	19
2.5	Summary	20
3	Background	22
3.1	Structural dynamics	22
3.2	Machining dynamics	24
3.2.1	Average tooth angle approach	25
3.2.2	Fourier series approach	31
3.3	Structural modification	35
3.3.1	Unit rank structural modification	36
3.3.2	Higher rank structural modification	37
3.4	Summary	38

4	The Effect of Tool Holder Geometry	40
4.1	Introduction	40
4.2	Background - Tool Holder Geometry	41
4.3	Experimental Methods	44
4.3.1	Impact testing	44
4.3.2	Experimental modal analysis	49
4.4	Experimental Investigation	51
4.4.1	The effect of tool stickout length	53
4.4.2	The effect of tool holder geometry	58
4.5	Summary	65
5	The Effect of Tool Holder Stiffness	66
5.1	Introduction	66
5.2	Numerical Modelling	67
5.2.1	The addition of pure mass	68
5.2.2	The addition of real mass	70
5.2.3	Discussion	75
5.3	Summary	75
6	Structural Modification of Tool Holder Geometry	76
6.1	Introduction	76
6.2	Theory	77
6.2.1	The direct method	78
6.2.2	The inverse method	79
6.3	Application of structural modification theory to milling	80
6.3.1	The stability of a milling operation	80
6.3.2	Inverse structural modification of tool holder geometry	82
6.4	Experimental Investigation: Spindle Rig	83
6.4.1	Methodology	86
6.4.2	Direct structural modification	91
6.4.3	Inverse structural modification	92
6.5	Direct Structural Modification on the FTV5 Milling Machine	96
6.5.1	Methodology	96

6.5.2	Undamped direct structural modification	97
6.5.3	Proportional damping	97
6.5.4	Damped Direct Structural Modification	100
6.5.5	Stability Prediction	102
6.5.6	Discussion	102
6.6	Inverse structural modification on the FTV5	104
6.6.1	Methodology	104
6.6.2	Discussion	105
6.7	Summary	105
7	Design and Testing of a Tuneable Tool Holder	108
7.1	Introduction	108
7.2	Design Specification	109
7.2.1	Performance	109
7.2.2	Environment	111
7.2.3	Health and safety	111
7.3	Design solution	112
7.3.1	Performance	114
7.3.2	Environment	115
7.3.3	Health and Safety	115
7.4	Testing the unbalance of the prototype	117
7.5	Testing the dynamics of the prototype	119
7.5.1	Initial observations	120
7.5.2	Methodology	124
7.6	Results	125
7.7	Discussion	128
7.8	Summary	129
8	Cutting Trials	130
8.1	Introduction	130
8.2	Impact tests, modal analysis, and structural modification	132
8.2.1	Results and discussion	134
8.3	Experimental determination of cutting force coefficients	135

CONTENTS

8.3.1	Analytical cutting forces	135
8.3.2	Experimental cutting forces	140
8.4	Cutting Tests	141
8.4.1	Experimental procedure	143
8.4.2	Chatter detection methods	143
8.5	Results and Discussion	147
8.5.1	Experiment 1	147
8.5.2	Experiment 2	150
8.5.3	Experiment 3	153
8.5.4	Discussion	153
8.6	Summary	154
9	Rotational Degree of Freedom Synthesis	156
9.1	Introduction	157
9.2	Background	160
9.2.1	Error analysis: forward differences	162
9.2.2	A new optimum spacing	165
9.2.3	Error analysis: central differences	165
9.3	Evaluating the fourth order derivative norms	167
9.3.1	The fourth derivative of beam mode shapes	168
9.3.2	A beam with arbitrary boundary conditions	169
9.3.3	Numerical validation	170
9.3.4	Results and discussion	172
9.4	Evaluating other high order derivative norms	172
9.5	Approximating the ‘perfect modes’	174
9.6	Experimental Investigation	180
9.6.1	Experimental calculation of optimum spacings	180
9.6.2	Experimental validation	181
9.6.3	Results and discussion	182
9.7	Summary	184
10	Conclusions	188
10.1	Thesis summary	188

10.2 Contributions to knowledge	190
10.3 Limitations and future research	192
A Finite Element Model	196
B Finite Difference Tables	202
C Experimental Sheet	204

CONTENTS

Nomenclature

α, β	Proportional viscous damping coefficients
$\alpha_{xx}, \alpha_{xy}, \alpha_{yx}, \alpha_{yy}$	Time varying dynamic force coefficients
$\bar{\phi}_r$	Measurement perturbation
λ_r	Modal eigenfunction
λ_{rm}	Experimentally determined eigenfrequency
B	Dynamic Stiffness (m N ⁻¹)
I	Identity matrix
μ_r	Mean
μ_x, μ_y	Orientation coefficients for average tooth angle approach
Ω	Spindle Speed (rpm)
ω	Frequency (rad s ⁻¹)
ω_r	Natural frequency (rad s ⁻¹)
ω_s	Frequency resolution (rad s ⁻¹)
ω_{rm}	Experimentally determined natural frequency (rad s ⁻¹)
ϕ, ϕ, Φ	Mode shapes
ϕ_{rm}	Experimental determined mode shapes

CONTENTS

ρ	Density (kg m^{-3})
σ_r	Standard deviation
θ, Θ, Θ	Rotation (rad)
φ	Angle of cutting tool (rad)
φ_s, φ_e	Entry and exit angle of tooth (rad)
ζ_r	Dimensionless viscous damping coefficient
A	Area (m^2)
a_k	Finite difference coefficients
b_{lim}	Absolute stability limit (m)
c, \mathbf{C}	Viscous damping matrix (Ns m^{-1})
D_δ^B	Backward finite difference operator
D_δ^C	Central finite difference operator
D_δ^F	Forward finite difference operator
E	Young's modulus (N m^{-2})
e_T	Total error
e_{per}	Permissible eccentricity (μm)
f, F, \mathbf{F}	Harmonic forcing (N)
f_c	Chatter frequency (Hz)
F_n, f_t	Normal and tangential cutting forces (N)
f_t	Feed per tooth (m/tooth)
F_{jk}	Low frequency residual

FRF_{or}, \bar{FRF}_{or} Oriented frequency response function (m N^{-1})

G, \mathbf{G} Displacement-Force receptance (m N^{-1})

G_{jk} High frequency residual

h Cutting chip thickness (m)

H, \mathbf{H} Frequency response function (FRF) (m N^{-1})

I Second area moment of inertia (m^4)

k, \mathbf{K} Stiffness matrix (N m^{-1})

$K_s, K_t, K_n, K_{te}, K_{ne}$ Empirical cutting force coefficients (N mm^{-2})

L, \mathbf{L} Displacement-Moment receptance (N^{-1})

m, \mathbf{M} Mass (kg)

M_r Upper bound on measurement perturbation

MSE_{ij} Modal strain energy

$MSECR_j^i$ Modal strain energy change ratio

n Relative displacement of cutting tooth (m)

N, \mathbf{N} Rotation-Force receptance (N^{-1})

N_A Number of actuators

N_M Number of modes

N_S Number of sensors

N_t Number of teeth

N_t^* Average number of teeth in a cut

N_W Highest frequency in modal model (rad s^{-1})

CONTENTS

P, \mathbf{P} Rotation-Moment receptance (Nm^{-1})

Q, \mathbf{Q} Moment (Nm)

$R_{j,k,r}$ Modal residue

S Frequency spectrum

T Truncation coefficient

t Time (s)

t_m Measurement time (s)

T_s Discrete time interval (s)

U_{per} Permissible unbalance (gmm)

y, Y, \mathbf{Y} Displacement (m)

δ Finite spacing (m)

TIR Total indicator runout (μm)

Chapter 1

Introduction

High speed machining operations, such as milling, are widely used in many industries including the aerospace sector. Elevated manufacturing costs coupled with ever more complex-geometry components have led to the need to cut deeper and faster than ever; the dynamics of the structures involved, however, greatly restrict these boundaries. As speed and depth of cut are increased, self-excited vibrations, known as chatter, can occur due to the dynamic interaction between the machining structure and the workpiece. This has undesirable consequences such as poor surface finish, rapid tool and machine wear, and high noise levels, all of which lead to a reduction in production rates and an increase in production costs. Efforts to avoid chatter and reduce its effect on manufacturing processes are therefore of great importance to both academic and industrial engineers alike.

During a milling operation a multi-flute tool is moved relative to a workpiece in order to remove material. The tool is clamped in a tool holder, which is in turn mounted in a rotating spindle. The spindle is usually attached, by a system of bearings, to some housing, which forms part of the main structure of the milling machine. The structure also consists of a machine bed, onto which the workpiece is fixed. An example of the key components of any milling machine are shown in Fig. 1.1.

Selection and design of appropriate cutting tools in an attempt to avoid the

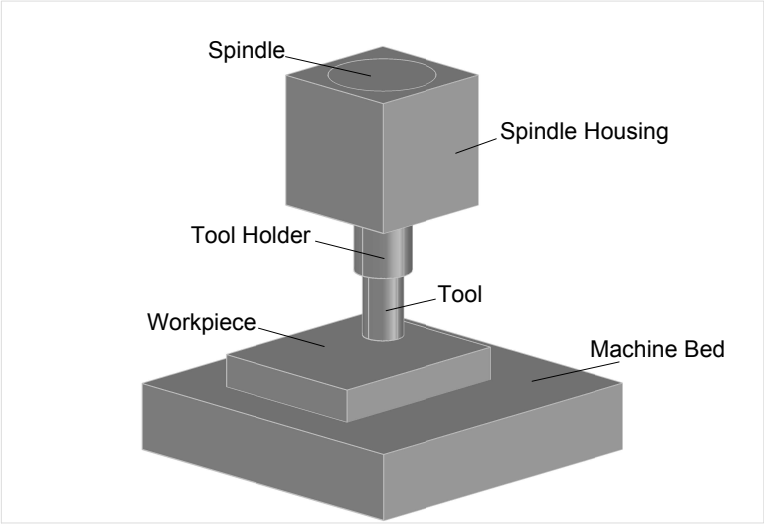


Figure 1.1: Schematic of vertical spindle milling machine

onset of chatter are well established methods in the manufacturing industry; however, the choice of tool (type, diameter, length) is often restricted by the required operation, and since the spindle is fixed by the machine itself, the only other variable component in the machining structure is the tool holder. Little attention has been given to the dynamics of the tool holder; therefore, the aim of this project is to study the effect of the tool holder on cutting stability, with the aim to improve the selection/design process.

1.1 Motivation and objectives

██
██
██
██
██

Whilst the industrial motivation formed the end goal of this research, the concept also sparked three interesting (more fundamental) research objectives. The first is to better understand the effect of tool holder mass (and/or geometry) on machining dynamics. As mentioned above, despite the seemingly simple application to chatter avoidance, little research has been published on the subject. The second objective is to develop the ability to model and optimise tool holder geometry. Aside from the new design, the ability to choose the optimum tool holder from the available range (without having to perform extensive testing) could have significant benefits for the manufacturing industry in general. One method, namely receptance coupling substructure analysis (RCSA), has already been proposed and has the potential to perform this task; however, its experimental limitations have hindered its advancement to the industrial sector. Therefore, another objective is to apply structural modification theory, as proposed by Mottershead and Ram [1], to the tool holder problem, which should alleviate the limitations of RCSA.

During the initial experimental investigations it became clear that the accuracy of the results was severely hampered by inaccurate measurement of rotational degrees of freedom. After reviewing the many possible measurement techniques and comparing this with the industrial capability; the finite difference method, first presented by Sattinger [2], was chosen as the most appropriate means of overcoming this challenge. However, previous research has lacked any robust discussion on the error of the method or how it may be minimised. Therefore, in addition to the objectives described above, this thesis will also explore an error analysis which seeks to minimise the experimental error of the finite difference method for rotational degree of freedom synthesis.

1.2 Outline of chapters

The chapters are written such that they (roughly) follow the development of the research over the previous four years; however, it should be noted that not all chapters were concluded before commencing research for the next chapter.

Chapter 2 : Literature Review

The first chapter reviews some of the published literature relevant to this project. Initially, the chapter discusses milling dynamics and in particular the prediction of milling stability. This leads onto the topic of chatter avoidance, where previous (and continuing) research is presented. Then the field of dynamic substructuring is outlined, before the application of receptance coupling substructure analysis to machining is considered.

Chapter 3 : Background

This chapter summarises the fundamental theory required during this thesis. The theory begins with an overview of structural dynamic modelling, before discussing (in more detail) some of the methods used to predict chatter during a milling operation. Finally the structural modification theory used throughout this thesis is presented.

Chapter 4 : The Effect of Tool Holder Geometry

In chapter 4 the objective to better understand the effect of tool holder geometry is tackled. An experimental data set is presented which details the effect that tool holder diameter has on the tool tip frequency response function (FRF) and thus its effect on chatter stability. The data compares the dynamics of tool holders from two leading manufacturers. The effect of tool holder geometry is also compared to the effect of stickout length, a parameter that has already been successfully used to avoid chatter. This chapter is also used to describe experimental methods, such as impact testing and experimental modal analysis, which are used throughout the thesis.

Chapter 5 : The Effect of Tool Holder Stiffness

In the original scope for the project, the idea of a tuned mass tool holder was proposed; however, the data presented in chapter 4 suggests the stiffness may also play an important role in the effect of tool holder geometry. Therefore, this chapter investigates the effect of stiffness on the tool tip FRF. It is concluded that the stiffness of the holder must be included in any modelling or optimisation methods.

Chapter 6 : Structural Modification of Tool Holder Geometry

Chapter 6 applies the structural modification method of Mottershead and Ram to the tool holder problem. Both the direct and inverse structural modification methods are applied which allow for both modelling and optimisation of holder geometry respectively. Two experimental investigations are carried out to determine the accuracy of the method, one on a simpler spindle rig and, another on a more complex milling machine.

Chapter 7 : [REDACTED]

[REDACTED]

[REDACTED]

[REDACTED]

[REDACTED]

Chapter 8 : Cutting Trials

Once the suitability of the prototype has been demonstrated, the results of a stability trial are presented. The results compare the prediction of the structural modification method with the experimental stability of the prototype. This verifies both the structural modification method and the ability of the prototype to tune the dynamics of an industry standard milling machine.

Chapter 9 : Rotational Degree of Freedom Synthesis

As touched upon above, one of the biggest drawbacks of dynamic substructuring is the need for experimental rotational degree of freedom information. This chapter looks at the application of the finite difference method for rotational degree

of freedom synthesis to beam and beam-like structures. The technique is limited by the user's choice of measurement spacing. Therefore this chapter introduces a new optimised finite difference method for use with non exact data.

Chapter 10 : Conclusions

Conclusions from the work are drawn and future work proposed.

Chapter 2

Literature Review

The thesis begins with a brief review of the relevant literature, focusing on the prediction and avoidance of chatter vibrations in milling operations, dynamic substructuring, and the application of the receptance coupling substructure analysis (RCSA) method to machining dynamics.

2.1 Chatter prediction

Thusty and Polacek [3] and Tobias and Fiswick [4] are today considered pioneers in the field of machining dynamics. They were the first to develop simple one degree-of-freedom stability models of the orthogonal cutting process; and in doing so, paved the way for many other researchers to develop our understanding of the prediction and avoidance of unstable chatter vibrations. Since these early works, several methods to predict the onset of chatter in the more complex milling operation have been proposed. This section will discuss some of the more prominent methods; however, a full and detailed review can be found in either [5] or [6].

Thusty was the first to extend his one degree-of-freedom model to the case of milling dynamics [7], applying his original stability model to a simplified milling problem. His method allowed the user to predict the stability threshold in the spindle speed verses depth of cut plane, a diagram that has come to be known as the stability lobe diagram (SLD) due to the stable peaks or lobes that occur.

Later, Sridhar [8] argued that the dynamics of the milling process are coupled in the feed and normal direction and, therefore, must be modelled in at least two degrees-of-freedom. However, no analytical solution was presented to the problem, instead relying on a numerical method. Tlustý's method has since been updated to include these two degrees-of-freedom [9, 10, 11]. Minis and Yanushevsky [12] also derived an analytical solution to the two degree-of-freedom system by applying Floquet theory to the governing delayed differential equation. Altintas and Budak [13] presented an approximate solution to the system by considering the first term in the Fourier series of the time dependent forces. This method, known as the zeroth order Fourier approach, has become the most widely cited and applied method in milling dynamics and has since been updated to consider multiple harmonics of the periodic cutting forces [14, 15].

Other noteworthy methods for the determination of the stability lobe diagram for a milling operation include the full [16] and semi [17, 18, 19] discretisation methods proposed by Insperger. These numerical time domain methods have the advantage of including several different types of bifurcation (loss of stability) in their analyses; however, the additional accuracy is compromised by long computational times.

2.2 Chatter avoidance

Due to the undesirable consequences of chatter, chatter avoidance is a necessary practice for all manufacturers. Furthermore, traditional milling machines are constantly improving giving the user the ability to cut faster than ever; however, this also results in the consequences of chatter becoming even more detrimental. Therefore the ability to avoid chatter becomes ever more important.

The simplest, and most often employed, chatter avoidance method is to predict the stability boundary, using the methods discussed in section 2.1, and make use of the lobing effect by selecting stable cutting parameters in one of the stable peaks. However, this can severely limit the production rate as the full potential

(maximum spindle speed) of the machine is not recognised. Moreover, it is often the case that certain spindle speeds are required to minimise tool wear, and there is no guarantee that these speeds will align with the stable peaks. Therefore, particularly at high speeds (where the lobing effect becomes more prominent), the ability to reassign or shift the stability lobes becomes particularly beneficial.

Many chatter avoidance methods have been proposed and they fall into two categories, namely passive and active methods. Passive methods include those that seek to modify or optimise the machine structure before cutting commences, whilst active methods involve some form of on-line chatter detection and/or correction. This thesis concentrates on passive methods; however, a good review of the active methods can be found in [5, 6].

Wang and Lee [20] were the first to propose passive modification for chatter avoidance in 1996. The authors performed a sensitivity analysis on data captured from a milling machine, which included the tool, tool holder, and spindle. They found that the spindle was the most flexible component of the three, and redesigned the structure to increase the stability at the tool tip. Whilst this was an important project, the spindle design is chosen by the machine manufacturer and little modification can be applied once the spindle is in place. Marui *et al.* [21] increased the damping capacity of a machine tool rig by inserting friction plates into the length of the tool. The results showed that additional friction could have a significant effect on the modes of the structure; although, the work was not advanced on to a milling machine. Semercigil and Chen [22] suggested a passive vibration absorber to limit the effect of vibrations during milling operations. Kim *et al.* [23] devised a mechanical damper to fix inside the tool, which increased friction and again reduced the amplitude of the vibrations. Sims [24] investigated the use of a vibration absorber attached to the workpiece and proposed a new method to tune its stiffness and damping. Most similar to the proposal of this project, Anderson *et al.* [25] suggested that the natural frequency of tool modes could be altered by attaching an additional stepped mass at the base of the tool; whilst the results on a tool rig were promising, they have not (in the published literature)

been repeated on a full machine structure. One area which has received considerable attention is that of non-uniform geometry milling tools [26, 27, 28, 29, 30]. When the pitch or helix angle of a milling tool is varied between the teeth, the dynamic process of regenerative chatter is disturbed. Therefore, by optimising the pitch and helix angles of a tool for a given milling operation, the chatter free zones of the stability lobe diagram can be controlled.

One research group's work is of particular importance to this project, Ertürk *et al* [31, 32] present the effect of many parameters on the tool tip frequency response function (FRF), including bearing stiffness and damping, and the contact that occurs between the tool and tool holder. Perhaps more importantly in this case, the authors also consider the effect that spindle, tool holder, and tool geometry have on the tool-tip FRF. Since tool geometry has previously been used to optimise the stability of a milling process [33], it is important to understand its effect on the tool tip dynamics.

Firstly, the paper [31] looks at the addition of the holder-tool structure to the spindle. Ertürk *et al.* report that their spindle (tested in free-free boundary conditions), has two rigid body modes at low frequencies and one elastic (bending) mode at a higher frequency. The addition of the holder-tool structure results in two additional elastic modes at higher frequencies; hence, they refer to the lowest frequency elastic mode as the spindle mode.

Ertürk *et al.* then go on to look at the effect of spindle geometry on the FRF. The paper splits the spindle into sections, and shows an increase in diameter or a decrease in length of any of these sections will result in an increase in the natural frequency of the spindle mode. This is true with or without the holder-tool structure in place; however, with it included an increase in natural frequency was also seen in the second and third elastic modes.

The group have also looked at the effect of tool and tool holder geometry on the stability of a milling operation; however, for these results to be fully understood it

is beneficial to first discuss the geometry of tools and tool holders in more detail. Therefore, their results are discussed, and then compared to a new experimental data set, in section 4.3.

A new chatter avoidance method will be developed in this thesis by applying structural modification [1] to milling dynamics; hence, a short review of the relevant literature in this field follows.

2.3 Dynamic substructuring

Throughout this thesis the term dynamic substructuring (DS) is used as a blanket term to include all methods in this field. To begin this section, the aims and outcomes of DS are discussed in general, before a simple categorisation of such methods is given. Then, some of the practical difficulties inherent in such methods are discussed. Following this, the focus shifts to receptance coupling substructure analysis (RCSA), an application of DS to machining.

Accurately capturing the dynamics of a modern engineering structure is difficult; numerical models are limited by unknown geometries, complex boundary conditions, and nonlinearities, whilst experimental models are plagued by measurement errors and poor signal quality. Any attempt to simplify the modelling process is, therefore, of great academic interest. Dynamic substructuring is a method by which different components of a structure can be modelled individually and later combined to form a global model. This allows for the separate components, and their individual difficulties, to be modelled using the most appropriate method (analytical, numerical, or experimental analysis); thus, alleviating some of the problems associated with dynamic modelling.

Moreover, DS is also a powerful tool in vibration control [34]. When combining two or more substructures, both of their resonant and anti-resonant frequencies effect the global dynamics. It is therefore logical that, if the geometry and/or material of one or more of these (preferably numerical) models are optimised,

vibration of the global structure may be minimised.

Dynamic substructuring [35], subcomponent modelling [36], structural modification [1], and component coupling [37], are all terms that have been used to refer to the method of determining the dynamic properties (output model) of a complex structure by combining the dynamic properties (input models) of two or more substructures. Although many other methods exist, a review of some of the most popular frequency domain methods is given below.

2.3.1 Categorisation

Consider the following linear models of two dynamic systems A and B with l and m degrees of freedom (DOF) respectively, which are to be combined at p locations to form the system C . Assuming harmonic forcing $f = Fe^{i\omega t}$, we have

$$\mathbf{Y}_A = [\mathbf{H}_A]_{l \times l} \mathbf{F}_A \quad \mathbf{Y}_B = [\mathbf{H}_B]_{m \times m} \mathbf{F}_B \quad \mathbf{Y}_C = [\mathbf{H}_C]_{n \times n} \mathbf{F}_C \quad (2.1)$$

where \mathbf{Y} is the harmonic displacement vector, \mathbf{F} is the harmonic force vector, \mathbf{H} is the frequency response function matrix containing receptances h_{ij} describing the displacement at DOF i due to forcing at DOF j , and $n = l + m - p$. In an attempt to solve the above problem many different, yet inherently similar, methods have been devised. In order to explain some of the differences in their aims and outcomes the categorisation summarised in Fig. 2.1 can be used. Whilst these labels used here are not original, they will help to highlight the advantages of the structural modification method in this thesis over similar methods that have already been applied to machining dynamics.

1. *Direct or inverse problem?*

The first example of DS is found in Duncan's article [38] in the Philosophical Magazine, which discusses determining the dynamics of a coupled structure from the known receptances of its subcomponents. This formed the basis of the *direct* subcomponent modelling problem, where the combined dynamics of C are predicted

from the models A and B [39]. The most common method is the so called dynamic stiffness, or impedance coupling method whereby compatibility ($\mathbf{Y}_C = \mathbf{Y}_A + \mathbf{Y}_B$) and equilibrium ($\mathbf{F}_C = \mathbf{F}_A + \mathbf{F}_B$) conditions are applied at the connecting degrees of freedom to combine the dynamic stiffness matrices ($\mathbf{H}_C^{-1} = \mathbf{H}_A^{-1} + \mathbf{H}_B^{-1}$). Extensions to this theory have been made, most notably by Jetmundsen *et al.* [40], who noted that matrix partitions could improve the accuracy and computational efficiency by reducing the number and size of the necessary matrix inversions. Such methods have been generalised by Gordis *et al.* [41, 42] and Ren and Beards [43].

The *inverse* DS problem, however, involves seeking particular properties of the subcomponent models that will assign certain dynamic properties to the combined model, usually in the form of particular eigenvalues and/or eigenfunctions. Weissenburger [44] first considered the inverse problem for undamped systems by assigning a natural frequency of C based on the mass and stiffness of one of its subcomponents (A or B). This was extended to the case of damped systems by Pomazal and Snyder [45] and Hallquist and Snyder [46]. O’Callahan and Caou [47] then furthered the research by applying the method to continuous beam-like structures. More recently, Mottershead and Ram [1] presented a solution to the inverse problem that, for simple structures, does not require the inversion of matrices. This is achieved by formulating the solution \mathbf{H}_C in terms of a specific numerator and denominator; then, by setting these terms to zero the user can reassign an antiresonance and/or resonance, respectively.

2. Structural modification or structural coupling?

Although both structural modification and structural coupling follow the same theory, they differ slightly in their input models. Structural modification refers to the coupling of a base model A and a certain modification B , in this case $l = n \geq m$. In other words, no additional DOFs occur in the coupling process. Structural coupling, however, is the process of modelling a complex engineering structure as the assembly of a set of simpler subcomponents, and this results in additional DOFs occurring during in coupling process, i.e. $l > m, n$.

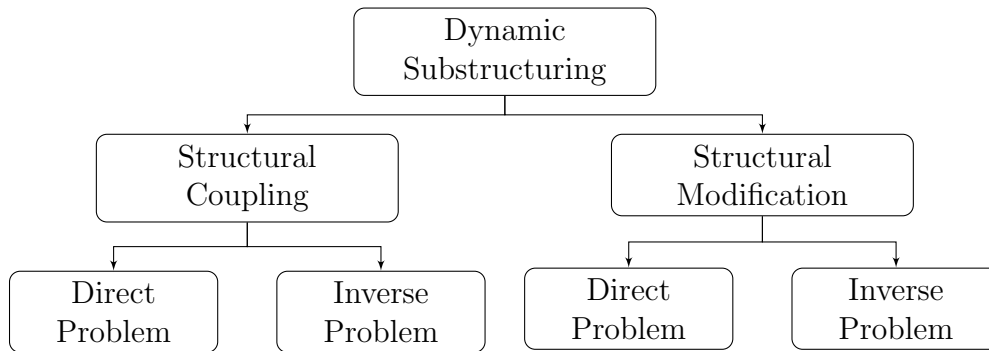


Figure 2.1: Dynamic Substructuring block diagram

Most solutions to the inverse problem fall into the first category as the simpler formulation allows for more direct manipulations of the linear system of equations; however, Kyprianou *et al.* [48] present an extension to the work of Mottershead and Ram that includes the addition of a single DOF. When solving the direct problem it is much simpler to account for additional degrees of freedom. Özgüven [49] presents a modern review of the dynamic stiffness method with extensions to both structural modification and structural coupling. Ferreira and Ewins [50] also present a general formula for coupling linear subcomponents with non-linear joint parameters using receptances.

2.3.2 Limitations of dynamic substructuring

The advantages of DS methods are many, yet it is important to also discuss their many limitations, and note that they should always be used with caution [51]. The above section concentrates on combining frequency domain models in FRF matrix format; however, the coupling procedure may also be carried out in the modal domain. Such methods have one main advantage over frequency domain methods, in that they require less input data (only one row or column of $[\mathbf{H}]$). The amount of analysis required, however, is greater for modal methods, particularly when using experimental data [51]. Hence, this work focuses on frequency domain methods (combining matrices of the form $[\mathbf{H}]$), because of their simplicity to implement, and because the format of their output matches the requirements

of the industrial application.

Receptance matrices (\mathbf{H}) may be constructed from several different sources, falling into three categories: experimental, numerical, and analytical. Each of these constructions has its own advantages and disadvantages in general practice, and some of these limit the usefulness and/or accuracy of DS.

DS methods inevitably involve matrix inversion, and some require the input models to be of dynamic stiffness format ($\mathbf{B} = \mathbf{H}_B^{-1}$), thus the problem can easily become ill-conditioned. Numerical models often need many closely spaced degrees-of-freedom for convergence; unfortunately, matrices with similar elements have high conditioning numbers as their rows and columns are almost linearly dependent [52]. Hence, the use of large finite element models with close nodes will give rise to large numerical errors in the output model. Unlike numerical models, where the dynamic stiffness can be found directly, experimental models are usually found in FRF format. Any small perturbation in the input such as signal noise, location error, or poor curve-fitting/smoothing, will become unstable during inversion and efforts must be taken to reduce any error in the experimental data. Such ill-conditioning problems will lead to spurious peaks appearing in the computed model, which may be difficult to differentiate from the new natural frequencies, several methods have been proposed to improve the quality of experimental models in subcomponent modelling [53, 54, 55].

Another problem that can occur in matrix inversion is rank deficiency, where no inverse exists [52]. When constructing a dynamic stiffness matrix from elemental matrices ($\mathbf{B} = \mathbf{K} - \omega^2\mathbf{M}$), it is essential the number of modes included in the model is greater or equal to that of the number of DOFs. It is also important to consider the out-of-range modes when deciding on the number of modes to include. When using numerical or analytical models, it is usually possible to include modes at much higher frequencies than is actually necessary; therefore, making sure that their effect on the global dynamics is not missed. In experimental modelling it is not always possible to measure higher frequency modes accurately, in

which case residual compensation must be made. Duarte has studied this problem for both modal and frequency domain substructuring methods [37, 56, 57, 58].

Another, perhaps more important, issue with dynamic substructuring arises when flexural behaviour is important in a model, particularly with beam-like structures. In which case, rotational degrees-of-freedom must be included in the model.

2.3.3 Spatial incompleteness

Standard methods to measure the dynamics of a structure usually include an excitation mechanism (impulse hammer or shaker) and a transduction system (piezoelectric accelerometer or Laser Doppler Velocimeter (LDV)) as well as some acquisition hardware. However, such experimental setups are only capable of measuring 25% of the full spatial model required for certain applications. The traditional methods determine the translational receptance \mathbf{H} which is the ratio of the resultant displacement (\mathbf{Y}) due to some excitation force (\mathbf{F}) as seen in 2.1. However, this does not account for the rotational behaviour of the structure. In fact, there are three further receptance FRFs which must also be determined for spatial completeness.

$$\mathbf{N} = \frac{\Theta}{\mathbf{F}} \quad \mathbf{L} = \frac{\mathbf{Y}}{\mathbf{Q}} \quad \mathbf{P} = \frac{\Theta}{\mathbf{Q}} \quad (2.2)$$

where Θ is the rotation of the structure and \mathbf{Q} is a linear moment. There have been many methods proposed to measure or approximate these results, some of the most common are summarised below.

Rotational transducers (most commonly accelerometers) have been available for some time now, and have been successfully used to accurately measure the rotation of a structure in several research papers [59, 60, 61, 62, 63, 64]. The devices are used similarly to that of a traditional accelerometer; however, the angular component of the acceleration is measured instead. Whilst the simplicity of this approach is a clear advantage, it suffers several drawbacks including cost and the inability to measure L and P receptances.

Similar to the idea of the rotational transducers the laser Doppler velocimetry (LDV) technique can be used as a non-contact method to measure the rotation of a structure [65, 66, 67, 68, 69, 70, 71, 72]. The advantage of non-contact methods being that no additional mass is added to the structure; therefore, the interaction of the measurement system does not affect the dynamics of the structure. LDV methods suffer the same drawbacks as rotational transducers, in that they are only capable of measuring rotation and cannot apply a moment. The systems can also easily become costly. The specific disadvantage to this project is the difficulty in positioning (and keeping) the laser on the very thin flute of the tool tip as the tool is impacted.

The more practically unachievable problem of applying a pure moment has also received a lot of attention. These methods attach a fixture (most commonly a T shaped block) to the structure, then by applying translational force the fixture, it is possible to apply both force and moment to the structure. Once the combined dynamics have been measured, the contribution of the T-block must be removed in order to identify the true dynamics of the structure. These methods are often plagued by ill-conditioning problems [73] and it can also be difficult to apply a moment in a single direction [74]. Such methods have not been applied to a milling machine for practical reasons. Attaching such a fixture to the thin flute of a tool would be difficult, moreover, it is likely to cause some damage rendering the tool unusable.

The most appropriate method for determining the rotational degrees of freedom in this project is the finite difference method, whereby the rotational information is synthesised from traditional measurements. Only the most basic equipment (hammer and accelerometer) is necessary and tests can be performed without damaging the tool. The method, including its advantages and disadvantages are discussed in more detail in chapter 9.

2.4 Receptance coupling substructure analysis

Throughout this thesis, the method first proposed by Schmitz *et al.* [75, 76, 77, 78] will be referred to as the receptance coupling substructure analysis (RCSA). In terms of the above categorisation, RCSA falls into the group of direct structural coupling methods and allows the user to predict, from a single measurement set, the tool-tip FRF of the spindle with various tool holders and tools. This involves experimentally modelling the dynamics of the complex spindle structure (\mathbf{H}_A), and combining this with a finite element model of a tool and tool holder (\mathbf{H}_B).

However the coupling methodology relies heavily on the accurate modelling or calculation of the interface properties between the tool and holder, and holder and machine - something which has proved difficult in practice. Several methodologies have been presented for the calculation of these stiffness and damping values, and most involve a multi-point connection with location dependent dynamic values [79, 80], which require a high level of expertise in dynamic modelling. Because of such issues the method has not found its place in industry; however, a lot of further research has been carried out based on the method.

Park *et al.* [33] included rotational degrees-of-freedom in the model, whilst Kivanc and Budak [81] improved on the finite element model of the tool by including a two-segment beam with different area moments of inertia for the fluted and unfluted section of the tool. Duncan and Schmitz [82] improved upon the RCSA method to include holders of varying geometries. One important advancement in the method, was the so-called inverse RCSA method [83], where the holder-spindle structure is tested experimentally, and then an FE model of the tool-holder is uncoupled leaving an experimental model of the spindle only. However, this method also includes two complex non-linear connections making practical applications very difficult.

Using RCSA and an analytical model of a free-free Timishenko beam, Ertürk *et al.* [84] proposed a method to improve upon the efficiency of an FE model. Similarly to the FE method, models for the tool, tool holder, and spindle are constructed

by coupling the dynamics of individual components (uniform Timishenko beams) calculated from the analytical model. The bearing dynamics are included using the structural modification technique presented by Özgüven [49]. Then the three component receptance coupling method is used to couple the three individual models. This was later improved upon to include rotational speed [85]. However, the problem of modelling the interface dynamics still exists.

As discussed in chapter 1, this project has (among others) two main objectives. Firstly, to develop a structural modification method similar to that of RCSA which allows for the optimum tool holder to be selected from a single set of measurements. Secondly, this model will be used with a tubeable tool holder to optimise the dynamics of the machine. Unlike the RCSA method, the work presented in this thesis falls into the structural modification category. The main advantage of this will be to remove the requirement of any knowledge of the interface dynamics. Moreover, both direct and inverse methods will be developed, allowing for simpler and more efficient optimisation of tool holder geometry.

2.5 Summary

In this chapter a review of some of the relevant literature has been presented. Several of the most common models for predicting the onset of chatter were explored, as well as several methods used to avoid such occurrences. Dynamic substructuring was categorised into several groups to include both direct and inverse, as well as coupling and modification methods. The limitations of such methods were also discussed, most notably the issue of spatial incompleteness. Finally, RCSA, an application of a direct structural coupling method to machining dynamics, was discussed, and the advantages of the new chatter avoidance method presented in this thesis highlighted.

Chapter 3

Background

In the previous chapter the relevant literature was reviewed. Now the focus shifts to the fundamental theory that underpins such research, focusing on the particular aspects important to this project. Therefore, this chapter presents an outline on structural dynamics, machining dynamics, and structural modification.

3.1 Structural dynamics

Consider the well known time domain model for a structure with n degrees-of-freedom (DOFs):

$$[\mathbf{M}]_{n \times n} \{\ddot{\mathbf{y}}(t)\}_{n \times 1} + [\mathbf{C}]_{n \times n} \{\dot{\mathbf{y}}(t)\}_{n \times 1} + [\mathbf{K}]_{n \times n} \{\mathbf{y}(t)\}_{n \times 1} = \{\mathbf{f}(t)\}_{n \times 1} \quad (3.1)$$

where \mathbf{M} , \mathbf{C} , and \mathbf{K} are the $n \times n$ square mass, damping, and stiffness matrices, $\ddot{\mathbf{y}}(t)$, $\dot{\mathbf{y}}(t)$, and $\mathbf{y}(t)$ are the $n \times 1$ vectors of accelerations, velocities, and displacements at time t , and $\mathbf{f}(t)$ is an $n \times 1$ vector of input forces at time t . Although many damping models exist [51], this project will consider only the most common viscous damping model and, in particular, the proportional viscous damping model, whereby the damping matrix may be written as a linear combination of the mass and stiffness matrices:

$$\mathbf{C} = \alpha \mathbf{M} + \beta \mathbf{K} \quad (3.2)$$

The dynamics of a structure may also be modelled in the frequency, and modal domains, and conversion between the three model types will play a vital role in this thesis. A frequency domain model can be found by applying the Fourier transform [86] to the time domain model in Eq. (3.1). Defining the Fourier transform of the vectors $\mathbf{y}(t)$ and $\mathbf{f}(t)$ as follows

$$\mathbf{Y}(j\omega) = \int_{-\infty}^{\infty} \mathbf{y}(t)e^{-j\omega t} dt \quad \mathbf{F}(j\omega) = \int_{-\infty}^{\infty} \mathbf{f}(t)e^{-j\omega t} dt \quad (3.3)$$

noting that each degree-of-freedom has its own transform, then it can be found that

$$(-\omega^2\mathbf{M} + j\omega\mathbf{C} + \mathbf{K})\mathbf{Y}(j\omega) = \mathbf{F}(j\omega) \quad (3.4)$$

the term in brackets is known as the dynamic stiffness and relates the input force to the output displacement in the frequency domain. Another more common result is the frequency response function (FRF) or receptance given by:

$$\mathbf{H}(j\omega) = \frac{\mathbf{Y}(j\omega)}{\mathbf{F}(j\omega)} = [-\omega^2\mathbf{M} + j\omega\mathbf{C} + \mathbf{K}]^{-1} \quad (3.5)$$

Here, each element of the $n \times n$ FRF matrix $\mathbf{H}(j\omega)$ contains a frequency dependent relationship between each of the DOFs in the model.

The time domain model can also be converted into a modal domain model via a method known as modal analysis. A full description of analytical modal analysis is not necessary for this thesis; instead, a brief outline is sufficient. Analytical modal analysis is the process of solving the eigenvalue problem that arises from the unforced equation of motion given in Eq. (3.1). The solution set includes the eigenfunctions or mode shapes ϕ_r and eigenvalues $\lambda_r = \omega_r^2$ (where ω_r are the natural frequencies). Since the mass, damping, and stiffness matrices are inherently coupled (i.e. the degrees-of-freedom are connected) analytical solutions only exist for the most simple of structures. Instead the system must be uncoupled by pre- and post-multiplying by the mode shapes matrix, which relies on the orthogonality properties of the model. The result is a set of uncoupled equations which can be solved in the same manner as any single degree-of-freedom sys-

tem. Experimental modal analysis is also a vital technique used to determine the dynamic properties of real structures, and this will be discussed later in chapter 4.

Using a similar method it is also possible to find a simple analytical relationship between the frequency and modal domain models. Let $[\Phi]_{n \times n} = [\phi_1, \phi_2, \dots, \phi_n]$ be a matrix of n orthonormal (or mass normalised) normal mode shapes ϕ_r , then we have that:

$$\begin{aligned} [\Phi]^T [\mathbf{M}] [\Phi] &= \mathbf{I} \\ [\Phi]^T [\mathbf{C}] [\Phi] &= \text{diag}(2\zeta_r \omega_r) \\ [\Phi]^T [\mathbf{K}] [\Phi] &= \text{diag}(\omega_r^2) \end{aligned} \quad (3.6)$$

where \mathbf{I} is the $n \times n$ identity matrix, ζ_r is the well known dimensionless viscous damping ratio for the r^{th} mode, ω_r is the natural frequency of the r^{th} mode, $\text{diag}(2\zeta_r \omega_r)$ is a matrix with diagonal elements $2\zeta_r \omega_r$, and $\text{diag}(\omega_r^2)$ is a matrix with diagonal elements ω_r^2 . Therefore it can be seen that:

$$\begin{aligned} [\Phi]^T [\mathbf{H}(j\omega)]^{-1} [\Phi] &= [\Phi]^T [-\omega^2 \mathbf{M} + j\omega \mathbf{C} + \mathbf{K}] [\Phi] \\ &= [-\omega^2 \mathbf{I} + j\omega [2\zeta_r \omega_r] + [\omega_r^2]] \end{aligned} \quad (3.7)$$

therefore

$$[\mathbf{H}(j\omega)] = [\Phi] [-\omega^2 \mathbf{I} + j\omega [2\zeta_r \omega_r] + [\omega_r^2]]^{-1} [\Phi]^T \quad (3.8)$$

then each individual element of the FRF matrix is given by

$$H_{ik}(j\omega) = \sum_{r=1}^n \frac{\phi_r(x_i) \phi_r(x_k)}{-\omega^2 + 2j\zeta_r \omega_r \omega + \omega_r^2} \quad (3.9)$$

where x_i refers to the input location and x_j refers to the output location.

3.2 Machining dynamics

Chatter is a form of self-excited vibration that can occur during cutting operations, and the field of machining dynamics tends to concentrate on the prediction

and prevention of such vibrations. In the case of milling, as each tooth on the cutter hits the workpiece a relative vibration between the two structures can occur, resulting in a wave being imprinted onto the surface of the workpiece. As the following tooth passes, this wavy surface is removed and replaced by another. If these waves are out of phase, the instantaneous thickness of the chip being removed will grow exponentially, causing an unstable excitation of the tool. Therefore, the stability of a milling system is governed by the instantaneous chip thickness h .

This thesis will make use of two methods to determine the stability of a milling operation, namely the average tooth angle and zeroth order Fourier series techniques, both of which are discussed below. These methods are both closed form frequency domain solutions to the equation of motion; thus, they require considerably less time and computing power than other numerical methods. Another advantage of their closed form solutions, is the ability to combine their results with structural modification theory analytically. The average tooth angle approach is perhaps the mathematically simplest of all such methods and will be used in the development of the structural modification method. Whilst the zeroth order Fourier series approach is most commonly applied in the reviewed literature and industrial software.

3.2.1 Average tooth angle approach

A full description of the mechanics of a cutting tool is not required for this thesis; however, the original derivation can be found in Tlustý's textbook [7]. As with any linear structure, the vibrations of a cutting tool can be determined from the models discussed in section 3.1 and are usually represented in the Cartesian coordinate system (X, Y) (the tool is assumed to be rigid in the Z or axial direction). However, the instantaneous chip thickness is measured along the instantaneous surface normal to the cutting tool. Therefore, Tlustý began his stability analysis [9] by projecting the x and y displacements of the tool onto the surface normal

n such that:

$$n = x \sin \varphi - y \cos \varphi \quad (3.10)$$

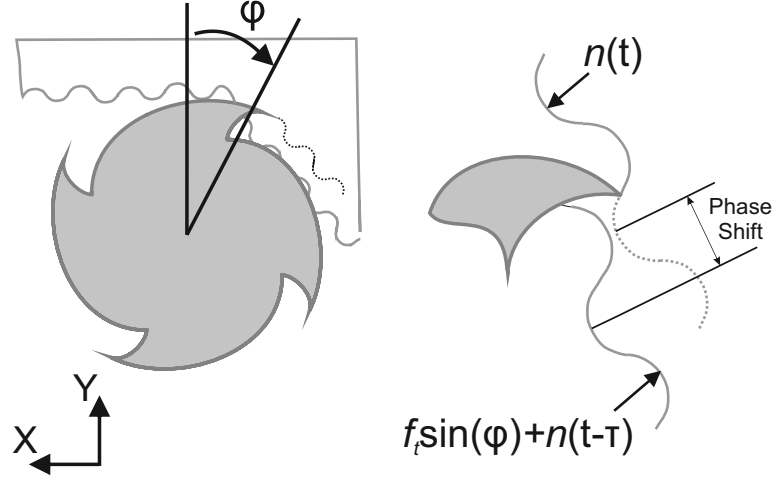


Figure 3.1: Geometry of instantaneous chip thickness calculation for milling

Here, φ is the instantaneous angle of the cutting tool as shown in Fig. 3.1. Then, the chip thickness is given by

$$h(t) = f_t \sin \varphi + n(t - \tau) - n(t) \quad (3.11)$$

$$= f_t \sin \varphi + \sin \varphi (x(t - \tau) - x(t)) + \cos \varphi (y(t - \tau) - y(t)) \quad (3.12)$$

where f_t is the feed per tooth, τ is the time delay between successive teeth, $n(t - \tau)$, $x(t - \tau)$, $y(t - \tau)$ are the relative displacement from the previous tooth pass in the surface normal, X, and Y directions respectively, and $n(t)$, $x(t)$, $y(t)$ are the relative displacement from the current tooth pass in the surface normal, X, and Y direction respectively. One of the obstacles in determining the stability of this system is the inherent time dependence of the force. Tlustý solved this by

assuming an average tool angle φ_{avg} , therefore Eq. (3.12) may be rewritten:

$$h(t) = f_t \sin \varphi_{avg} + \sin \varphi_{avg}(x(t - \tau) - x(t)) + \cos \varphi_{avg}(y(t - \tau) - y(t)) \quad (3.13)$$

$$= h_0 + \sin \varphi_{avg}(x(t - \tau) - x(t)) + \cos \varphi_{avg}(y(t - \tau) - y(t)) \quad (3.14)$$

The cutting forces which act upon the tool are then approximated as the product of the chip area A and an empirical coefficient K_s , which is dependent on the specific workpiece material [87], tool geometry [88], and to lesser extent spindle speed [89, 90]. Therefore the cutting force is given by

$$F = K_s A = K_s b h \quad (3.15)$$

where b is the axial depth of cut. The cutting force can then be resolved into its normal (F_n) and tangential (F_t) components such that:

$$F_n = \cos(\beta) K_s b h(t) \quad \text{and} \quad F_t = \sin(\beta) K_s b h(t) \quad (3.16)$$

where β is the angle of the cutting force F relative to the cut as seen in Fig. 3.2.

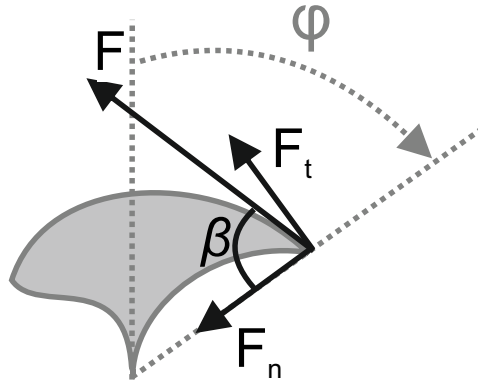


Figure 3.2: Cutting force geometry for milling operations

These forces can then be projected into the X and Y direction to give that:

$$F_X = F_t \cos(\varphi_{avg}) + F_n \sin(\varphi_{avg}) \quad \text{and} \quad F_Y = F_t \sin(\varphi_{avg}) - F_n \cos(\varphi_{avg}) \quad (3.17)$$

Then combining Eq. 3.15 with Eq. 3.17 gives:

$$\begin{Bmatrix} F_X \\ F_Y \end{Bmatrix} = K_s b h \begin{bmatrix} \sin(\beta) & \cos(\beta) \\ -\cos(\beta) & \sin(\beta) \end{bmatrix} \begin{Bmatrix} \cos(\varphi_{avg}) \\ \sin(\varphi_{avg}) \end{Bmatrix} \quad (3.18)$$

The time dependent forces are then transformed into the Laplace domain using the well known Laplace transform [86]:

$$\begin{Bmatrix} F_X(s) \\ F_Y(s) \end{Bmatrix} = K_s b h(s) \begin{bmatrix} \sin(\beta) & \cos(\beta) \\ -\cos(\beta) & \sin(\beta) \end{bmatrix} \begin{Bmatrix} \cos(\varphi_{avg}) \\ \sin(\varphi_{avg}) \end{Bmatrix} \quad (3.19)$$

The time domain model that relates the displacements x and y with the forces F_X and F_Y respectively (i.e. Eq. 3.1) can also be transformed into the Laplace domain, resulting in:

$$\begin{Bmatrix} x(s) \\ y(s) \end{Bmatrix} = \begin{bmatrix} H_X(s) & 0 \\ 0 & H_Y(s) \end{bmatrix} \begin{Bmatrix} F_X(s) \\ F_Y(s) \end{Bmatrix} \quad (3.20)$$

Combining Eq. 3.19 with Eq. 3.20 gives that:

$$\begin{Bmatrix} x(s) \\ y(s) \end{Bmatrix} = K_s b h(s) \begin{bmatrix} \sin(\beta) & \cos(\beta) \\ -\cos(\beta) & \sin(\beta) \end{bmatrix} \begin{Bmatrix} \cos(\varphi_{avg}) \\ \sin(\varphi_{avg}) \end{Bmatrix} \begin{bmatrix} H_X(s) & 0 \\ 0 & H_Y(s) \end{bmatrix} \quad (3.21)$$

$$= K_s b h(s) \begin{bmatrix} \tilde{\mu}_X H_X(s) & 0 \\ 0 & \tilde{\mu}_Y H_Y(s) \end{bmatrix} \quad (3.22)$$

Now, the equation for the dynamic chip thickness (Eq. 3.14) is also transformed into the Laplace domain:

$$h(s) = h_0 + \sin(\varphi_{avg})(e^{-s\tau} - 1)x(s) + \cos(\varphi_{avg})(e^{-s\tau} - 1)y(s) \quad (3.23)$$

Substituting Eq. 3.22 into Eq. 3.23 results in:

$$h(s) = h_0 + (e^{-s\tau} - 1)K_s b h(s) (\sin(\varphi_{avg}) \tilde{\mu}_X H_X(s) + \cos(\varphi_{avg}) \tilde{\mu}_Y H_Y(s)) \quad (3.24)$$

$$= h_0 + (e^{-s\tau} - 1)K_s b h(s) (\mu_X H_X(s) + \mu_Y H_Y(s)) \quad (3.25)$$

$$= h_0 + (e^{-s\tau} - 1)K_s b h(s) (H_{or}(s)) \quad (3.26)$$

where $H_{or}(s)$ is commonly referred to as the oriented transfer function. Then rearranging to find the transfer function between the dynamic chip thickness and static chip thickness:

$$\frac{h(s)}{h_0} = \frac{1}{1 + (1 - e^{-s\tau})K_s b H_{or}(s)} \quad (3.27)$$

which has characteristic equation

$$1 + (1 - e^{-s\tau})K_s b H_{or}(s) \quad (3.28)$$

Thusty then determined the stability of the characteristic equation by setting the root equal to $s = \sigma + j\omega_c$. When the real part is positive ($s > 0$) the system is unstable, whilst when the real part is negative the system is stable. Finally, when the real part is zero ($s = j\omega_c$) the system is critically stable. Therefore to determine the stability threshold of the milling system, Thusty considered the critically stable characteristic equation:

$$1 + (1 - e^{-j\omega_c\tau})K_s b_{lim} H_{or}(j\omega_c) \quad (3.29)$$

where b_{lim} is the critical or limiting axial depth of cut. The stability threshold in the spindle speed vs. axial depth of cut plane can be found by setting both the

real and imaginary parts of the characteristic equation to zero:

$$b_{lim} = \frac{-1}{2K_s \text{Re}[H_{or}(j\omega_c)]} \quad (3.30)$$

$$\Omega = \frac{60f_c}{(L + \frac{\epsilon}{2\pi})}$$

with

$$\epsilon = 2\pi - 2 \tan^{-1} \left(\frac{\text{Re}[H_{or}(j\omega_c)]}{\text{Im}[H_{or}(j\omega_c)]} \right) \quad (3.31)$$

where f_c is the chatter frequency (ω_c) in Hz and $L = 0, 1, 2, \dots$ is the stability lobe number.

The stability analysis presented above assumes that only one tooth on the tool is engaged in the cut at any given time, which is not always true depending on the radial depth of cut and tool geometry. Therefore, Tlustý extended his stability analysis to consider forces from the average number of teeth in the cut at any one time (N_t^*), where

$$N_t^* = \frac{N_t(\varphi_e - \varphi_s)}{2\pi} \quad (3.32)$$

and φ_e and φ_s are the exit and entry angles of the tool in radians. Performing the same stability analysis as above, now with the average forces, results in:

$$b_{lim} = \frac{-1}{2K_s \text{Re}[H_{or}(j\omega_c)]N_t^*} \quad (3.33)$$

$$\Omega = \frac{60f_c}{N_t(L + \frac{\epsilon}{2\pi})}$$

with

$$\epsilon = 2\pi - 2 \tan^{-1} \left(\frac{\text{Re}[H_{or}(j\omega_c)]}{\text{Im}[H_{or}(j\omega_c)]} \right) \quad (3.34)$$

In the relevant literature it is common to see the oriented transfer function/frequency response function ($H_{or}(j\omega_c)$) denoted as $\text{FRF}_{or}(j\omega_c)$ and this notation will be adopted throughout the rest of this thesis.

3.2.2 Fourier series approach

Altintas and Budak [91] also developed a frequency domain technique for stability lobe determination, using a different method to remove the time dependence of the dynamic system. The initial difference in their approach is that the positive X direction is now taken to be in the feed direction. This results in the projection of the x and y displacements to be:

$$n = -x \sin \varphi - y \cos \varphi \quad (3.35)$$

Then, similarly to above the instantaneous chip thickness is given by

$$h(\varphi_j) = (f_t \sin \varphi_j + n_{j-1} - n_j)g(\varphi_j) \quad (3.36)$$

where the subscript j refers to the current tooth and $j - 1$ to the previous tooth, and

$$g(\varphi) = \begin{cases} 1, & \text{if } \varphi_s \leq \varphi_j \leq \varphi_e. \\ 0, & \text{if } \varphi_j < \varphi_s, \varphi_j > \varphi_e. \end{cases} \quad (3.37)$$

Although the notation used by Altintas and Budak differs slightly from the Trusty method, this is essentially the same equation as Eq. (3.12). The time dependence of the system comes from Eq. (3.35) where $\varphi = 2\pi\Omega t/60$. The static component of Eq. (3.36) can be neglected as it does not contribute to the dynamic chip thickness regeneration, then substituting Eq. (3.35) into Eq. (3.36) results in:

$$h(\varphi_j) = (\Delta x \sin \varphi_j + \Delta y \cos \varphi_j)g(\varphi_j) \quad (3.38)$$

where $\Delta x = x_j - x_{j-1}$ and $\Delta y = y_j - y_{j-1}$, and the subscripts j and $j - 1$ refer to the current and previous tool respectively. Similarly to the previous method, the force components in the tangential and radial directions are given by

$$F_t(\varphi_j) = K_t b h(\varphi_j) \quad F_n(\varphi_j) = K_n F_t = K_n K_t b h(\varphi_j) \quad (3.39)$$

These forces are then projected onto the Cartesian coordinate system of the tool,

such that

$$\begin{aligned} F_X(\varphi_j) &= -F_t \cos \varphi_j - F_n \sin \varphi_j \\ F_Y(\varphi_j) &= F_t \sin \varphi_j - F_n \cos \varphi_j \end{aligned} \quad (3.40)$$

the contributions from all teeth are then summed to account for potentially multiple teeth in the cut at any one time

$$F_X = \sum_{j=1}^{N_t} F_X(\varphi_j) \quad F_Y = \sum_{j=1}^{N_t} F_Y(\varphi_j) \quad (3.41)$$

These individual force expressions are combined and arranged (with the help of some well known trigonometric identities) into the following matrix format

$$\begin{pmatrix} F_X \\ F_Y \end{pmatrix} = \frac{1}{2} b K_t \begin{bmatrix} \alpha_{XX}(t) & \alpha_{XY}(t) \\ \alpha_{YX}(t) & \alpha_{YY}(t) \end{bmatrix} \begin{pmatrix} \Delta x \\ \Delta y \end{pmatrix} = \frac{1}{2} b K_t [\mathbf{A}(t)] (\mathbf{\Delta}) \quad (3.42)$$

where $\alpha_{XX}(t)$, $\alpha_{XY}(t)$, $\alpha_{YX}(t)$, and $\alpha_{YY}(t)$ are known as the time varying dynamic force coefficients. To determine the stability of the system the time dependence of these coefficients must be removed, Altintas and Budak achieved this by approximating the matrix $\mathbf{A}(t)$ with its zeroth order Fourier series expansion giving

$$[\mathbf{A}_0] = \frac{N_t}{2\pi} \begin{bmatrix} \alpha_{XX} & \alpha_{XY} \\ \alpha_{YX} & \alpha_{YY} \end{bmatrix} \quad (3.43)$$

where

$$\begin{aligned} \alpha_{XX} &= \frac{1}{2} \left(\cos 2\varphi - 2K_n \varphi + K_n \sin 2\varphi \right) \Big|_{\varphi_s}^{\varphi_e} \\ \alpha_{XY} &= \frac{1}{2} \left(-\sin 2\varphi - 2\varphi + K_n \cos 2\varphi \right) \Big|_{\varphi_s}^{\varphi_e} \\ \alpha_{YX} &= \frac{1}{2} \left(-\sin 2\varphi + 2\varphi + K_n \cos 2\varphi \right) \Big|_{\varphi_s}^{\varphi_e} \\ \alpha_{YY} &= \frac{1}{2} \left(-\cos 2\varphi - 2K_n \varphi - K_n \sin \varphi \right) \Big|_{\varphi_s}^{\varphi_e} \end{aligned} \quad (3.44)$$

are now time independent.

This system is then transformed into the Laplace domain by taking the Laplace transform and substituting for the tool transfer function matrix $[\mathbf{H}(s)]$, resulting in

$$\{F(s)\} = \frac{1}{2}bK_t\{[\mathbf{A}_0](1 - e^{-js\tau})[\mathbf{H}(s)]\}\{F(s)\} \quad (3.45)$$

where τ (as above) is the delay between two consecutive teeth. The stability problem is now reduced to a simple eigenvalue problem. If the root of the characteristic equation is given by $s = \sigma + j\omega_c$. Then, if the real part of the root is positive ($\sigma > 0$), the chatter vibration will grow indefinitely and the system will be unstable; whilst if the real part is negative ($\sigma < 0$), the vibration will subside over time and the system will be stable. When the real part of the root is zero ($s = j\omega_c$), the system is said to be critically stable; therefore, in order to predict the stability threshold the eigenvalue problem becomes:

$$[\mathbf{I}] = \frac{1}{2}bK_t[\mathbf{A}_0](1 - e^{-j\omega_c\tau})[\mathbf{H}(j\omega_c)] \quad (3.46)$$

where both sides of Eq. 3.45 have been divided by the force vector. The notation can be further simplified by introducing the oriented FRF matrix $[\overline{\mathbf{FRF}}_{or}(j\omega_c)]$:

$$[\overline{\mathbf{FRF}}_{or}(j\omega_c)] = \begin{bmatrix} \alpha_{XX}H_{XX}(j\omega_c) & \alpha_{XY}H_{YY}(j\omega_c) \\ \alpha_{YX}H_{XX}(j\omega_c) & \alpha_{YY}H_{YY}(j\omega_c) \end{bmatrix} = \frac{2\pi}{N_t}[\mathbf{A}_0][\mathbf{H}(j\omega_c)] \quad (3.47)$$

Here, $H_{XX}(j\omega_c)$ and $H_{YY}(j\omega_c)$ are the X- and Y-direction direct tool FRFs respectively, and the cross FRF terms relating the X- and Y-directions have been set to zero. This assumes that, due to the orthogonal relationship between the X- and Y-directions, the crosstalk between the two is substantially lower than the direct measurements and will therefore have very little effect on the final solution. Therefore:

$$[\mathbf{I}] = \frac{N}{4\pi}bK_t(1 - e^{-j\omega_c\tau})[\overline{\mathbf{FRF}}_{or}(j\omega_c)] \quad (3.48)$$

Then the eigenvalue of the characteristic equation is given by:

$$\Lambda = -\frac{N_t}{4\pi}bK_t(1 - e^{-j\omega_c\tau}) \quad (3.49)$$

and

$$[\mathbf{I}] + \Lambda[\overline{\mathbf{FRF}}_{or}(j\omega_c)] = 0 \quad (3.50)$$

The system is solved by setting the determinant of the characteristic equation (Eq. 3.50) to zero. This results in the equivalent equations for the limiting axial depth of cut b_{lim} and the spindle speed Ω

$$b_{lim} = -\frac{2\pi\text{Re}[\Lambda]}{N_tK_t} \left(1 + \left(\frac{\text{Im}[\Lambda]}{\text{Re}[\Lambda]} \right)^2 \right) \quad (3.51)$$

and

$$\Omega = \frac{60}{N_t\tau} \quad (3.52)$$

$$\tau = \frac{1}{\omega_c}(\epsilon + 2k\pi) \quad \text{with} \quad \epsilon = \pi - 2 \tan^{-1} \left(\frac{\text{Im}[\Lambda]}{\text{Re}[\Lambda]} \right)$$

where $k = 0, 1, 2, \dots$ is the number of waves between teeth and is equivalent to N in the Tlustý model. To generate the stability lobe diagrams using this model, firstly the α values are calculated. These are dependent on ϕ_s and ϕ_e and thus on the type of milling operation. Then, for a particular frequency, the oriented FRF matrix ($\overline{\mathbf{FRF}}_{or}$) is calculated and the eigenvalue problem in Eq. (3.50) solved. The eigenvalue problem simplifies to a second order polynomial giving two solutions; therefore, the stability limit for both solutions must be calculated and the lowest value of b_{lim} used. Once the stability limit has been calculated the spindle speeds are evaluated.

Both of the methods presented above make use of an approximation in order to remove the time dependence of the cutting forces, which results in some level of inaccuracy. The accuracy of both techniques increases as the width of cut is increased [76]. This thesis will only focus on milling operations with a width of

cut at least 50% of the tool diameter, and are therefore considered to produce accurate results [92]. There are, however, cases where the Fourier series produces more accurate predictions. For instance, in the case of slotting (where the width of cut is 100% of tool diameter) the directional orientation factor μ_Y in the average tooth angle method is zero, and the contribution of the dynamics in the Y direction is neglected. This causes some discrepancy in the stability limit b_{lim} . The stability lobe diagrams produced from both methods for an exemplar slotting cut are given in Fig. 3.3. It can be seen that whilst there is some discrepancy in the stability limit, the locations of the peaks (controlled by natural frequency) are very similar. For this reason the experimental investigations in this project will make use of the zeroth order Fourier series method, whilst the simpler average tooth angle technique is used to calculate the location of these peaks.

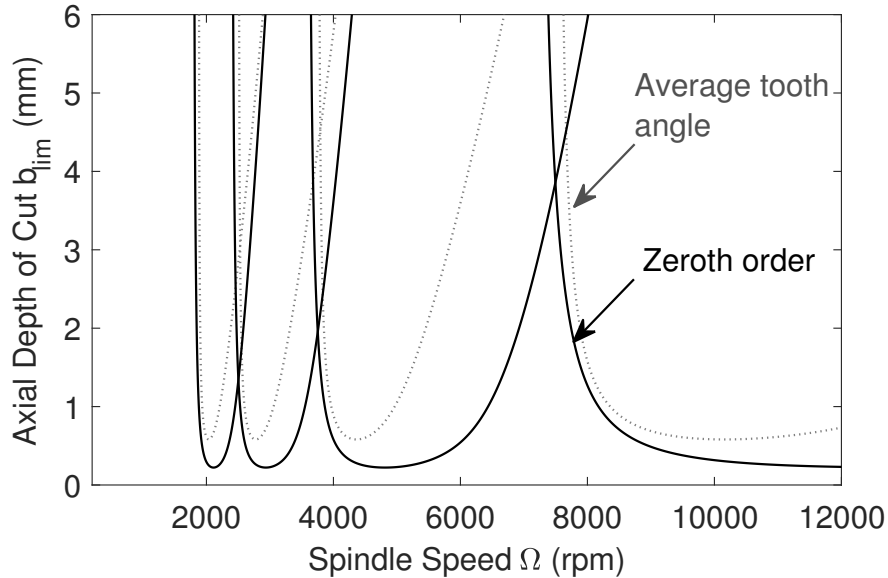


Figure 3.3: Stability lobe diagrams for an exemplar slotting cut using the average tooth angle (---) and the zeroth order Fourier series (—) methods

3.3 Structural modification

This purpose of this section is to give a brief outline of the structural modification method as presented by Mottershead and Ram [1]. The authors begins with

a discussion on unit rank structural modifications, which include point masses, grounded springs, and springs connected between two points. Before moving onto the more realistic higher rank method that allows for modification by continuous structures such as beams.

3.3.1 Unit rank structural modification

For simple single degree-of-freedom modifications, of the form $b(j\omega) = k + j\omega c - \omega^2 m$, structural modification may be carried out without matrix inverses as follows. By applying compatibility and equilibrium conditions to models A and B (given in Eq. (2.1)), it is given that:

$$\mathbf{H}_C^{-1}(j\omega) = \mathbf{H}_A^{-1}(j\omega) + \mathbf{B}(j\omega) \quad (3.53)$$

at a particular frequency ω . Therefore

$$\mathbf{H}_C(j\omega) = (\mathbf{H}_A^{-1}(j\omega) + \mathbf{B}(j\omega))^{-1} \quad (3.54)$$

Since \mathbf{B} now has only a single element b we may rewrite this as:

$$\mathbf{H}_C(j\omega) = (\mathbf{H}_A^{-1}(j\omega) + b_r(j\omega) \mathbf{e}_r \mathbf{e}_r^T)^{-1} \quad (3.55)$$

where \mathbf{e}_r is the r^{th} unit vector of length l , and r is the DOF to be modified. Then by applying the Sherman-Morrison formula [93]:

$$(\mathbf{A} + \mathbf{b} \mathbf{c}^T)^{-1} = \mathbf{A}^{-1} - \frac{\mathbf{A}^{-1} \mathbf{b} \mathbf{c}^T \mathbf{A}^{-1}}{1 + \mathbf{c}^T \mathbf{A}^{-1} \mathbf{b}} \quad (3.56)$$

we have that

$$\mathbf{H}_C(j\omega) = \mathbf{H}_A(j\omega) - \frac{b_r(j\omega) \mathbf{H}_A(j\omega) \mathbf{e}_r \mathbf{e}_r^T \mathbf{H}_A(j\omega)}{1 + b_r(j\omega) \mathbf{e}_r^T \mathbf{H}_A(j\omega) \mathbf{e}_r} \quad (3.57)$$

The pq^{th} element from \mathbf{H}_C can then be selected by

$$\begin{aligned} h_{C_{pq}}(j\omega) &= \mathbf{e}_p^T \mathbf{H}_C \mathbf{e}_q \\ &= \frac{h_{A_{pq}}(j\omega) + b_r(j\omega)(h_{A_{pq}}(j\omega)h_{A_{rr}}(j\omega) - h_{A_{pr}}(j\omega)h_{A_{rq}}(j\omega))}{1 + b_r(j\omega)h_{A_{rr}}(j\omega)} \end{aligned} \quad (3.58)$$

The poles (or natural frequencies) of C may then be determined by setting the denominator of Eq. (3.58) to zero. Similarly the zeros (or antiresonances) can be found by setting the numerator to zero.

Certain simplifications to this can also be made in the following cases:

(i) A point receptance of the modified system, $p = q$

$$h_{C_{qq}} = \frac{h_{A_{qq}}(j\omega) + b_r(j\omega)(h_{A_{qq}}(j\omega)h_{A_{rr}}(j\omega) - h_{A_{qr}}(j\omega)h_{A_{rq}}(j\omega))}{1 + b_r(j\omega)h_{A_{rr}}(j\omega)} \quad (3.59)$$

(ii) A cross-receptance with modification at one of the coordinates, $p = r$

$$h_{C_{rq}} = \frac{h_{A_{rq}}(j\omega)}{1 + b_r(j\omega)h_{A_{rr}}(j\omega)} \quad (3.60)$$

(ii) A point receptance with modification at the same coordinate, $p = q = r$

$$h_{C_{rr}} = \frac{h_{A_{rr}}(j\omega)}{1 + b_r(j\omega)h_{A_{rr}}(j\omega)} \quad (3.61)$$

Whilst the unit rank method has the benefit of simplicity, for more realistic modifications (such as the addition of a beam [94]), the higher rank method produces more accurate results.

3.3.2 Higher rank structural modification

Using the dynamic stiffness model discussed above, models A and B are combined such that:

$$\mathbf{H}_C^{-1} = \mathbf{H}_A^{-1} + \mathbf{B} \quad (3.62)$$

The notation $(j\omega)$ has been dropped here for simplicity; however, it should be noted that the equations in this section are still applicable at a given frequency ω .

This formulation is inconvenient for numerical application as it involves multiple matrix inversions; therefore, it may be rewritten as:

$$\begin{aligned}\mathbf{H}_C^{-1} &= \mathbf{H}_A^{-1}[\mathbf{I} + \mathbf{H}_A\mathbf{H}_B^{-1}] \\ \mathbf{H}_C &= [\mathbf{I} + \mathbf{H}_A\mathbf{H}_B^{-1}]^{-1}\mathbf{H}_A\end{aligned}\quad (3.63)$$

This equation is referred to as the direct structural modification method. Given the dynamics of two structures A and B , the direct method allows for simple prediction of their combined dynamics C . However, this is not an effective method for optimisation purposes, instead the inverse structural modification method is derived.

If model B is only partially constructed, leaving it as a function of some unknown geometric modification parameter α i.e. $\mathbf{B} = \mathbf{B}(\alpha)$, then the inverse structural modification equation can be found by multiplying the numerator and denominator of Eq. (3.63) by the determinant of the inverse term, such that

$$\mathbf{H}_C = \frac{\det(\mathbf{I} + \mathbf{H}_A\mathbf{B}(\alpha))[\mathbf{I} + \mathbf{H}_A\mathbf{B}(\alpha)]^{-1}\mathbf{H}_A}{\det(\mathbf{I} + \mathbf{H}_A\mathbf{B}(\alpha))} = \frac{\text{adj}(\mathbf{I} + \mathbf{H}_A\mathbf{B}(\alpha))\mathbf{H}_A}{\det(\mathbf{I} + \mathbf{H}_A\mathbf{B}(\alpha))}\quad (3.64)$$

The antiresonance of the ij^{th} receptance is then given by $[\text{adj}(\mathbf{I} + \mathbf{H}_A\mathbf{B}(\alpha))\mathbf{H}_A]_{ij} = 0$, whilst its natural frequencies are given by $\det(\mathbf{I} + \mathbf{H}_A\mathbf{B}(\alpha)) = 0$. For simple modifications these equations may have algebraic solutions for the modification parameter (α), however for more complex modifications a numerical solution may be necessary. The full derivation of this equation can be found in [1].

3.4 Summary

In this chapter an outline of some the more relevant theory has been developed. Firstly, the fundamentals of structural dynamics were discussed, including con-

verting models between domains. Secondly, the average tooth angle and zeroth order Fourier series approaches for determining the stability lobe diagram of a milling operation were presented. Finally, the structural modification formulation of Mottershead and Ram was summarised.

Chapter 4

The Effect of Tool Holder Geometry

The main purpose of this chapter is to verify the initial observations from the industrial partner, who have proposed that tool holder geometry can have a significant effect on the dynamics of a milling machine. To the author's knowledge, there exists no experimental data set that demonstrates the effect of this geometry on the tool-tip frequency response function (FRF). Therefore, in this chapter an experimental investigation is carried out to establish the potential of the tool holder geometry to influence chatter stability boundaries. Since it has already been demonstrated that tool stickout length may be used to avoid chatter [31], this parameter is also investigated for comparison purposes. This chapter will also highlight that interface properties between tool and tool holder are a key parameter when using stickout length as a chatter avoidance method.

4.1 Introduction

As discussed already, regenerative chatter vibrations can occur during cutting operations due to dynamic interactions between the tooling structure (spindle-tool holder-tool) and the workpiece. This can have undesirable consequences such as poor surface finish, rapid tool and machine wear, and high noise levels [6]. Today, it is possible to select stable (chatter free) cutting parameters from a stability lobe

diagram for a given tooling structure; however, in doing so production rates are reduced and production costs are increased. Hence, a lot of research has been carried out in an attempt to reduce the effect that chatter has on the production environment. The aims of such research projects usually include maximising the stable regions of a stability diagram and optimising the location (or spindle speed) at which the stable lobes occur. Since the size and location of the stability lobes are directly related to the dynamics at the tool tip, previous studies have been dominated by the effect that the tool has on these stability diagrams, and little research has been carried out on the tool holder itself. To the author's knowledge, this project is the first of its kind to concentrate solely on the effect of tool holder geometry on the dynamics of a milling machine.

4.2 Background - Tool Holder Geometry

The geometry of a tool holder can vary significantly based on factors such as the spindle or tool clamping technology, the milling operation, and tool diameter. However, all tool holders are essentially constructed in three sections, the spindle interface, the flange, and the main body. This thesis focuses on HSKA63 shrink fit tool holders, a typical example of which can be seen in Fig. 4.1.

The name HSKA (Hohlschaftkegel or hollow shank taper) refers to a set of industry standards [95, 96] on the interface between the tool holder and the spindle that were introduced to meet the demand for higher speeds and feeds within the manufacturing industry. By standardising the geometry of both the tool holder and spindle interfaces, higher clamping forces can be achieved, leading to a more rigid structure and, therefore, improved performance. The 63 label refers to the diameter of the flange. For each of the holders considered in this thesis, the geometry of both the spindle interface and flange are fixed by these standards. There are, however, no standards on the geometry of the tool holder body.

As mentioned above, this project considers only shrink fit holders, a standard in modern high-speed milling. The name refers to the tool clamping technology,

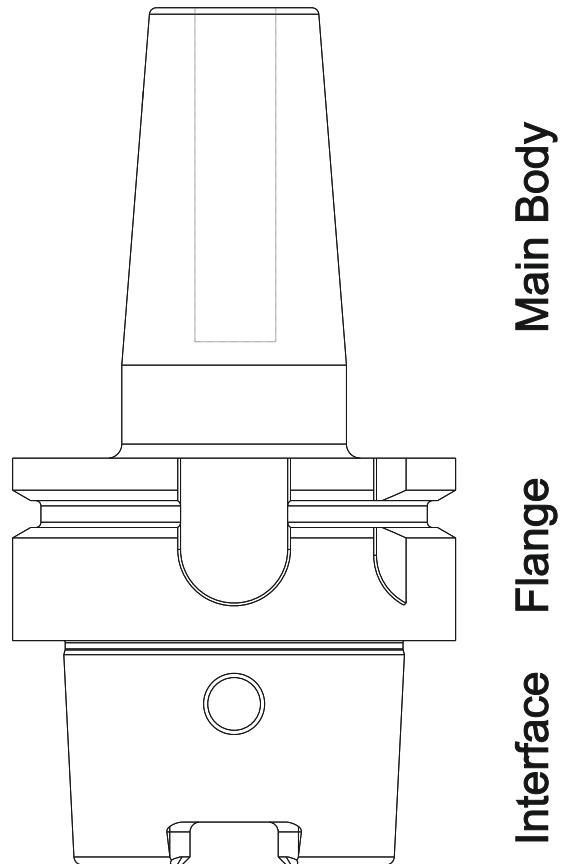


Figure 4.1: Exemplar HSKA63 shrink fit tool holder

whereby the holder is heated in an induction coil to the point of expansion and a tool inserted into the main body (Fig. 4.1), which is then clamped upon cooling. This method requires that the body of such holders be tapered, similar to the example shown in Fig. 4.1, since the smaller diameter at the tip accelerates the thermal expansion process.

It has been observed by the industrial partner to this project, that the tool holders of one manufacturer (manufacturer A) are predominantly less chatter prone than the equivalent from other manufacturers. The only evident difference between these holders is their geometry. Manufacturer A's holders have a larger base diameter leading to a larger taper angle. Therefore, it has been proposed that, the geometry of a tool holder may be used to reduce chatter. With this in mind, this chapter sets out to test the following hypotheses.

- As the stickout length is increased, the natural frequency and stiffness at the tool tip will be reduced.

Euler-Bernoulli beam theory [97] states that the natural frequencies of a cantilever beam are inversely proportional to the square of its length, whilst beam stiffness is inversely proportional to the cube of its length. Therefore, as length is increased the natural frequencies and stiffness are reduced. Although a milling machine spindle does not accurately match the boundary conditions of a cantilever beam, it is expected that a similar relationship should exist between these parameters. In testing this hypothesis, it is also expected that the results from Ertürk et al.'s paper [31] (discussed in chapter 2) will be experimentally validated.

- The geometry (length and diameter) of a tool holder can influence the natural frequency and stiffness at the tool-tip to a similar extent to that of stickout length.

Beam theory demonstrates that the natural frequency of a circular cantilever beam is directly proportional to the square of its radius, whilst the beams stiffness is directly proportional to the quartic of its radius. Therefore, it is expected that the diameter of the tool holder will have a positive non-linear

relationship with both the natural frequency and stiffness (at the the tool tip).

This chapter will also highlight the dependency between tool stickout length and the properties of the interface between the tool and tool holder. As discussed already in chapter 2, the main disadvantage of the RCSA method is that interface stiffness and damping must be either measured or modelled in order to produce accurate results.

4.3 Experimental Methods

Before the results are presented, the experimental methods used in this and following chapters are outlined.

4.3.1 Impact testing

There are both analytic and numeric [9, 13, 98] approaches to finding the stability lobe diagram for a certain tooling structure, however both rely on knowledge of the dynamics of the free end of the structure, which is captured in the form the 'tool tip' frequency response function. It should be noted that throughout the remainder of this thesis, the tool tip FRF is always used to refer to the FRF that is both measured and excited at the tool tip. The most common method to obtain the tool tip FRF is via impact testing [92]. By impacting the free end of the tool with an instrumented hammer, a force, $f(t)$, is applied, and a wide range of frequencies can be excited simultaneously, then the resulting acceleration, $\ddot{x}(t)$, can be measured using a low mass accelerometer. By taking the Fourier transform of both the force and response, the FRF can be obtained. Assuming periodicity of the signals $f(t)$ and $\ddot{x}(t)$ these are expressed as:

$$F(i\omega) = \frac{1}{t_m} \int_0^{t_m} f(t)e^{-i\omega t} dt \quad (4.1)$$

$$\ddot{X}(i\omega) = \frac{1}{t_m} \int_0^{t_m} \ddot{x}(t)e^{-i\omega t} dt \quad (4.2)$$

where $F(i\omega)$ is the Fourier transform of $f(t)$, $\ddot{X}(i\omega)$ is the Fourier transform of $\ddot{x}(t)$, ω is the frequency, and t_m is the measurement time. The frequency response function ($H_{acc}(i\omega)$) is then given by:

$$H_{acc}(i\omega) = \frac{\ddot{X}(i\omega)}{F(i\omega)} \quad (4.3)$$

The above equation describes the accelerance FRF as it relates the the input force to the acceleration of the structure. For the rest of this thesis, however, we will be concerned with the receptance FRF, which relates the input force to the displacement of the structure. Since acceleration $\ddot{x}(t)$ and displacement $x(t)$ are related (when the excitation is harmonic), by the relationship $\ddot{x}(t) = (i\omega)^2 X e^{i\omega t} = (i\omega)^2 x(t)$, the receptance FRF is calculated as

$$H_{rec}(i\omega) = \frac{X(i\omega)}{F(i\omega)} = \frac{\ddot{X}(i\omega)}{(i\omega)^2 F(i\omega)} \quad (4.4)$$

H is used to refer to H_{rec} for the rest of this thesis.

In practice, the force and acceleration signals are measured at discrete time intervals (T_s) using a data acquisition (DAQ) board attached to a computer. If a frequency resolution of ω_s is required in the measurement data, measurements must be collected for a total time of $t_m = 2\pi/\omega_s$, with $N = t_m/T_s$ data samples, therefore

$$t_m = \frac{2\pi}{\omega_s} = NT_s \quad (4.5)$$

Hence, the DAQ system works with Eqs. (4.1) and (4.2) in the discrete time form, Making the substitutions $t = nT_s$, $\omega = k\omega_s$, and $dt = T_s$, the Fourier transforms become

$$F(ik\omega_s) = \frac{1}{N} \sum_{n=0}^{N-1} f(nT_s) e^{-ik\frac{2\pi}{N}n} \quad (4.6)$$

$$\ddot{X}(ik\omega_s) = \frac{1}{N} \sum_{n=0}^{N-1} \ddot{x}(nT_s) e^{-ik\frac{2\pi}{N}n} \quad (4.7)$$

where $F(ik\omega_s)$ and $\ddot{X}(ik\omega_s)$ are the discrete Fourier transforms or spectra of the measured force and acceleration respectively. There are a number of additional steps that must be taken in practice to accurately calculate the FRF.

A necessary and sufficient condition for the correct reconstruction of a sampled signal, known as the Nyquist-Shannon sampling theorem, is that the sampling rate ($1/T_s$ in Hz) is twice that of the highest frequency content in the signal (or twice that of the highest frequency of interest). If this condition is not met, alias signals at higher frequencies will disrupt the reconstructed signal. To prevent such occurrences, data acquisition systems apply an anti-aliasing filter to the analogue signal, which attenuates the high frequency content above the Nyquist frequency. Such filters are known as low pass filters because frequency content below a certain frequency passes through the filter whilst higher frequency content is removed. In the impact testing system used throughout this thesis an 8th order Bessel function filter is applied at 12500 Hz.

The contact time between the hammer and the tool is inherently very short and much shorter than the time for which the structure vibrates. Therefore a typical force signal contains a sharp peak followed by low amplitude noise. The effect of this noise on the quality of the FRF can be reduced by windowing the digital signals. Both the force and acceleration signals are multiplied by an exponential window function, which multiplies the signals by unity during the period of contact and by an exponentially decreasing value thereafter. Once the signals have been windowed, the Fourier transforms can be calculated.

Despite the benefits of windowing the Fourier transforms will still contain some noise which results in Eq. (4.4) becoming inaccurate. The influence of noise can be attenuated by calculating the cross spectrum. The cross spectrum ($S_{\ddot{x}f}$) of force and acceleration is found by multiplying the acceleration spectrum by the complex conjugate of the force spectrum, i.e.

$$S_{\ddot{x}f} = \ddot{X}(ik\omega_s) \cdot F^*(ik\omega_s) \quad (4.8)$$

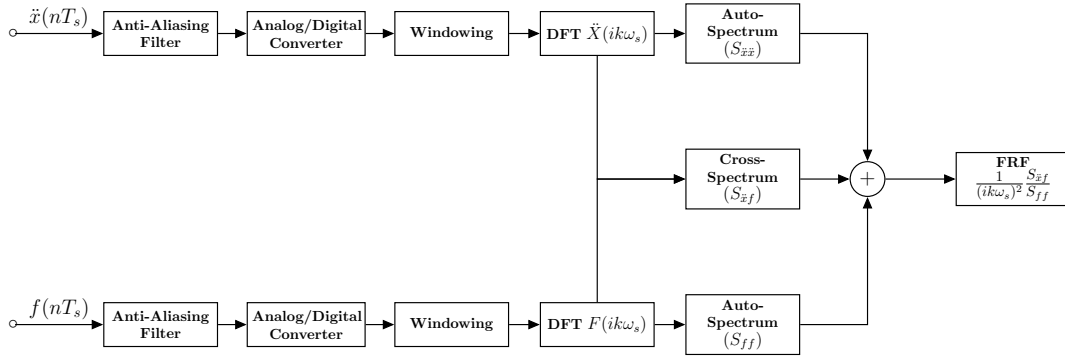


Figure 4.2: Diagram showing the dimensions for both the unmodified and modified holders

where * denotes the complex conjugate. The FRF is then found by dividing the cross spectrum by the auto spectrum of the force signal such that

$$H(i\omega) = \frac{1}{(ik\omega_s)^2} \frac{S_{\ddot{x}f}}{S_{ff}} = \frac{1}{(ik\omega_s)^2} \frac{\ddot{X}(ik\omega_s) \cdot F^*(ik\omega_s)}{F(ik\omega_s) \cdot F^*(ik\omega_s)} \quad (4.9)$$

It is also common to average a number of cross and auto spectra in order to further attenuate the noise in the signals, throughout this project five spectra were averaged before calculating the FRF.

The dual channel DAQ system which performs this signal processing can be expressed as a block diagram as show in Fig. 2. There are many papers that discuss the accuracy of this form of impact testing, two noteworthy examples include Kim and Schmitz’s [99] paper, which discusses more physical problems in impact testing such as the effect of the mass of the accelerometer, and misalignment between the hammer and accelerometer, and Sims *et al.* [100], who list potential limitations with this type of impact test, such as the requirement of a skilled user, poor repeatability, and the ineffectiveness of the hammer to tap small tools.

One of the largest shortcomings of impact testing with a modal hammer is the inability to produce an impulse [99]. The frequency spectrum of an infinitely

narrow impulse signal is equal across all frequencies; meaning that, if a structure were excited by a true impulse all frequencies would be excited equally. Clearly, it is not possible to produce an impulse with a hammer, and instead the input signal usually resembles that of a half sine curve, the frequency spectrum of which decays with frequency. Therefore during modal testing, higher frequency modes may not be excited properly, causing error in the FRF. Moreover, as the input spectrum tends to zero, the FRF will tend to infinity, causing infinite flexibility around resonance, something which is not possible in reality. Therefore during the tests it is vital to monitor the frequency spectrum of the input and output signals to assure the structure is properly excited over the whole measurement range.

Visual inspections of the measured FRF data sets should also be made, either during or shortly after measurement. For instance, when the magnitude of an FRF is plotted on a logarithmic axes, the low frequency asymptote characterises the support conditions for the test. In the case of a milling machine, the bearings should produce results similar to those testing under cantilever conditions, therefore, the low frequency asymptote should tend to a stiffness line that corresponds to the static stiffness of the structure. Moreover, both the resonant and anti-resonant peaks should exhibit similar sharpness. This is an indication of adequate vibration levels and satisfactory frequency resolution. It is also important to examine the linearity of the structure, as the above theory is only applicable to linear structures. The point FRF of a linear structure should contain an antiresonance after each resonance, whilst the cross FRF (of two well spaced points) should contain more resonances than antiresonances.

Although an experimental modal analysis is not carried out in this chapter, the method will be used throughout the remainder of this thesis. Since it follows on directly from impact testing, it is sensible to discuss the theory of the method at this point.

4.3.2 Experimental modal analysis

Once the FRF(s) has been calculated an experimental modal model can be constructed by performing an experimental modal analysis. Before the fundamentals of experimental modal analysis can be explained a theoretical overview is needed, a full description of modal analysis can be found in [51]. For the case of impact testing, we have forced vibration with harmonic excitation and response, for which the governing equation is given by:

$$\begin{aligned}
 & ([\mathbf{K}]_{n \times n} + i\omega[\mathbf{C}]_{n \times n} - \omega^2[\mathbf{M}]_{n \times n})[\mathbf{X}]_{n \times 1}e^{i\omega t} = [\mathbf{F}]_{n \times 1}e^{i\omega t} \\
 \text{or } & \mathbf{X}e^{i\omega t} = (\mathbf{K} + i\omega\mathbf{C} - \omega^2\mathbf{M})^{-1}\mathbf{F}e^{i\omega t} = [\mathbf{H}(i\omega)]_{n \times n}\mathbf{F}e^{i\omega t} \quad (4.10)
 \end{aligned}$$

where \mathbf{K} , \mathbf{C} , and \mathbf{M} are the stiffness, damping, and mass matrices, \mathbf{X} is the displacement vector, \mathbf{F} is the force vector, and $\mathbf{H}(i\omega)$ is the complex frequency response function matrix at a particular frequency ω . Each element of this matrix is given by

$$H_{jk}(i\omega) = \sum_{r=0}^{N_M} \frac{\phi_r(x_j)\phi_r(x_k)}{\omega_r^2 + 2i\zeta_r\omega_r\omega - \omega^2} = \sum_{r=0}^{N_M} \frac{R_{jk,r}}{\omega_r^2 + 2i\zeta_r\omega_r\omega - \omega^2} \quad (4.11)$$

Here, j refers to the response location x_j , k refers to the input location x_k , $\phi_r(x_j)$ is the r^{th} mass-normalised mode shape at location x_j , ω_r is the r^{th} natural frequency, ζ_r is the r^{th} damping ratio, N_M is the total number of modes in the model, and $R_{jk,r}$ is known as the residue that relates the r^{th} mode at locations x_j and x_k .

It should be noted that Eq. 4.11 is only valid for mass-normalised mode shapes. The mass normalised mode shapes ϕ_r have the important property that:

$$[\Phi]^T[\mathbf{M}][\Phi] = [\mathbf{I}] \quad \text{and} \quad [\Phi]^T[\mathbf{K}][\Phi] = \begin{bmatrix} \ddots & & & \\ & \omega_r^2 & & \\ & & \ddots & \\ & & & \ddots \end{bmatrix} \quad (4.12)$$

The relationship between the r th mass-normalised mode shape ϕ_r and its more

general form ψ_r is given by:

$$\phi_r = \frac{1}{\sqrt{m_r}} \psi_r \quad \text{where} \quad m_r = \psi_r^T [\mathbf{M}] \psi_r \quad (4.13)$$

Experimental modal analysis is the process of fitting the experimental FRF in Eq. (4.9) with the analytical FRF in Eq. (4.11), and solving for unknown residues, natural frequencies, and damping ratios. The measured FRF is now referred to as \bar{H}_{jk} . As discussed in section 4.3.1, the frequency of the measured FRF has a limited range due to the limitations of the equipment as well as the anti-aliasing filter. As well as this the lower frequency range can be corrupted by high noise levels and is particularly difficult to measure [51]. Therefore the analytical FRF is sectioned into three, such that:

$$H_{jk}(i\omega) = -\frac{F_{jk}}{\omega^2} + \sum_{r=0}^{N_M} \frac{R_{jk,r}}{\omega_r^2 + 2i\zeta_r\omega_r\omega - \omega^2} + G_{jk} \quad (4.14)$$

where F_{jk} is known as the low frequency residual and describes the dynamics at low frequencies, and G_{jk} the high frequency residual, describing the dynamics outside the measurement range. Now the measured FRF can be fitted with its analytical counterpart. It can be seen from Eq. (4.14) that the analytical model H_{jk} is linear with respect to the unknowns $F_{jk,r}$, $R_{jk,r}$, $G_{jk,r}$, and ζ_r but not the natural frequency ω_r . Therefore the identification method used in this project, works with an initial estimate on ω_r and finds the unknowns by solving the linear least squares problem

$$p = \arg_p \min \left(\sum_{j,k,r,\omega=0}^{N_S, N_A, N_M, N_W} |(H_{jk}(\omega; p) - \bar{H}_{jk}(\omega))^2| \right) \quad (4.15)$$

where $p = p(F_{jk,r}, R_{jk,r}, G_{jk,r}, \zeta_r)$ is the set of identified modal parameters, $\arg_p \min$ stands for the argument of the minimum (or the set p that results in the minimum value), N_S is the number of sensors, N_A is the number of actuators, N_M is the number of identified modes, and N_W is the highest frequency of the model. Therefore, for the initial estimates ω_r the least squares problem is solved to calculate p . Then, based on the cost or error between the model p and the measured

data, the natural frequencies are optimised iteratively. For each new estimate ω_r , p is calculated, and each set p will carry an individual error. The final solution is the set of natural frequencies ω_r that produce the set p with the lowest error. A full methodology for the method can be found in [101].

Once the residues have been calculated the mode shapes can be identified from any row or column of the residue matrix, due to the reciprocity of the system. For example, consider the k^{th} column

$$\begin{pmatrix} R_{1k,r} \\ \vdots \\ R_{kk,r} \\ \vdots \\ R_{N_S k,r} \end{pmatrix} = \begin{pmatrix} \phi_r(x_1)\phi_r(x_k) \\ \vdots \\ \phi_r(x_k)\phi_r(x_k) \\ \vdots \\ \phi_r(x_{N_S})\phi_r(x_k) \end{pmatrix} \quad (4.16)$$

then the r^{th} mode shape at location x_k is found as $\phi(x_k) = \sqrt{R_{kk,r}}$ and all other locations are found by:

$$\phi_r(x_j) = \frac{R_{jk,r}}{\sqrt{R_{kk,r}}} \quad (4.17)$$

This is then repeated for each of the N_M modes.

4.4 Experimental Investigation

In order to test the two hypotheses, data was collected across two milling machines, namely the Cinnatti FTV5 and the Starrag ZT-1000. Two tools of similar geometry but differing length were selected, meaning both tools may be clamped with identical insertion lengths but differing stickout lengths. It is hoped that by keeping the insertion length constant, the contact parameters are, in turn, kept constant. In reality the contact stiffness/damping are also affected by tool diameter and surface roughness. Since the tools are guaranteed to be within ISO standards it is hoped that manufacturing imperfections have minimal effect. The geometries of the tools used in the experiment are given in Table 4.1.

4.4. EXPERIMENTAL INVESTIGATION

	Diameter (mm)	Total Length (mm)	Flute Length (mm)	No. of Flutes
Short	12	84	36	2
Long	12	101	36	2

Table 4.1: Tool geometry for both short and long tools

Tool holders from manufacturer A and another leading competitor manufacturer B were selected, since their geometries varied only in the base diameter. The geometries of each of the holders is given in Fig. 4.3 and Table 4.2. The holders are categorised by tool diameter (12 mm, 16 mm, and 25 mm tools), and each category contains a holder from each of the two manufacturers. It can be seen that the holders differ only by their base diameter d_2 . Also, as the tool diameter increases the difference in geometry between the two tool holders decreases. The base diameter of the 12 mm holders differs by 19 mm, whilst the 25 mm holders differ by just 0.5 mm.

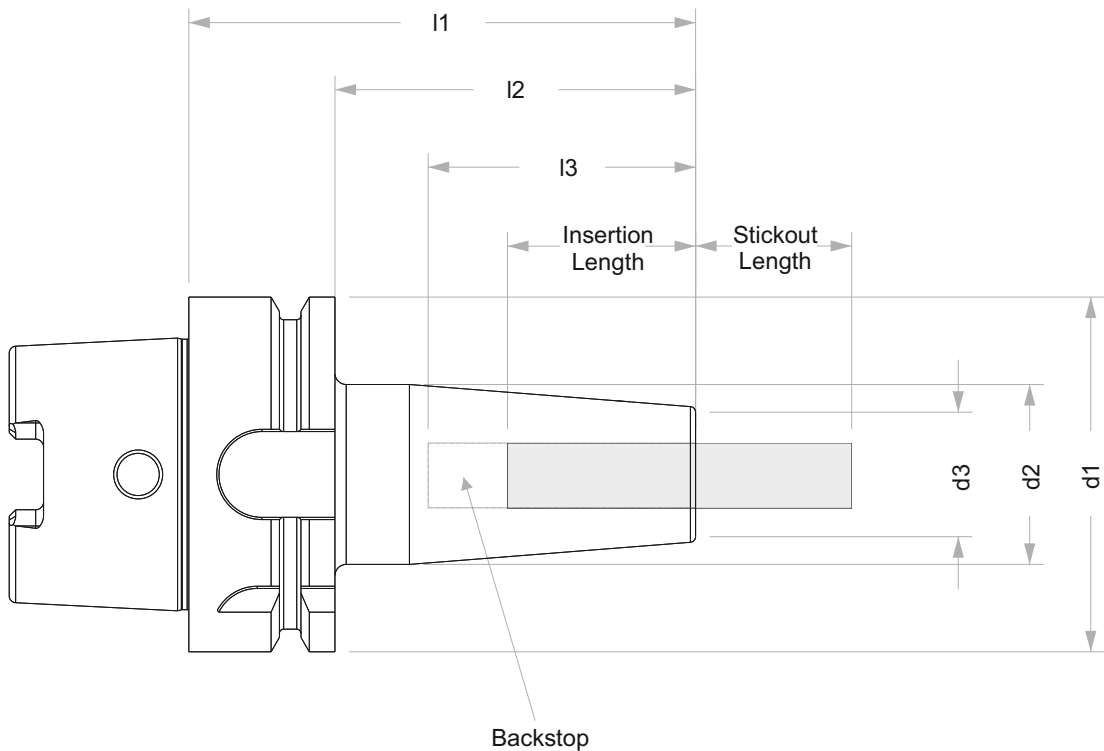


Figure 4.3: Diagram showing the dimensions of the HSKA63 tool holders

	l1 (mm)	l2 (mm)	l3 (mm)	d1 (mm)	d2 (mm)	d3 (mm)
12 mm						
Manufacturer A	160	134	47	64	53	24
Manufacturer B	160	134	47	64	34	24
16 mm						
Manufacturer A	160	134	50	64	53	27
Manufacturer B	160	134	50	64	42	27
25 mm						
Manufacturer A	160	134	58	64	53	34
Manufacturer B	160	134	58	64	52.5	34

Table 4.2: Table giving the dimensions of the HSKA63 tool holders

Before the effect of tool holder geometry on tool tip dynamics is discussed, the effect of tool stickout length is examined.

4.4.1 The effect of tool stickout length

The effect of stickout length on tool tip dynamics is well observed, both numerically and experimentally [31, 32, 33], and its ability to optimise the stability lobes of a machine proposed. The most common method used in predicting the effect of stickout length is receptance coupling substructure analysis, as discussed in chapter 2. An important drawback of the method, however, is the difficulty in modelling the stiffness and damping that occurs at the interface between the tool and tool holder. Since the contact parameters are a function of insertion length, and in turn stickout length, both variables must be mutually considered.

Experimental data, thus far, has demonstrated the significant effect that stickout (and thus the contact parameters) has on the dynamics of machining structures; however, its effect has never been experimentally observed in isolation (i.e. without also varying the contact parameters). Ertürk *et al.* [31] used an analytical model of a spindle/holder/tool structure to isolate the effect of stickout length. By increasing the external tool length by 10 mm (a 12.5% increase) and then 20 mm (a 25% increase), it was found that each elastic bending mode (between 800 Hz and 2000 Hz) sees a reduction in natural frequency and an increase in

amplitude as stickout is increased. The paper presented stickout lengths of 80 mm, 90 mm, and 100 mm, with a contact stiffness of 1.5×10^7 N/mm. Since the analytical model was constructed using RCSA (in a similar manner to a finite element model) the contact parameters remained constant.

The paper then goes on to consider the effect of contact stiffness, a subject considered in more depth by the same authors in [31]. Their research shows that by fixing the stickout length (at 80 mm) and altering the contact stiffness (1.5×10^7 N/mm, 1.25×10^7 N/mm, and 1.0×10^7 N/mm) the same bending modes also see a reduction in natural frequency, albeit considerably smaller than for the stickout results, whilst their amplitude remains constant, as stiffness is reduced.

Whilst the results in [31] are promising, the paper suffers a major drawback. Although the analytical model was experimentally validated in a single configuration, neither the effect of stickout length nor contact stiffness were explicitly validated. Therefore, in this study, an experiment has been designed so that the effect of stickout length may be isolated.

Both the short and long tools were clamped into the 12 mm tool holders from manufacturers A and B with stickout lengths of 40 mm and 57 mm respectively. These setups were then inserted into the Cincinnati FTV5 and the Starrag ZT-1000 milling machines, and the tool tip FRFs measured. The measurement system consisted of the National Instruments 9234 24 bit DAQ box, Kistler 9724A500 instrumented hammer, and Dytran 3244C accelerometer, as well as the MAL inc. Cutpro software, which performed the stability analysis.

The results from the Starrag ZT-1000 are presented in Fig. 4.4. The natural frequency of all dominant modes (modes with substantially higher amplitudes) are decreased; in particular, the three modes above 2000 Hz see the largest shift in frequency. The natural frequencies of all dominant modes for short and long tools are plotted against one another in Fig. 4.5. It can be seen that despite the considerable difference in the tool-tip dynamics between the two manufactur-

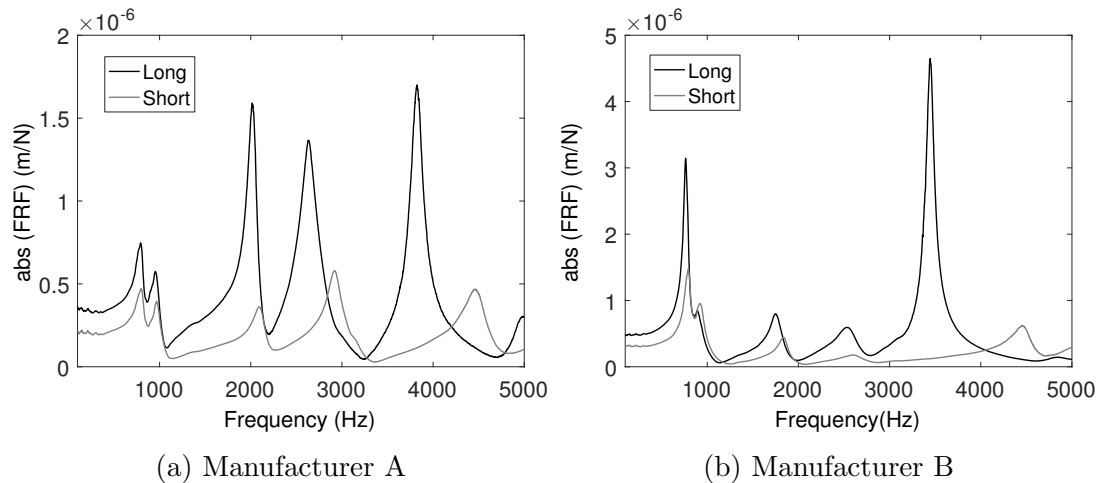


Figure 4.4: FRF magnitude comparing 12 mm holders with long and short stick-out lengths for (a) manufacturer A and (b) manufacturer B on the Starrag ZT-1000

ers, their natural frequency shifts are highly correlated, thus suggesting that the effect of stickout length is independent of the tool holder geometry. The effect of stickout length on the amplitude of the modes is less simple. The modes for Manufacturer A all see similar increases in amplitude as the stickout length is increased, with the highest modes (above 1500 Hz) becoming the most dominant modes. In contrast the highest mode of Manufacturer B is disproportionately affected by the stickout length, suggesting that the effect of stickout length is not completely independent of tool holder geometry.

The effect of stickout length on milling stability can be seen in Fig. 4.6. In the case of both manufacturers the shorter (stiffer) tool produces a considerably higher absolute stability limit, which would be highly beneficial for a manufacturing engineer. The relationship between stickout length and the stability lobe location is less apparent; however, it is clear that for both manufacturers the number of competing lobes (i.e. dominant modes) is affected by tool length.

The results from the Cincinnati FTV5 are plotted in Fig. 4.7. Whilst there is a clear difference in the dynamics of the two machines (particularly in the low frequency rigid body modes), the trends in natural frequency and amplitude are

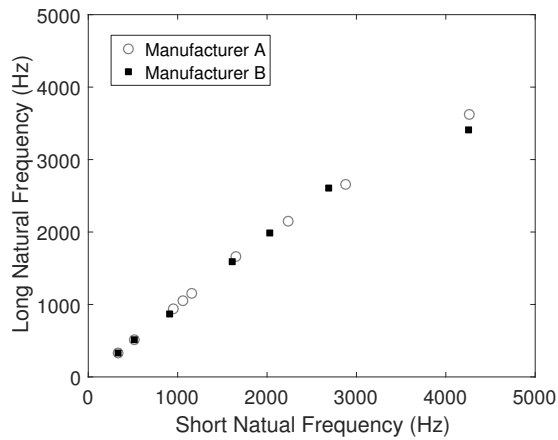


Figure 4.5: Graph comparing the natural frequencies of the short and long tools for both Manufacturer A and B on the Starrag ZT-1000

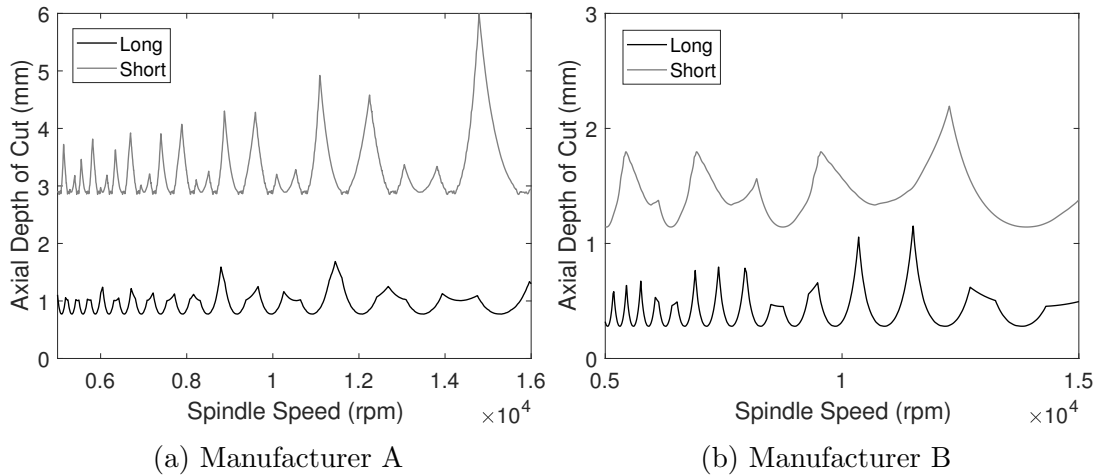


Figure 4.6: Stability Lobe Diagrams comparing 12 mm holders with long and short stickout lengths for (a) manufacturer A and (b) manufacturer B on the Starrag ZT-1000

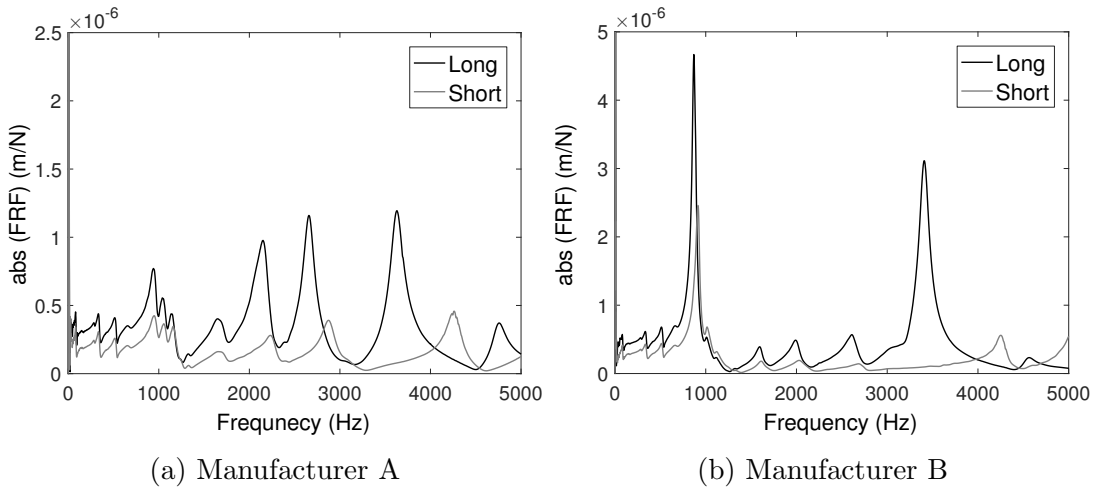


Figure 4.7: FRF magnitude comparing 12 mm holders with long and short stick-out lengths for (a) manufacturer A and (b) manufacturer B on the Cincinnati FTV5

comparable across the two machines.

As discussed already the impact hammer technique used to collect this data is limited, in that it may fail to fully excite the system at higher frequencies. Therefore, it is difficult to accurately measure these modes. Whilst the repetition of the results on the two machines brings some confidence in the conclusions drawn, it is possible that the modes at higher frequencies were not measured correctly.

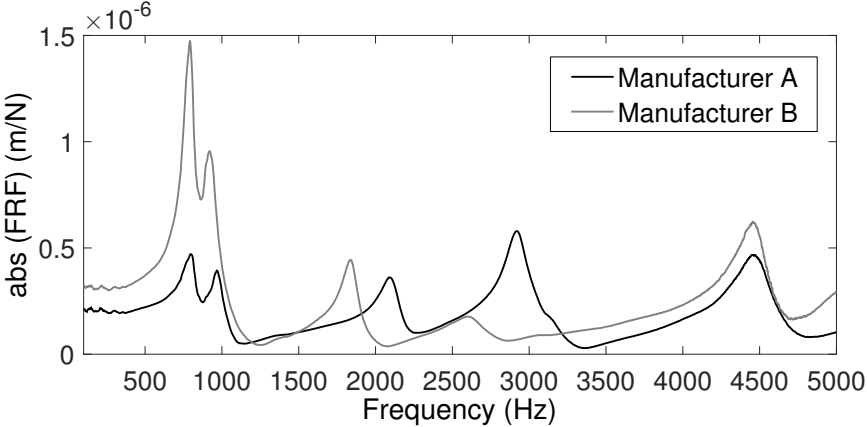
The data presented here validates the results of Ertürk *et al.* [31] and suggests that tool stickout length may be used to modify the stability of a milling operation, indicating that stickout length may be used to optimise tool-tip dynamics. Therefore it may be possible to design a set of tools, similar to the two used above, with the same geometry but differing lengths so that stickout length may be optimised in isolation. However, this makes the assumption that two tools with identical insertion length will always have identical contact stiffness and damping. It is for this reason that research into the modelling of contact parameters between tool and tool holder interfaces is still ongoing.

4.4.2 The effect of tool holder geometry

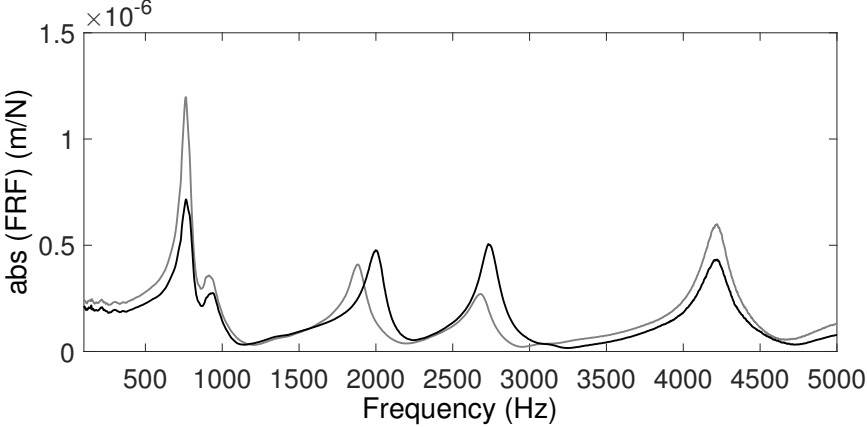
Little research has been carried out on the effect of tool holder geometry on tool-tip dynamics, and to the author's knowledge, the paper by Ertürk *et al.* is the only one of its kind to discuss the subject (albeit rather briefly). Similar to the idea of stickout length, the paper looks at the effect of increasing the length of the holder. Using the receptance coupling model the external section of the holder is increased in length by 10 mm (an increase of around 15%) and then by 40 mm (an increase of around 66%). By increasing the middle section of the holder the tool clamping is unaffected. It is found that tool holder length has a similar effect to that of stickout length; however, the change in tool tip dynamics is much less acute. It can be presumed that it is for this reason that the authors did not peruse the subject further. The paper does not go on to look at the effect of tool holder diameter.

In order to observe the effect that tool holder base diameter has on the tool-tip dynamics, the short tools were clamped into their respective tool holders (12 mm, 16 mm, and 25 mm) for manufacturers A and B. These configurations were each clamped onto the Starrag ZT-1000 and Cincinnati FTV5 machines, and the tool tip FRF measured. The same measurement system as above was used. The process was then repeated with the long tools.

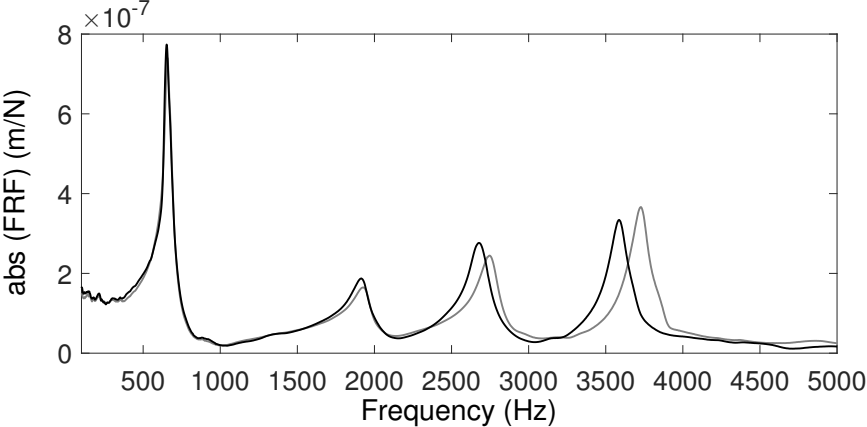
The results of the tool holders with short tools on the Starrag ZT-1000 are presented in Fig. 4.8. The three figures compare the tool tip FRFs for the 12 mm (4.8a), 16 mm (4.8b), and 25 mm (4.8c) tool holders of both manufacturers. The difference between the two 12 mm holders is severe, in fact the amplitude of the most dominant mode for manufacturer B is around three times larger than that of manufacturer A. Although the effect on the natural frequencies is somewhat less severe, the modes between 1500 Hz and 3500 Hz see a considerable reduction in natural frequency as the base diameter is increased. As the difference in the holder geometry reduces, the difference in the tool tip FRF also diminishes. The 16 mm holders have very similar natural frequencies and amplitudes.



(a) 12 mm Tool Diameter

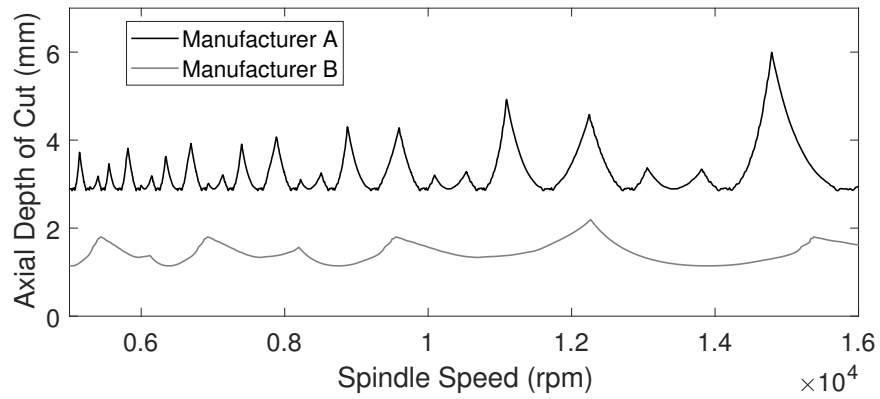


(b) 16 mm Tool Diameter

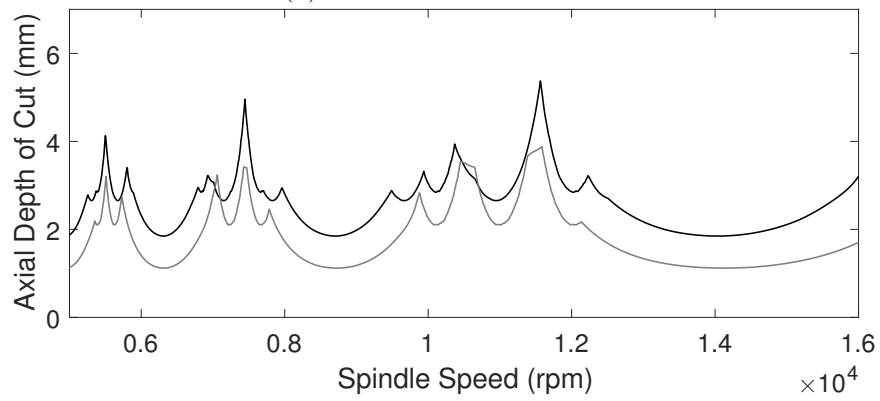


(c) 25 mm Tool Diameter

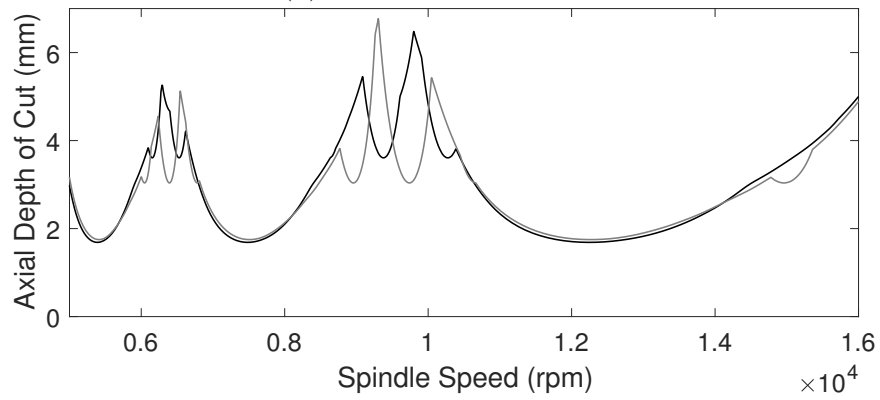
Figure 4.8: FRF magnitude comparing tool holders from manufacturer A and B for the 12 mm, 16 mm, and 25 mm cases with short tool on the Starrag ZT-1000



(a) 12 mm Tool Diameter



(b) 16 mm Tool Diameter



(c) 25 mm Tool Diameter

Figure 4.9: Stability lobe diagrams comparing tool holders from manufacturer A and B for the 12 mm, 16 mm, and 25 mm cases with short tool on the Starrag ZT-1000

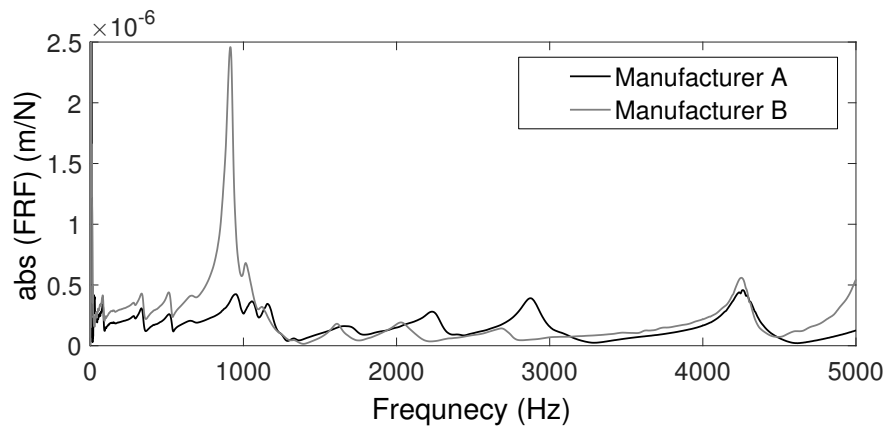
The 25 mm holders (4.8c), which have almost identical diameters, produce extremely similar results. The most dominant modes in both cases (now at around 600 Hz) are highly correlated in terms of both natural frequency and amplitude. The equivalence of the two holders begins to break down as frequency is increased.

The stability of these six setups can be seen in Fig. 4.9. For the 12 mm tool holders (Fig. 4.9a), the increased diameter of manufacturer A produces a substantially larger absolute stability limit. The effect on the lobe location is once again more complex. The most dominant mode for manufacturer A is at around 3000 Hz (Fig. 4.8a), much higher than that of manufacturer B at around 750 Hz. This results in more closely spaced lobes seen in 4.9a. Once again, as the geometry of the holders converges so to does their stability. Figs. 4.9b and 4.9c compare the stability of the 16 mm and 25 mm holders. It can be seen that both the absolute stability limit and lobe location converge with base diameter.

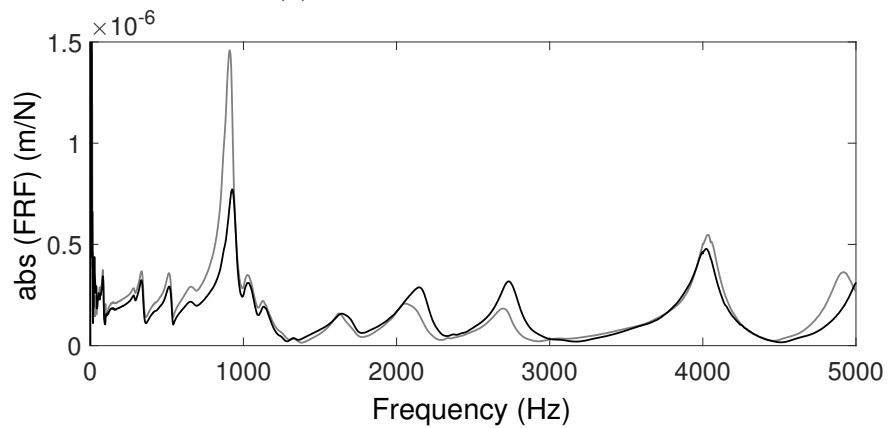
The results from the Cincinnati FTV5 with the short tool are presented in Fig. 4.10. Despite the differences in the spindle (and machine) dynamics, the trend in the results corresponds to those on the ZT-1000. Figs. 4.11 and 4.12, show the results from the Cincinnati FTV5 and Starrag ZT-1000 with long tools. What is important to observe is that again the trend in the results agrees with that of the short tools. Of particular note are the results of the 25 mm holders on the Cincinnati FTV5 (4.12c), which produce virtually identical results.

It has been shown, across two machines and two tool lengths, that the tool holder base diameter has a significant effect on the tool tip dynamics. As the diameter increases the natural frequencies of the structure increase whilst the amplitudes of the modes decrease. As the geometries of the holders from the two manufacturers converge, so too do their tool tip FRFs. This supports the observation from the industrial partner that tool holder diameter can have a significant effect on the tool tip dynamics, and thus the stability of a milling process.

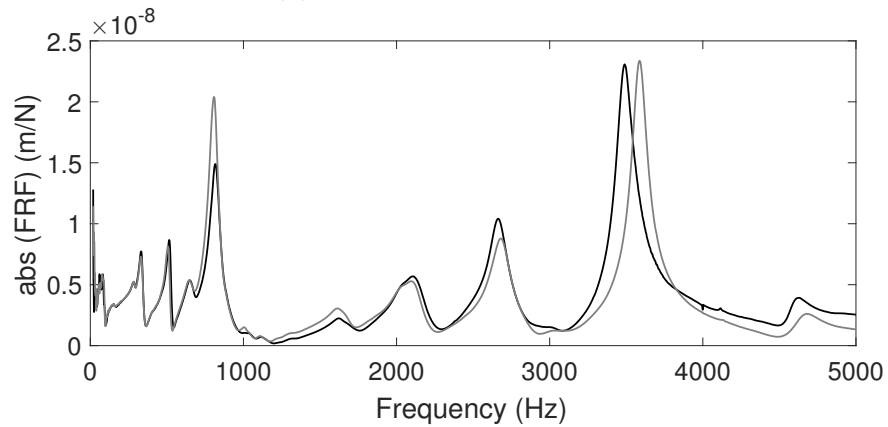
Whilst it is perfectly reasonable to propose that the RCSA method be used



(a) 12 mm Tool Diameter

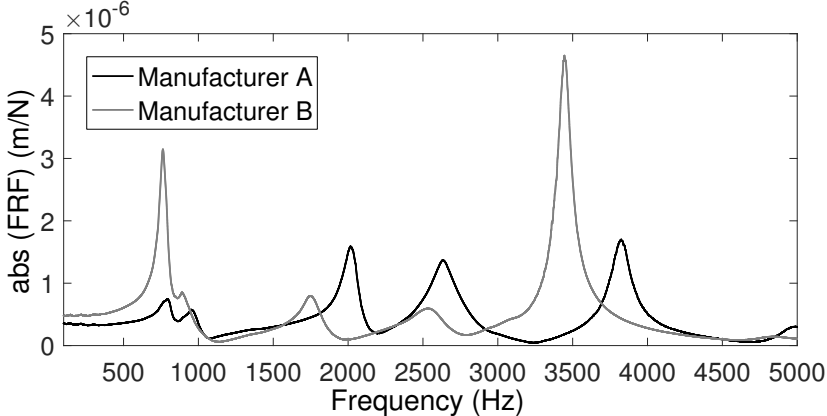


(b) 16 mm Tool Diameter

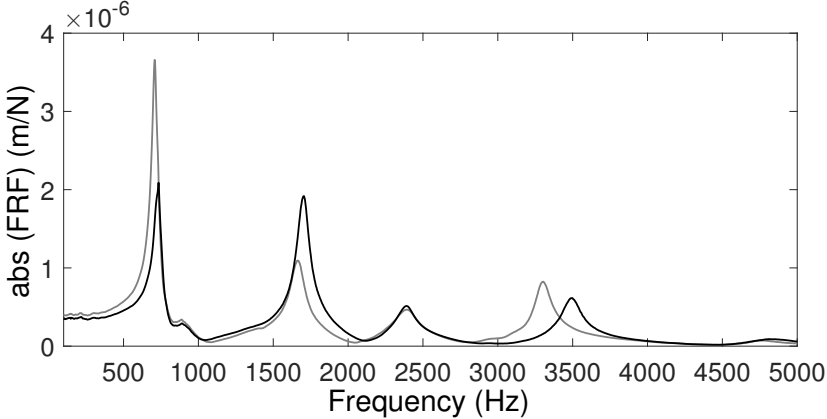


(c) 25 mm Tool Diameter

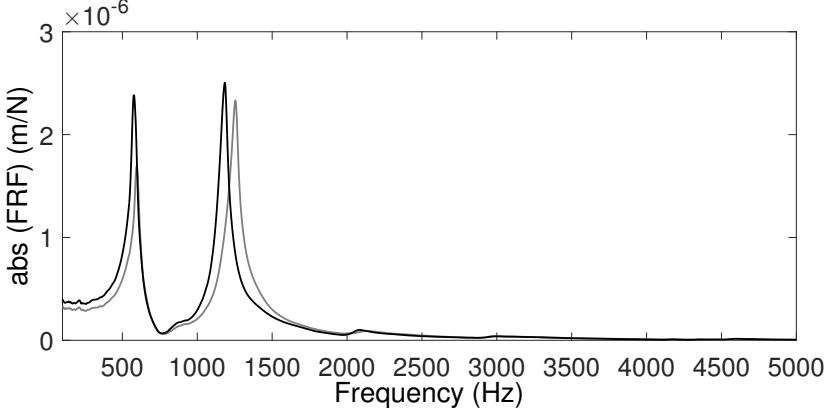
Figure 4.10: FRF magnitude comparing tool holders from manufacturer A and B for the 12 mm, 16 mm, and 25 mm cases with short tool on the Cincinnatti FTV5



(a) 12 mm Tool Diameter

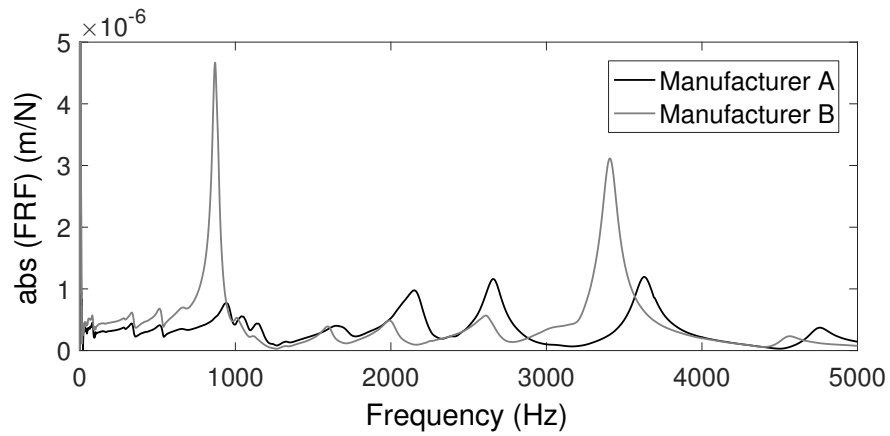


(b) 16 mm Tool Diameter

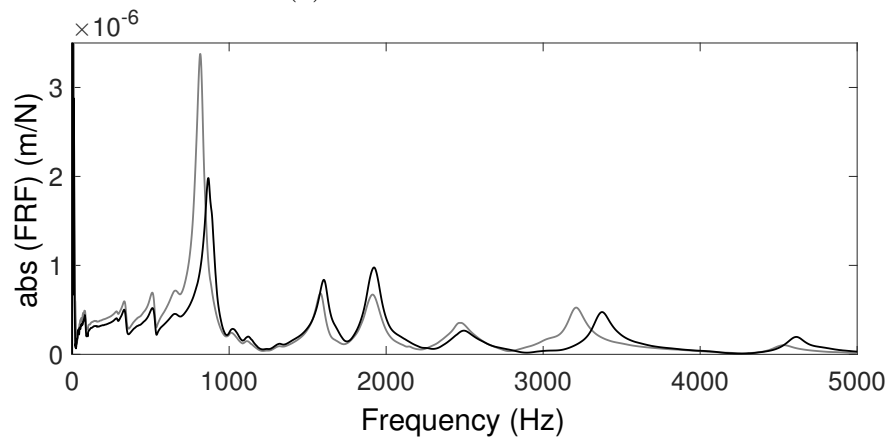


(c) 25 mm Tool Diameter

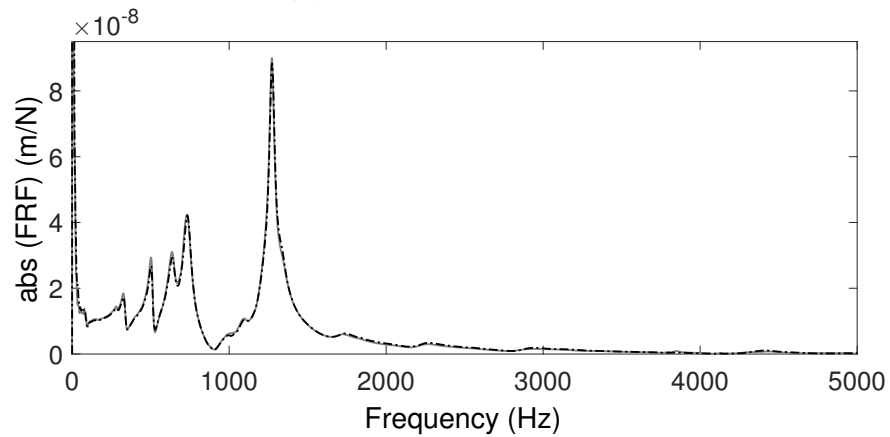
Figure 4.11: FRF magnitude comparing tool holders from manufacturer A and B for the 12 mm, 16 mm, and 25 mm cases with long tool on the Starrag ZT-1000



(a) 12 mm Tool Diameter



(b) 16 mm Tool Diameter



(c) 25 mm Tool Diameter

Figure 4.12: FRF magnitude comparing tool holders from manufacturer A and B for the 12 mm, 16 mm, and 25 mm cases with long tool on the Cincinnati FTV5

to model changes in tool holder geometry, in an attempt to optimise the tool tip FRF, the method still suffers the same shortcoming, in that the interface properties must be known. It is for this reason that this thesis proposes a new method to eliminate this problem.

4.5 Summary

The main contribution to knowledge from this chapter was the presentation of a data set that supports the observation that tool holder geometry can have a significant effect on the tool tip dynamics and thus the stability of a milling operation.

Firstly the experimental procedure was outlined from a theoretical viewpoint. This included the data collection and signal processing techniques used in impact testing, as well as the procedure for experimental modal analysis. The results of an experimental investigation were then discussed. The results demonstrate that both tool stickout length and tool holder base diameter can have a significant effect on the tool tip FRF, and may both potentially be used as a chatter avoidance method.

Whilst previous research has focussed on using stickout to avoid chatter, this chapter has discussed the contribution of the tool/tool holder interface dynamics, and the difficulty this causes when using receptance coupling substructure analysis.

No research has been published on using the tool holder geometry to avoid chatter. However, this chapter has shown that the effect of tool holder diameter is comparable to that of stickout length, and therefore may also be used as a chatter avoidance technique. The receptance coupling method still suffers the same drawback when modelling holder diameter, and therefore in the following chapters a new method will be discussed which allows the user to model and optimise tool holder diameter without having to measure or model the interface dynamics.

Chapter 5

The Effect of Tool Holder Stiffness

In chapter 4 it was shown that the geometry of the tool holder can have a substantial effect on the dynamics at the tool tip and, therefore, the onset of chatter. Hence, it was suggested that tool holder geometry may be used as a chatter avoidance technique. The initial proposal for this project assumed that such changes in tool tip dynamics could be largely attributed to the change in mass at the tool holder, with any change in stiffness having a negligible effect. Therefore, before any modelling or optimisation methods are applied, it must first be established how accurately the continuous geometry of the tool holder negates the theory that underpins this assumption.

5.1 Introduction

The motivation behind this project was that of a tuned mass tool holder, whereby the mass of the holder could be optimised to avoid the onset of chatter. However, this assumes that the effect of tool holder geometry on the tool tip dynamics is attributable to the holder's mass and not its stiffness. If this assumption holds, then it may be possible to use unit rank structural modification to model changes in the distributed (or tapered) mass of the holder as a simple point mass system. This aim of this chapter is to test the validity of this assumption.

Based on the experimental results presented in chapter 4, it is reasonable to suggest that the change in stiffness also contributes significantly to the effect on the tool tip FRF. Using a numerical model the effect of adding pure mass (or increasing density) is compared to the effect of adding real mass (increasing both mass and stiffness). The results are used to propose that the stiffness of any modification to the tool holder must also be modelled and optimised in order to successfully avoid chatter.

5.2 Numerical Modelling

A finite element (FE) model was constructed in order to trial any optimisation algorithms before performing experimental tests, providing a versatile model on which changes could be made and data recaptured with relative ease and speed. It also allows for comparison of tool holder geometry without the added complexities that occur due to signal noise and sources of non-linearity such as interface dynamics.

The business models prevalent in the aerospace manufacturing sector involve machine tool builders purchasing spindles from subcontractors, this leads to secrecy around spindle design. Therefore, many necessary parameters including some spindle geometry and bearing properties (stiffness) of the Cincinnati FTV5 and Starrag ZT-1000 milling machines are unavailable. For this reason, the finite element model is not experimentally validated. The model has been designed using the small amount of information about the spindles available. Experimental results from both the Starrag and FTV5 machines (presented in the previous chapter) suggest the model is reasonable enough to carry out some analysis on the effect of tool holder geometry.

The necessary geometry, material properties, and boundary conditions to construct the finite element model can be found in appendix A, along with the MATLAB script used.

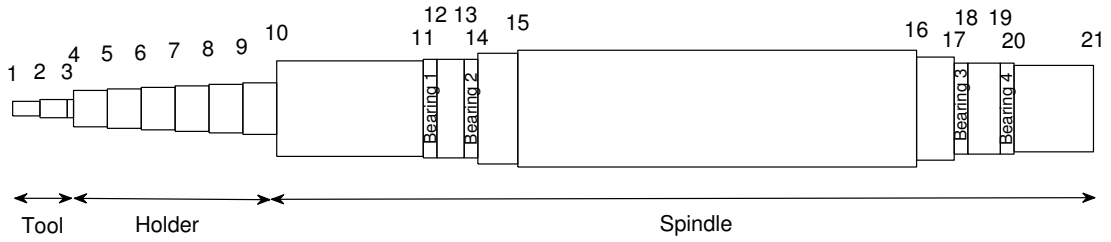


Figure 5.1: Schematic drawing of the finite element model geometry showing node numbers, bearing locations, and tool/holder/spindle locations

5.2.1 The addition of pure mass

When mass is added to the tool holder on a physical system the change in geometry causes a simultaneous increase in stiffness. Since the initial proposal involves optimising the mass alone, it is important to confirm that it is the change in mass and not the change in stiffness that is responsible for the change in dynamics. In all likelihood, the improvement is due to a combination of the two. In order to test this, the material density on the tapered section of the tool holder was increased to reflect a change in diameter.

The tapered section of the tool holder is modelled as six elements each with a different diameter. The tip diameter of all shrink fit tool holders is fixed at 24 mm and then increases gradually up to the base diameter. The geometry of the holder from manufacturer B (discussed in chapter 4) was used to construct the model, which has a base diameter of 34 mm. A harmonic analysis was carried out and the tool tip FRF extracted. Then the density of the tool holder elements were increased to reflect an increase in base diameter, and the harmonic analysis performed again. Base diameters of 45 mm and 53 mm were chosen, their respective densities are given in Table 5.1. The tool tip FRF results are plotted in Fig. 5.2.

As expected all modes see a decrease in natural frequency with additional mass, this frequency shift will also cause the stability lobes to occur at a lower spindle speed effectively allowing the user to cut deeper at lower speeds. Although this is beneficial, it is a very slight change in the dynamics especially when compared to

Density values (kg/m^3)			
Element No.	34mm	45mm	53mm
4	7750 (24)	7750 (24)	7750 (24)
5	7750 (26)	9117 (28.2)	10181 (29.8)
6	7750 (28)	10377 (32.4)	12528 (35.6)
7	7750 (30)	11535 (36.6)	14759 (41.4)
8	7750 (32)	12599 (40.8)	16861 (47.2)
9	7750 (34)	13576 (45)	18832 (53)

Table 5.1: Material density values to reflect a change in tool holder geometry for tool holders with 34 mm, 43 mm, and 53 mm base diameter (with theoretical diameter values in mm)

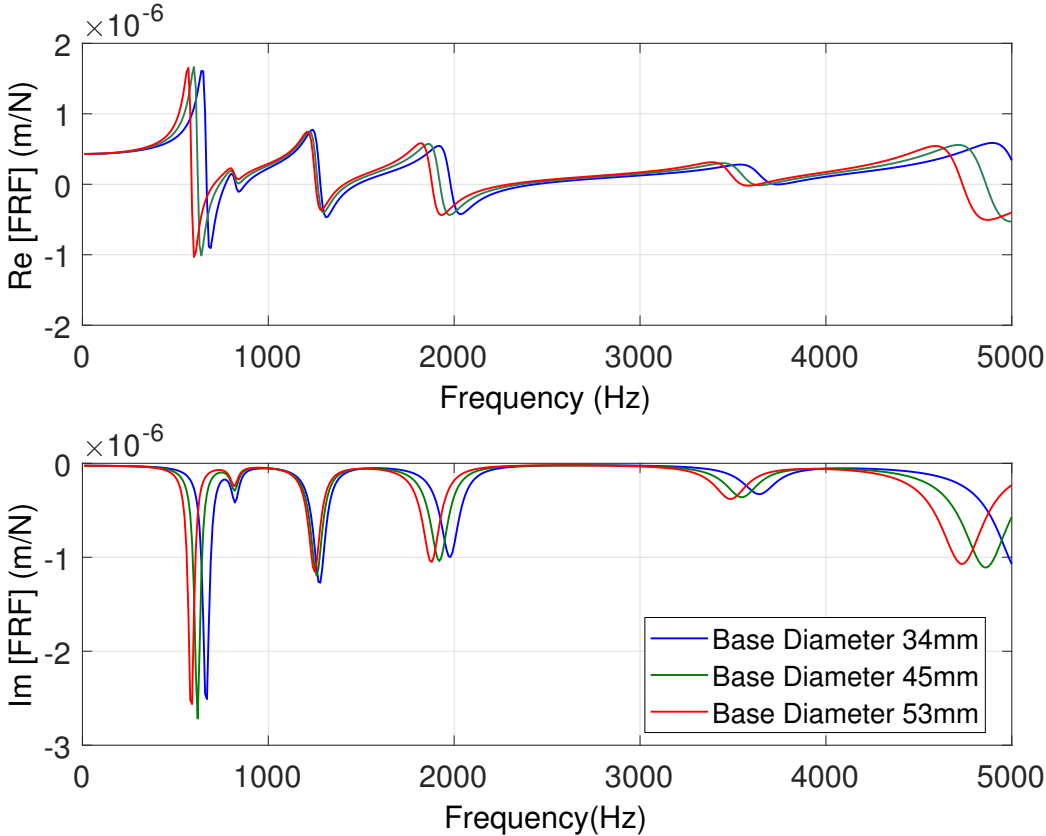


Figure 5.2: The effect of adding pure mass to the tool holder - frequency response results for tool holders with base diameters of 34, 45, and, 53 mm

experimental results in chapter 4 (Figs. 4.10-4.11). The amplitudes of all modes are unchanged by the addition of pure mass, meaning the absolute cutting depth limit (b_{lim}) is unaltered. It should be noted that the geometry of the holder is over simplified in that the tapered geometry is modelled using six stepped beam elements. At the time of research no tapered elements were available in the finite element software. Therefore it is also possible that this is not an accurate representation of the tapered geometry.

5.2.2 The addition of real mass

The concept of adding pure mass by varying the density throughout the tool holder is a purely theoretical one, in reality the change in stiffness that occurs with mass change may be just as important. For the same cases as are plotted in Fig. 5.2, a *real* mass was added to the FE model by changing the geometry of the tool holder; the diameters for the stepped section of the tool holder are given in Table. 5.1. The results of a harmonic analysis are shown in Fig. 5.3, with the associated mode shapes in Fig. 5.4.

The first two modes, in Fig. 5.3, see a similar decrease in natural frequency when compared to their pure mass counterparts; however, the added stiffness has decreased their amplitude. This is likely to lead to an increase in b_{lim} as the amplitude of the most dominant mode (500-600 Hz) has been reduced. Comparing this result to the experimental trends seen in chapter 4 ((Figs. 4.10-4.11)), it is clear to see there is some disagreement. The equivalent experimental modes actually see an increase in natural frequency when the diameter is increased from 34 mm to 53 mm. This may be due to the additional rigid body modes in the experimental model (the machine structure is not included in the FE model), or possibly it is due to the oversimplification of the holder geometry and inaccurate spindle properties in the FE model.

All higher frequency modes (1000+ Hz) see an increase in their natural frequency which is somewhat more significant than the frequency change seen with pure mass addition. This corresponds to the trends in the experimental data, sug-

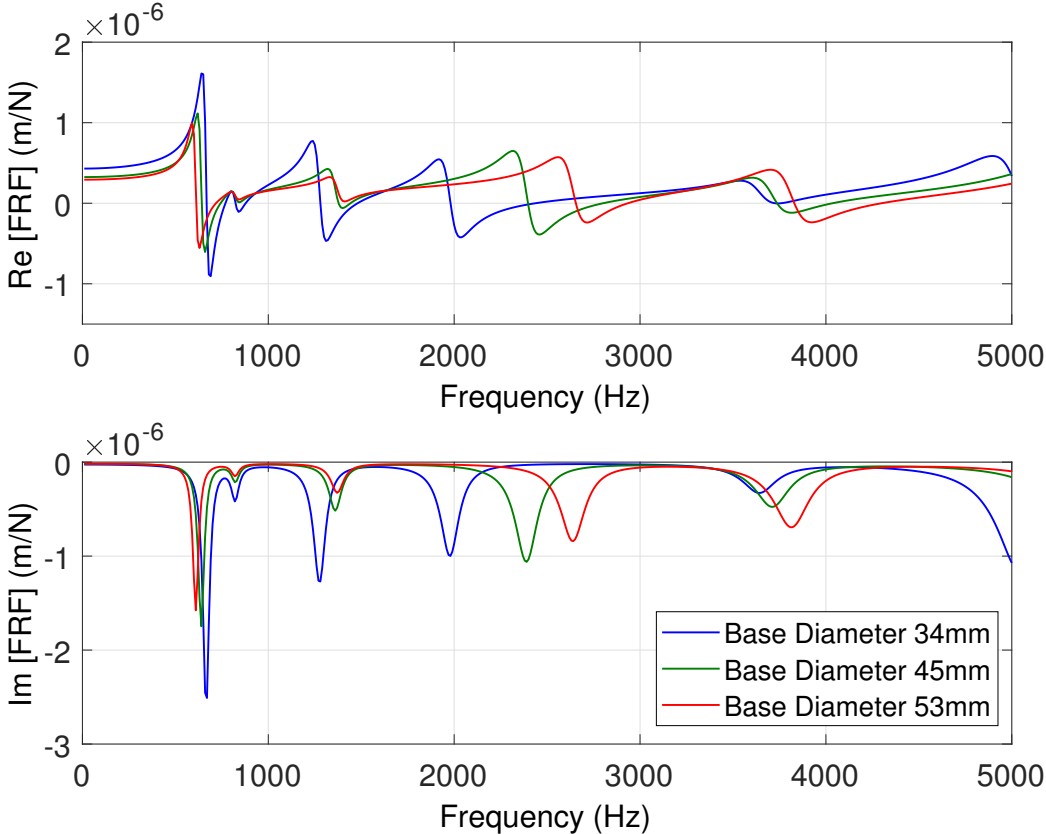


Figure 5.3: The effect of adding real mass to the tool holder - frequency response results for tool holders with base diameters of 34, 45, and, 53 mm

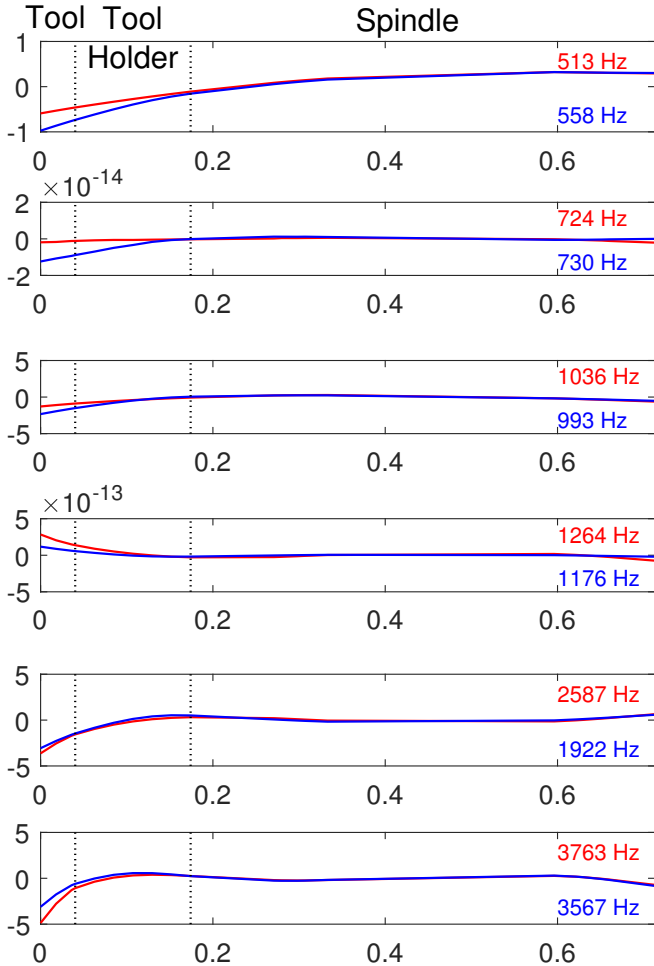


Figure 5.4: Finite element model modal analysis results - mass normalised mode shapes comparing 34mm diameter tool holder (blue) and 53mm diameter tool holder (red)

gesting the stiffness change may be of some importance in the later optimisation algorithm. This conclusion may be further validated by calculating the modal strain energy change ratio (MSECR) for both the 34 mm and 53 mm cases.

Modal strain energy methods have been adapted for use in structural health monitoring, where a damage is assumed to cause a local reduction in stiffness thus affecting the mode shapes in a localised region [102]. The method is used to detect such damage by comparing the MSECR of both the damaged and undamaged structures. The same method is adapted here by comparing the modified tool holder (53 mm) with the unmodified (34 mm) to see how critical the local reduction in stiffness is. The modal strain energy of the j th element of the i th mode of the modified (MSE_{ij}^m) and unmodified (MSE_{ij}) structures respectively are given as follows:

$$MSE_{ij}^m = \Phi_i^{mT} \mathbf{K}_j^m \Phi_i^m \qquad MSE_{ij} = \Phi_i^T \mathbf{K}_j \Phi_i \qquad (5.1)$$

which are functions of the mode shape (Φ) and elemental stiffness matrices \mathbf{K} . The modal strain energy change ratio for element j and mode i is then given by:

$$MSECR_j^i = \frac{|MSE_{ij} - MSE_{ij}^m|}{MSE_{ij}^m} \qquad (5.2)$$

If the MSE for m modes are considered together, the $MSECR_j$ of the j th element is defined as the average of the sum of the $MSECR_j^i$ for each mode, normalised with respect to the largest value $MSECR_{max}^i$ for that mode.

$$MSECR_j = \frac{1}{m} \sum_{i=1}^m \frac{MSECR_j^i}{MSECR_{max}^i} \qquad (5.3)$$

The normalised results are plotted in Fig. 5.5 considering the first (most dominant) mode as well all 6 modes.

It is expected that the MSECR will have large values where a change in stiffness has occurred and very small values at the far away nodes. However, the value can

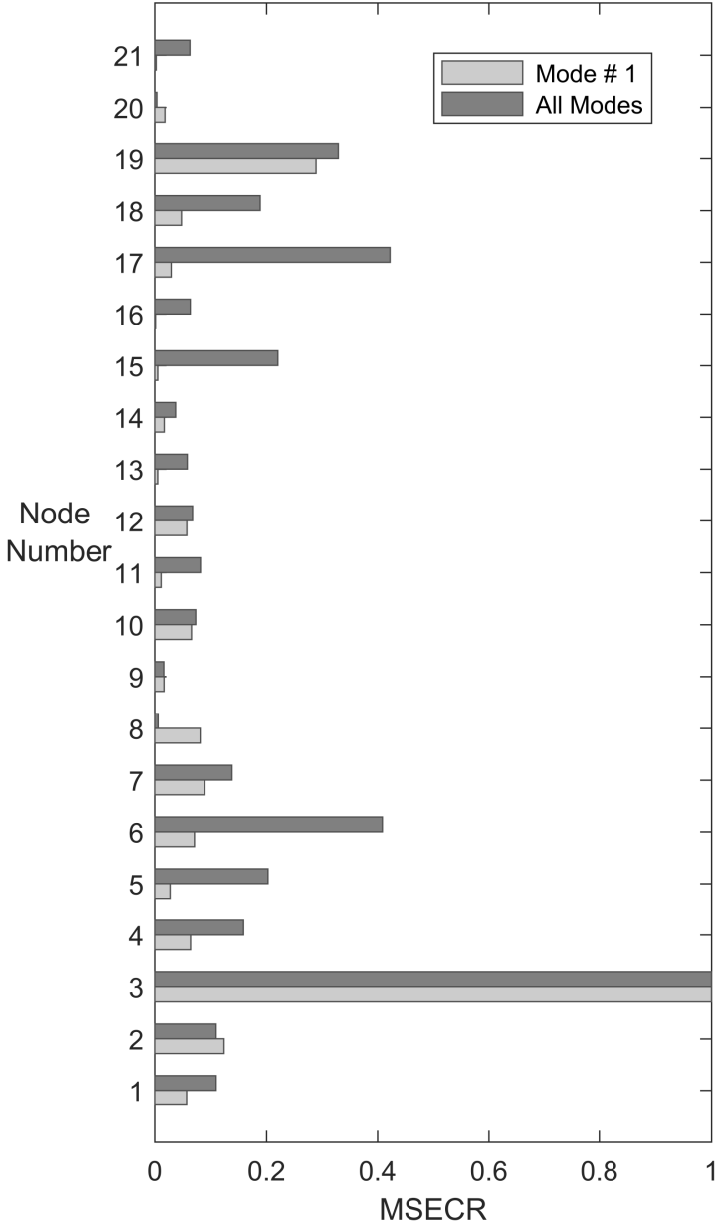


Figure 5.5: Normalised modal strain energy change ratio for tool holder diameters of 34 mm and 53 mm - change in tool holder mass occurs between nodes 3 and 9

be erroneously large or small at the nodal points of the mode shapes. Comparing the results with the mode shapes plotted in Fig. 5.4 may explain why the values between nodes 15 and 19 are so large when no stiffness change has occurred - as these nodes lie between the two sets of bearings on the spindle where little deflection occurs. However it is also possible that a change in stiffness at the tool holder may also cause a change in the stiffness on the spindle. The actual change in stiffness occurs between nodes 4 and 9, and the high result at node 3 suggests that changing the stiffness over the geometry of the already fairly rigid tool holder actually increases the stiffness at the tip of the tool holder (beginning of the tool).

5.2.3 Discussion

Comparing the trends when pure mass and real mass are added to the tool holder, with the trends in the experimental data in chapter 4, it is clear to see that the stiffness of the holder plays a vital role in the tool tip dynamics. The MSECR also suggests that increasing the stiffness of the holder increases the stiffness at its tip; the effect of which can clearly be seen in the mode shapes shown in Fig. 5.4. Therefore, it is sensible to conclude that when modelling changes in tool holder geometry, the change in stiffness must be considered.

5.3 Summary

The main contribution of this chapter is the contradiction of the initial assumption, which followed from industrial observations of tool holder geometry. It was noticed that tool holder geometry could have a significant effect on the stability of a milling operation, and this was accredited to the mass of the holder. The results presented in this chapter undermine this assumption. Therefore, it is now proposed that in order to use tool holder geometry as a chatter avoidance method, a new modelling/optimisation method must be developed which considers both mass and stiffness.

Chapter 6

Structural Modification of Tool Holder Geometry

Chapter 4 showed that the geometry of a tool holder can have a significant effect on the dynamics at the tool-tip and in turn, on the stability of the milling process. Then, chapter 5 demonstrated the importance of stiffness in tool holder modifications, The purpose of this chapter is to introduce a new higher rank structural modification (SM) method for chatter avoidance in high speed milling that can be used to model and optimise changes in tool holder geometry. Once the theory has been presented, it is experimentally validated.

6.1 Introduction

As discussed in previous chapters, chatter vibrations can severely limit the mass removal rate (MRR) of milling operations. Therefore, the ability to avoid the onset of chatter and maximise the MRR for a given operation is of great interest to industrial and academic engineers alike.

Perhaps the simplest method to do so is to select the optimum tooling setup (tool and tool holder); however, experimental evaluation of numerous tools and tool holders is expensive; moreover, the choice of tool is often fixed by the cutting

operation. For this reason receptance coupling substructure analysis (RCSA) was proposed in order to reduce the experimental cost of such operations. The method uses a small set of experimental FRFs (both translational and rotational) from a milling machine with a standard tool holder. A structural coupling method is then applied to remove the standard tool holder and replace it with another; therefore, allowing the user to predict the stability of an operation with any tool holder. However, the method suffers from two drawbacks. Firstly, the accuracy of the result is dependent on knowledge of the interface dynamics between the tool and tool holder. Secondly, the optimum tool holder geometry must be found indirectly by repeating the process for every possible tool holder.

The structural modification method presented in this chapter provides the user with the same capability; however, removes the dependency on interface dynamics and allows for easy optimisation.

6.2 Theory

Structural modification, as presented by Mottershead and Ram [1], involves the combination of two (or more) dynamic models to predict the dynamic properties of more complex structures. Consider models A and B (as described in section 2.3.1), with l and m degrees of freedom respectively, which are to be combined at p locations to form model C . At a particular frequency, we have that:

$$\mathbf{Y}_A = [\mathbf{H}_A]_{l \times l} \mathbf{F}_A \quad \mathbf{Y}_B = [\mathbf{H}_B]_{m \times m} \mathbf{F}_B \quad \mathbf{Y}_C = [\mathbf{H}_C]_{n \times n} \mathbf{F}_C \quad (6.1)$$

where \mathbf{Y} is the harmonic displacement vector, \mathbf{F} is the harmonic force vector, \mathbf{H} is the frequency response function matrix containing receptances H_{ij} , describing the displacement at degree of freedom i due to forcing at degree of freedom j , and $n = l + m - p$.

To repeat Eqn. (3.62), compatibility ($\mathbf{X}_C = \mathbf{X}_A + \mathbf{X}_B$) and equilibrium ($\mathbf{F}_C = \mathbf{F}_A + \mathbf{F}_B$)

conditions are applied at the p connection nodes; thus, we have that:

$$\mathbf{H}_C^{-1} = \mathbf{H}_A^{-1} + \mathbf{H}_B^{-1} \quad (6.2)$$

this formulation is inconvenient for numerical application as it involves multiple matrix inversions, however it may be rewritten as:

$$\begin{aligned} \mathbf{H}_C^{-1} &= \mathbf{H}_A^{-1}[\mathbf{I} + \mathbf{H}_A\mathbf{H}_B^{-1}] \\ \mathbf{H}_C &= [\mathbf{I} + \mathbf{H}_A\mathbf{H}_B^{-1}]^{-1}\mathbf{H}_A \end{aligned} \quad (6.3)$$

This forms the basis of both the direct and inverse methods.

6.2.1 The direct method

Since model B is a local modification (i.e. $m < l$), further simplifications can be made using the method by Özgüven [49]. Both models may be partitioned into sub-matrices, separating DOFs that are involved with the modification and those that are not.

$$\mathbf{H}_A = \begin{bmatrix} \mathbf{H}_{AOO} & \mathbf{H}_{AOI} \\ \mathbf{H}_{AIO} & \mathbf{H}_{AII} \end{bmatrix} \quad [\mathbf{H}_B]^{-1} = \begin{bmatrix} \mathbf{0} & \mathbf{0} \\ \mathbf{0} & \mathbf{B}_{II} \end{bmatrix} \quad (6.4)$$

where the subscript O denotes the DOFs not involved with the modification and I denotes the DOFs that are modified. This partitioned matrix form reduces the number and size of the operation to one matrix inversion of an $m \times m$ matrix. The global model is then given by:

$$\begin{aligned} \mathbf{H}_{CII} &= [\mathbf{I} + \mathbf{H}_{AII}\mathbf{B}_{II}]^{-1}\mathbf{H}_{AII} \\ \mathbf{H}_{COI}^T &= \mathbf{H}_{CIO} = \mathbf{H}_{AOI}[\mathbf{I} - \mathbf{B}_{II}\mathbf{H}_{CII}] \\ \mathbf{H}_{COO} &= \mathbf{H}_{AOO} - \mathbf{H}_{AOI}\mathbf{B}_{II}\mathbf{H}_{CIO} \end{aligned} \quad (6.5)$$

Numerical optimisation algorithms could then be run in order to optimise the modification \mathbf{B} .

6.2.2 The inverse method

If we are to only partially construct the modification matrix in Eq. (6.3), leaving it as a function of some unknown geometric modification parameter α i.e. $\mathbf{B} = \mathbf{B}(\alpha)$, then the inverse problem may also be solved.

$$\mathbf{H}_C = \frac{\text{adj}(\mathbf{I} + \mathbf{H}_A \mathbf{B}(\alpha)) \mathbf{H}_A}{\det(\mathbf{I} + \mathbf{H}_A \mathbf{B}(\alpha))} = \frac{\det(\mathbf{I} + \mathbf{H}_A \mathbf{B}(\alpha)) [\mathbf{I} + \mathbf{H}_A \mathbf{B}(\alpha)]^{-1} \mathbf{H}_A}{\det(\mathbf{I} + \mathbf{H}_A \mathbf{B}(\alpha))} \quad (6.6)$$

The antiresonance of the ij^{th} receptance is then given by $[\text{adj}(\mathbf{I} + \mathbf{H}_A \mathbf{B}(\alpha)) \mathbf{H}_A]_{ij} = 0$, whilst its natural frequencies are given by $\det(\mathbf{I} + \mathbf{H}_A \mathbf{B}(\alpha)) = 0$. For simple modifications these equations may have algebraic solutions for the modification parameter α ; however, for more complex modifications a numerical solution may be necessary.

It is possible to make further simplifications to Mottershead's [1] method by applying the same matrix partitions as with the direct method (Eq. (6.4)); by doing so the size of the matrix operations are reduced and the likelihood of an algebraic solution increased. Eq. (6.6) can then be written as:

$$\begin{aligned} \mathbf{H}_{CII} &= \frac{\text{adj}(\mathbf{I} + \mathbf{H}_{AII} \mathbf{B}_{II}(\alpha)) \mathbf{H}_{AII}}{\det(\mathbf{I} + \mathbf{H}_{AII} \mathbf{B}_{II}(\alpha))} \\ \mathbf{H}_{COI}^T = \mathbf{H}_{CIO} &= \frac{\det(\mathbf{I} + \mathbf{H}_{AII} \mathbf{B}_{II}(\alpha)) \mathbf{H}_{AOI} [\mathbf{I} - \mathbf{B}_{II}(\alpha) \mathbf{H}_{CII}]}{\det(\mathbf{I} + \mathbf{H}_{AII} \mathbf{B}_{II}(\alpha))} \\ \mathbf{H}_{COO} &= \frac{\det(\mathbf{I} + \mathbf{H}_{AII} \mathbf{B}_{II}(\alpha)) [\mathbf{H}_{AOO} - \mathbf{H}_{AOI} \mathbf{B}_{II}(\alpha) \mathbf{H}_{CIO}]}{\det(\mathbf{I} + \mathbf{H}_{AII} \mathbf{B}_{II}(\alpha))} \end{aligned} \quad (6.7)$$

This formulation allows for the natural frequencies of the global structure to be repositioned using only the measured receptances at the modification DOFs I .

6.3 Application of structural modification theory to milling

Since the geometry, and more specifically the diameter, of the tool holder has a significant effect on the tool tip dynamics, and in turn the stability of the milling operation, a simple method of avoiding chatter would be to choose a tool holder that results in stability lobes at a preferred spindle speed. Using the direct SM method presented above, this section will show that, it is possible to predict the dynamics of a number of different tool holders with a single experimental model. Whilst this is useful, it is a long winded method of optimising the tool holder geometry. However, this section will also show that, since the location of the stability lobes is directly proportional to the natural frequencies of the structure, the inverse method may be used to optimise to the geometry by solving a single equation.

6.3.1 The stability of a milling operation

In order to apply SM theory to the chatter avoidance problem, it is helpful to revisit the average tooth angle approach for the prediction of stability lobe diagrams. Tlustý's method (section 3.2.1, Eqns. (3.34) and (3.32)) gives us that

$$b_{lim} = \frac{-1}{2K_s \text{Re}[\text{FRF}_{or}]N_t^*} \quad \text{where} \quad N_t^* = \frac{N_t(\varphi_e - \varphi_s)}{360} \quad (6.8)$$

where b_{lim} is the stability limit of the axial depth of cut in m, K_s is the specific force, FRF_{or} is the oriented FRF (a linear combination of the x - and y -direction FRFs), N_t^* is the average number of teeth in the cut at any one time, N_t is the number of teeth on the tool, and φ_e and φ_s are the exit and entry angle of the tool respectively. The stability limit also depends upon the spindle speed of the operation and this is given by

$$\Omega = \frac{f_c}{N_t(L + \frac{\epsilon}{2\pi})} \quad \text{where} \quad \epsilon = 2\pi - 2 \tan^{-1} \left(\frac{\text{Re}[\text{FRF}_{or}]}{\text{Im}[\text{FRF}_{or}]} \right) \quad (6.9)$$

CHAPTER 6. STRUCTURAL MODIFICATION OF TOOL HOLDER GEOMETRY

where Ω is the spindle speed in revolutions per second, f_c is the valid chatter frequency range, and $L \in \mathbb{Z}$ is the lobe number. In order to produce a stability lobe diagram, Ω is calculated for a number of lobes ($N = 0, 1, 2, \dots$) over the valid chatter frequency range(s) i.e. where $\text{Re}[\text{FRF}_{or}] \leq 0$, then each of these lobes are plotted against b_{lim} .

Eq. (6.8) tells us that the stability limit tends to infinity as the real part of the oriented FRF tends to zero. Since the real part of any FRF will tend to zero at resonance, by shifting the resonance frequencies, the peaks in the stability lobes are also shifted. Considering Eq. (6.9) at resonance (where $\text{Re}[\text{FRF}_{or}] = 0$), we have that

$$\Omega_{best} = \frac{f_n}{N_t(N+1)} \quad (6.10)$$

Where Ω_{best} is the location of the peak in the stability lobes, and f_n is the natural frequency of the oriented FRF in Hz. The oriented FRF is given by:

$$\text{FRF}_{or} = \mu_x \text{FRF}_x + \mu_y \text{FRF}_y \quad (6.11)$$

where FRF_x and FRF_y are the frequency response functions in the x - and y -directions respectively, and μ_x and μ_y are the directional orientation factors used to project the cutting force model onto the surface normal direction.

Hence, the tool tip FRF in both the x - and y -directions are required to predict the stability of a given milling operation. Whilst this has no effect on the application of the direct SM method to high speed milling, as FRF_x and FRF_y can be predicted individually (using Eq. (6.5)) and used to generate the stability lobe diagram. When applying the inverse method, the location of the optimum spindle speed (Ω_{best}) is dependent not on the resonant frequencies of the individual FRFs but on FRF_{or} , therefore the inverse method in Eq. (6.6) must be updated to take into account the oriented FRF.

6.3.2 Inverse structural modification of tool holder geometry

It will now be shown that, because of the properties inherent in any FRF curve, by shifting the resonance of either the x - or y -direction using the inverse method, the resonance of the oriented FRF is also shifted.

Consider an experimental model of some standard tool holder \mathbf{H}_A , and a partially constructed numerical model ($\mathbf{B}(d)$) with diameter d unknown. The inverse SM method set out in Eq. (6.6) may be applied to optimise d in terms of the natural frequency of either the x or y direction FRFs. Now, let \mathbf{H}_A^x be an experimental model in the x direction, and let \mathbf{H}_A^y be an experimental model in the y direction, then the inverse SM equations are given by:

$$\mathbf{H}_C^x = \frac{\text{adj}(\mathbf{I} + \mathbf{H}_A^x \mathbf{B}(d)) \mathbf{H}_A^x}{\det(\mathbf{I} + \mathbf{H}_A^x \mathbf{B}(d))} \quad \mathbf{H}_C^y = \frac{\text{adj}(\mathbf{I} + \mathbf{H}_A^y \mathbf{B}(d)) \mathbf{H}_A^y}{\det(\mathbf{I} + \mathbf{H}_A^y \mathbf{B}(d))} \quad (6.12)$$

where Matrix partitions have been removed for simplicity. However, since the location of the stability lobes depends on FRF_{or} , the equations in Eq. (6.12) must be combined in the same manner as FRF_{or} , this gives

$$\begin{aligned} \mu_x \mathbf{H}_C^x + \mu_y \mathbf{H}_C^y &= \mu_x \frac{\text{adj}(\mathbf{I} + \mathbf{H}_A^x \mathbf{B}(d)) \mathbf{H}_A^x}{\det(\mathbf{I} + \mathbf{H}_A^x \mathbf{B}(d))} + \mu_y \frac{\text{adj}(\mathbf{I} + \mathbf{H}_A^y \mathbf{B}(d)) \mathbf{H}_A^y}{\det(\mathbf{I} + \mathbf{H}_A^y \mathbf{B}(d))} \\ &= \frac{\det(\mathbf{I} + \mathbf{H}_A^y \mathbf{B}(d)) \det(\mathbf{I} + \mathbf{H}_A^x \mathbf{B}(d)) [\mu_x [\mathbf{I} + \mathbf{H}_A^x \mathbf{B}(d)]^{-1} \mathbf{H}_A^x + \mu_y [(\mathbf{I} + \mathbf{H}_A^y \mathbf{B}(d))^{-1} \mathbf{H}_A^y]}{\det(\mathbf{I} + \mathbf{H}_A^x \mathbf{B}(d)) \det(\mathbf{I} + \mathbf{H}_A^y \mathbf{B}(d))} \end{aligned} \quad (6.13)$$

Then, the natural frequencies of the oriented FRF can be set by solving

$$\det(\mathbf{I} + \mathbf{H}_A^x \mathbf{B}(d)) \det(\mathbf{I} + \mathbf{H}_A^y \mathbf{B}(d)) = 0 \quad (6.14)$$

which clearly has solutions when either $\det(\mathbf{I} + \mathbf{H}_A^x \mathbf{B}(d)) = 0$ or $\det(\mathbf{I} + \mathbf{H}_A^y \mathbf{B}(d)) = 0$. Therefore, the inverse SM method, as set out in Eqs. (6.6) and (6.7) can be applied in either the x - or y -directions in order to reposition the stability lobes.

This is a standard property for any structure; when adding two FRFs together, the infinitesimal nature of resonance in either curve will also cause resonance in their sum.

When selecting which direction to modify, it is important to keep in mind that the most dominant mode (the mode with the largest amplitude) will have the lowest stability limit and thus determine the absolute stability limit; therefore, this mode should be optimised. However the magnitude of μ_x and μ_y should also be taken into consideration, as they may change the dominance of the modes.

6.4 Experimental Investigation: Spindle Rig

Before validating the SM theory on a full milling machine, it was decided to first test the theory on a spindle rig. The spindle rig consists of a HSKA63 milling spindle, bearings and bearing housing, similar to any five axis milling machine, but is suspended on a smaller simpler structure. Validation on a spindle rig has several advantages over validation on a milling machine. Firstly, because of the simpler supporting structure, many of the low frequency modes associated with the machine are removed; therefore, concentration can be given to the dominant bending modes of the tool, tool holder, and spindle. Secondly, the spindle rig can be tested in cold conditions, meaning nonlinearities such as thermal softening of the bearings [103] are removed, thus making the data more repeatable. Finally, because of the simpler support, the rig is axisymmetric, meaning the dynamics are identical in the x and y direction, and therefore the natural frequencies of the oriented FRF are identical to that of the x or y direction; therefore either may be used for optimisation purposes. For the rest of this section, the y -direction is considered. A schematic diagram of the spindle rig's geometry is shown in Fig. 6.1

In order to investigate SM for chatter avoidance in high speed milling, two tool holders of different geometries were chosen. A cylindrical untapered holder of length 0.134 m and diameter 0.024 m; and a tapered tool holder of length 0.134 m and diameter ranging between 0.024 m and 0.034m. These holders will be re-

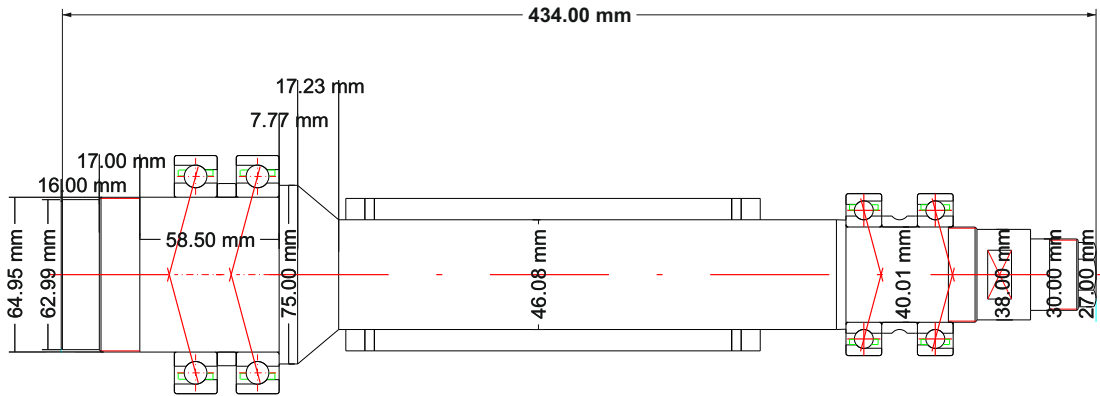


Figure 6.1: Diagram showing the dimensions and bearing locations of the experimental spindle rig

ferred to as the unmodified and modified holders, respectively. Both holders had a HSKA63 spindle interface. The geometries of both holders are summarised in Fig. 6.2 and Table. 6.1. It is important to note that the geometries of the tool holders differ only in the base diameter d_2 , as this is this parameter that will be modified.

A two fluted end mill of total length 0.083 m was inserted into both holders with a stickout length of 0.037 m. Then, each of the tool holders were clamped into the spindle, and their tool tip frequency response functions measured, these results are compared in Fig. 6.3. It can be seen that the simpler structure of the spindle rig results in a single dominant bending mode in both cases, and similarly to the results presented in chapter. 4, the larger base diameter gives rise to a mode with lower amplitude and higher natural frequency.

	l1(mm)	l2(mm)	l3	d1(mm)	d2(mm)	d3(mm)
Unmodified	160	134	47	64	24	24
Modified	160	134	47	64	34	24

Table 6.1: Dimensions of the modified and unmodified tool holders

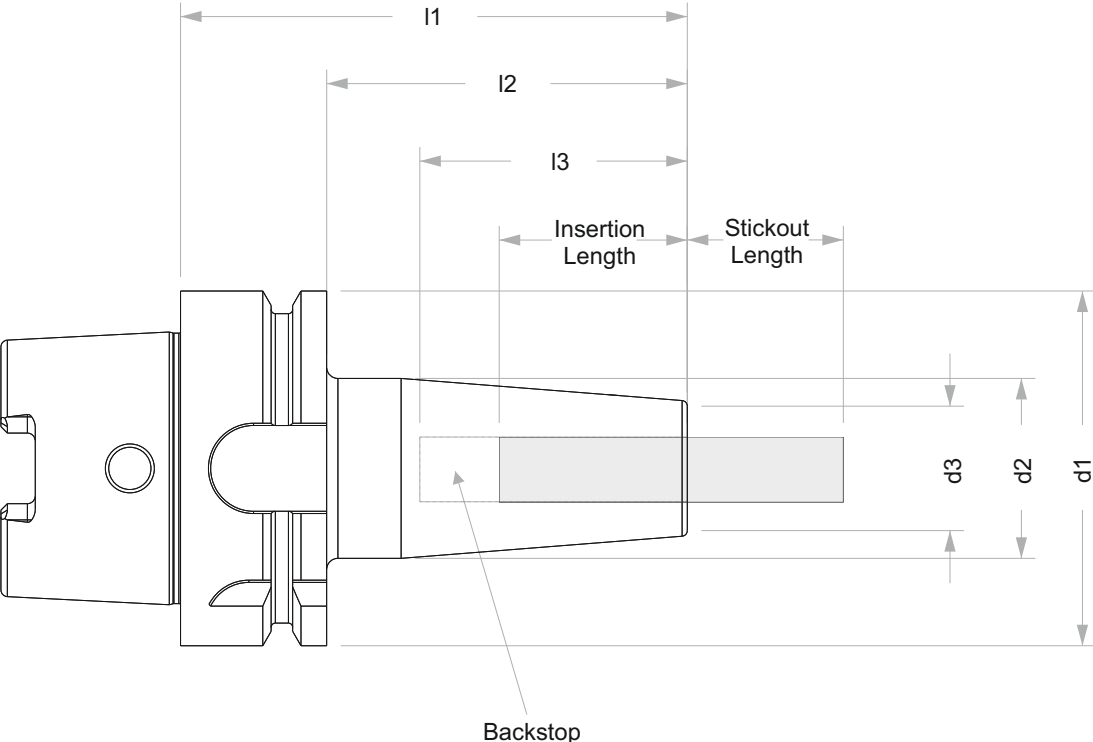


Figure 6.2: Diagram showing the dimensions for both the unmodified and modified holders

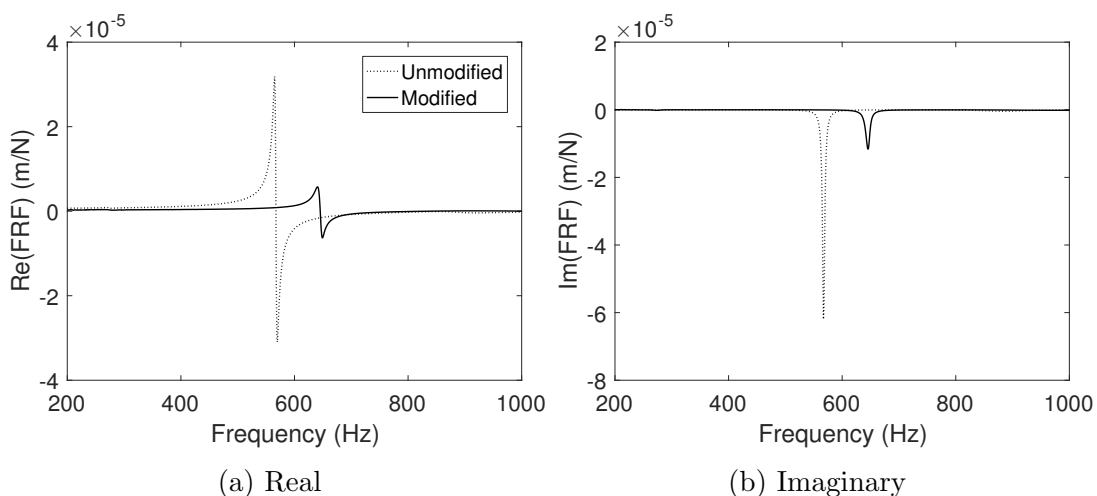


Figure 6.3: Real (a) and Imaginary (b) frequency response function plots comparing the tool tip dynamics of the unmodified (\cdots) and modified (—) holders on the spindle rig

The hypothesis behind the following experiment is that, using only data from the unmodified tool holder, it is possible to predict, and hence optimise, the tool tip frequency response function of the modified tool holder using SM.

6.4.1 Methodology

This section describes how each of the models (A and B), defined in section 6.2 and shown in Fig. 6.4 are constructed in order to apply higher rank SM theory to the tool holder problem.

Model B

It is convenient to begin the methodology by discussing model B, or the modification model, which is a numerical model that describes the difference in diameter between the unmodified and modified holders. The geometry is a circular tube of length 0.134 m with an inner diameter of 0.024 m. The outer diameter varies between 0.024 m and 0.034 m, as shown in Fig. 6.2. A numerical model was constructed with the geometrical properties shown, and standard steel material properties (density $\rho = 7750 \text{ kg m}^{-3}$, Young's Modulus $E = 200 \text{ GPa}$).

It is important to keep the dimensions of model B as low as possible for two reasons. Firstly, each node in the numerical model must also occur in the experimental model A, and experimental data inherently contains error. But also, if the inverse SM method is to be used, by keeping the number of nodes to a minimum, it is more likely that a solution can be found.

Whilst minimising the dimensions of model B has its advantages, it also carries with it some disadvantages. The number of modes included in a numerical model equals the size of the elemental matrices (stiffness \mathbf{K} and mass \mathbf{M}), i.e. a numerical model with a 2×2 stiffness matrix only accounts for the first two modes of the structure. Hence, when model B is minimised it becomes a truncated model and does not account for the out of range modes.

However, in order to minimise the experimental cost of the method, it was decided that the geometry of model B would be modelled using only two beam elements, one for the tapered section of the holder and one for the untapered section. The first beam lies between nodes n_2 and n_3 and the second between nodes n_3 and n_4 and each beam has two degrees of freedom, translation y and rotation θ , as shown in Fig. 6.4. Therefore the dimensions of the element matrices are 6×6 .

Beam one is a tapered Timoshenko tube, constructed from the beam element matrices given in [104], it has an inner diameter of 0.024 m, an outer diameter between 0.024 m and 0.034 m, and a length of 0.064 m. Whilst the second beam is an untapered Timoshenko tube, constructed from the standard Timoshenko beam element matrices [105], with an inner diameter of 0.024 m, an outer diameter of 0.034 m, and a length of 0.07 m. Timoshenko beam elements were used over Euler-Bernoulli beam elements, since it has already been shown that they describe the dynamics of tool holders with greater accuracy [84].

The global mass and stiffness matrices for model B were then assembled using the direct stiffness method, which applies compatibility and equilibrium conditions

in a similar manner to SM. The global mass and stiffness matrices are then given by

$$\mathbf{M} = \begin{bmatrix} \begin{bmatrix} \mathbf{M}_{22} \end{bmatrix}_{2 \times 2} & \begin{bmatrix} \mathbf{M}_{23} \end{bmatrix}_{2 \times 2} & \mathbf{0} \\ \begin{bmatrix} \mathbf{M}_{32} \end{bmatrix}_{2 \times 2} & \begin{bmatrix} \mathbf{M}_{33} \end{bmatrix}_{2 \times 2} & \begin{bmatrix} \mathbf{M}_{34} \end{bmatrix}_{2 \times 2} \\ \mathbf{0} & \begin{bmatrix} \mathbf{M}_{43} \end{bmatrix}_{2 \times 2} & \begin{bmatrix} \mathbf{M}_{44} \end{bmatrix}_{2 \times 2} \end{bmatrix} \quad (6.15)$$

and

$$\mathbf{K} = \begin{bmatrix} \begin{bmatrix} \mathbf{K}_{22} \end{bmatrix}_{2 \times 2} & \begin{bmatrix} \mathbf{K}_{23} \end{bmatrix}_{2 \times 2} & \mathbf{0} \\ \begin{bmatrix} \mathbf{K}_{32} \end{bmatrix}_{2 \times 2} & \begin{bmatrix} \mathbf{K}_{33} \end{bmatrix}_{2 \times 2} & \begin{bmatrix} \mathbf{K}_{34} \end{bmatrix}_{2 \times 2} \\ \mathbf{0} & \begin{bmatrix} \mathbf{K}_{43} \end{bmatrix}_{2 \times 2} & \begin{bmatrix} \mathbf{K}_{44} \end{bmatrix}_{2 \times 2} \end{bmatrix} \quad (6.16)$$

$$(6.17)$$

respectively, where the subscripts ij refer to the nodes $n2$ - $n4$, and

$$\begin{bmatrix} K_{ij} \end{bmatrix}_{2 \times 2} = \begin{bmatrix} K_{y_i y_j} & K_{y_i \theta_j} \\ K_{\theta_i y_j} & K_{\theta_i \theta_j} \end{bmatrix} \quad (6.18)$$

Then finally, for a particular frequency ω model B is given by:

$$\mathbf{B}_{II} = \mathbf{K} - \omega^2 \mathbf{M} \quad (6.19)$$

Model A

To construct model A, the experimental translational mode shapes ϕ_r were measured using standard impact test equipment. An impulse hammer was used to excite the system at the base of the holder, and the response was measured at eighteen equally spaced locations between the tool tip and the base of the holder. The tip of the holder was chosen as the excitation location because the tool tip was found to be too flexible for a steel tipped hammer. To the eighteen measured

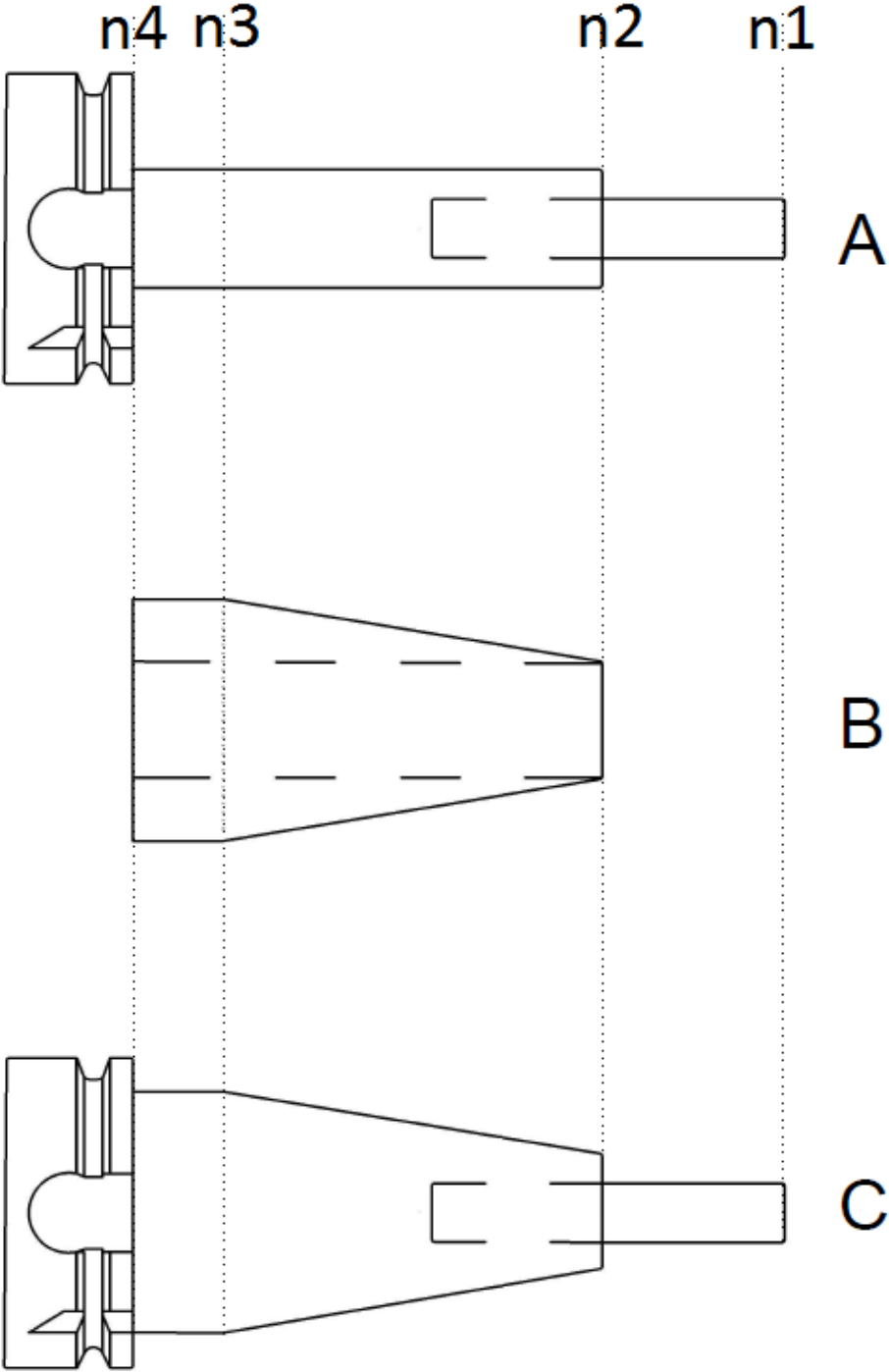


Figure 6.4: Diagram detailing the location of the nodes included in models A B C

frequency response functions H_{ij} , where $i \in \{1, 2, \dots, 18\}$ and $j = 5$, curves were fitted between 0 Hz and 5000 Hz and a modal model extracted using the experimental modal analysis method outlined in chapter 4.

In total eight modes (ϕ_r) were extracted with natural frequencies between 273 Hz and 4045 Hz. Then to each of the eight modes a polynomial of order three was fitted in the least-squares sense. A least squares curve fit finds the optimum fit to the measured mode shapes by minimising the sum of the squared residuals, where a residual is defined as the difference between the measured value and the fitted value. Each of the eight polynomials were then differentiated to get the rotational mode shapes $\phi_r^{(1)}$. Then for each of the four nodes n_1 to n_4 shown in Fig. 6.4, the translational and rotational FRFs (H_{ij} , N_{ij} , L_{ij} , P_{ij}) were constructed. The accuracy of this method depends largely on the number of data points included in the polynomial fitting. Increasing the number of data points was found to increase the accuracy of the rotational mode shapes, whilst decreasing the efficiency of the method. It was found that using eighteen data points continuously produced accurate results for all modes, although it was not always necessary.

Although some of the translational FRFs (H_{ij}) were measured directly, the regenerated curves were used so as not to include noise in the SM equations. As discussed already, small errors, such as noise, in the input can lead to large errors in the output because of the matrix inversions. Whilst curve fitting also causes small errors, it was found that better results could be obtained using the smooth regenerated FRFs.

Model A was then constructed, for a particular frequency ω , as follows:

$$\begin{aligned} \mathbf{H}_A &= \begin{bmatrix} [\mathbf{H}_{AOO}]_{2 \times 2} & [\mathbf{H}_{AOI}]_{2 \times 6} \\ [\mathbf{H}_{AIO}]_{6 \times 2} & [\mathbf{H}_{AII}]_{6 \times 6} \end{bmatrix} \\ &= \begin{bmatrix} [\mathbf{G}_{11}]_{2 \times 2} & | & [\mathbf{G}_{12}]_{2 \times 2} & [\mathbf{G}_{13}]_{2 \times 2} & [\mathbf{G}_{14}]_{2 \times 2} \\ \hline [\mathbf{G}_{21}]_{2 \times 2} & | & [\mathbf{G}_{22}]_{2 \times 2} & [\mathbf{G}_{23}]_{2 \times 2} & [\mathbf{G}_{24}]_{2 \times 2} \\ [\mathbf{G}_{31}]_{2 \times 2} & | & [\mathbf{G}_{32}]_{2 \times 2} & [\mathbf{G}_{33}]_{2 \times 2} & [\mathbf{G}_{34}]_{2 \times 2} \\ [\mathbf{G}_{41}]_{2 \times 2} & | & [\mathbf{G}_{42}]_{2 \times 2} & [\mathbf{G}_{43}]_{2 \times 2} & [\mathbf{G}_{44}]_{2 \times 2} \end{bmatrix} \end{aligned} \quad (6.20)$$

where the subscripts 1-4 refer to the nodes n_1 - n_4 , and

$$[\mathbf{G}_{ij}]_{2 \times 2} = \begin{bmatrix} H_{ij}(\omega) & N_{ij}(\omega) \\ L_{ij}(\omega) & P_{ij}(\omega) \end{bmatrix} \quad (6.21)$$

6.4.2 Direct structural modification

Using the models constructed in section. 6.4.1, the direct SM method was carried out by applying Eq. (6.5) over a frequency range of 1 Hz to 5000 Hz with a 1 Hz increment. The resultant matrix (for each frequency) \mathbf{H}_{CII} contains the four FRFs ($H_{11}, N_{11}, L_{11}, P_{11}$), from which the translational FRF H_{11} was extracted. The predicted result is presented in Fig. 6.5 alongside its experimental counterpart and the unmodified holder. It should be noted that the experimental tool tip FRF from the modified holder was constructed from the measured mode shapes, since the excitation was applied at the base of the holder and not the tool tip.

It can be seen that the predicted result shows a very high correlation with the experimental data. The single mode occurs at 646 Hz, within 1% of the measured mode at 649 Hz, whilst the predicted amplitude (of the imaginary part) is within 7% of the measured value. It is clear that the direct SM of tool holder geometry has a clear advantage over receptance coupling, in that these results have been obtained without including any unknown interface properties. Hence, using this method it is possible to choose the optimum holder for a given operation without having to take any further measurements such as contact stiffness or damping.

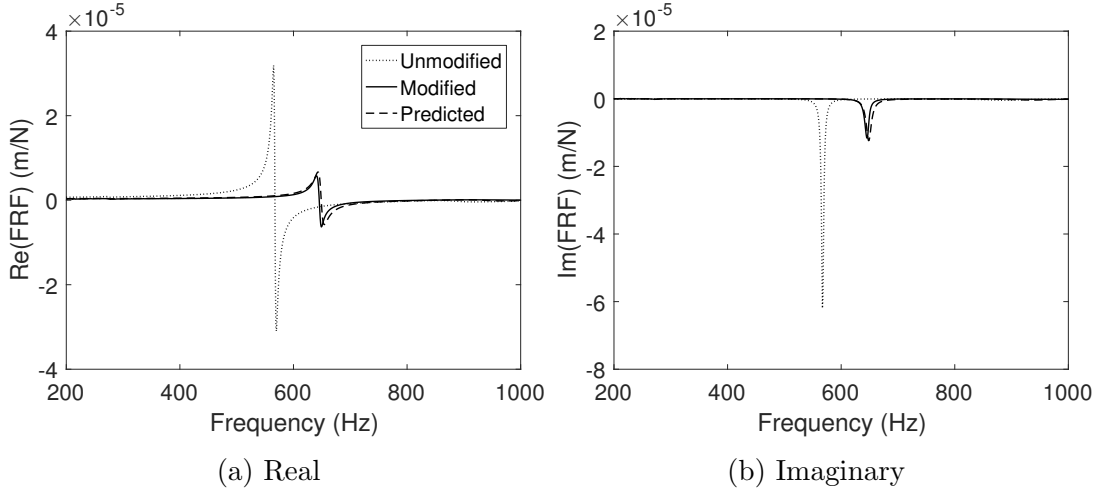


Figure 6.5: Real (a) and Imaginary (b) frequency response function plots comparing the experimental tool tip dynamics of the unmodified (\cdots) and modified holders (—), with the predicted result (- -) from the spindle rig

The inverse SM method is now applied to the same problem.

6.4.3 Inverse structural modification

It has already been shown that the spindle speed at which the peaks in the stability lobes occur is directly proportional to the natural frequency of the oriented FRF (6.11)

$$\Omega_{best} = \frac{f_n}{(N + 1)N_t} \quad (6.22)$$

Hence, by shifting the natural frequency of a particular mode it is possible to reposition the stability lobes. For instance, it may be desirable to cut at a particular spindle speed in order to minimise tool wear, or the user may want to position a peak at the maximum spindle speed of the machine in order to maximise its full potential. Since the spindle rig is axisymmetric, the natural frequency of the y direction matches that of the oriented FRF; therefore the inverse method given in Eq. (6.7) is applied to optimise the tool holder diameter d_2 in the y -direction.

To apply inverse SM, model A was constructed using the same methodology as in section 6.4.1. Then, the same beam elements as before were used to construct

CHAPTER 6. STRUCTURAL MODIFICATION OF TOOL HOLDER GEOMETRY

model B; however, a symbolic variable $d2$ was used for the outer diameter of the beams instead of inputting an actual value. Therefore, the tapered beam has an inner diameter of 0.024 m and an outer diameter ranging between 0.024 m and $d2$, and the untapered beam has an inner diameter of 0.024 m and an outer diameter of $d2$. In doing so, model B becomes a symbolic matrix and a function of $d2$.

Since the natural frequency of the modified holder occurs at 646 Hz, inverse SM was used to seek a value of $d2$ which would result in a mode at 646 Hz, therefore $w_{seek} = 2\pi(646)$ rad/s. Referring back to section 6.2, Eq. (6.7), the natural frequencies of the modified model C are given by

$$\det(\mathbf{I} + \mathbf{H}_{AII}\mathbf{B}_{II}(d2)) = 0 \quad (6.23)$$

To solve this, the matrix \mathbf{H}_{AII} is given by

$$\mathbf{H}_{AII} = \begin{bmatrix} \left[\mathbf{G}_{22}(\omega_{seek}) \right]_{2 \times 2} & \left[\mathbf{G}_{23}(\omega_{seek}) \right]_{2 \times 2} & \left[\mathbf{G}_{24}(\omega_{seek}) \right]_{2 \times 2} \\ \left[\mathbf{G}_{32}(\omega_{seek}) \right]_{2 \times 2} & \left[\mathbf{G}_{33}(\omega_{seek}) \right]_{2 \times 2} & \left[\mathbf{G}_{34}(\omega_{seek}) \right]_{2 \times 2} \\ \left[\mathbf{G}_{42}(\omega_{seek}) \right]_{2 \times 2} & \left[\mathbf{G}_{43}(\omega_{seek}) \right]_{2 \times 2} & \left[\mathbf{G}_{44}(\omega_{seek}) \right]_{2 \times 2} \end{bmatrix} \quad (6.24)$$

and model B is given by

$$\mathbf{B}_{II}(d2) = \mathbf{K}(d2) - \omega_{seek}^2 \mathbf{M}(d2) \quad (6.25)$$

Then, evaluating Eq. (6.23) results in a polynomial in $d2$ of order 36, with complex coefficients. Since $d2$ is real, the real and imaginary parts of the polynomial are set to zero and solved individually. The polynomials are too large to solve analytically, however using MATLAB's `vpasolve` function, a numerical solution was found, giving 36 possible diameters. However, some of these solutions can be instantly disregarded, firstly all negative solutions were removed, and then solutions outside of the possible range for $d2$ were also discounted. Since the base diameter $d2$ cannot exceed the flange diameter $d1$, it has an allowable range of $0.024 < d2 < 0.064$ m. This resulted in two possible solutions, 0.033 m and 0.042

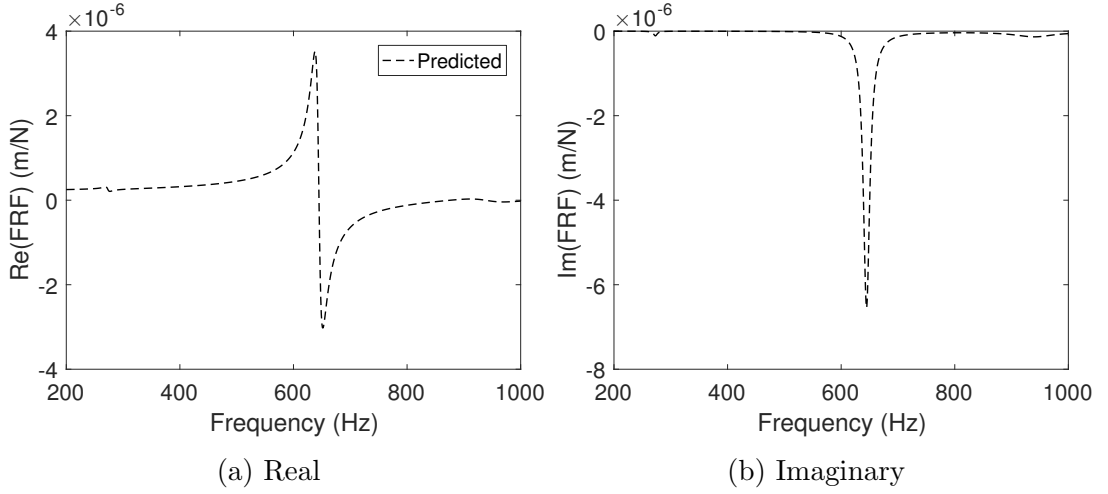


Figure 6.6: Real (a) and Imaginary (b) frequency response function plots showing the predicted result (...) from the direct SM method on the spindle rig with a base diameter $d_2=0.042$ m

m. It is already known that a diameter of 0.034 m results in a mode at 646 Hz, hence the first solution is correct to within 1 mm.

The validity of the second solution was verified by carrying out the direct SM method covered in section 6.4.2. This time a base diameter of 0.042 m was used in model B. The results are shown in Fig. 6.6.

It can be seen that, as predicted, a mode occurs at 646 Hz when the tool holder has a diameter of 0.042 m. Whilst it is difficult to know whether this is the same mode as for the 0.032 m case, it is possible, using the multivariate mode indicator function (MMIF) to derive the number of modes in this region.

For a set of FRFs \mathbf{H} , the ratio of the real part of the response is considered in relation to the total response as follows:

$$\text{MMIF} = \frac{\mathbf{F}^T [\text{Re}(\mathbf{H})^T \text{Re}(\mathbf{H})] \mathbf{F}}{\mathbf{F}^T [\mathbf{H}^T \mathbf{H}] \mathbf{F}} \quad (6.26)$$

where \mathbf{F} is the input force. Then as the real part tends to zero, the resonances

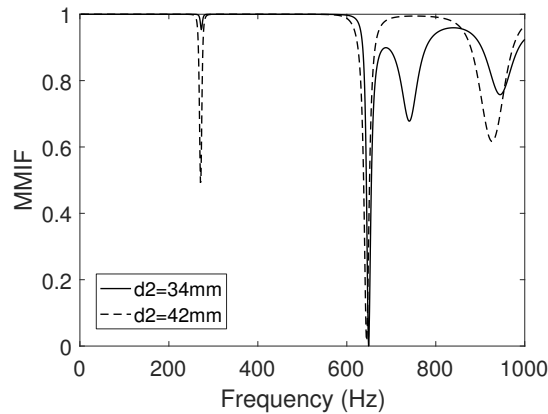


Figure 6.7: Multivariate mode indicator function (MMIF) for results of inverse SM on the spindle rig with $d2=0.034$ m (—) and $d2=0.042$ m (- -)

are determined by the minimum values of MMIF.

The MMIF was applied to the predicted FRFs for the 0.034 m and 0.042 m cases, and the results are plotted in Fig. 6.7. Whilst the 0.042 m holder has a single mode in the vicinity of ω_{seek} , the 0.032 m holder also has an additional mode at 740 Hz.

Discussion

It has been shown that using inverse SM theory, of higher rank, it is possible to determine a base diameter $d2$ that will result in a mode at a particular frequency and therefore will result in a stability lobe at a particular spindle speed. The advantage of this method is clear. Using direct SM it is possible to predict the tool tip dynamics for any holder; however to optimise this for a particular operation, numerical models of each and every tool holder must be constructed, which is computationally expensive. On the contrary, using a single (partially constructed) numerical model and the inverse method, the optimum tool holder geometry can be found by solving a single equation. It should also be taken into consideration that this validation was carried out using data from a spindle rig, which has much simpler dynamics than a milling machine.

6.5 Direct Structural Modification on the FTV5 Milling Machine

Whilst the results from the spindle rig are promising, the over simplification of the support structure simplifies the experimental data in that fewer low frequency modes occur. In addition, the data collected from the rig contains less measurement noise since no motors, fans, or coolant systems are running whilst the data is collected. Hence, it must now be shown that, despite the additional complexities associated with a milling machine, it is possible to use direct SM to model changes in the tool holder geometry.

This section repeats the experiment carried out in section 6.4.2, this time with the tool holders clamped on the FTV5 milling machine, which also has a HSKA63 spindle interface. Since both x - and y -direction tool-tip FRFs are required to predict the stability lobe diagram for a particular operation, the experiment is carried out separately for both directions. Then both results are used to generate a stability lobe diagram. The y -direction is considered first.

6.5.1 Methodology

With the unmodified tool holder clamped in the FTV5 spindle, the translational mode shapes ϕ_r were measured, again using a steel tipped impulse hammer and a light weight accelerometer. The response was measured at the same eighteen locations between the tool tip and the base of the holder. Applying the same curve fitting technique, nine modes with natural frequencies between 348 Hz and 4730 Hz were extracted. Least squares fitted polynomials for each mode were then differentiated to get the rotational mode shapes $\phi_r^{(1)}$. Finally, the four FRFs (H , N , L , and P) were constructed at the five nodes $n1$ - $n4$ as before. Then, for a particular frequency, \mathbf{H}_A was assembled (as in Eq. (6.20)) to give an 8×8 matrix.

Since the modification occurs on the tool holder alone, and is independent of the spindle or machine, the same numerical model as in section 6.4.1 was used for

model **B**. This gives the 6×6 modification model, for a particular frequency, as shown in Eq. (6.19).

Eq. (6.5) was then applied at frequencies between 1 and 5000 Hz, with a 1 Hz increment. From the resultant \mathbf{H}_{COO} , the translational tool tip FRF H_{11} was extracted.

6.5.2 Undamped direct structural modification

The results of the direct SM method in the y direction on the FTV5 are plotted in Fig. 6.8, along with the measured tool tip FRFs for the unmodified and modified holders. The dominant mode of the modified holder was measured at 936 Hz, and Fig. 6.8 shows that the direct SM method predicts this mode at 949 Hz, which is accurate to within 1.5%. However, it can clearly be seen that the amplitude of the predicted mode is significantly larger than its measured counterpart. In fact, the amplitude of the imaginary part of the predicted mode is -9.96×10^{-6} m/N, whilst it was measured at -2.55×10^{-6} m/N.

This would suggest that the larger diameter of the modified holder not only changes the mass and stiffness of the structure, but is also an additional source of damping, something which does not occur on the spindle rig. Therefore, when using the direct SM method on a machining structure, it is vital that damping is included in the modification matrix **B**.

6.5.3 Proportional damping

The inclusion of damping in numerical models is still the topic of much research [106, 107], most of which is beyond the scope of this thesis. However, the simple well-known case of proportional viscous damping is quite sufficient here [51]. Proportional damping, where the damping matrix is modelled as a linear combination of the mass and stiffness matrices, has the advantage of being practically simple

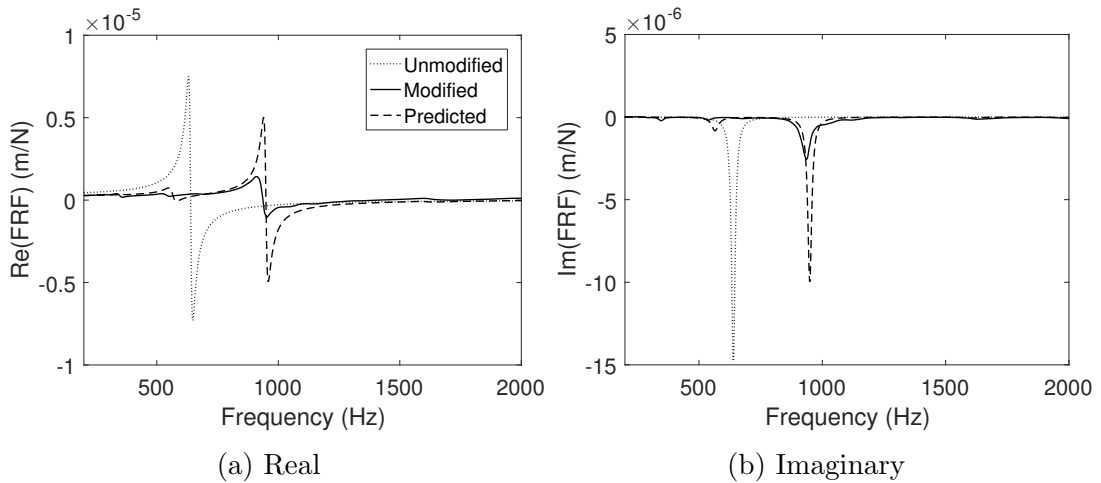


Figure 6.8: Real (a) and Imaginary (b) frequency response function plots comparing the experimental tool tip dynamics of the unmodified (\cdots) and modified (—) holders, with the results of the undamped direct SM in the y -direction (- -) on the FTV5.

to include in a model. Additionally, the modes of a proportionally damped model are almost identical to those of the undamped modal model, in that the mode shapes are identical and the natural frequencies very similar. This is important as it was shown in section 6.5.2 that, the undamped SM correctly identifies the modified natural frequency. The biggest limitation of this form of damping is that a viscous model is frequency dependent, for this reason it can be difficult to find damping coefficients that are accurate over a large frequency range. However, since the machine tool FRFs are dominated by a single mode, the viscous damping model is appropriate for this application.

In chapter 3 it was shown that, due to the orthogonality properties of the mass and stiffness matrices, a proportionally damped system may be decoupled, meaning each of the n equations of an n DOF system, may be solved separately as a single DOF system with the following properties:

$$m_r \ddot{x} + c_r \dot{x} + k_r x = 0 \quad (6.27)$$

with

$$\omega_r = \omega_n \sqrt{1 - \zeta_r^2} \quad \omega_n = \sqrt{\frac{k_r}{m_r}} \quad \zeta_r = \frac{c_r}{2\sqrt{k_r m_r}} \quad (6.28)$$

It was also shown that, for a proportionally damped system

$$\zeta_r = \frac{c_r}{2\sqrt{k_r m_r}} = \frac{\alpha}{2\omega_n} + \frac{\beta\omega_n}{2} \quad (6.29)$$

The constants α , β , w_r , and ζ_r for the modification model are unknown, and whilst they may be approximated by choosing sensible values for ζ_r , it is more robust to use the information from the experimental modal model.

From the nine measured mode shapes ϕ_r , we have nine values for the damped natural frequency ω_r and damping ratio ζ_r , allowing us to calculate the nine undamped natural frequencies ω_n . Then the nine equations for the proportional damping coefficients may written

$$2 \begin{Bmatrix} \zeta_1 \\ \zeta_2 \\ \vdots \\ \zeta_9 \end{Bmatrix} = \begin{bmatrix} \frac{1}{\omega_{n1}} & \omega_{n1} \\ \frac{1}{\omega_{n2}} & \omega_{n2} \\ \vdots & \vdots \\ \frac{1}{\omega_{n9}} & \omega_{n9} \end{bmatrix} \begin{Bmatrix} \alpha \\ \beta \end{Bmatrix} \quad (6.30)$$

Since there are only two unknowns, this is an overdetermined set of equations. However, the least squares method may be used to find an approximate solution. Eq. (6.30) is of the form $\mathbf{b} = \mathbf{A}\mathbf{x}$, therefore by multiplying both sides by \mathbf{A}^T , a standard square system of equations is found. Then the approximate solution is given by

$$\begin{Bmatrix} \alpha \\ \beta \end{Bmatrix} = 2 \begin{bmatrix} \left[\begin{array}{cc} \frac{1}{\omega_{n1}} & \omega_{n1} \\ \frac{1}{\omega_{n2}} & \omega_{n2} \\ \vdots & \vdots \\ \frac{1}{\omega_{n9}} & \omega_{n9} \end{array} \right]^T & \left[\begin{array}{cc} \frac{1}{\omega_{n1}} & \omega_{n1} \\ \frac{1}{\omega_{n2}} & \omega_{n2} \\ \vdots & \vdots \\ \frac{1}{\omega_{n9}} & \omega_{n9} \end{array} \right] \end{bmatrix}^{-1} \begin{bmatrix} \frac{1}{\omega_{n1}} & \omega_{n1} \\ \frac{1}{\omega_{n2}} & \omega_{n2} \\ \vdots & \vdots \\ \frac{1}{\omega_{n9}} & \omega_{n9} \end{bmatrix}^T \begin{Bmatrix} \zeta_1 \\ \zeta_2 \\ \vdots \\ \zeta_9 \end{Bmatrix} \quad (6.31)$$

Once α and β have been determined, damping can be added to the modification

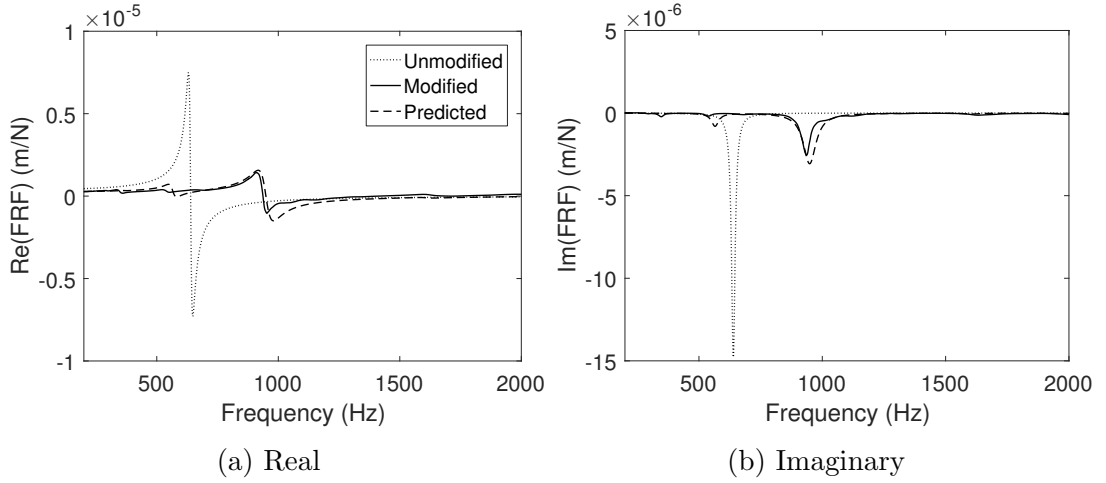


Figure 6.9: Real (a) and Imaginary (b) frequency response function plots comparing the experimental tool tip dynamics of the modified (—) holder, with the results of the damped direct SM in the y -direction (- -) on the FTV5

matrix \mathbf{B} as follows:

$$\begin{aligned} \mathbf{B}_{II} &= \mathbf{K} + i\omega\mathbf{C} - \omega^2\mathbf{M} \\ &= (1 + i\beta\omega)\mathbf{K} - (\omega^2 - i\alpha\omega)\mathbf{M} \end{aligned} \quad (6.32)$$

6.5.4 Damped Direct Structural Modification

Using the same experimental model as section 6.5.1 and the damped numerical model outlined in the previous section, the direct SM method was again applied using Eq. (6.5). The results are presented in Fig. 6.9. The natural frequency of the predicted result matches that of the undamped case; however, the addition of the proportional viscous damping has brought the amplitude of the imaginary part to within 20% of the measured value, a vast improvement on the undamped case.

As discussed earlier, in order to predict the stability lobe diagram, both the x and y direction tool tip FRFs are required. The above analysis has concentrated on the y direction; hence, the same experiment was also carried out using experimental data collected in the x direction. The results of the prediction are

CHAPTER 6. STRUCTURAL MODIFICATION OF TOOL HOLDER GEOMETRY

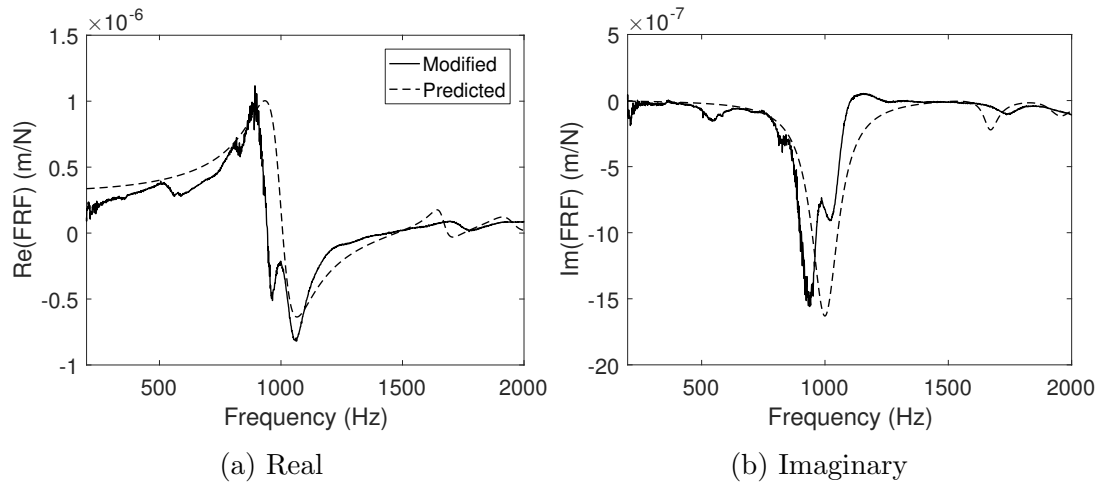


Figure 6.10: Real (a) and Imaginary (b) frequency response function plots comparing the experimental tool tip dynamics of the unmodified (\cdots) and modified (—) holders, with the results of the damped direct SM in the feed direction (- -) on the FTV5

compared with the measured modified holder in Fig. 6.10.

When capturing the modified FRF, an unknown source of noise occurred around the region of resonance, causing some uncertainty in the amplitude of the modes. The FTV5 milling machine is situated in an active machine shop floor and external noise from nearby machinery may be transmitted to the machine, it is also possible that an internal motor or fan was running at the time of the experiment; however, steps were taken to mitigate such a problem.

The results in Fig. 6.10 show that the SM method predicts a single mode at 1000 Hz, in comparison to the measured data in which two separate modes occur at 983 Hz and 1025 Hz. Axisymmetric structures such as spindles, often contain very close modes which are coupled by low-levels of non-proportional damping [108]. Hence, when an additional source of damping is added to a structure, these modes can become uncoupled. It has already been shown that the tool holder is a source of damping; therefore, in this case it is likely that the addition of the modified tool holder has separated the modes. Since the modes were identified from the unmodified structure, the two modes cannot be defined uniquely,

and are instead identified as a single mode. Since the SM method is only capable of modifying modes and not creating them, the result also contains a single mode.

6.5.5 Stability Prediction

The purpose of this experiment is to predict the stability of a milling operation; therefore, a stability lobe diagram was generated from both the measured and predicted tool tip FRFs. A 50% radial immersion (6 mm) down milling operation was chosen as an example, which gives us:

$$\mu_x = \cos(45 + \beta) \cos(\beta) \quad \text{and} \quad \mu_y = \cos(\beta - 45) \cos(45) \quad (6.33)$$

where β is the force angle of 68 deg. The entry and exist angles for up milling are given by $\varphi_s=90$ deg and $\varphi_e=180$ deg. An aluminium alloy was chosen as the material for the workpiece which has a specific force of $K_s = 750$ N/mm² [109], and the 12 mm tool has two teeth. The results are compared in Fig. 6.11. It can be seen that the SM method very accurately predicts the absolute stability limit at Ω_{worst} , which is determined by the minimum of the real part of the FRF_{or}; as well as the location of Ω_{best} , determined by the natural frequency of the oriented FRF. There is however some error in the gradient of the stability limit between Ω_{worst} and the next peak, this is determined by the rate at which the real part of the FRF returns to zero following a mode, and so could be caused by error in the damping. The effect of the separated mode can also be seen, as the predicted results contains a single peak, whilst in the measured data, competing lobes can be seen at around 2 mm.

6.5.6 Discussion

The direct SM method has been successfully applied to the optimisation of tool holder geometry for chatter avoidance in high speed milling. It has been shown that changes in the diameter of the tool holder, can contribute additional damping to the structure and; therefore, damping must be included in the modification

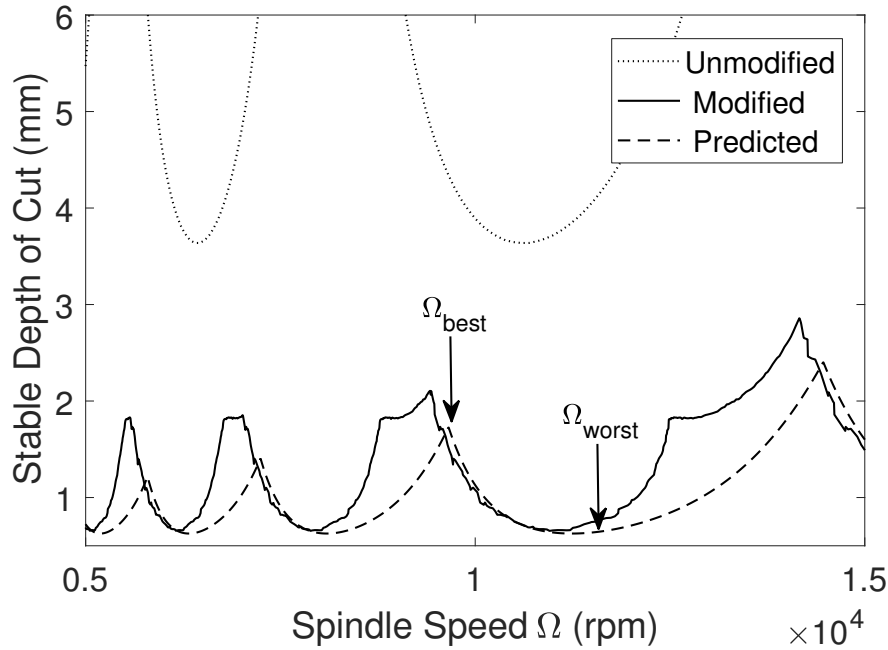


Figure 6.11: Stability lobe diagrams for the modified tool holder on the FTV5 (experimental (—) vs. predicted (- -))

matrix. Using the experimental modal model, proportional viscous damping was added to the numerical model, without having to take any further measurements. The results of the damped direct SM method show good correlation with their experimental counterparts. In the x direction, the change in tool holder geometry caused two close modes to separate, a feature that the SM method is not able to predict. Despite this, the experimental and predicted stability lobe diagrams, for an example milling operation, are in good agreement with one another. The direct SM method is particularly accurate in the prediction of natural frequency and absolute stability limit.

When compared to the RCSA method, the direct SM method has a simple advantage, in that only a single experimental model from a standard tool holder is required, and no further measurements (such as connection parameters) are needed. Despite this the optimisation process still requires the construction of several numerical models, which could easily become a lengthy process.

6.6 Inverse structural modification on the FTV5

The advantage of inverse SM method over the direct method is that the tool holder geometry can be optimised by solving a single equation. This involves building a single partially constructed numerical model and is thus computationally less expensive than the direct method. It will now be shown that, despite the additional complexities of machine data, the inverse SM method may be used to optimise tool holder geometry.

In section 6.3.2 it was shown that the tool holder geometry may be optimised in terms of the stability lobe location, by applying the inverse SM method in a single direction. Since the amplitude of the dominant mode in the y -direction is larger than that of the x -direction, it was used for optimisation purposes, as this mode will have the lowest stability limit. In practice, consideration must be given to the values of μ_x and μ_y , as they may change the dominance of these modes when the oriented FRF is calculated.

It was shown earlier that the undamped direct method was capable of accurately predicting the natural frequency of the modified structure. For this reason, it is unnecessary to include damping when using the inverse method.

6.6.1 Methodology

The data from the modified holder on the FTV5 demonstrates that the modified holder produces a dominant mode at 936 Hz. Therefore using the y -direction experimental model \mathbf{H}_A as described in section (6.5.1) and the undamped numerical model $\mathbf{B}(d2)$ given in Eq. (6.19), both evaluated at $\omega_{seek} = 2\pi(936)$ rad/s, the inverse SM method was applied using Eq. (6.7). Again this resulted in a polynomial of degree 36 with complex coefficients, since $d2$ is real, the real and imaginary parts were set to zero and solved using MATLAB's `vpasolve`. From the 36 solutions, the negative results and the results out of the possible range of $d2$ were removed, leaving a single acceptable solution of 0.0336 m, within 1.2% of the expected value of 0.034 m.

6.6.2 Discussion

It has been shown that, despite the added complexities of machine data, the inverse SM method, can be used to optimise the tool holder geometry. Despite the fact that, the location of the stability lobes depends on the resonant frequencies of the oriented FRF, because of the inherent properties of any FRF, the inverse method may be successfully applied in a single direction.

Whilst the direct SM method has the advantage over receptance coupling, that no additional measurements (such as contact stiffness and damping) must be taken; it was shown in section 6.5.2 that damping must still be included in the modification matrix. Moreover, optimising the tool holder geometry using the direct method, still involves the construction of several numerical models. However, the inverse method may be used, without the inclusion of damping, to optimise the holder geometry by solving a single equation, a feature that is not present in the receptance coupling method.

6.7 Summary

The purpose of this chapter was to apply the higher rank SM method to the problem of chatter avoidance in high speed milling operations. The first important contribution from this investigation was that the inverse SM method may be applied in either the x - or y -direction, despite the stability of a milling operation being dependent on a linear combination of them both. This is an important finding as it simplifies the inverse method, making a solution more likely. Both the direct and inverse SM methods were then applied to experimental data from a spindle rig. The direct method can be successfully used to model how changes in the tool holder geometry affect the tool tip dynamics, and thus the stability of the milling operation. In terms of optimisation, the inverse method has greater potential, as a single equation can be solved to predict a tool holder diameter that will result in stability lobes at a particular spindle speed. When applying the direct method to data from the FTV5 milling machine, a viscous damping model was included in the modification matrix, to improve the amplitude prediction.

Importantly, unlike receptance coupling, no further measurements were needed. The inverse method was applied to data from the FTV5; however in this case, it is unnecessary to include the damping model, as it has little or no effect on the natural frequency. The results of this investigation are important for two reasons, firstly, it provides an efficient method of optimising the tool holder geometry for a given milling operation, which has obvious benefits over the receptance coupling method. And secondly, it provides a new passive chatter avoidance method, that is much simpler than anything that has been presented in previous research.

Chapter 7

Design and Testing of a Tuneable Tool Holder

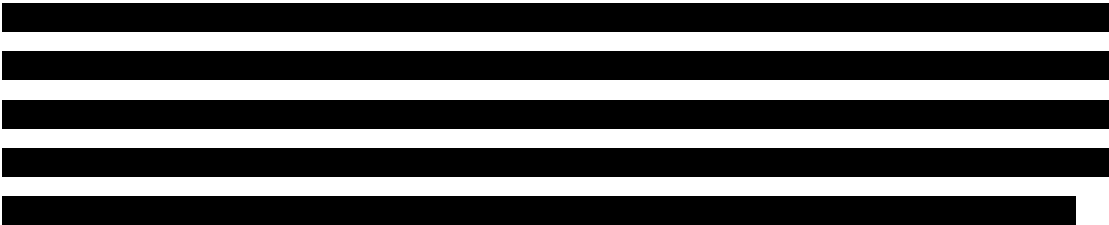
The previous chapter demonstrated how structural modification (SM) theory may be used to model and optimise the geometry of a standard HSKA63 tapered tool holder. Consequently, an optimal tooling structure may be selected in order to maximise the mass removal rate of a milling operation. However, the method shown still relies on the user having a large selection of tool holders, with a range of geometries, from which to choose. [REDACTED]

[REDACTED]

7.1 Introduction

Production rates in high value manufacturing are severely limited by the self-excited vibration known as chatter, and research efforts have thus far concentrated on using the cutting tool to avoid the onset of such vibrations. Using the method outlined in Chapter 6, it is possible to optimise the dynamics of a machine by selecting a tool holder with optimal geometry; however, this involves a signifi-

cant financial investment. Similar to the idea of the variable pitch and helix angle tools [30], a range of tool holders, with variable geometries must be purchased, so that any operation can be optimised.



This chapter will, firstly, describe the design process for the new tool holder, from design specification to finalisation and manufacturing. Subsequently, the finished prototype will be tested tested in terms of its suitability for machining trials, and its ability to tune the dynamics of a spindle.

7.2 Design Specification

The following design specification details the required features that the prototype tool holder must contain, as well as some further considerations that were taken into account during the design process.

7.2.1 Performance

Spindle interface - The prototype tuneable tool holder must be fit for purpose on a HSKA63 milling machine such as the FTV5, and therefore must have the HSKA63 spindle interface manufactured to BS-ISO (British Standards - Industrial Standards Organisation) standards. The dimensions and tolerances are available in the BS ISO 12164-1:2001 [95] and BS ISO 12164-2:2001 [96] documents.

Tool clamping - The holder must be capable of clamping a standard milling tool using the heat shrink technology and must therefore have undergone heat

treatment as is standard with any heat shrink tool holder. The clamping force on the tool must be within the industry standards, and therefore the tolerance in the diameter of the tool cavity must be to ISO standards [95]. It must also be compatible with the dimensions of the Bilz Thermogrip Machine: ISG3200WK [110], which is used for tool clamping.

[REDACTED]

Balancing - As with any rotating structure the tool holder must be balanceable. The ISO standards state that a milling tool holder must be balanced to grade G2.5 [111]. The Haimer: Tool Dynamic 2009 balancing machine will be used to measure the unbalance of the holder; therefore, the prototype must be compatible with the balancing machine, and all its components. In order to balance the prototype, the holder must be compatible with either the balancing screws or balancing rings available with balancing machine. Dynamic unbalance and balancing of rotating structures is considered in greater depth in section 7.4.

[REDACTED]

Ease of manufacture - Since the holder will be manufactured between The University of Sheffield and The AMRC, the manufacturing processes involved must be within the capabilities of the two sites.

7.2.2 Environment

Materials - The holder will be used on the FTV5 milling machine and therefore will be in constant contact with coolant, aluminium swarf, dirt and dust.

[REDACTED]

[REDACTED]

7.2.3 Health and safety

Tool Clamping - For health and safety reasons it is important that the holder is capable of achieving the industry standard clamping force [95]. Before a product is brought to market, a tool holder would undergo rigorous testing to ensure that the product meets these standards; however, such testing is beyond the scope of this project, and for that reason, the prototype must be re-manufactured from an existing tool holder that is known to meet these standards. Consequently it is important that the design of the tool holder does not alter the section of the holder where the tool is clamped.

[REDACTED]



Table 7.1: [Redacted]

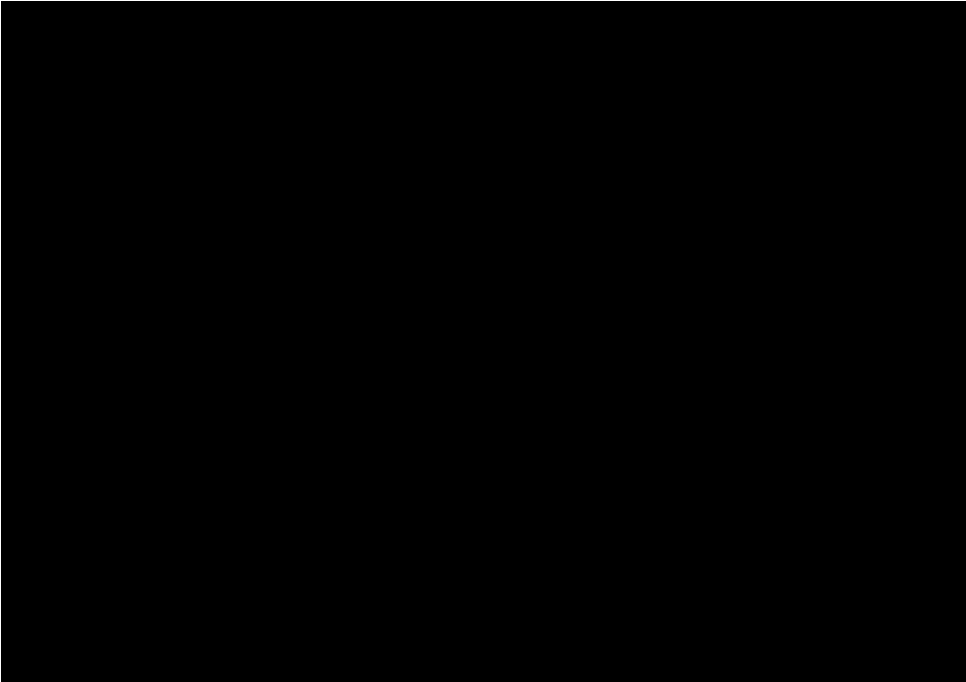
7.3 Design solution

[Redacted] Fig. (7.1). Fig. (7.1a)
[Redacted]
[Redacted]
[Redacted] Fig. (7.1b), [Redacted]
[Redacted]

[Redacted]
[Redacted]
[Redacted]
[Redacted]
[Redacted]

[Redacted]
[Redacted] Table. 7.1. [Redacted]
[Redacted]
[Redacted]
[Redacted]
[Redacted]
[Redacted]
[Redacted]
[Redacted]
[Redacted]

Each of the design decisions is now justified in relation to the design specification in section. 7.2.



(a) [Redacted]



(b) [Redacted]

Figure 7.1: [Redacted]

7.3.1 Performance

Spindle interface - As mentioned earlier, it was decided that the prototype would be re-manufactured from a tool holder purchased from another manufacturer. Hence a standard HSKA63 tool holder, of the correct length and diameter larger than that of the prototype design was used as a starting point in the manufacturing process. By doing so the HSKA63 interface was guaranteed to be within the ISO standards.

Tool clamping - Similarly, since the prototype was re-manufactured from a commercial tool holder, all necessary heat treatment had already been performed before purchase, the tool cavity was within ISO standards, and the holder was compatible with the Bilz Thermogrip Machine.

[REDACTED] - [REDACTED]
[REDACTED]
[REDACTED]
[REDACTED]
[REDACTED]

Balancing - The unbalance of the holder could only be tested post manufacturing; however, the prototype was designed with axisymmetry in an attempt to reduce the unbalance. The holder may be hard balanced, as with any other HSKA63 holder, by drilling into the flange at a particular location, in order shift the centre of gravity onto the centre of rotation. Whilst the design has no capability for balancing with screws, it is possible to balance the prototype with balancing rings. In addition to the design of the holder, a set of balancing rings with a diameter to match the prototype were purchased.

[REDACTED] - [REDACTED]
[REDACTED]
[REDACTED] [112] [REDACTED]
[REDACTED] 7.5.1

[REDACTED]
[REDACTED]
[REDACTED]

Ease of manufacture - [REDACTED]
[REDACTED]
[REDACTED]
[REDACTED]
[REDACTED]

7.3.2 Environment

Materials - Again, since the holder was remanufactured, the material of the tool holder had all the necessary properties. [REDACTED]
[REDACTED]

Dimensions - [REDACTED]
[REDACTED]

[REDACTED] Figs. 7.3 and 7.3.

7.3.3 Health and Safety

Tool clamping - Based upon the guidance of the cutting tool manufacturer, the minimum insertion length of the tool should be twice the diameter. Since the holder is capable clamping a 12 mm tool, the first 24 mm of the holder must be unchanged during manufacturing. [REDACTED]
[REDACTED]
[REDACTED]

[REDACTED] - [REDACTED]
[REDACTED]

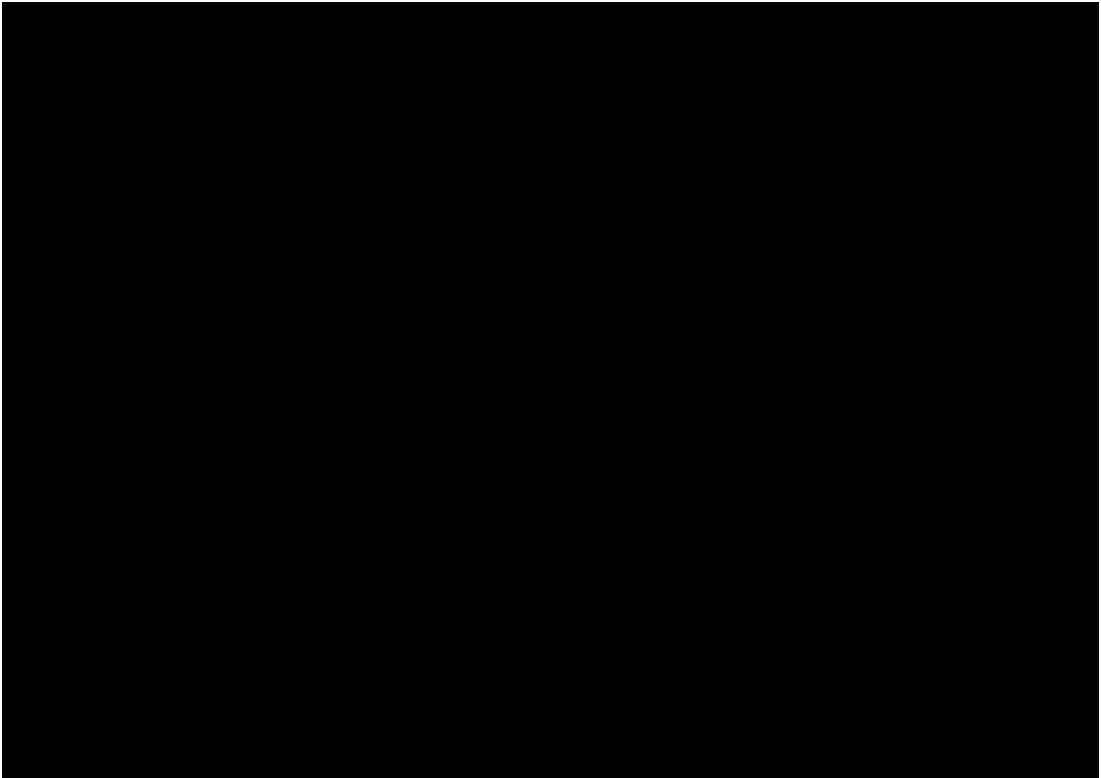


Figure 7.2: [REDACTED]

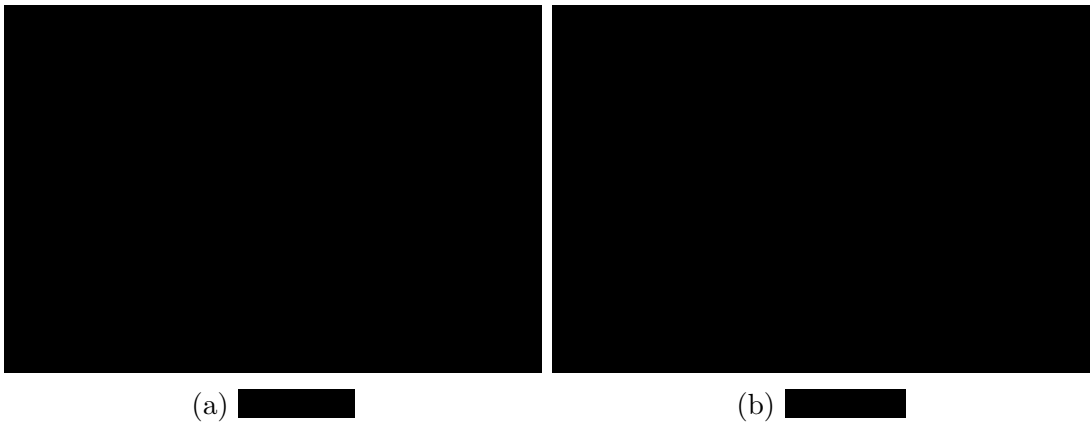


Figure 7.3: [REDACTED]

7.4 Testing the unbalance of the prototype

A rotating structure is said to have static unbalance when the centre of gravity is offset from the centre of rotation. As the structure rotates, imperfections such as manufacturing faults cause a centripetal acceleration normal to the axis of rotation. In practice, such imperfections are not limited to a single plane and the structure is said to have dynamic unbalance. Even if the dynamic unbalance is such that the structure is in static unbalance (where the multiple eccentric masses counteract each other), as the structure rotates a moment occurs, which is again normal to axis of rotation. Both the force and moment are proportional to the square of the rotation speed, and hence as the speed is increased so is the unbalance [113].

Similar to chatter vibrations during a milling operation, the unbalance force/moment cause vibrations that lead to increased cutting forces, noise, and poor surface finish. Since the prototype will be used in an experimental chatter investigation, where the onset of chatter is determined by monitoring the forces, sound, and surface finish, it is important that the unbalance of the prototype is kept to within an acceptable limit, so as not to conceal the true onset of chatter.

The ISO 1940 [111] standards define the permissible unbalance in a rotating structure as a balancing quality grade G . Such that

$$U_{per} = \frac{Gm}{\Omega} \times 9549 \quad (7.1)$$

where U_{per} is the permissible unbalance in gmm, m is the mass of the structure in kg, Ω is the speed in rpm, and 9549 is a constant produced after conversion of the measurement units. This shows that the permissible unbalance changes with speed. The spindle manufacturers for the machines used in this project recommend a balance quality grade of $G=2.5$.

The Haimer tool dynamic balancing machine was used throughout the project to measure the unbalance of various holders. The holder is clamped into the ma-

chine which contains a plane cylindrical spindle with a HSKA63 interface. The spindle is then rotated at the operating speed (Ω). The machine has force sensors attached at two planes of the spindle, which measure both the amplitude and angle of the centripetal acceleration. From this information it is possible to calculate the unbalance force and moment, and therefore the dynamic unbalance at the tool holder.

If a holder is found to have unbalance beyond the spindle manufacturer's recommendations, the holder must be balanced. A holder may be hard (or permanently) balanced by drilling into its flange to remove mass. This should be carried out without a tool so the unbalance of the holder itself is reduced. A particular configuration of tool/holder/collar may be soft balanced using a couple of balancing rings, which have a defined unbalance. When the rings are secured at a certain location along the shaft of the holder, the unbalance of the rings is used to counteract the unbalance of the tool holder.

During balancing, the axis of rotation is presumed to be the central axis of the tool holder. However, during operation the holder rotates around the axis of the spindle. Milling spindles will have a certain runout which tends to increase with age. The total indicator runout (TIR) causes an eccentricity of

$$e = \frac{\text{TIR}}{2} \quad (\mu m) \quad (7.2)$$

The permissible unbalance specified by the spindle manufactures can be related to the permissible eccentricity by:

$$e_{per} = \frac{U_{per}}{m} = \frac{G}{\Omega} \times 9549 \quad (7.3)$$

Therefore, even with a well balanced tool holder, once clamped into the machine, it is important that the runout (TIR) is measured and this still lies within the balance quality grade of $G=2.5$.

Before the prototype was used for any dynamic or cutting tests, the unbalance

was measured at an operating speed of 15000 rpm. Firstly, for the holder with no tool or collar, and then for several configurations of tool, tool holder, and collar. The prototype was always found to be within the recommended limit of $G=2.5$, and therefore no balancing was required. However, when the holder was clamped into the FTV5 milling machine, very high runout of between $10\ \mu\text{m}$ and $20\ \mu\text{m}$ was measured, which results in eccentricity of between $5\ \mu\text{m}$ and $10\ \mu\text{m}$. However the recommended limit (with $G=2.5$, and $\Omega=15000\ \text{rpm}$) is $1.6\ \mu\text{m}$. The spindle interface was cleaned, and the tool re-clamped in an attempt to reduce the runout; however, little improvement was made. Since this is the only HSKA63 milling machine available for the project it was used to carry out cutting trials, always considering the ability of runout to disguise the onset of chatter.

7.5 Testing the dynamics of the prototype

The prototype tool holder must have the following functionality in order that it may be used to tune the dynamics of a milling machine:

- [REDACTED]
- [REDACTED]
- [REDACTED]
- [REDACTED]

A series of tests were carried out on the spindle rig in order to test the functionality of the prototype in terms of its dynamics and its ability to significantly alter

the dynamics at the tool tip. Each of the three collars was tested individually, by initially securing it at the base of the holder and measuring the tool-tip FRF, then gradually moving it along the shaft towards the tip, taking measurements at several locations along the shaft of the holder.

7.5.1 Initial observations

During the initial testing of the prototype, it was noticed that rather than increasing the natural frequency of the dominant mode, as in the previous chapter, the addition of a collar reduces its natural frequency. Considering the lengths of the three collars, it is not surprising that the shorter collars do not have a significant effect on the stiffness of the overall structure; however, it was expected that the longest of the the collars would produce results similar to that of the tapered holder in the previous chapter. Under closer inspection of the static stiffnesses, it became apparent that little or no change is seen when a collar is added to the holder. This suggested that the collars were in fact modifying the mass of the structure and not the stiffness. Direct SM theory was used to confirm these observations.

The details of how SM is applied to the prototype are discussed thoroughly in the next section, for now a general overview is sufficient. Firstly, collar A was fixed onto the prototype at the base of the holder, and the tool tip FRF was measured. Then, the direct SM method was carried out using data from the prototype (with no collar attached) to construct model A, and model B was constructed using only the mass matrix \mathbf{M} . Finally, the SM method was carried out with model B containing both the mass \mathbf{M} and stiffness \mathbf{K} matrices as before. The results are plotted in Fig. 7.4.

The experimental results show that with the addition of the collar the natural frequency decreases from 625 Hz to 609 Hz. The SM results with B containing only mass also predict the natural frequency to occur at 609 Hz, whilst the results with B containing both mass and stiffness predict an increase on the natural

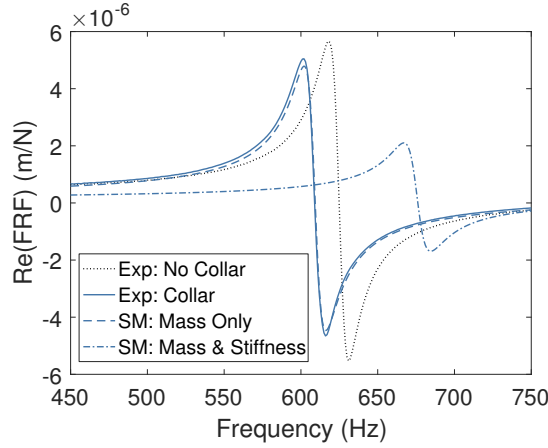


Figure 7.4: Experimental tool tip FRFs of the prototype with no collar (...) and with collar C1 (—) compared with the SM prediction with only mass \mathbf{M} (- -) and mass and stiffness \mathbf{M} and \mathbf{K} (-.-)

frequency from 625 Hz to 676 Hz.

The reason for this is likely to be the flexible connection between the tool holder and the collar. If the connection stiffness is very low in comparison to the stiffness of the collar, the overall or equivalent stiffness will also be very low. Consider for example, a single degree of freedom system with stiffness k , that is connected to another structure with a connection stiffness k_s , then the equivalent stiffness of the SDOF structure and the connection stiffness is given by:

$$k_{eq} = \frac{k k_s}{k + k_s} \rightarrow 0 \quad \text{as} \quad k_s \rightarrow 0 \quad (7.4)$$

Although this is an over simplification of the prototype, it gives some insight into why the stiffness of the collar does not affect the natural frequencies of the main structure. Whilst it is not possible to know the exact contact stiffness between the collar and the holder, it is reasonable to assume that it is much lower than the stiffness of the collar itself. For that reason it can be assumed that the effective stiffness of the collar is very low in comparison to the stiffness of the tool holder, and therefore, has little or no effect on the natural frequencies of the combined structure.

This issue was further investigated using a simple finite element model of a cantilever beam, created in ANSYS Workbench. A steel beam of length 100 mm and diameter 10 mm was loaded at the free end with a force of 1 N. A static structural analysis was then performed to determine the maximum displacement of the beam, before carrying out a convergence study. The model is shown in Fig. 7.5a. The bending stiffness of the beam was calculated according to Euler-Bernoulli beam theory [114]:

$$k = \frac{f}{y} \quad (7.5)$$

where k is the bending stiffness, f is the applied force, and y is the resultant displacement. The simple cantilever beam had a bending stiffness of $4.66 \times 10^6 \text{ N mm}^{-1}$.

The model was then updated by increasing the beam's diameter to 15 mm across a 20 mm section of the beam, 50 mm from the fixed end as is seen in Fig. 7.5b. This simulated the addition of a collar with an infinite connection stiffness i.e. a single body. A static structural analysis was performed, as above, and the bending stiffness calculated as $4.94 \times 10^6 \text{ N mm}^{-1}$.

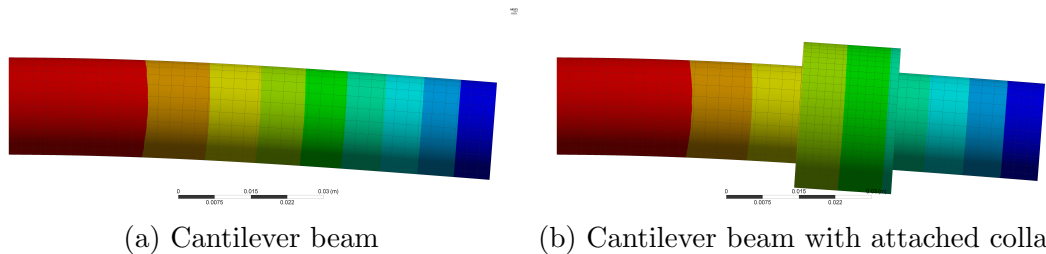


Figure 7.5: Static structural analysis on (a) cantilever beam and (b) cantilever beam with attached collar

A third model was then created on which the connection stiffness between collar and beam could be controlled. CONTA176 elements were added to the surface of the beam, with corresponding TARGE170 elements on the inside surface of the collar. The normal contact stiffness can then be varied using a normal penalty

stiffness factor (FKN), where $FKN < 1$. A series of static structural analyses were carried out with FKN values of between 1 and 1×10^{-6} , each time calculating the beam's bending stiffness. The results are plotted in Fig. 7.6.

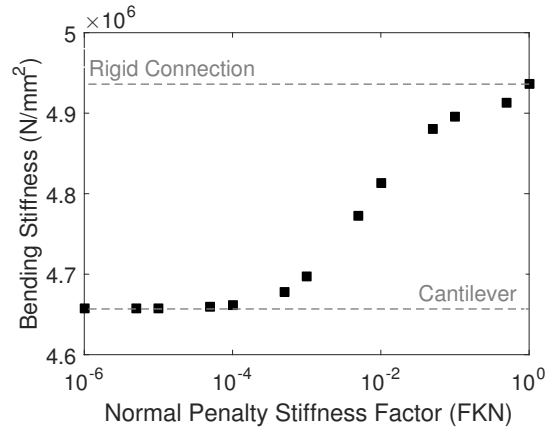


Figure 7.6: The effect of contact stiffness between beam and collar on overall beam bending stiffness

It can be seen from Fig. 7.6 that with a maximum FKN value of 1 (maximum contact stiffness), the separate body model performs similarly to that of the single body model. However, the figure also shows that as the contact stiffness is reduced the overall bending stiffness tends to that of the cantilever beam. This supports the conclusion that the prototype only modifies the mass of the structure due to low contact stiffness resulting in a low effective stiffness.

During the design stage it was thought that for SM to work the connection between collar and holder would have to be rigid enough that the two structures could be modelled as a single body. If this were not the case, connection stiffness would have to be included in the modification, and since this is difficult to model it would have to be measured; thus rendering the method somewhat redundant. However, although it was not the intention of the design to have such flexible connections, it allows the modification to be modelled using only the mass matrix. Thus eliminating the problem of unknown connection parameters. These assumptions are validated in the next section, by performing the mass modification for

each of the collars in several locations.

7.5.2 Methodology

To the prototype, a two fluted end-mill of 12 mm diameter was clamped with a stickout length of 40 mm. The tool was clamped so that the flutes of the tool aligned with the flats of the holder. The holder was then clamped into the spindle rig and the frequency response function measured at nineteen equally spaced locations between the tool tip and the base of the holder. The beginning of the flat along the side of the holder was chosen as the excitation location so as to minimise the misalignment error between input and output measurements. Then to each of the nineteen FRFs, a curve was fitted and a modal model extracted, which included nine modes. From which, the rotational mode shapes were approximated using the curve fitting technique from the previous chapter.

Then for a particular length collar, in a particular location, the direct and cross FRFs (H_{ij} , N_{ij} , L_{ij} , and P_{ij}) were extracted. Model A contains three nodes, x_t , the tool tip, x_f , where the front of the collar will be, and x_b , where the back of the collar will be, each of which has two degrees of freedom translation y and rotation θ . Then at a particular frequency model A is constructed as:

$$\begin{aligned} \mathbf{H}_A &= \begin{bmatrix} [\mathbf{H}_{AOO}]_{2 \times 2} & [\mathbf{H}_{AOI}]_{2 \times 4} \\ [\mathbf{H}_{AIO}]_{4 \times 2} & [\mathbf{H}_{AII}]_{4 \times 4} \end{bmatrix} \\ &= \left[\begin{array}{c|cc} [\mathbf{G}_{tt}]_{2 \times 2} & [\mathbf{G}_{tf}]_{2 \times 2} & [\mathbf{G}_{tb}]_{2 \times 2} \\ \hline [\mathbf{G}_{ft}]_{2 \times 2} & [\mathbf{G}_{ff}]_{2 \times 2} & [\mathbf{G}_{fb}]_{2 \times 2} \\ [\mathbf{G}_{bt}]_{2 \times 2} & [\mathbf{G}_{bf}]_{2 \times 2} & [\mathbf{G}_{bb}]_{2 \times 2} \end{array} \right] \end{aligned} \quad (7.6)$$

where

$$[\mathbf{G}_{ij}]_{2 \times 2} = \begin{bmatrix} H_{ij}(\omega) & N_{ij}(\omega) \\ L_{ij}(\omega) & P_{ij}(\omega) \end{bmatrix} \quad (7.7)$$

The numerical model B, which describes the dynamics of the collar itself is simply an untapered Timoshenko tube, constructed from the elemental matrices (\mathbf{M} and

\mathbf{K}) in [105] using the geometry in Table. 7.1. Viscous damping was again included in the model using the experimental modal model from model A. As discussed in the previous section (7.5.1) stiffness was not included in the numerical model, and hence only the mass and damping are modified. Therefore, for a particular frequency ω , model B is given by:

$$\begin{aligned}\mathbf{B}_{II} &= i\omega\mathbf{C} - \omega^2\mathbf{M} \\ &= (i\beta\omega)\mathbf{K} - (\omega^2 - i\alpha\omega)\mathbf{M}\end{aligned}\quad (7.8)$$

where α and β are the proportional damping coefficients found from the experimental modal model, and

$$\mathbf{K} = \begin{bmatrix} \begin{bmatrix} \mathbf{K}_{ff} \end{bmatrix}_{2 \times 2} & \begin{bmatrix} \mathbf{K}_{fb} \end{bmatrix}_{2 \times 2} \\ \begin{bmatrix} \mathbf{K}_{bf} \end{bmatrix}_{2 \times 2} & \begin{bmatrix} \mathbf{K}_{bb} \end{bmatrix}_{2 \times 2} \end{bmatrix} \quad \text{and} \quad \mathbf{M} = \begin{bmatrix} \begin{bmatrix} \mathbf{M}_{ff} \end{bmatrix}_{2 \times 2} & \begin{bmatrix} \mathbf{M}_{fb} \end{bmatrix}_{2 \times 2} \\ \begin{bmatrix} \mathbf{M}_{bf} \end{bmatrix}_{2 \times 2} & \begin{bmatrix} \mathbf{M}_{bb} \end{bmatrix}_{2 \times 2} \end{bmatrix} \quad (7.9)$$

where

$$\begin{bmatrix} K_{ij} \end{bmatrix}_{2 \times 2} = \begin{bmatrix} K_{y_i y_j} & K_{y_i \theta_j} \\ K_{\theta_i y_j} & K_{\theta_i \theta_j} \end{bmatrix} \quad (7.10)$$

Then the direct SM method was applied using the following relationship:

$$\begin{aligned}\mathbf{H}_{CII} &= [\mathbf{I} + \mathbf{H}_{AII}\mathbf{B}_{II}]^{-1}\mathbf{H}_{AII} \\ \mathbf{H}_{COI}^T &= \mathbf{H}_{CIO} = \mathbf{H}_{AOI}[\mathbf{I} - \mathbf{B}_{II}\mathbf{H}_{CII}] \\ \mathbf{H}_{COO} &= \mathbf{H}_{AOO} - \mathbf{H}_{AOI}\mathbf{B}_{II}\mathbf{H}_{CIO}\end{aligned}\quad (7.11)$$

before translational tool tip FRF $H_{tt}(\omega)$ was extracted from \mathbf{H}_{COO} .

7.6 Results

Each of the three collars was considered in turn, firstly applying the direct SM method with the collar in several different locations, and secondly measuring the experimental tool tip FRF with the collar in these same positions.

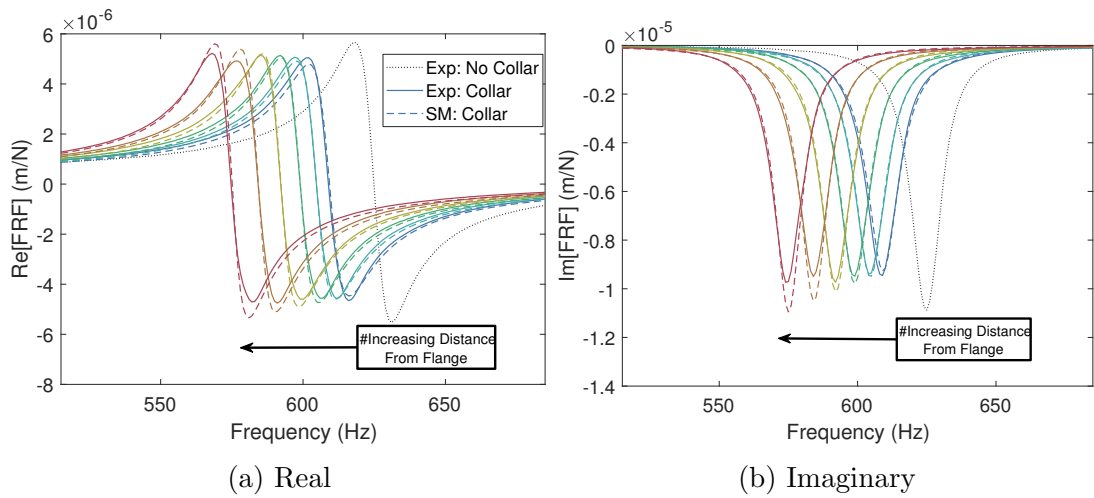


Figure 7.7: Experimental tool tip FRFs of the prototype with no collar (...) and with collar C1 (—) compared with the SM prediction (- -). From right to left the collar is positioned at 4, 14, 24, 34, 44, 54 mm from the flange of the holder.

With a length of ████████ and an outer diameter of ████████, collar C1 is the shortest of the collars; however, it has the potential to be the most useful. The collar's shorter length means it can be positioned in more locations along the length of the holder making it more appropriate for tuning purposes. Starting with the collar at the base of the holder (4 mm from the holder flange), the collar was moved in 10 mm increments to 54 mm away from the flange. The 4 mm initial location is the first location where the holes of the collar align with the flats on the holder. Each of these measurements was taken from the back of the collar. The experimental and predicted results are presented in Fig. 7.7.

With the addition of collar C1, a reasonably small decrease in the dominant natural frequency of 16 Hz is seen. Then, the natural frequency decreases linearly with the distance from the base of the holder. With the collar at 54 mm, a total shift of 52 Hz occurs, which for a tool with two flutes, would result in a shift of 1560 rpm in the first stability lobe. However, there is also the potential to move this collar further, and hence the potential for larger frequency shifts.

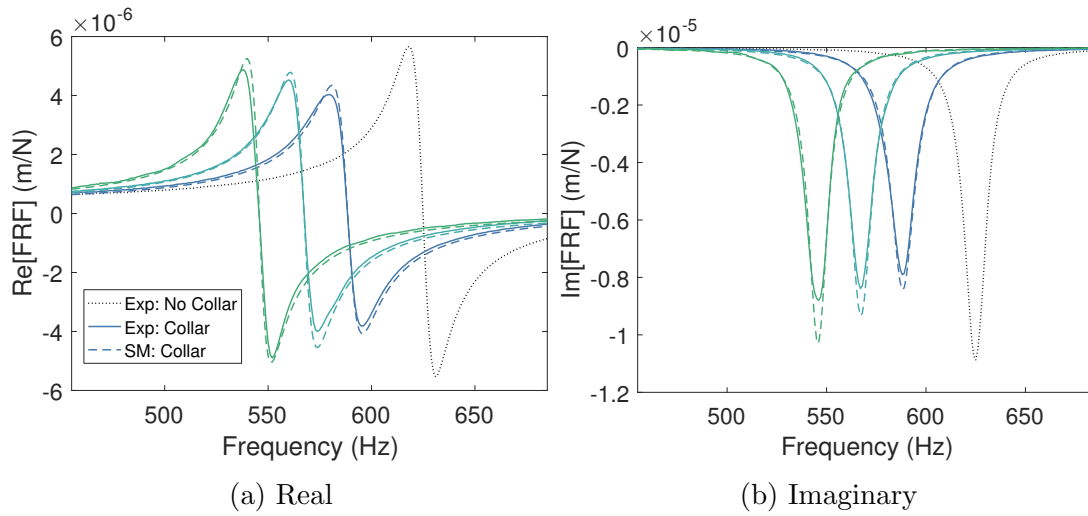


Figure 7.8: Experimental tool tip FRFs of the prototype with no collar (...) and with collar C2 (—) compared with the SM prediction (- -). From right to left the collar is positioned at 4, 24, 44 mm from the flange of the holder.

The second collar, has the same outer diameter as collar C1 but is twice the length at [REDACTED]. This collar was again added to the structure at a distance of 4 mm from the flange, and moved in 20 mm increments to a total distance of 44 mm. The results are presented in Fig. 7.8. [REDACTED]

[REDACTED] it is not possible to fix the collar in as many locations as C1. However, because of the extra mass associated with the longer collar, the addition of C2 produces a 37 Hz shift, more than double that of collar C1. At 44 mm, C2 produces a total shift in the dominant natural frequency of 79 Hz, a 2370 rpm shift in the first lobe for a two fluted tool.

Collar C3 is the longest of the three collars at [REDACTED]; however the outer diameter has been reduced to [REDACTED]. Obviously, the addition of this collar results in the largest natural frequency shift (70 Hz), [REDACTED]

[REDACTED] The results for collar C3 are presented in Fig. 7.9. The results show that it is only possible to move the collar by around 5 mm, resulting in a total shift of 78 Hz.

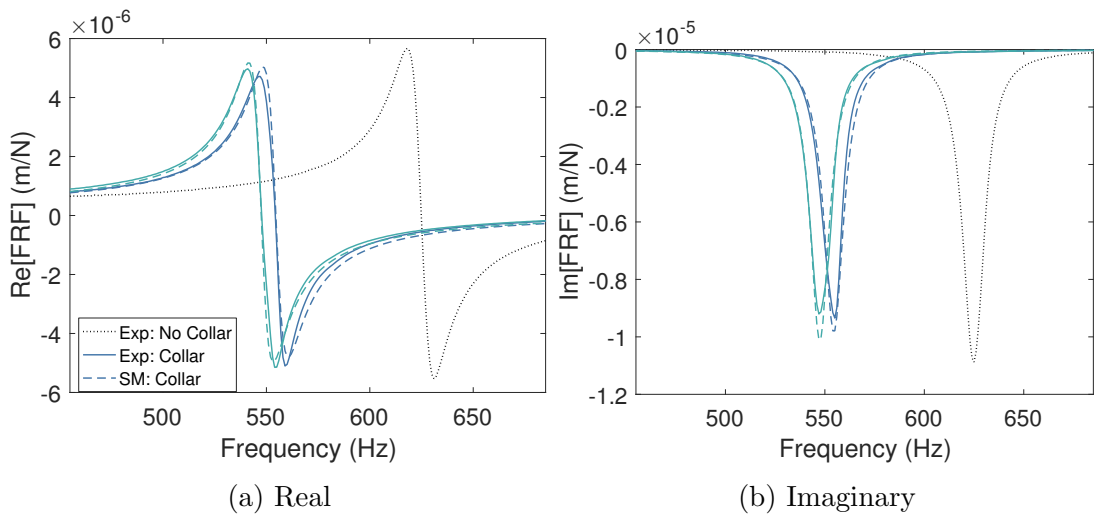


Figure 7.9: Experimental tool tip FRFs of the prototype with no collar (...) and with collar C3 (—) compared with the SM prediction (- -). From right to left the collar is positioned at 4, 9 mm from the flange of the holder.

7.7 Discussion

The dynamics of the prototype and each of the three collars have been tested to determine the ability of the design to tune a high speed milling operation. Taking into account the functionality discussed in section 7.5.1, the design may be considered a success.

Each of the three collars produces a significant shift in the natural frequency of the dominant mode when added to the prototype. It is possible to shift the natural frequency of the spindle rig by at least 79 Hz and potentially more, which would produce a significant shift in the lobes at high speeds. From all three sets of results it can be seen that the mass modification method has been successfully implemented to model the prototype, and predict the tool tip dynamics for several configurations.

The curve fitting method for rotational degree of freedom synthesis has a particular advantage when using the prototype in that a full modal model is constructed, from which FRFs at any location along the length of the tool/holder can be ex-

tracted i.e. the mode shapes are continuous in the spatial coordinate. Since the location of the collar (x_f and x_b) is variable, it is possible to apply the SM method with the collar in any location using a single experimental model. Therefore it is not necessary to know the location or length of the collar before measuring the modal model.

7.8 Summary

The main contribution from this chapter was the design and manufacture of a new tool holder, which can be used to tune the dynamics of a milling machine, in order to avoid chatter. This single holder may be used, in place of a range of holders with differing geometries, to successfully shift the stability lobes for a given milling operation to a more desirable spindle speed. Previous research has focused on using tools, with optimised pitch and helix angles, as an avoidance method; however, tools have a short lifespan due to the forces that occur during milling operations, meaning that expensive optimised tools must be purchased regularly. On the contrary the tunable tool holder has a long shelf life, if properly cared for.

Once the prototype had been manufactured it was tested in terms of its suitability for machining trials. It was found that the axisymmetrical design meant that the prototype was always within the permissible unbalance limit. The dynamics of the prototype were also tested. [REDACTED]

[REDACTED] the prototype holder is still fit for purpose, as the mass modification method may be used to model the changes in the tool tip dynamics as the collars are moved.

Chapter 8

Cutting Trials

In the previous chapter a new tool holder was designed and manufactured with the objective of tuning the dynamics of a milling spindle. The prototype was then tested, in various configurations, in terms of unbalance and dynamic performance. The unbalance of the tool holder always measured within the recommended limit. It was also found that the design is capable of shifting the natural frequency of the spindle rig. However, the collars were found to have little effect on the overall stiffness of the structure and therefore the mass modification method was used to successfully predict the tool tip frequency response function (FRF) of the prototype in its various configurations. Because of the industrial application of this research, this chapter will demonstrate that the holder can also perform successfully in an industrial environment.

8.1 Introduction

The ability to tune the dynamics of a spindle in an attempt to avoid chatter will have significant financial benefits for industrial manufacturers. Currently, engineers must select the optimum tooling setup, from a range of tools and tool holders, for each and every milling operation. In chapter 6, it was shown that the structural modification (SM) method may be used to model and optimise the tool holder geometry, allowing for simpler selection of the optimum tool holder; however, this still relies on a significant financial investment, as a selection of tool

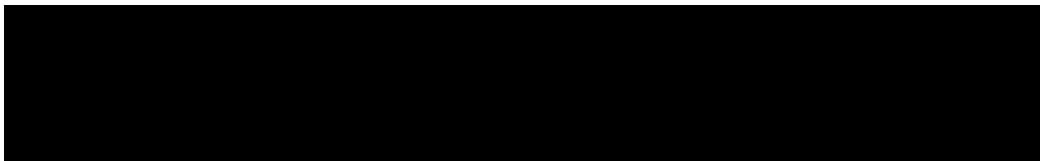
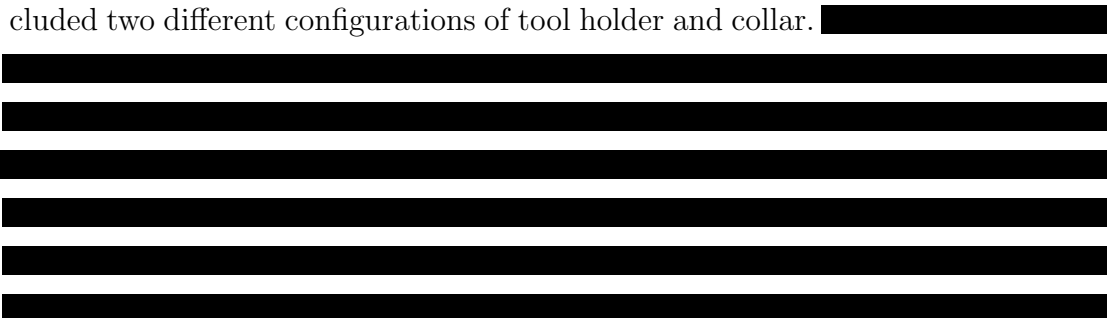


Table 8.1: Dimensions of collars C1-C3

holders with differing geometries must be purchased. Consequently, a new tunable tool holder was designed and tested in chapter 7, allowing the manufacturer to perform the same process optimisation with just a single tool holder.

It has already been demonstrated that, when using data from the spindle rig, the direct mass modification method may be used to predict the tool tip frequency response function of the prototype in various configurations. This chapter will firstly show that similar results may also be achieved from an industrial standard milling machine. For the prototype to have a significant financial benefit to the manufacturing industry, the user must be able to predict stable cutting parameters from the predicted stability lobe diagram. Therefore secondly, this chapter will focus on the cutting performance of the holder. Results of a milling trial are used to determine the experimental stability of the prototype in its various configurations. These experimental results are then compared to their predicted counterparts, calculated using the mass modification method.

The geometry of each of the collars is reiterated in Table 8.1. Three experiments were designed to demonstrate the ability of the prototype, each of which included two different configurations of tool holder and collar.



The three experiments are summarised in Table. 8.2.

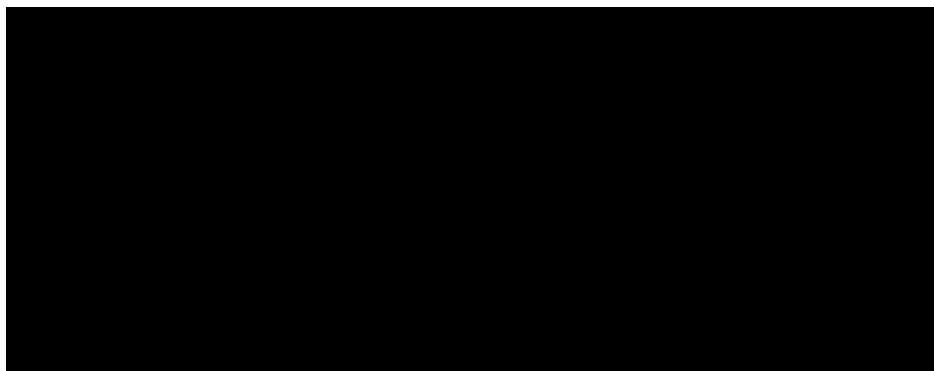


Table 8.2: Table describing the individual setups (collar and collar location) for each of the three experiments

8.2 Impact tests, modal analysis, and structural modification

In order to produce the stability lobe diagrams for each of the six setups, the tool-tip FRF must first be predicted. Therefore, similarly to in the previous chapter, impact tests were carried out on the prototype. Firstly, the 12 mm 2 fluted end-mill was clamped into the holder with a stickout length of 40 mm, again ensuring the flutes of the tool aligned with the flats of the holder. The tool holder was then clamped into the FTV5 milling machine. Using the same impulse hammer and accelerometer as previously, the response was measured at nineteen equally spaced measurement locations between the tool tip and the flange of the holder, each time exciting the structure at the beginning of the thread. To each of the FRFs, a curve was fitted and nine modes extracted. From the translational mode shapes, nine rotational modes were approximated using the polynomial curve fitting technique discussed in chapter 7.

Then for a particular setup (collar length and location) the translational and rotational FRFs (H_{ij} , N_{ij} , L_{ij} , and P_{ij}) were extracted at the three locations x_t , x_f , and x_b . Here, x_t is the tool tip, x_f is the front of the collar, and x_b is the

back of the collar. Then for a particular frequency ω model A is constructed:

$$\begin{aligned} \mathbf{H}_A &= \begin{bmatrix} [\mathbf{H}_{AOO}]_{2 \times 2} & [\mathbf{H}_{AOI}]_{2 \times 4} \\ [\mathbf{H}_{AIO}]_{4 \times 2} & [\mathbf{H}_{AII}]_{4 \times 4} \end{bmatrix} \\ &= \left[\begin{array}{c|cc} [\mathbf{G}_{tt}]_{2 \times 2} & [\mathbf{G}_{tf}]_{2 \times 2} & [\mathbf{G}_{tb}]_{2 \times 2} \\ \hline [\mathbf{G}_{ft}]_{2 \times 2} & [\mathbf{G}_{ff}]_{2 \times 2} & [\mathbf{G}_{fb}]_{2 \times 2} \\ [\mathbf{G}_{bt}]_{2 \times 2} & [\mathbf{G}_{bf}]_{2 \times 2} & [\mathbf{G}_{bb}]_{2 \times 2} \end{array} \right] \end{aligned} \quad (8.1)$$

Model B was constructed (for each of the three collars) using the mass matrix of the untapered Timoshenko beam element in [105]. Viscous damping was again included in the model using the experimental modal model. Therefore for a particular frequency ω :

$$\begin{aligned} \mathbf{B}_{II} &= i\omega\mathbf{C} - \omega^2\mathbf{M} \\ &= (i\beta\omega)\mathbf{K} - (\omega^2 - i\alpha\omega)\mathbf{M} \end{aligned} \quad (8.2)$$

where α and β are the proportional damping coefficients found from the experimental modal model, and

$$\mathbf{K} = \left[\begin{array}{c|c} [\mathbf{K}_{ff}]_{2 \times 2} & [\mathbf{K}_{fb}]_{2 \times 2} \\ \hline [\mathbf{K}_{bf}]_{2 \times 2} & [\mathbf{K}_{bb}]_{2 \times 2} \end{array} \right] \quad \text{and} \quad \mathbf{M} = \left[\begin{array}{c|c} [\mathbf{M}_{ff}]_{2 \times 2} & [\mathbf{M}_{fb}]_{2 \times 2} \\ \hline [\mathbf{M}_{bf}]_{2 \times 2} & [\mathbf{M}_{bb}]_{2 \times 2} \end{array} \right] \quad (8.3)$$

The direct SM method was then applied using the following relationship:

$$\begin{aligned} \mathbf{H}_{CII} &= [\mathbf{I} + \mathbf{H}_{AII}\mathbf{B}_{II}]^{-1}\mathbf{H}_{AII} \\ \mathbf{H}_{COI}^T &= \mathbf{H}_{CIO} = \mathbf{H}_{AOI}[\mathbf{I} - \mathbf{B}_{II}\mathbf{H}_{CII}] \\ \mathbf{H}_{COO} &= \mathbf{H}_{AOO} - \mathbf{H}_{AOI}\mathbf{B}_{II}\mathbf{H}_{CIO} \end{aligned} \quad (8.4)$$

and the translational tool tip FRF $H_{tt}(\omega)$ extracted from \mathbf{H}_{COO} .

Once the tool tip FRFs for each of the six setups had been predicted using the mass modification method, their experimental counterparts were measured directly. For each setup, the correct collar was secured onto the holder in the

correct location using grub screws, and the tool tip FRF measured by exciting the structure at the tool tip and measuring the response at the same location. The results for experiments 1-3 are shown in Figs. 8.1-8.3 respectively.

8.2.1 Results and discussion

The SM predictions are compared with the measured tool tip FRFs in Figs. 8.1-8.3, which show that the mass modification method accurately predicts the natural frequency of the modified mode in each case. For each setup the results in the y -direction show significantly higher correlation than in the x -direction. As was discussed in chapter 6, during the impact testing on the FTV5, an unknown source of noise occurred in the x -direction creating difficulty in accurately capturing the modes. Moreover, when collecting the data for model A, two close modes were measured in the x -direction, as can be seen in the result with no collar in Fig. 8.3. The experimental modal analysis (or curve fitting) technique used to extract the mode shapes relies on the structure having distinct modes that can be treated as single degree of freedom systems, and failure to meet these assumptions causes error in the extracted mode shapes. Therefore, the two close modes are likely to have caused some error in the translational mode shapes, and thus, in the SM prediction.

Of all three experiments, Experiment 1 in Fig. 8.1 shows particularly high accuracy in the y -direction. This is possibly due to the shorter length of collar C1, used in this experiment, which produces a smaller shift in the natural frequencies, or perhaps it is due to the differing thread qualities of each of the collars. It is possible that collar C1 meets the assumptions of the mass modification matrix more closely than the other two collars.

It can also be seen that, away from resonance the stiffness of the SM results differ slightly from measured results, which suggests that the collars are in fact modifying the stiffness of the structure. However, it is also clear that the stiffness has little effect on or around the natural frequencies, and since the purpose of these experiments is to predict the stability lobe diagrams (calculated from the

negative real part of the FRF), it is not necessary to accurately predict the static stiffness of the modified structure. Therefore, it can be concluded that the mass modification method is sufficiently accurate for use on the FTV5 milling machine.

8.3 Experimental determination of cutting force coefficients

In order to calculate the stability lobe diagrams for the operation in question, the cutting force model must be calibrated to the correct tool and workpiece material, and this may be achieved using the mechanistic cutting force coefficient (CFC) method as proposed in [115]. A set of milling tests at various feed rates, but constant immersion and axial depth of cut, are performed and the cutting forces in the x - and y -directions measured. To avoid the influence of runout, the average cutting forces per revolution on each tooth is calculated from the measured force signals. Then the experimental cutting forces are equated to the analytical cutting force model, described in chapter 3, leading to the identification of cutting force coefficients for a specific tool and workpiece material. The same 12 mm two fluted tool as above will be used in the cutting trials, with an AL60826 Aluminium workpiece.

8.3.1 Analytical cutting forces

Before the CFCs can be calculated, the analytical cutting force model must first be updated. The description of the forces presented in chapter 3 relied on the assumption that the resultant cutting force is directly proportional to the chip thickness such that

$$F_n = K_n bh \quad \text{and} \quad F_t = K_t bh \quad (8.5)$$

where F_n is the force in the normal direction, F_t is the force in the tangential direction, K_n is the CFC in the normal direction, K_t is the CFC in the tangential

8.3. EXPERIMENTAL DETERMINATION OF CUTTING FORCE COEFFICIENTS

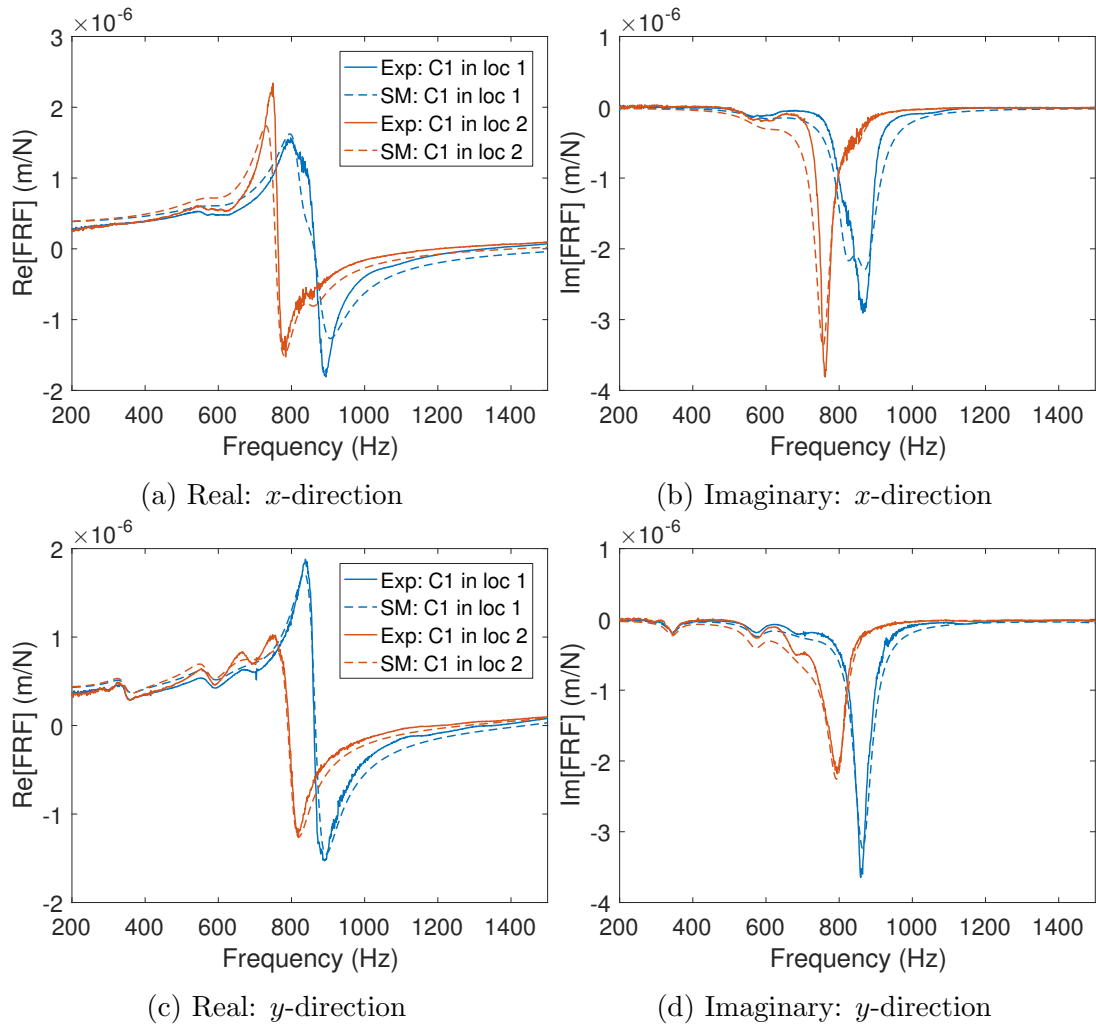


Figure 8.1: Experiment 1: Real and imaginary parts of the tool tip FRF (in both the x - and y -direction) for the prototype with collar C1 4 mm from flange (measured (—) and predicted (---)) and collar C1 64 mm from flange (measured (—) and predicted (---))

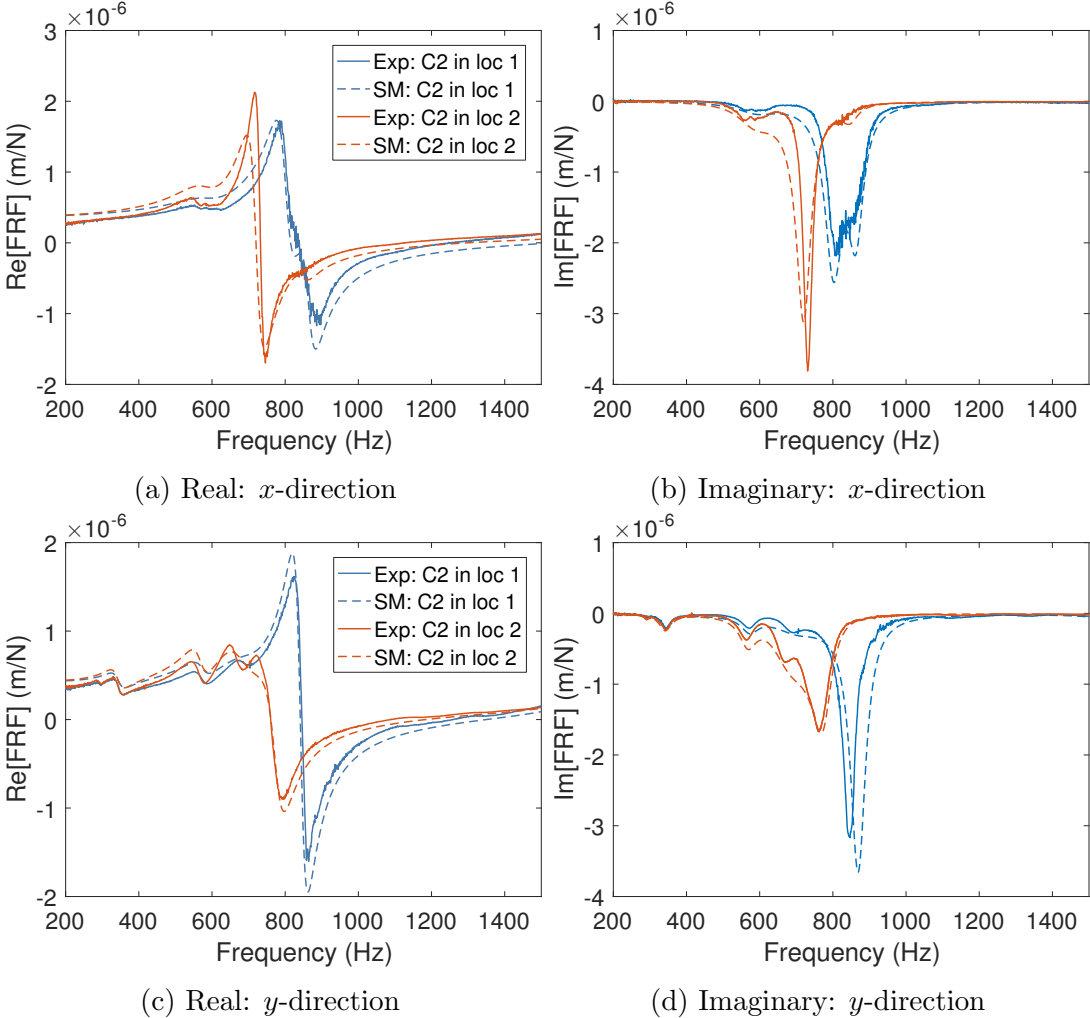


Figure 8.2: Experiment 2: Real and imaginary parts of the tool tip FRF (in both the x - and y -direction) for the prototype with collar C2 4 mm from flange (measured (—) and predicted (---)) and collar C4 54 mm from flange (measured (—) and predicted (---))

8.3. EXPERIMENTAL DETERMINATION OF CUTTING FORCE COEFFICIENTS

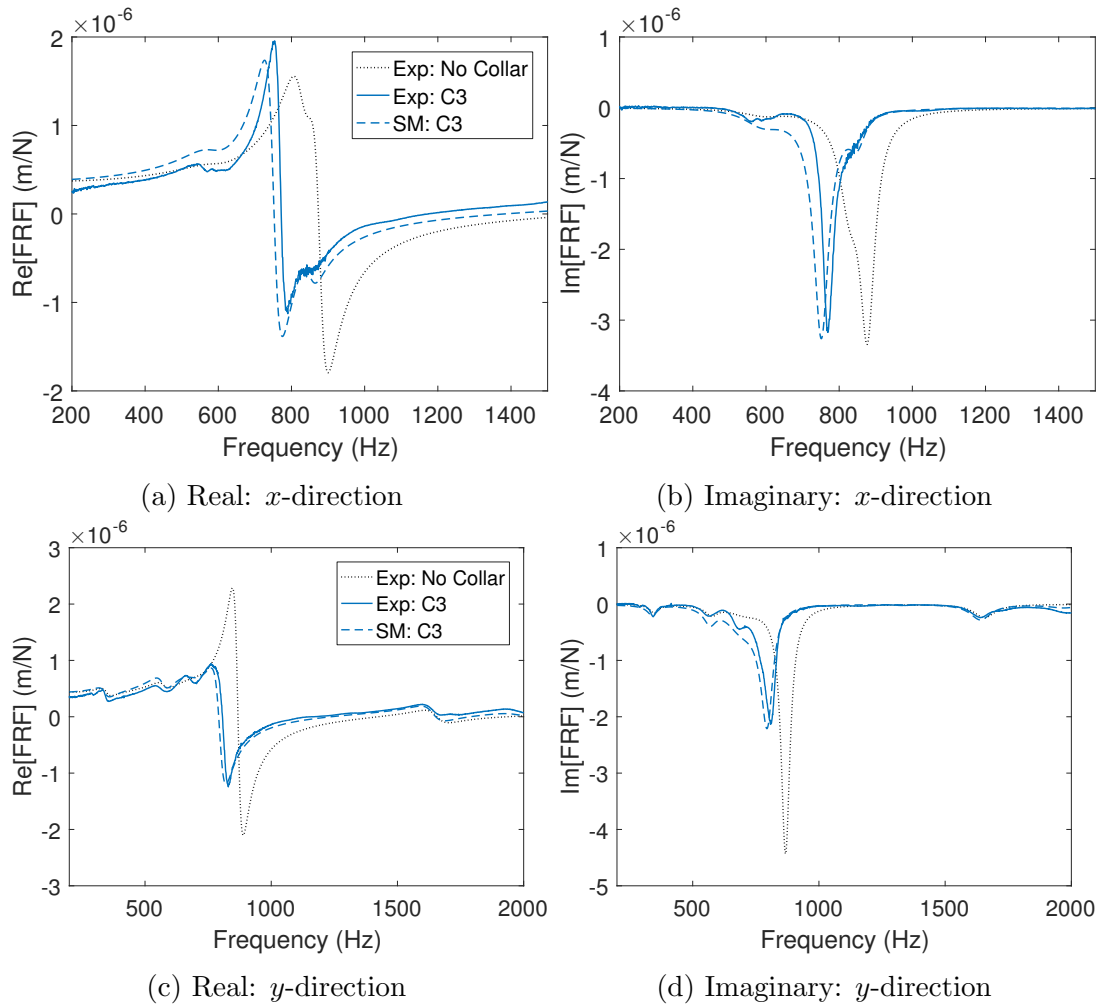


Figure 8.3: Experiment 3: Real and imaginary parts of the tool tip FRF (in both the x - and y -direction) for the prototype with collar no collar (...) and collar C3 4 mm from flange (measured (—) and predicted (- -))

direction, b is the axial depth of cut, and h is the variable chip thickness.

Whilst this model has reasonable accuracy for the determination of stability lobes, and in particular for the calculation of optimum spindle speeds, in reality, measured cutting forces are often significantly higher than this model predicts. In practice the cutting forces are also dependent on the cutting edge radius, in that, when the chip thickness is of a similar magnitude to the cutting edge radius, rubbing occurs between the cutting edge and the workpiece [109]. Rubbing or ploughing occurs when the tool moves through the workpiece without removing any material. This phenomenon may be included in the cutting force model as a constant force which is independent of the chip thickness, such that

$$F_n = K_nbh + K_{ne}b \quad \text{and} \quad F_t = K_tbh + K_{te}b \quad (8.6)$$

where K_{ne} and K_{te} are the cutting edge CFCs in the normal and tangential directions.

In order to equate the average experimental forces to the above analytical model, the average milling force expressions must be derived. Firstly, the normal and tangential cutting force components are projected into the x - and y -directions as before:

$$\begin{aligned} F_x &= K_tbf_t \sin \varphi \cos \varphi + K_{te}b \cos \varphi + K_nbf_t \sin^2 \varphi + K_{ne}b \sin \varphi \\ F_y &= K_tbf_t \sin^2 \varphi + K_{te}b \sin \varphi - K_nbf_t \sin \varphi \cos \varphi - K_{ne}b \cos \varphi \end{aligned} \quad (8.7)$$

Then applying double angle trigonometric identities it is found that

$$\begin{aligned} F_x &= \frac{1}{2}K_tbf_t \sin 2\varphi + K_{te}b \cos \varphi + \frac{1}{2}K_nbf_t(1 - \cos 2\varphi) + K_{ne}b \sin \varphi \\ F_y &= \frac{1}{2}K_tbf_t(1 - \cos 2\varphi) + K_{te}b \sin \varphi - \frac{1}{2}K_nbf_t \sin 2\varphi - K_{ne}b \cos \varphi \end{aligned} \quad (8.8)$$

The average cutting forces per revolution are then found by integrating over a full revolution (between φ_s and φ_e) and dividing by the pitch angle $\varphi_p = 2\pi/N_t$,

8.3. EXPERIMENTAL DETERMINATION OF CUTTING FORCE COEFFICIENTS

such that

$$\bar{F}_x = \frac{N_t}{2\pi} \int_{\varphi_s}^{\varphi_e} F_x d\varphi \quad \text{and} \quad \bar{F}_y = \frac{N_t}{2\pi} \int_{\varphi_s}^{\varphi_e} F_y d\varphi \quad (8.9)$$

Therefore, it can be shown that

$$\begin{aligned} \bar{F}_x &= \left[\frac{N_t b f_t}{8\pi} (-K_t \cos 2\varphi + K_n(2\varphi - \sin 2\varphi)) + \frac{N_t b}{2\pi} (K_{te} \sin \varphi - K_{ne} \cos \varphi) \right]_{\varphi_s}^{\varphi_e} \\ \bar{F}_y &= \left[\frac{N_t b f_t}{8\pi} (K_t(2\varphi - \sin 2\varphi) + K_n \cos 2\varphi) - \frac{N_t b}{2\pi} (K_{te} \cos \varphi + K_{ne} \sin \varphi) \right]_{\varphi_s}^{\varphi_e} \end{aligned} \quad (8.10)$$

The above equations are easiest to evaluate for 100% radial immersion milling since $\varphi_s = 0$ and $\varphi_e = 2\pi$ radians, therefore:

$$\begin{aligned} \bar{F}_x &= \frac{N_t b K_n}{8\pi} f_t + \frac{N_t b K_{ne}}{2\pi} \\ \bar{F}_y &= \frac{N_t b K_t}{8\pi} f_t + \frac{N_t b K_{te}}{2\pi} \end{aligned} \quad (8.11)$$

Since the equations given in (8.11) are of the form $y = mx + c$, where the feed per tooth (f_t) is the independent variable and average cutting force (\bar{F}_x, \bar{F}_y) the dependent variable, the four CFCs K_t, K_{te}, K_n , and K_{ne} are experimentally determined though linear regression of the average measured cutting forces in the x - and y -directions over a range of feed per tooth (f_t) values.

8.3.2 Experimental cutting forces

In order to calculate the four CFCs for the two fluted end mill with an Aluminium AL60826 workpiece, a set of experiments were carried out using the prototype tool holder. The Kistler 9255C dynamometer was clamped onto the machine bed of the Cincinnati FTV5 milling machine. The dynamometer was clocked and readjusted in order to achieve parallelism of less than 100 μm . To the dynamometer an aluminium block was mounted using the six M8 bolt holes available. Then a face milling operation was performed to remove 1 mm from the top of the block, so that the surface of the workpiece was normal to the z -axis of the machine. Five cutting tests were performed using the prototype tool holder and the

2 fluted end mill, each with 100% radial immersion of 12 mm, 2 mm axial depth of cut, 10000 rpm spindle speed, and feed per tooth values of 0.05, 0.075, 0.1, 0.125, 0.15 mm/tooth respectively. The five cuts lasted the length of the block (260 mm). During each of the five experiments the cutting forces in the x - and y -directions were measured using the dynamometer with a sample rate of 25600 Hz, an example of the recorded signals is shown in Fig. 8.4. A clear difference in the amplitude of the cutting force can be seen as each of the two flutes engages in the cut, which can be put down to the high runout on the FTV5. It is for this reason that the average cutting force per revolution is calculated. Hence, for each of the experiments, a section of each of the cutting force signals equivalent to 100 revolutions was taken, and the average (\bar{F}_x , \bar{F}_y) found. The average cutting forces for all five experiments are plotted in Fig. 8.5, along with a first degree polynomial fitted using MATLAB's polyfit function, which uses the linear least squares model to fit a polynomial to a given data set. The equations for the polynomials are given (in N) by:

$$\bar{F}_x = 19f_t + 27 \quad \text{and} \quad \bar{F}_y = 767f_t + 25 \quad (8.12)$$

Comparing the fitted polynomials in Eq. (8.12) to the polynomials in Eq. (8.11) the following values for the cutting force coefficients were found: $K_t=614.24$ MPa, $K_r=-15.01$ MPa, $K_{te}=-15.48$ MPa, and $K_{re}=-17.16$ MPa.

Once both the tool-tip FRFs and cutting force coefficients had been determined the stability lobe diagrams were calculated. However, before these are presented the experimental stability is discussed.

8.4 Cutting Tests

The purpose of these trials was to determine the experimental stability of the six tool holder setups so that they may be compared to the predicted results. Each of the configurations was tested in turn. A number of milling operations were performed over a set of spindle speeds and depths of cut, following the experimental procedure outlined in section 8.4.1. Then for each combination of

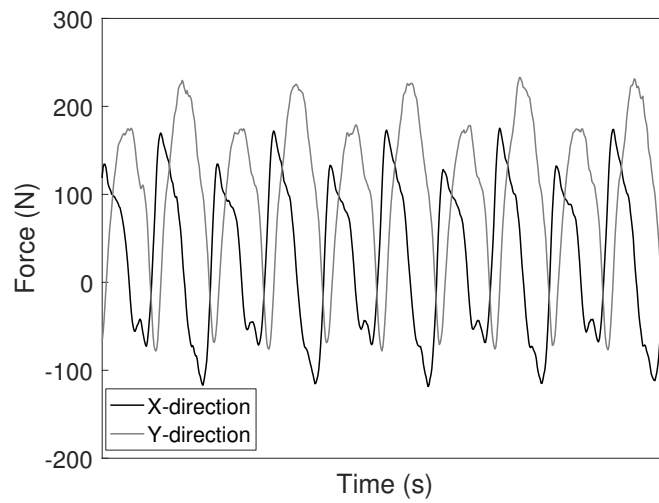


Figure 8.4: Measured milling forces in the x - and y -directions for 100% radial immersion, 2 mm axial depth of cut, 10000 rpm, and 0.1 mm/tooth feed

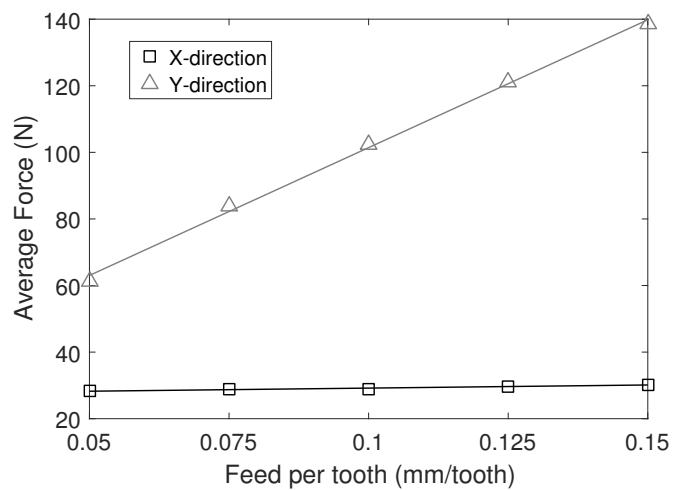


Figure 8.5: Average milling forces in the x - and y -directions for 100% radial immersion, 2 mm axial depth of cut, 10000 rpm, and feed per tooth between 0.05 and 0.15 mm/tooth

speed and depth the stability was determined using the various techniques that are discussed in section 8.4.2.

8.4.1 Experimental procedure

Before clamping the tooling setup onto the FTV5 milling machine, the unbalance was again measured to ensure the recommended standards were achieved. Once the holder was clamped into the spindle, the runout was measured. As discussed in the previous chapter the FTV5 spindle produces high runout values, and whilst all possible steps were taken to reduce this, values of between 10 μm and 20 μm were recorded. It should be noted that this is beyond the recommended limit.

The Kistler dynamometer was again mounted on the machine and an aluminium block attached, as before. From the block a stepped workpiece was machined with the geometry shown in Fig. 8.6. The steps allowed for multiple (up to seventeen) depths of cut to be achieved with a single pass of the tool, thus increasing the efficiency of the experiment. A microphone was also attached to the spindle housing so as to record the sound during each cut. Both the force and sound measurements were recorded with a sample rate of 25600 Hz.

Each setup was tested in turn, cutting at spindle speeds of between 5000 rpm and 15000 rpm. The speeds and depths were chosen based on the individual stability lobe diagrams, so as to accurately capture the characteristics of each in enough detail to validate the prediction. A milling operation with half radial immersion (6 mm) and feed per tooth of 0.05 mm/tooth was chosen based on the recommendations of the tool manufacturer. Full details of the experimental procedure can be found in appendix C.

8.4.2 Chatter detection methods

Chatter detection techniques can be classified as on line or off line. On line methods are often used to detect instability during the operation using sensors such as accelerometers, force sensors, or microphones, and are often used in place

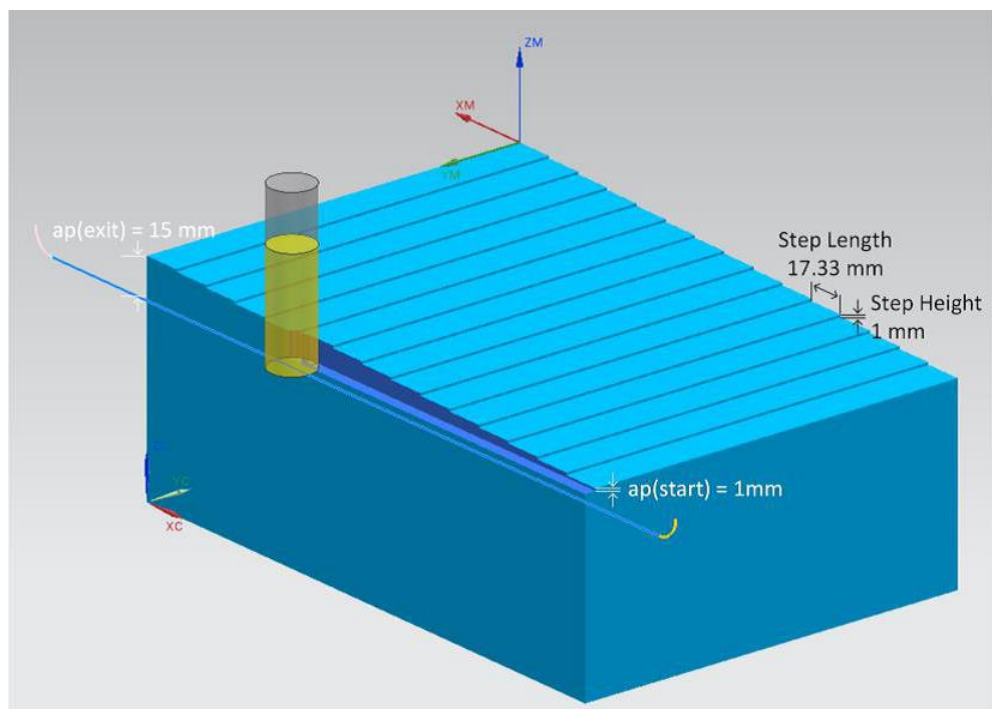


Figure 8.6: The dimensions of the stepped workpiece and the orientation of the cutting pass

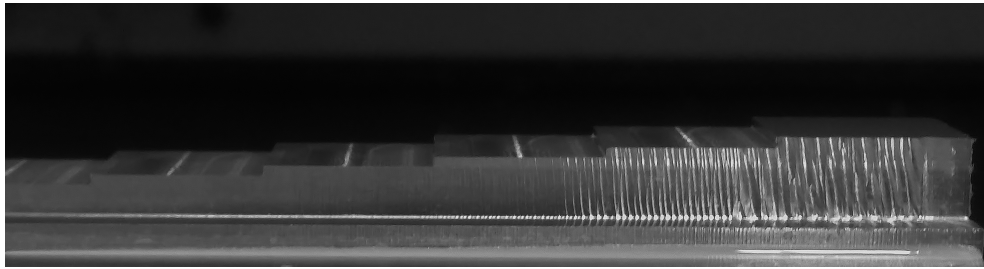


Figure 8.7: Profile image of machined surface showing the occurrence of chatter marks

of predictive techniques. Signal processing forms a vital part of any on line technique and results can be obtained in both the time and frequency domains. Off line methods are often simpler and involve detecting chatter after the cut is complete, such as surface roughness measurements.

Surface Roughness

Undesirable (wavy) surface finish means it is often possible to detect chatter through visual inspection. The main issue with this method is making the distinction between unstable chatter marks and stable feed marks resulting from tooth engagement, as both of them can leave very similar surface topographies. One solution for this is to measure the surface roughness with a (diamond) stylus instrument. The stylus is dragged along a straight line by a skid which in turn measures the waviness of the surface. The two most commonly used roughness parameters are the centre-line average (R_a) and the root-mean square (R_q) [116]. By setting an acceptable or stable value for either of these parameters the point at which stability is lost can be determined. Since the workpiece could not be removed from the machine after each cut, it was not possible to measure the surface roughness; however, visual inspection of possible chatter marks was carried out throughout the trials, and as can be seen in Fig. 8.7, due to the flexible nature of the prototype, the chatter marks were often severe and easily distinguishable from the stable feed marks.

Frequency domain detection

Sound and force signals, recorded during a milling operation, usually display certain characteristics in both their time and frequency domain signals which can in turn be related to chatter. During a milling operation, periodic cutting forces occur at the tooth passing frequency (f_t) and its harmonics:

$$f_t = \frac{N_t \Omega}{60} \quad (8.13)$$

where N_t is the number of cutter teeth, and Ω is the spindle speed. These are therefore the dominant frequencies of any stable frequency spectrum, and the presence of other frequencies suggests instability [117]. This, however, describes ‘ideal’ milling and, in practice, runout, where the geometric axis of the tool differs from the rotation axis, leads to additional frequency content in the signal. Variations in chip thickness due to runout are synchronous with spindle speed i.e. any imperfections in the tool enter the cut at the same frequency as the spindle rotates ($f_r = \Omega/60$ Hz) causing peaks in the frequency spectrum at this frequency and its harmonics. The effect of runout on the frequency signals and their stability has been investigated several times [118, 119]. The frequency spectrum of the sound signals recorded during exemplar milling operation are presented in Fig. 8.8, Fig 8.8 (a) exhibits stable characteristics whilst the content at additional frequencies in Fig 8.8 (b) suggests instability.

Time domain detection

Another common approach to stability analysis of such measurement signals is that of the Poincaré sectioning technique (or once per revolution sampling). Originally observed by Davies *et al.* [10], stable cutting signals will give a discrete cluster of once per revolution sampled points when plotted in the X-Y plane. In the same manner, quasi-periodic chatter (Hopf bifurcation) leads to an elliptical distribution in the Poincaré section. It was also noticed that similar patterns were seen in plots of the time history. Examples of these occurrences can be seen in Fig. 8.9.

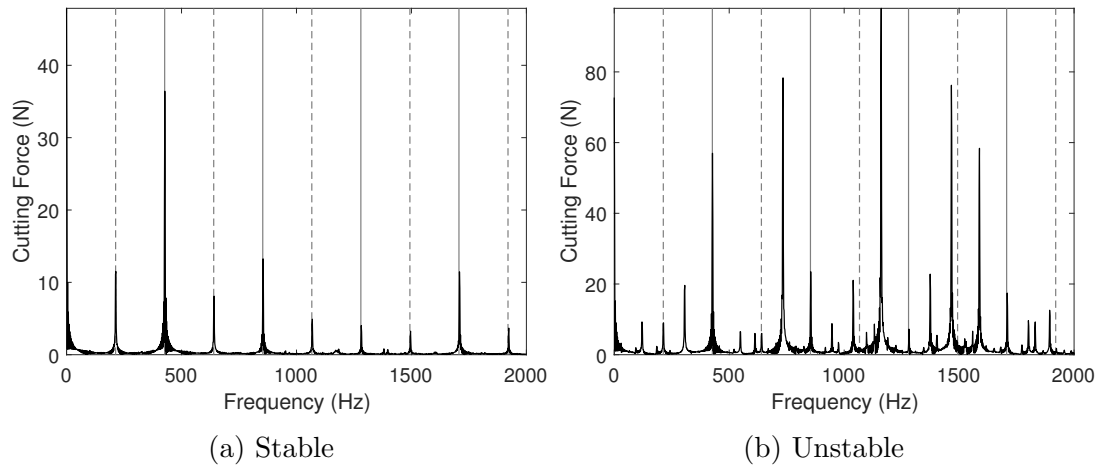


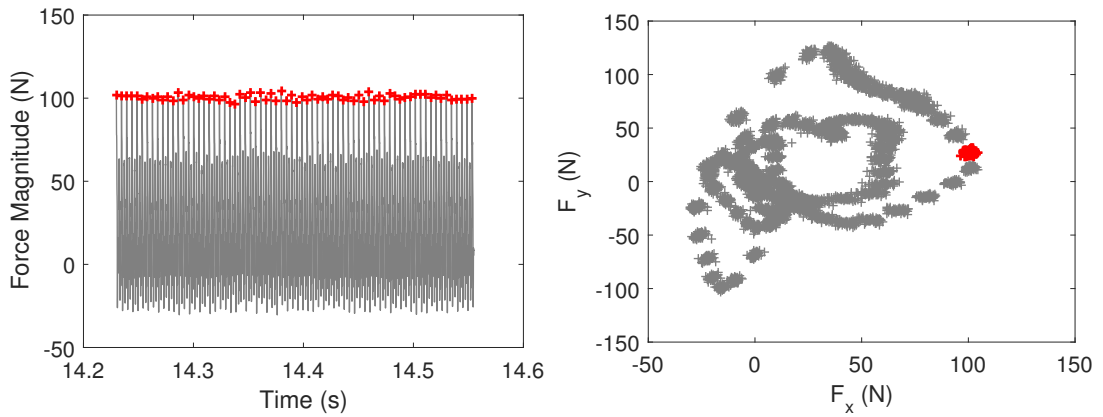
Figure 8.8: Frequency spectrum of force signals displaying stability (a) and instability (b) as well as stable tooth passing frequency (—) and the runout frequency (- -) and their harmonics

Using the three methods discussed above the experimental stability limit was determined for each of the six setups at spindle speeds of between 5000 and 15000 rpm. The results are compared with the predicted/measured stability lobe diagrams in the next section.

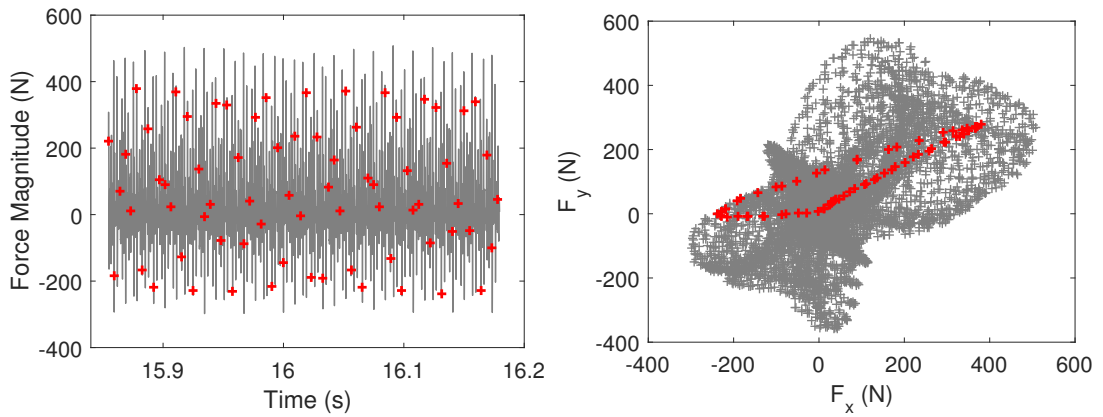
8.5 Results and Discussion

8.5.1 Experiment 1

The results from experiment 1 are presented in Fig. 8.10. The SM prediction for collar C1 in location 1 (Fig. 8.10a) shows high correlation with both the experimental stability lobe diagram as well as the experimental stability points. Each of the four lobes predicted also occur in the experimental data, and the absolute stability limit matches that of the force and sound data. Fig. 8.10b shows the results for collar C1 in location 2, and demonstrates similar accuracy to that of the first configuration. In this case, the three lobes are predicted at the correct spindle speed and the stability limit complements the experimental data. Comparing the two diagrams, a significant shift in the lobes can be seen. The accuracy of the results, as well as the shift in the lobes, draw the conclusion that

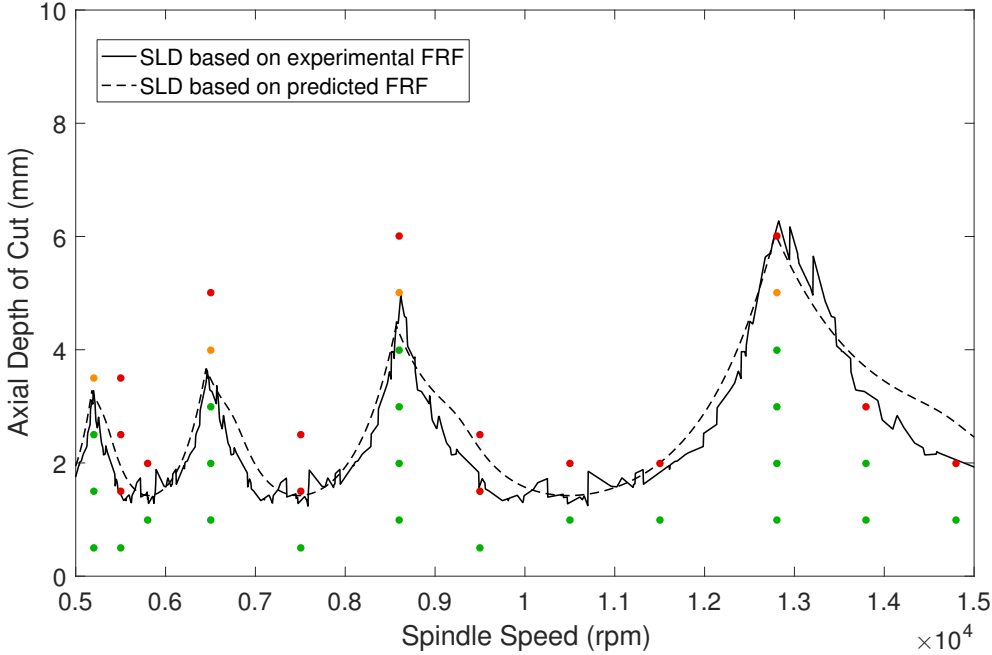


(a) Time history of x -direction forces. (b) x -vs. y -direction forces. Once per revolution sampled data (+) demonstrates stable behaviour

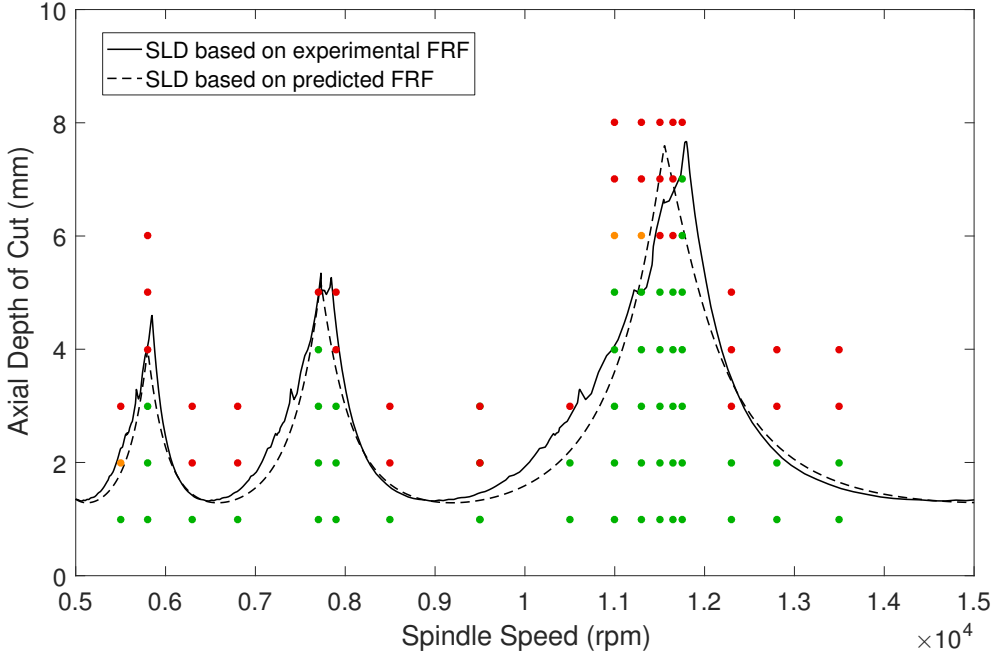


(c) Time history of x -direction forces. (d) x -vs. y -direction forces. Once per revolution sampled data (+) demonstrates Hopf bifurcation

Figure 8.9: Examples of stable and unstable cutting forces



(a) Collar C1 in location one (4 mm from the flange)



(b) Collar C1 in location two (64 mm from the flange)

Figure 8.10: Experiment 1: Experimentally validated stability lobe diagrams for prototype with collar C1 in location one (a) and location two (b)

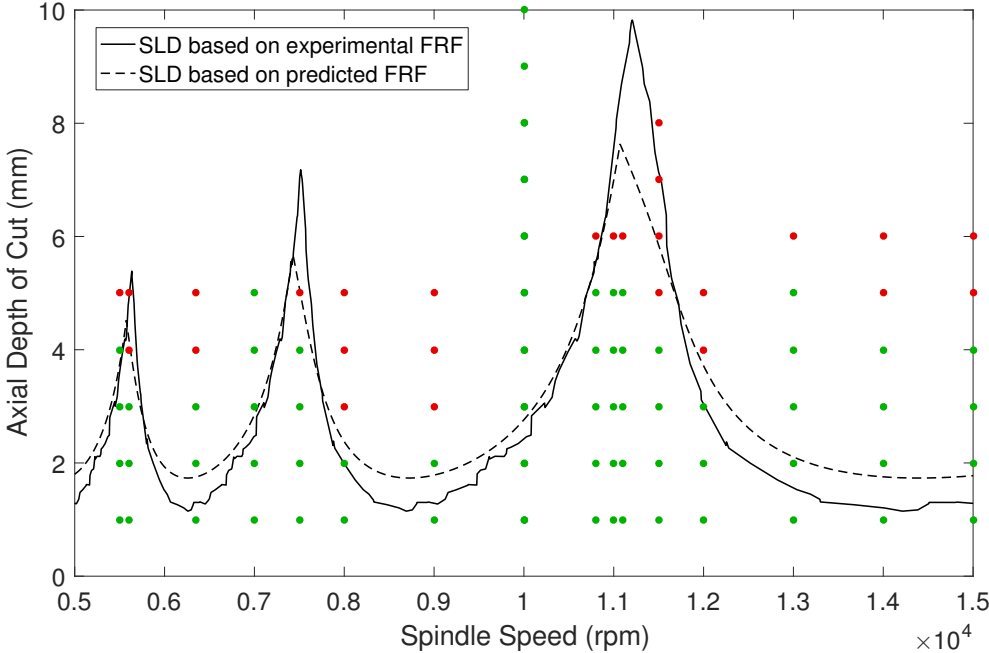
collar C1 can be used with the mass modification method to tune the dynamics of a milling spindle.

8.5.2 Experiment 2

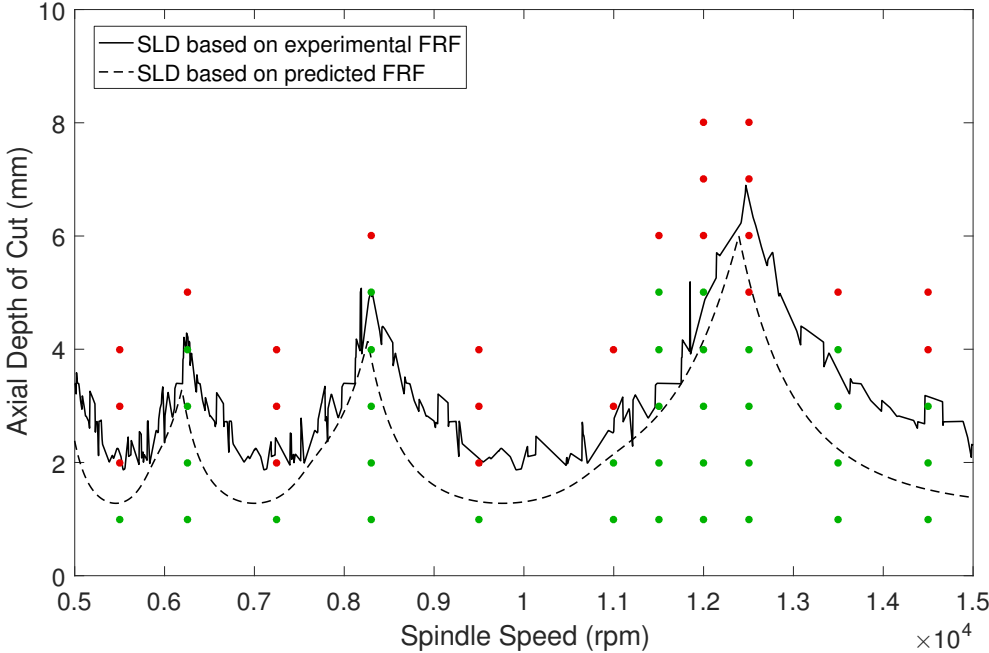
The SM prediction for experiment 2 is compared with the experimental results in Fig. 8.11. Fig. 8.11a shows the results for collar C2 in location 1. When compared to the experimental stability lobe diagram the prediction underestimates the absolute stability limit; however, the force and sound data suggests that the predicted limit is correct to within 1 mm. In terms of the lobe positions, the predicted SLD is in good agreement with the experimental SLD, although the accuracy is not as high as for experiment 1. This can be attributed to the error in the FRF prediction, discussed in section 8.2.1, which is likely due to the large collar size. However, both the predicted and experimental SLDs differ from the analysis of the cutting data with regard to the highest lobe.

The results for collar C2 in location 2 are presented in Fig. 8.11b. The predicted and experimental stability lobe diagrams are again in good agreement, although the amplitude of the peaks are underestimated by the SM method. The cutting data, however, differs from the SLDs in terms of both absolute stability limit and lobe location. Although the user would find it difficult to use the predicted results to select stable cutting parameters, the traditional method (impact testing) also fails to accurately determine the location of the lobes.

Comparing the two sets of data in Figs. 8.11a and 8.11b, a clear shift in the location of the lobes can be seen in both the stability lobe diagrams and the cutting data; therefore, it can be concluded that collar C2 can be used to successfully shift the stability lobes of a milling spindle.

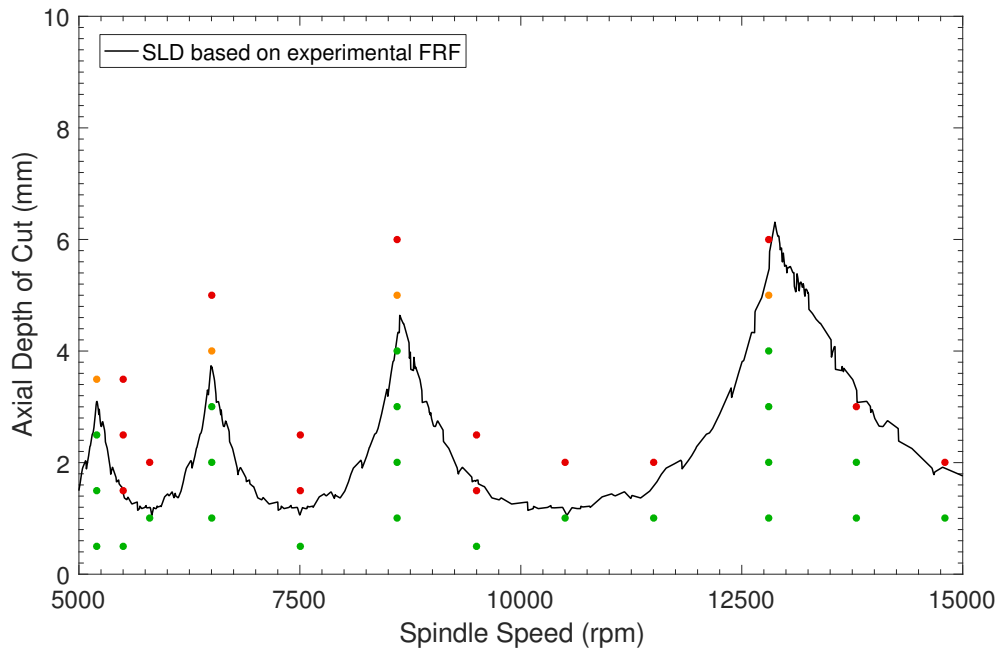


(a) Collar C2 in location one (4 mm from the flange)

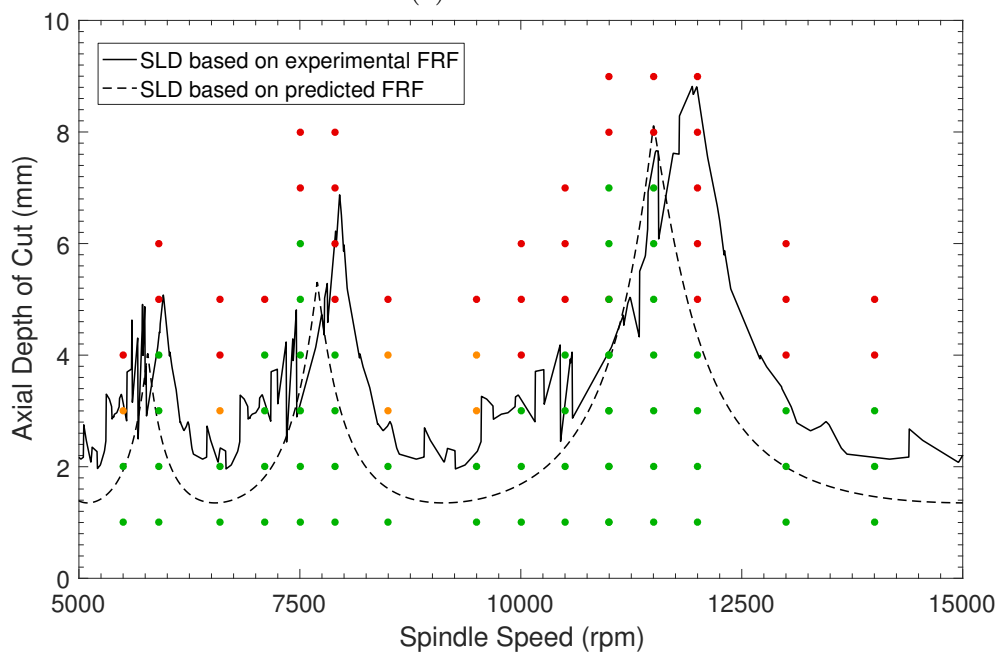


(b) Collar C2 in location two (54 mm from the flange)

Figure 8.11: Experiment 2: Experimentally validated stability lobe diagrams for prototype with collar C2 in location one (a) and location two (b)



(a) No Collar



(b) Collar C3 in location one (4 mm from the flange)

Figure 8.12: Experiment 3: Experimentally validated stability lobe diagrams for prototype with no collar (1) and collar C3 in location two (b)

8.5.3 Experiment 3

Since no modification has been made to the tool holder in experiment 3 setup 1, the experimental stability lobe diagram is compared with the chatter detection results in Fig. 8.12a. The two results are again in good agreement, with accuracy in line with experiment 1.

The results of the holder with collar C3 are shown in Fig. 8.12b. Despite noise disturbing the stability limit of the experimental stability lobe diagram, the predicted and experimental SLDs are in good agreement. A small discrepancy in the location of the lobes can be attributed to the difference in natural frequency shown in Fig. 8.3. Similar to the results of experiment 2 the cutting force data displays lobes at a lower spindle speed than the SLDs, although their stability limits are in good agreement.

Comparing the two figures a noticeable shift in the location of the lobes can again be seen, demonstrating the ability of collar C3 to shift the stability of the machine.

8.5.4 Discussion

Overall the results of the cutting trials validate the mass modification method for the prediction of tool tip FRFs with the tunable tool holder. Corresponding to the the impact test data captured on the spindle rig and presented in chapter 7, the accuracy of the method is dependent on the choice of collar. Collar C1 repeatedly produced superior results to the other two collars. This is possibly due to the smaller size of the collar, or the thread quality.

In each of the three experiments, the stability lobes of the FTV5 milling machine were successfully shifted to a significantly lower spindle speed. As expected the larger collars produced a slightly larger shift; however, considering the difference in their sizes, the difference in the shift is inconsequential. It may therefore be concluded that a tuneable tool holder for chatter avoidance in high speed milling has successfully been designed and manufactured.

8.6 Summary

The main contribution of this chapter was the demonstration of the industrial capability of the tuneable tool holder. Using impact data the mass modification method was successfully applied on the FTV5, an industry standard milling machine. Stability lobe diagrams were predicted by calibrating the mechanistic force model with experimental force measurements and calculating the specific cutting force coefficients for the correct tool and workpiece material. Several milling trials were performed and cutting signals recorded and analysed to experimentally determine the stability of the prototype in various configurations. By comparing the experimental stability with the predicted stability lobe diagrams the ability of the holder and the mass modification method were demonstrated in an industrial environment.

Chapter 9

Rotational Degree of Freedom Synthesis

In the previous chapters it has been demonstrated that tool holder geometry may be used as a chatter avoidance method. As discussed in chapter 1, the purpose of this project is to apply the structural modification method of Mottershead and Ram [1] to the tool holder problem. Due to the beam-like nature of machine tools, however, this application relies on the experimental determination of their rotational degrees of freedom. Whilst there are many methods to ascertain the rotational degrees of freedom of a structure (some of which were discussed in chapter 3), the finite difference method for rotational degree of freedom synthesis best meets the requirements and capabilities of the industrial partner.

The finite difference technique involves numerically differentiating the translational mode shapes to approximate the rotational modes using a finite difference algorithm. During initial application of the method, it was observed that the approach is limited by the user's choice of the measurement spacing between data points, an issue which has often been overlooked in the published literature. Therefore the purpose of this chapter is to introduce a new optimised finite difference method for use with non exact data. This has the potential to improve the accuracy of the predictions presented in previous chapters and, therefore, improve the ability of the tool holder geometry as a chatter avoidance technique.

Although the eventual application of this research is tool holder modification, the derivation of the new method was simplified by considering beams. Beams share similar properties in terms of their continuous geometry, but may also be tested in a laboratory environment.

Firstly, it will be proved that the use of a finite difference approach can become unstable when using non-exact measured data and a small measurement spacing, for beam-like structures. Then, a generalised analytical error analysis is used to propose an optimised measurement spacing, which balances the numerical error of the finite difference equation with the propagation error from the perturbed data. The approach is then demonstrated using both numerical and experimental investigations. It is shown that by obtaining a small number of test measurements it is possible to optimise the measurement accuracy, without any further assumptions on the characteristics of the measurement error or the boundary conditions of the structure.

9.1 Introduction

It has already been discussed that experimental rotational degrees of freedom will be required to accurately model changes in the tool holder geometry. Whilst the measurement of translational data is now commonplace, the same cannot be said for their rotational counterparts. Although techniques exist to directly measure RDOFs, they usually require specialist equipment, such as laser vibrometers or rotational accelerometers, which are not readily available to the industrial partner. For this reason, a synthesis method must be used to extract rotational information from translational data, which can be measured using standard test equipment. The most common is the finite difference (FD) technique, first proposed by Sattinger in 1978 [2].

The method applies a finite difference equation to data collected from closely spaced sensors to numerically differentiate the translational data with respect to the spatial coordinate. However, as with any numerical method, its accuracy is

dependent on the choice of spacing between data points. It is well documented that the accuracy of a FD equation can be improved by reducing the spacing; this chapter will show that when using non-exact measured data (data containing some error), the method becomes unstable. As the spacing is decreased, small errors or perturbations in the input data, such as noise or misalignment, give rise to large errors in the output. Hence, a compromise must be found, which balances the numerical error of the FD equation with the perturbation propagation error from the data.

Whilst the numerical errors associated with finite difference equations are well known, little attention has been paid to the propagation error. For this reason the application of the FD method for rotational degree of freedom synthesis is not robust. In this chapter, a full analytic error analysis of the FD method in the modal domain is carried out, showing that, for any structure, the method becomes unstable when using non-exact data. The results from the error analysis are used to propose an optimum spacing to balance the two errors. However, the optimum spacing relies on knowledge of two unknown quantities, the high order derivatives of the translational data and the error contained in the measurement. Analytical solutions for the mode shapes of beams are used to show that, for certain finite difference equations, this information can be found from the translational modal model, whilst for all other finite difference equations, a good approximation can also be found. An experimental investigation is also carried out to show how effective the method can be when approximating the measurement error.

The applications of experimentally derived rotational degrees of freedom are vast and varied. For instance, the receptance coupling method [120, 83] discussed in chapter 3, can be used to model the changes in tool or tool holder geometry. Moorhouse *et al.* [121] used the finite difference method in order to characterise structure-borne sound sources for use in assembled structures, such as vehicles and machinery. And the Craig-Bampton method [35] (more commonly known today as component mode synthesis) was originally proposed as a model reduction method. Whilst these applications are promising, they are all limited by

the need for highly accurate information on the rotational degrees of freedom. As stated above, this thesis concentrates on the FD method, partly due to its applicability to the industrial environment, but also due to the lack of robust error analysis available for the method.

Sattinger first considered the problem of rotational degree of freedom synthesis in 1980 [2], showing that any rotational frequency response function (FRF) is equal to the spatial derivative of its translational equivalent. The finite difference method was then used to approximate such derivatives. Using a free-free beam as an example, it was found that the results were accurate close to resonance, whilst other areas of the FRF showed considerable scatter. Although it was shown (using theoretical data) that a smaller spacing increases the accuracy of the numerical method, the link between increasing the spacing and decreasing the scatter was not made. Sestieri *et al.* [122] also used the example of a free-free beam, this time with experimental data. They suggested an improvement in the result could be found by using a spacing of between 5% and 8% of the total beam length; however, they failed to recognise that the error level may vary between different experiments and with different beams.

Duarte and Ewins [37, 58] later looked at the same problem and had similar issues, noting that the spacing of the accelerometers affects not only the scatter in the results but also the position of the antiresonances. The paper was also the first to apply the finite difference method in the modal domain. Again using data from a free-free beam, rotational mode shapes were approximated by applying the FD equation directly to the measured mode shapes, and then the rotational FRFs constructed from the result. This was found to give more accurate results than application in the frequency domain, but carried the added difficulty of how to include high frequency residuals. A high frequency pseudo mode was found to give satisfactory results. Although the paper suggests that the quality of the result is directly linked to the spacing, it is also concluded that the selection of the appropriate spacing remains a problem.

The only theoretical error analysis of the finite difference method for use in rotational DOF synthesis came from Elliot [123, 124]. In this case, using a simply supported beam as an example, it was shown that the numerical error associated with FD equations is directly proportional to the spacing between the sensors. However, the paper does not go on to show that the perturbation propagation error is inversely proportional to the spacing; instead arguing that, due to improvements in measurement equipment/practice, this should be less of a problem.

For this project it was decided that the finite difference method would only be considered in the modal domain. Firstly, because it has been shown that this produces more accurate results [58], and secondly, because the reconstructed (from the modal modal) FRFs are inherently smooth. As discussed in chapter 3, due to the matrix inverses inherent in dynamic substructuring methods they require both highly accurate and smooth frequency response function (FRF) data.

9.2 Background

The translational displacement of a structure can be characterised by its mode shapes $\phi_r(x)$ and their corresponding eigenvalues λ_r , which are easily related to the frequency response function (FRF), H_{ij} , usually measured in modal testing.

$$H_{ij}(\omega) = \frac{Y_i(\omega)}{F_j(\omega)} = \sum_{r=1}^N \frac{\phi_r(x_i)\phi_r(x_j)}{\lambda_r - \omega^2} \quad (9.1)$$

Here, $H_{ij}(\omega)$ is the FRF excited at location i and measured at location j for a particular frequency ω , Y_i is the Fourier transform of the displacement at location i , F_j is the Fourier transform of the input force at location j , N is the total number of modes measured, $\phi_r(x_i)$ is the r^{th} mode at location i , and λ_r is the r^{th} eigenvalue.

However, the above equation only makes up part of the full response model required for the application of higher rank structural modification, as it only considers the translational displacement, Y , and excitation force, F . To fully

understand the vibration of any structure both rotational displacement Θ and excitation moment Q must also be included, giving rise to three further FRFs:

$$N_{ij}(\omega) = \frac{\Theta_i}{F_j} = \sum_{r=1}^N \frac{\phi_r^{(1)}(x_i)\phi_r(x_j)}{\lambda_r - \omega^2} \quad L_{ij}(\omega) = \frac{Y_i}{Q_j} = \sum_{r=1}^N \frac{\phi_r(x_i)\phi_r^{(1)}(x_j)}{\lambda_r - \omega^2}$$

$$P_{ij}(\omega) = \frac{\Theta_i}{Q_j} = \sum_{r=1}^N \frac{\phi_r^{(1)}(x_i)\phi_r^{(1)}(x_j)}{\lambda_r - \omega^2} \quad (9.2)$$

Whilst the measurement of these FRFs is difficult, mainly due to the application of a pure moment, Eq. (9.2) shows that they can be constructed from the standard modal model (ϕ_r, λ_r) and the rotational mode shapes $\phi_r^{(1)}$ (where the superscript (1) represents the first derivative). Hence, by measuring the mode shapes and eigenvalues, and using this data to approximate the rotational mode shapes, it is possible to construct a full response model.

Perhaps the simplest method of approximating the derivative of a mode shape is the first order forward finite difference equation, a standard result derived from the truncated Taylor series [125]. Defining the forward finite difference operator, D_δ^F , we have that:

$$\phi_r^{(1)}(x) \approx D_\delta^F \phi_r(x) = \frac{\phi_r(x + \delta) - \phi_r(x)}{\delta} \quad (9.3)$$

where x is the coordinate of interest on the structure, δ is a small length on the structure, and ϕ_r has a continuous bounded derivative. In application, the mode shape is measured using two sensors (separated by δ), as shown in Fig. 9.1, then Eq. (9.3) is used to approximate its derivative. It should be noted that it is not necessary for the co-located FRF to occur at the point of interest, and higher order finite difference equations can be also be applied using additional sensors.

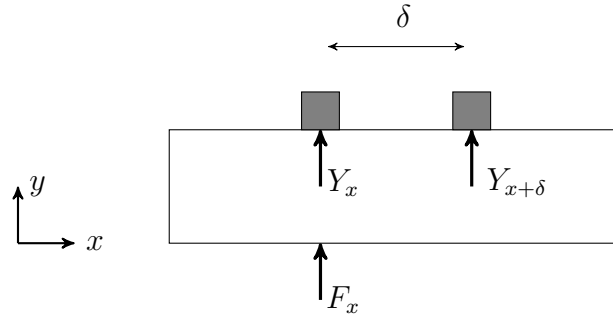


Figure 9.1: Application of the first order forward finite difference equation in the modal domain

9.2.1 Error analysis: forward differences

Using Taylor's theorem it is possible to derive a bound on the truncation error of the finite difference equation given in Eq. (9.3). The theorem states that if a real valued function $\phi_r(x)$ is differentiable at point x , then a linear approximation to the function at point $x + \delta$, where δ is a real positive constant, can be found as:

$$\phi_r(x + \delta) = \phi_r(x) + \delta\phi_r^{(1)}(x) + \frac{\delta^2}{2}\phi_r^{(2)}(x) + \dots \quad (9.4)$$

Eq. (9.4) can be rearranged to give an approximation of the first derivative at point x ($\phi_r^{(1)}(x)$):

$$\phi_r^{(1)}(x) = \frac{\phi_r(x + \delta) - \phi_r(x)}{\delta} - \frac{\delta}{2}\phi_r^{(2)}(x) + \dots \quad (9.5)$$

resulting in the well known first order forward finite difference equation. Substituting for the forward finite difference operator D_δ^F we have that

$$\phi_r^{(1)}(x) = D_\delta^F \phi_r(x) - \frac{\delta}{2}\phi_r^{(2)}(x) + \dots \quad (9.6)$$

Rearranging and taking the absolute value, the error associated with the finite difference approximation is found from the first truncation term in the Taylor series

$$|\phi_r^{(1)}(x) - D_\delta^F \phi_r(x)| = \left| \frac{\delta}{2}\phi_r^{(2)}(x) + \dots \right| \quad (9.7)$$

Using the well known subadditivity property of the absolute value ($|a + b| \leq |a| + |b|$) it is found that

$$|\phi_r^{(1)}(x) - D_\delta^F \phi_r(x)| \leq \frac{\delta}{2} |\phi_r^{(2)}(x)| + \dots \quad (9.8)$$

Since the value of $\phi_r^{(2)}(x)$ is unknown, a bound on the error can be found by taking the Euclidean norm of the function $\phi_r^{(2)}$.

$$|\phi_r^{(1)}(x) - D_\delta^F \phi_r(x)| \leq \frac{\delta}{2} \|\phi_r^{(2)}\| \quad (9.9)$$

where $\|\phi_r^{(2)}\|$ is the Euclidean norm of the vector $\phi_r^{(2)}$. This makes the assumption that ϕ_r has a continuous bounded second derivative ($\phi_r^{(2)}$).

The general form of such forward difference equations (for the first derivative) can be written as

$$D_\delta^F \phi_r(x) = \frac{1}{\delta} \sum_{k=0}^n a_k \phi_r(x + k\delta) \quad (9.10)$$

Here, $a_k \in \mathbb{R}$ are the coefficients found from the Taylor series derivation, and n is the number of additional nodes in the finite difference method. For the example given in Eq. (9.3), $a_k = \{-1, 1\}$, and $n = 1$. Similar to the above example, the general truncation error is bounded by

$$|\phi_r^{(1)}(x) - D_\delta^F \phi_r(x)| \leq T \delta^n \|\phi_r^{(n+1)}\| \quad (9.11)$$

where the specific truncation coefficient $T \in \mathbb{R}$ can be found by analysing the Taylor series truncation. For the example given in Eq. (9.9), $T = 1/2$.

This, however, is not the only error when using finite different equations with measured data [126]. Consider the measured mode shape ϕ_{rm} , which is the sum of the actual mode shape ϕ_r and some measurement perturbation $\bar{\phi}_r$. Hence,

$$\phi_{rm} = \phi_r + \bar{\phi}_r \quad (9.12)$$

This perturbation may contain signal noise as well as measurement or curve fitting errors. When a finite difference equation is applied to such data, it is applied to both the mode shape and the perturbation, giving rise to the so called propagation error. Similar to the idea of the truncation error in Eq. (9.9), an upper bound on the propagation error must also be found. Consider any point x in the region of interest, then

$$|\phi_r(x) - \phi_{rm}(x)| \leq \|\phi_r - \phi_{rm}\| = M_r \quad (9.13)$$

Here, $\|\phi_r - \phi_{rm}\|$ is the Euclidean distance between the vectors ϕ_r and ϕ_{rm} , and M_r is defined as the upper bound on the measurement perturbation of the r^{th} mode, i.e.

$$|\bar{\phi}_r| \leq M_r \quad (9.14)$$

Then, applying the above forward difference equation (Eq. (9.10)) to the perturbed data, we have that

$$\begin{aligned} D_\delta^F \phi_{rm}(x) &= \frac{1}{\delta} \sum_{k=0}^n a_k \phi_{rm}(x + k\delta) \\ &= \frac{1}{\delta} \left(\sum_{k=0}^n a_k \phi_r(x + k\delta) + \sum_{k=0}^n a_k \bar{\phi}_r(x + k\delta) \right) \\ &= D_\delta^F \phi_r(x) + \frac{1}{\delta} \sum_{k=0}^n a_k \bar{\phi}_r(x + k\delta) \end{aligned} \quad (9.15)$$

Therefore, the propagation error can be bounded by:

$$\begin{aligned} |D_\delta^F \phi_r(x) - D_\delta^F \phi_{rm}(x)| &= \left| \frac{1}{\delta} \sum_{k=0}^n a_k \bar{\phi}_r(x + k\delta) \right| \\ &\leq \frac{M_r}{\delta} \sum_{k=0}^n |a_k| \end{aligned} \quad (9.16)$$

Hence, by combining the truncation error in Eq. (9.11) with the propagation

error in Eq. (9.16), a bound on the total error (e_T) is found to be:

$$\begin{aligned} e_T &= |\phi_r^{(1)}(x) - D_\delta^F \phi_{rm}(x)| \leq |\phi_r^{(1)}(x) - D_\delta^F \phi_r(x)| + |D_\delta^F \phi_r(x) - D_\delta^F \phi_{rm}(x)| \\ &\leq T\delta^n \|\phi_r^{(n+1)}\| + \frac{M_r}{\delta} \sum_{k=0}^n |a_k| \end{aligned} \quad (9.17)$$

Herein lies the most significant problem of the application of finite difference formulae with real data. As $\delta \rightarrow 0$ the truncation error tends to zero, whilst the propagation error tends to infinity and the method becomes unstable.

9.2.2 A new optimum spacing

By minimising the upper bound of the total error, the total error itself will be minimised; therefore, a value of δ must be chosen so as to balance the two terms and minimise the right hand side (RHS) of Eq. (9.17). This may be found by setting the first derivative (with respect to δ) of the RHS of Eq. (9.17) to zero, then the resultant δ_{min}^F is found to be:

$$\delta_{min}^F = \left(\frac{M_r}{nT} \sum_{k=0}^n |a_k| \|\phi_r^{(n+1)}\|^{-1} \right)^{\frac{1}{n+1}} \quad (9.18)$$

Making the same assumptions on the continuity of ϕ_r as above, and following the same process, the optimum spacing for the general backward difference equations (δ_{min}^B) is found to be the same function.

The formulae and necessary coefficients ($T, \sum a_k$) for the forward and backward difference equations for $n = 1$, $n = 2$, and $n = 3$ are summarised in Tables B.1, B.2, and B.3 respectively.

9.2.3 Error analysis: central differences

Combining a forward and a backward difference formula, both with n points, results in a more accurate approximation to the first order derivative, called a central difference formula. Although a higher degree of accuracy can be achieved

using the same number of measurement points, central differences cannot be used to evaluate the boundaries.

Consider, once again, the first order forward $D_\delta^F \phi_r(x)$ and backward $D_\delta^B \phi_r(x)$ finite difference equations given by

$$\begin{aligned}\phi_r^{(1)}(x) &= D_\delta^F \phi_r(x) - \frac{\delta}{2} \phi_r^{(2)}(x) - \frac{\delta^2}{6} \phi_r^{(3)}(x) + \dots \\ \phi_r^{(1)}(x) &= D_\delta^B \phi_r(x) + \frac{\delta}{2} \phi_r^{(2)}(x) - \frac{\delta^2}{6} \phi_r^{(3)}(x) + \dots\end{aligned}\quad (9.19)$$

By adding these equations together and defining the central difference operator D_δ^C we have that

$$\phi_r^{(1)}(x) = D_\delta^C \phi_r(x) - \frac{\delta^2}{6} \phi_r^{(3)}(x) + \dots\quad (9.20)$$

It can now be seen that the order of the first truncation term has been doubled. Following the same procedure as for the forward difference example in Eqs. (9.7)-(9.9), a bound on the truncation error of the second order central difference equation is found to be

$$|\phi_r^{(1)}(x) - D_\delta^C \phi_r(x)| \leq \frac{\delta^2}{6} \|\phi_r^{(3)}\|\quad (9.21)$$

The general form of such central difference equations (for the first derivative) is written as

$$D_\delta^C \phi_r(x) = \frac{1}{\delta} \sum_{k=-n}^n a_k \phi_r(x + k\delta)\quad (9.22)$$

which has a general truncation error bounded by

$$|\phi^{(1)}(x) - D_h^C \phi(x)| \leq T \delta^{2n} \|\phi^{(2n+1)}\|\quad (9.23)$$

Since the upper bound on the measurement perturbation is independent of the finite difference equation in question, M_r is used once again, and the propagation

error is found to be bounded such that

$$|D_\delta^C \phi_r(x) - D_\delta^C \phi_{rm}(x)| \leq \frac{M_r}{\delta} \sum_{k=-n}^n |a_k| \quad (9.24)$$

Again combining the truncation error (Eq. (9.23)) and the propagation error (Eq. (9.24)) the total error can be bounded from above by

$$\begin{aligned} e_T &= |\phi_r^{(1)}(x) - D_\delta^C \phi_{rm}(x)| \\ &\leq T\delta^{2n} \|\phi_r^{(2n+1)}\| + \frac{M_r}{\delta} \sum_{k=-n}^n |a_k| \end{aligned} \quad (9.25)$$

The optimum spacing for the central difference equations is then given by

$$\delta_{min}^C = \left(\frac{M_r}{2nT} \sum_{k=-n}^n |a_k| \|\phi_r^{(2n+1)}\|^{-1} \right)^{\frac{1}{2n+1}} \quad (9.26)$$

The formulae and necessary coefficients ($T, \sum a_k$) for the central difference equations for $n = 1$, $n = 2$, and $n = 3$ are summarised in Tables B.1, B.2, and B.3 respectively.

However, the optimum spacings given in Eqs. (9.18) and (9.26) still contain two unknown values, firstly, the high order derivative norm $\|\phi_r^{(p)}\|$ (where $p = n + 1$ for forward/backward differences, and $p = 2n + 1$ for central differences), and secondly, the measurement perturbation bound M_r .

The next two sections deal with how to evaluate the derivative norms $\|\phi_r^{(p)}\|$. A numerical investigation is used to validate the optimised measurement spacing when assuming perfect knowledge of the measurement perturbation bound M_r .

9.3 Evaluating the fourth order derivative norms

The aim of the section is to validate the new optimum spacings for the finite difference method with non-exact data. Numerical examples are used so that the

measurement perturbation bound M_r can be calculated exactly, leaving the only unknown value as the high order derivative norm $\|\phi_r^{(p)}\|$. Using the analytical solutions for the mode shapes of beams with arbitrary boundary conditions, it will be shown that for forward/backward finite difference equations of order $n = 4k - 1$ where $k = 1, 2, 3, \dots$, the exact value of $\|\phi_r^{(p)}\|$ can be calculated from the translational modal model (ϕ_r, ω_r) .

9.3.1 The fourth derivative of beam mode shapes

The general form of the r th mode shape for an Euler-Bernoulli beam is given by:

$$\phi_r(x) = C_1 \cosh(\lambda_r x) + C_2 \sinh(\lambda_r x) + C_3 \cos(\lambda_r x) + C_4 \sin(\lambda_r x) \quad (9.27)$$

where constants C_1 to C_4 are found from the boundary conditions and

$$\lambda_r^4 = \frac{\rho A \omega_r^2}{EI} \quad (9.28)$$

where ρ is the material density, A is the cross-sectional area, E is the Young's modulus, and I is second moment of inertia.

Due to the inherent trigonometric/hyperbolic nature of such mode shapes, certain relationships between Eq. (9.27) and its higher order derivatives can be found. The trigonometric functions will repeat every fourth derivative, and the hyperbolic functions every second, therefore:

$$\phi_r^{(4)} = \lambda_r^4 \phi_r \quad (9.29)$$

Hence, when using the forward/backward difference equations and the optimum spacing given in Eq. (9.18), by choosing $n = 3$ the norm of the fourth derivative is required, meaning the finite difference equation can be optimised without any approximation. The optimum spacing then simplifies to

$$\delta_{min}^F = \frac{1}{\lambda_r} \left(\frac{80M_r}{9\|\phi_r\|} \right)^{\left(\frac{1}{4}\right)} \quad (9.30)$$

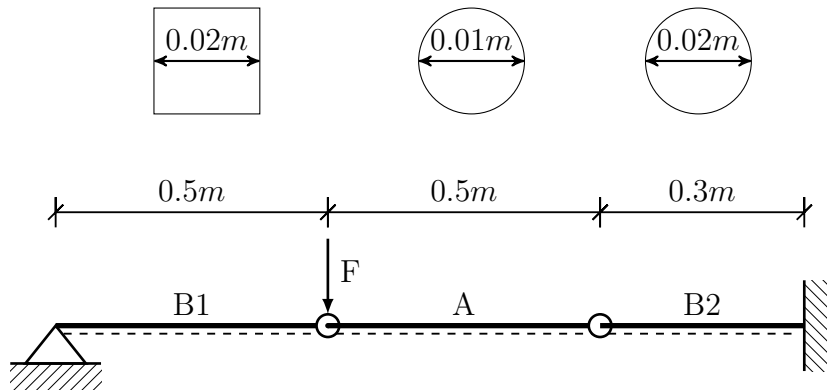


Figure 9.2: The geometry and boundary conditions of a beam used for numerical validation of error analysis

Following the same logic it is also possible to show that

$$\phi_r^{(4k)} = \lambda_r^{4k} \phi_r \quad \text{where} \quad k = 1, 2, 3, \dots \quad (9.31)$$

meaning the exact value for d_{min}^F can be found for all finite differences of order $n = 4k - 1$.

9.3.2 A beam with arbitrary boundary conditions

Since no assumptions on the boundary conditions (BCs) of the beam were made, the above result may be applied to both beam and beam like structures. Hence for validation purposes, a finite element model of a 0.5 m circular section beam of diameter 0.01 m (shown in Fig. 9.2 section A) was constructed, and extended in both directions to give arbitrary BCs. One boundary (B1) was comprised of a 0.5 m square beam of 0.02 m width pinned at one end, whilst the other (B2) consisted of a 0.3 m cylindrical beam of diameter 0.02 m fixed at one end. The eigenvalue problem was solved over the whole beam and a normal mode model extracted across section A, which contained 501 equally spaced nodes. The response to an impulse, applied at boundary B1, with maximum amplitude of 1 N and time step of 1.25×10^{-5} s, was then simulated for each of the 501 nodes.

9.3.3 Numerical validation

Since noise and error in measurement is random and varies from test to test and from signal to signal, a statistical investigation is needed to validate the error analysis.

Firstly, using the result given in Eq. (9.30) the optimum spacings for the first 5 bending modes were calculated by following the process shown on the left hand side of the diagram in Fig. 9.3. To each of the 501 time domain response signals ($y_i(t)$) and the input force signal ($f_j(t)$), white Gaussian noise with a signal to noise ratio (SNR) of 50dB was added, and the Fourier transform ($\tilde{Y}_i(\omega)$, $\tilde{F}_j(\omega)$) calculated. In the frequency domain, alignment error between the input force and measured response was simulated by multiplying the force signal by a cosine error ($\bar{F}_j(\omega) = \tilde{F}_j(\omega) \cos \beta$), where β , the angle between the direction of the input and output measurements, is normally distributed with mean 3 and standard deviation of 0.625, based on the data given in [99]. Then, to the FRFs, curves were fitted between 0 Hz and 1500 Hz and the measured mode shapes (ϕ_{rm}) extracted. The measurement perturbation bound (M_r) was found as the Euclidean norm of the difference between the extracted mode shapes (ϕ_{rm}) and the ‘perfect modes’ (ϕ_r) from the finite element model. This gave optimum spacings of 0.0481 m, 0.04 m, 0.0282 m, 0.0245 m, and 0.0225 m for the first five modes.

Secondly, the finite difference equation was applied at fifty δ values between 0.001 m and 0.05 m, by following the right hand side of the diagram in Fig. 9.3. For a particular value of δ , $i = 0.5/\delta + 1$ time domain response signals were extracted from the FD model. Measurement noise, sensor alignment, and curve fitting errors were introduced as above and the measured mode shapes extracted. Then, the finite difference equation was applied and the total error (e_T) calculated as

$$e_T = \left| \phi_r^{(1)}(x) - D_\delta \phi_{rm}(x) \right| \quad (9.32)$$

This was repeated 500 times to give a sufficiently large population of errors for each of the spacings, from which a random sample of 50 was taken and a 95%

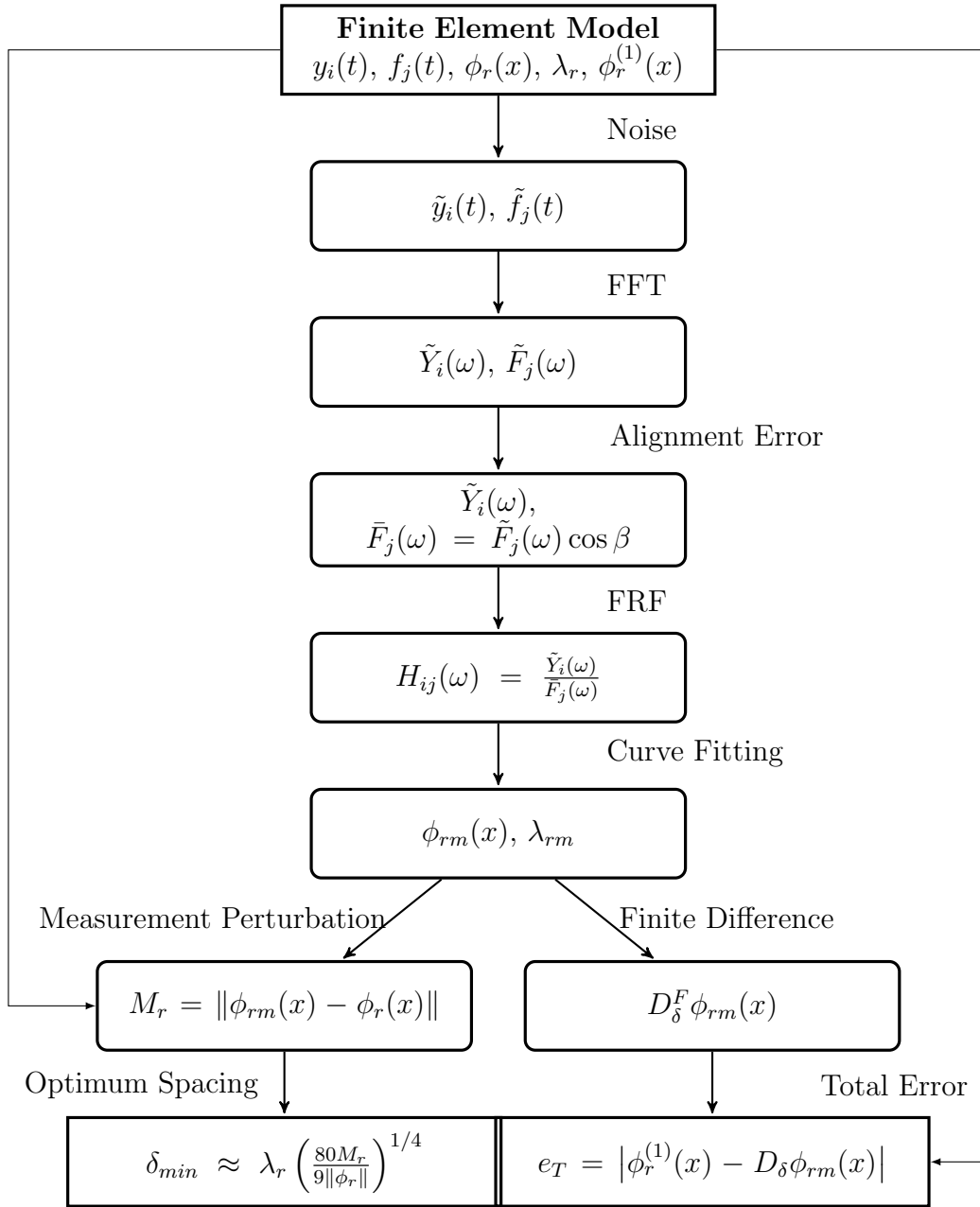


Figure 9.3: Flow chart detailing the process followed to calculate optimum spacings δ_{min} (left hand side) in numerical investigation, and and total error e_T (right hand side) for numerical validation of error analysis.

confidence interval calculated.

9.3.4 Results and discussion

The results of the numerical validation are presented in Figs. 9.4a-9.4e for modes 1-5 respectively. In each case, the total error (e_T) mean is shown with its confidence interval. The figures show that by using the δ_{min} value calculated by the optimisation method, the error can be minimised, thus validating the approach. For each mode, values below δ_{min} give rise to much higher mean errors, showing that the likelihood of the perturbation propagation error will affect the solution rapidly increases as δ shrinks. Contrastingly, as δ becomes larger, the likelihood of the truncation error effecting the solution increases, albeit more gradually than for the propagation error. From this it is sensible to conclude that when δ_{min} is unknown, a larger δ value is more likely to give accurate results. The gradient of the curves increases with wave number, which implies greater sensitivity to the spacing δ . This is to be expected as the $n = 3$ finite difference equation becomes less accurate as the frequency of the wave increases.

Whilst encouraging, this numerical example suffers from two drawbacks. First, the result appears to be restricted to the use of a 3rd order finite difference scheme (Table B.3). Second, the measurement perturbation bound has been assumed to be known perfectly, which is of course impossible in a practical scenario. These issues will be dealt with in Section 9.4 and 9.5 respectively.

9.4 Evaluating other high order derivative norms

Whilst it is advantageous to use the $n = 4k - 1$ forward/backward difference equation, as $\|\phi_r^{(p)}\|$ can be evaluated exactly, it may not always be practicably beneficial. In this case, a method to approximate $\|\phi_r^{(p)}\|$ from the standard modal model (ϕ_r, ω_r) must be found. It will now be shown, using the same numerical example as above, that for forward/backward differences with $n = 1$ and $n = 2$ a good approximation to the optimum spacing can be found using the following

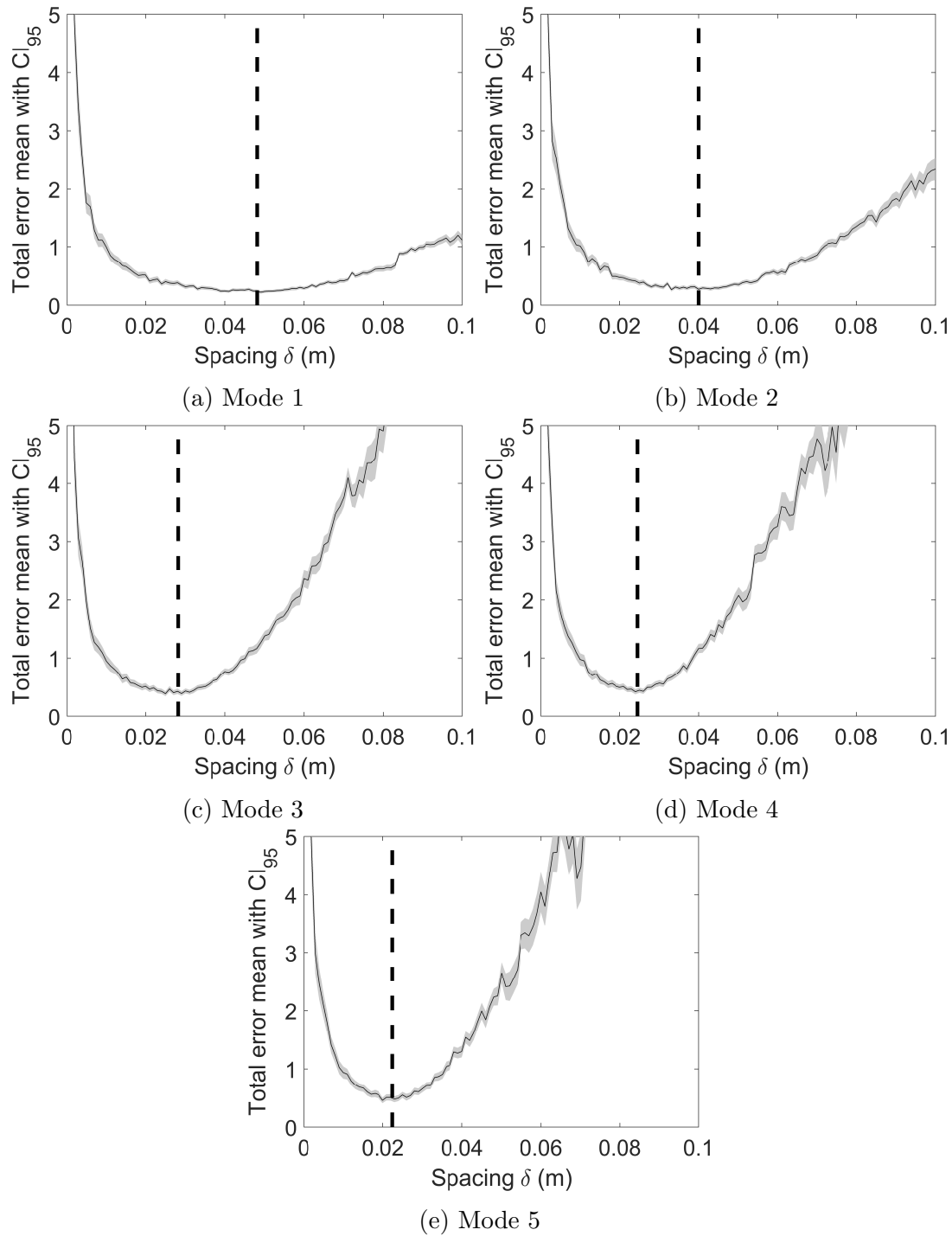


Figure 9.4: Results of the numerical validation using a beam with arbitrary boundary conditions for the first 5 bending modes (a)-(e) using the $n = 3$ forward FD equation: Spacing (δ) vs. Total error mean (—) (and 95% confidence interval) as well as predicted optimum spacing δ_{min} (- -)

relationship:

$$\|\phi_r^{(p)}\| \approx \lambda_r^{(p)} \|\phi_r\| \quad (9.33)$$

which yields optimum spacings approximately given by:

$$\delta_{min}^F \approx \frac{1}{\lambda_r} \left(\frac{4M_r}{\|\phi_r\|} \right)^{(1/2)} \quad \text{and} \quad \delta_{min}^F \approx \frac{1}{\lambda_r} \left(\frac{6M_r}{\|\phi_r\|} \right)^{(1/3)} \quad (9.34)$$

respectively.

Using the process outlined in Fig. 9.3 the same numerical investigation was carried out on the structure shown in Fig. 9.2, this time using the approximate optimum spacings given in Eq. (9.34). The results for the first and fifth modes for the $n = 1$ and $n = 2$ forward difference equations are presented in Figs. 9.5a-9.5d respectively.

The results follow the same trends as those of the $n = 3$ forward FD equations presented in section 9.3, with the propagation error tending to infinity at small spacings, and the numerical error tending to infinity more gradually as δ increases. Most importantly, the approximate optimum spacings still result in the lowest total errors in each case meaning that by using the approximate value for $\|\phi_r^{(p)}\|$ given in Eq. (9.33) it is possible to optimise the method for any finite difference equation.

9.5 Approximating the ‘perfect modes’

The above examples have assumed perfect knowledge of the measurement perturbation bound M_r , in that the mode shapes ϕ_r could be directly extracted from the finite element model. In practice, this information is unknown and must somehow be approximated. The example from section 9.3 is now revisited, allowing the high order norm $\|\phi_r^{(p)}\|$ to be calculated explicitly, leaving the only error in approximating the ‘perfect modes’ ϕ_r .

Assuming that the measurement perturbation ($\bar{\phi}_r$) at any location x has a random

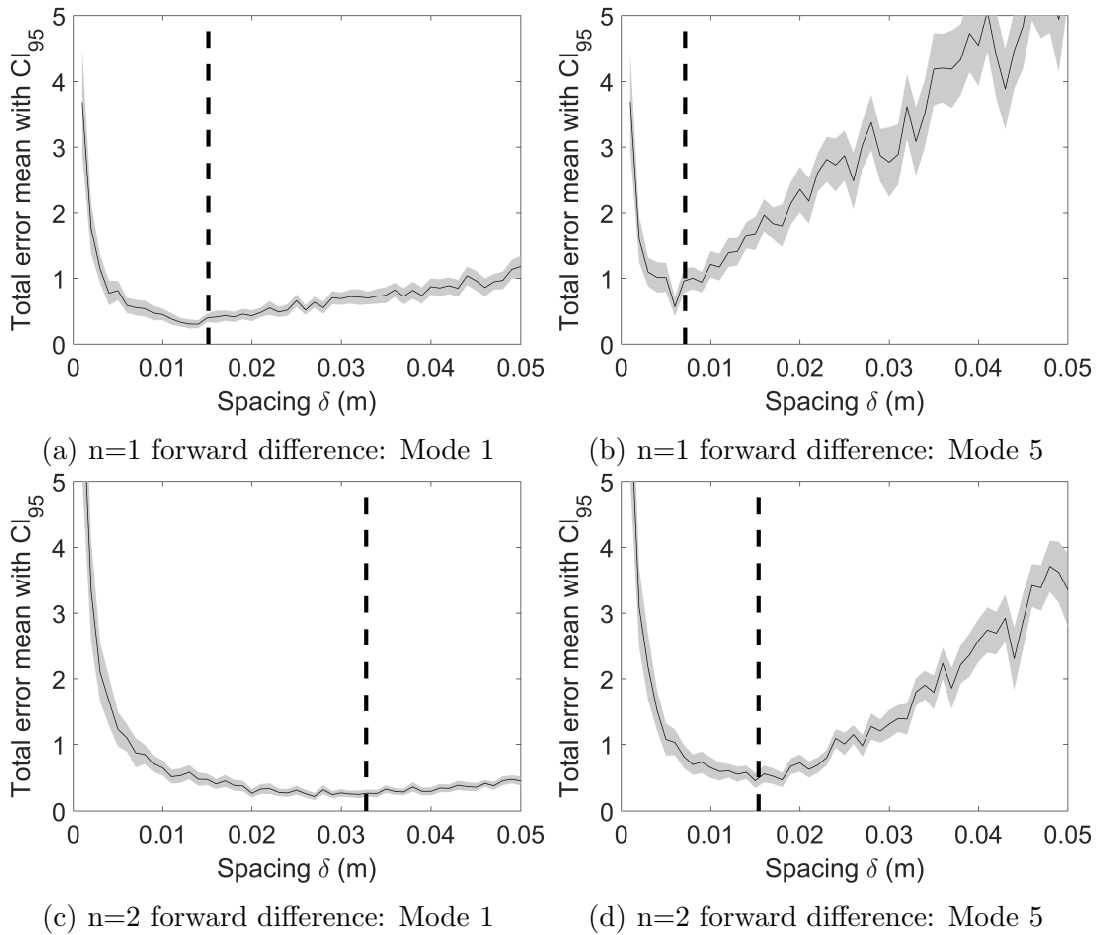


Figure 9.5: Results of the numerical validation using a beam with arbitrary boundary conditions: Spacing (δ) vs. Total error mean (—) (and 95% confidence interval) as well as predicted optimum spacing δ_{min} (- -)

distribution, the mode shapes $\phi_r(x)$ may be approximated as the mean of a set of K measured mode shapes $\{\phi_{rm1}(x), \phi_{rm2}(x), \dots, \phi_{rmK}(x)\}$, i.e.

$$\phi_r(x) \approx \mu_r(x) = \mu(\phi_{rm1}(x), \phi_{rm2}(x), \dots, \phi_{rmK}(x)) \quad (9.35)$$

where $\mu_r(x)$ is the mean at location x of the r^{th} mode. This approximation should improve as $K \rightarrow \infty$.

In order to approximate the bound M_r it is also assumed that the set of measured values $\{\phi_{rm1}(x), \phi_{rm2}(x), \dots, \phi_{rmK}(x)\}$ is also normally distributed. It is well known that 95% of values from any normally distributed variable lie within the range $\mu \pm 2\sigma$, where σ is the standard deviation. Therefore, considering the measurement perturbation defined in Eq. (9.12), it can be deduced that approximately 95% of the values of $\bar{\phi}_r$ lie within the following region

$$\begin{aligned} [\bar{\phi}_r(x)]_{95\%} &= [\phi_{rm}(x) - \phi_r(x)]_{95\%} \\ &\approx (\mu_r(x) \pm 2\sigma_r(x)) - \mu_r(x) \\ &\approx \pm 2\sigma_r(x) \end{aligned} \quad (9.36)$$

Substituting this into the measurement perturbation bound defined in Eq. (9.14) an approximation on M_r can be found:

$$\|2\sigma_r\| \leq M_r \quad (9.37)$$

The accuracy of which should improve with the number of measurements K .

Before discussing the effect of this approximation on δ_{min} , the assumptions made above are discussed. It is a perfectly valid assumption that measurement error such as noise will be randomly distributed; however, errors such as curve fitting (especially if the process is automated) may be more systematic in nature and will effect the accuracy of this approximation. The validity of the second assumption, that a set of measured mode shapes at any location x is normally distributed, is now demonstrated using the example given in section 9.3. To the finite element

mode shapes ϕ_r noise, misalignment, and curve fitting errors were introduced as before. This was then repeated 1000 times to represent $K = 1000$ experimental repetitions. The data sets at $x = 0$ m and $x = 0.25$ m were extracted and individual histograms generated. The results for modes 1 and 5 are plotted in Fig. 9.6, along with the normal density function generated using the associated μ and σ . The figures demonstrate that independent of wave number or measurement location, the measured data sets all have a (roughly) normal distribution, thus validating the assumption made above.

The impracticality of repeating an experiment 1000 times would obviously render the method worthless; therefore, the above approximation must now be validated for small values of K . Consequently, the numerical investigation from section 9.3 was repeated, yielding δ_{min} values of 0.0481 m and 0.0225 m for the first and fifth bending modes respectively.

Additionally, from the 1000 sets of measured modes, a random sample of size $K = 3$ were extracted. Using this sample δ_{min} was calculated for the first and fifth bending modes ($r = 1, 5$) using the following result:

$$\delta_{min}^F = \frac{1}{\lambda_r} \left(\frac{80 \|2\sigma_r\|}{9 \|\mu_r\|} \right)^{\left(\frac{1}{4}\right)} \quad (9.38)$$

This process was then repeated for sample sizes between $K = 3$ and $K = 1000$. The approximate δ_{min} values are plotted against the expected values (0.0481 m, and 0.0225 m) in Fig. 9.7. The figures clearly show that increasing the sample size (i.e. the number of measurement repetitions) increases the accuracy of the approximation as expected. In both cases, the data tends to a value at or near the expected δ_{min} value. However, even with very small sample sizes of $K = 3$, the prediction is accurate to within 0.62% for mode 1 and 0.81% for mode 5; thus, yielding inaccuracies of just +0.14 mm and -0.39 mm respectively. Due to the accuracy in these approximations the optimum spacings given in Eq. (9.18)

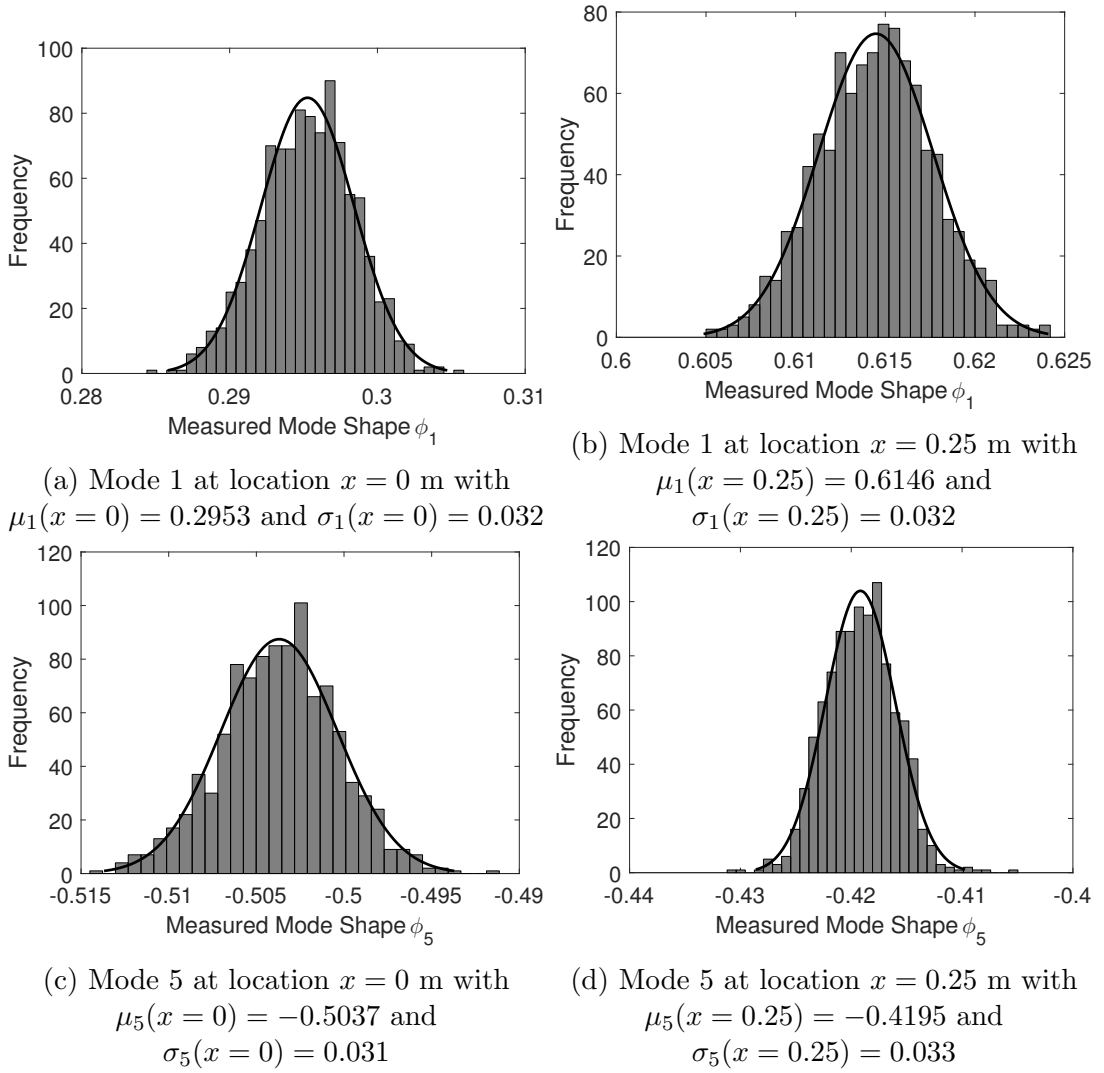


Figure 9.6: Histograms of 1000 measured mode shapes (ϕ_r) with normal density function for modes 1 and 5 at locations $x = 0$ m and $x = 0.25$ m

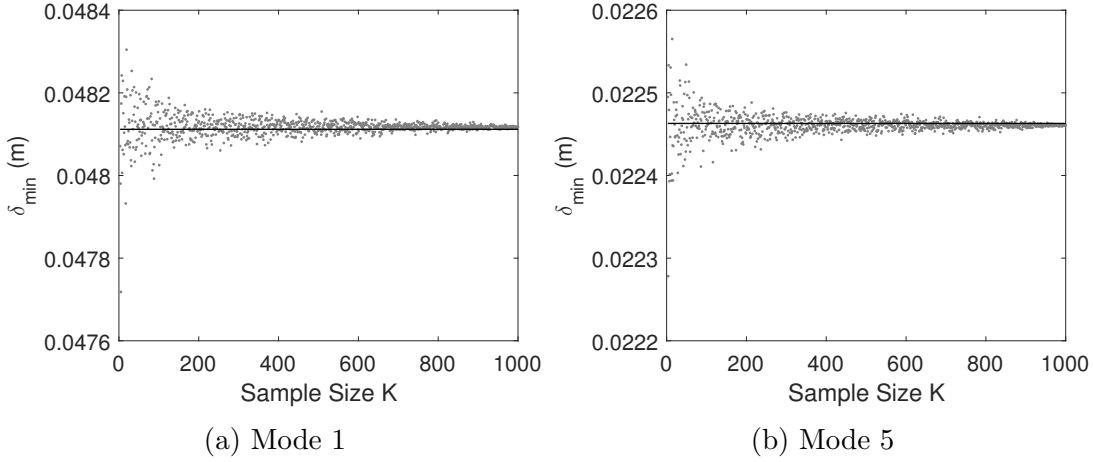


Figure 9.7: The effect of sample size (or number of measurement repetitions) on δ_{min} prediction for mode 1 (a) and mode 5 (b)

and Eq.(9.26) are redefined such that:

$$\begin{aligned}\delta_{min}^F &\approx \frac{1}{\lambda_r} \left(\frac{\|2\sigma_r\|}{\|\mu_r\|} \sum_{k=0}^n \frac{|a_k|}{nT} \right)^{\frac{1}{n+1}} \\ \delta_{min}^C &\approx \frac{1}{\lambda_r} \left(\frac{\|2\sigma_r\|}{\|\mu_r\|} \sum_{k=-n}^n \frac{|a_k|}{2nT} \right)^{\frac{1}{2n+1}}\end{aligned}\quad (9.39)$$

where $\lambda_r \approx \mu(\lambda_{rm})$.

This section has concentrated on approximating the ‘perfect modes’ from a measured data set, showing that by obtaining a very small number of mode shape measurements, it is possible to accurately calculate the optimum spacing. Thus far, the effect of approximating the high order measurement norm ($\|\phi_r^{(p)}\|$), and the effect of approximating the ‘perfect’ mode shapes (ϕ_r) have been discussed in isolation, using numerical examples. The next section, looks to utilise an experimental data set to combine both approximations, and validate the effectiveness of the optimised finite difference method in practice.

9.6 Experimental Investigation

This section experimentally validates the error analysis, utilising data from a free-free beam to demonstrate how effective the optimum spacings can be in practice. The ‘perfect modes’ are approximated from three repetitions (i.e. $K = 3$), and the $n = 1$ finite difference scheme is used to include the effect of approximating the high order norm. A free-free beam was chosen as an example since the boundary conditions can be easily reproduced under test conditions; therefore, the finite difference results can be compared with the analytical solutions to the beam equation.

9.6.1 Experimental calculation of optimum spacings

A cylindrical beam of length 0.5 m and diameter 0.02 m was suspended at each end using light strings to produce the free-free boundary conditions. The beam had standard steel material properties (density $\rho = 7750 \text{ kg m}^{-3}$, Young’s Modulus $E = 200 \text{ GPa}$) and standard geometry (cross section $A = 3.14 \times 10^{-4} \text{ m}^2$, area moment of inertia $I = 7.9 \times 10^{-9} \text{ m}^4$). The response was measured with a single accelerometer at 11 equally spaced nodes ($\{x_1, x_2, \dots, x_{11}\}$) separated by 0.025 m, by striking the beam at node 1 with an impulse hammer, as shown in Fig. 9.8.

In order to calculate the optimum spacing using only experimental data the process depicted in Fig. 9.9 was followed. An experimental modal analysis was carried out on the data set to extract the measured mode shapes (ϕ_{rm}) and natural frequencies (ω_{rm}), from which the eigenvalues were calculated as

$$\lambda_{rm}^4 = \frac{\rho A \omega_{rm}^2}{EI} \quad (9.40)$$

considering only the first five bending modes. This was repeated three times, always replacing the accelerometer so as to include location error in the data, resulting in three modal models. The optimum spacings for the $n = 1$ FD equation

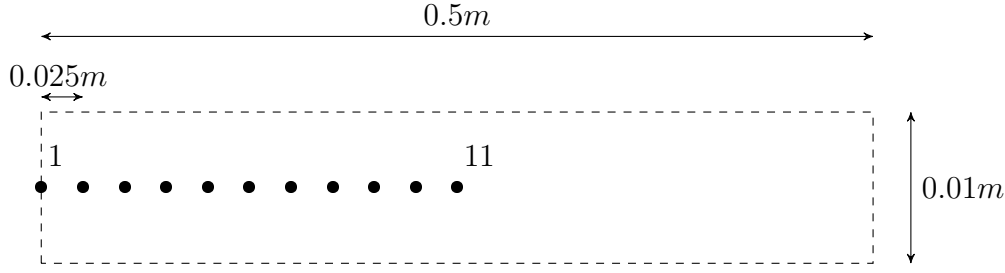


Figure 9.8: A free-free beam of length 0.5 m, diameter 0.01 m, with 11 equally spaced nodes, used for experimental validation of error analysis

were then calculated from the three repetitions, using the following result:

$$\delta_{min}^F \approx \frac{1}{\lambda_r} \sqrt{\frac{4\|2\sigma_r\|}{\|\mu_r\|}} \quad (9.41)$$

giving δ_{min} values of 0.038 m, 0.055 m, 0.056 m, 0.032 m, 0.033 m for the first five modes respectively.

Placing an accelerometer at a location correct to the nearest 0.001 m is difficult in practice, and seeing as the accelerometer has a width of 0.005m, the five optimum spacings were averaged, and a value of 0.04 m used as the optimum spacing for all five modes.

9.6.2 Experimental validation

The experimental data set included measurements at the eleven nodes of interest $\{x_1, x_2, \dots, x_{11}\}$ as well as eleven finite difference nodes $\{x_1 + 0.04 \text{ m}, x_2 + 0.04 \text{ m}, \dots, x_{11} + 0.04 \text{ m}\}$. The following process (outlined in Fig. 9.10) was performed for validation purposes only, and would usually be unnecessary.

From the data set of twenty-two response signals, the measured mode shapes and eigenvalues were extracted, the FD equation applied to the mode shapes to obtain $D_\delta^F \phi_{rm}$, and the eigenvalues were used with the solution to the beam equation to construct an analytical model (ϕ_r , and $\phi_r^{(1)}$). The input error to the finite

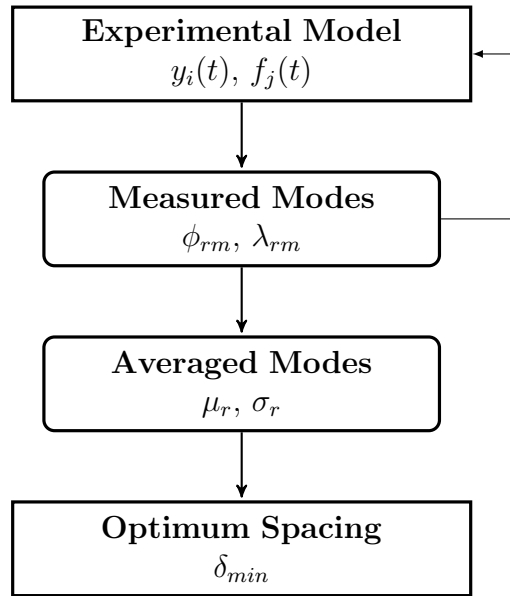


Figure 9.9: Flow chart detailing the experimental process for calculation of optimum spacings

difference equation was calculated as the difference between the measured and analytical modes, whilst the output error was taken as the difference between $D_{\delta}^F \phi_{rm}$ and the analytical rotational modes ($\phi_r^{(1)}$).

In this context, the aim is therefore to minimise the output error, compared to the input error, by adjusting the measurement spacing δ . To compare the optimum spacing with other arbitrary spacings, the process was repeated at four other spacings, 0.005 m, 0.01 m, 0.06 m, and 0.1 m, each time calculating both the input and output errors.

9.6.3 Results and discussion

The results of the experimental validation are presented in Fig. 9.11, which shows the ratio of the output error to the input error averaged over the eleven nodes, for each of the five spacing values. It can be seen that the optimum spacing (or a value close to it) can significantly reduce the error of the finite difference method with non-exact data.

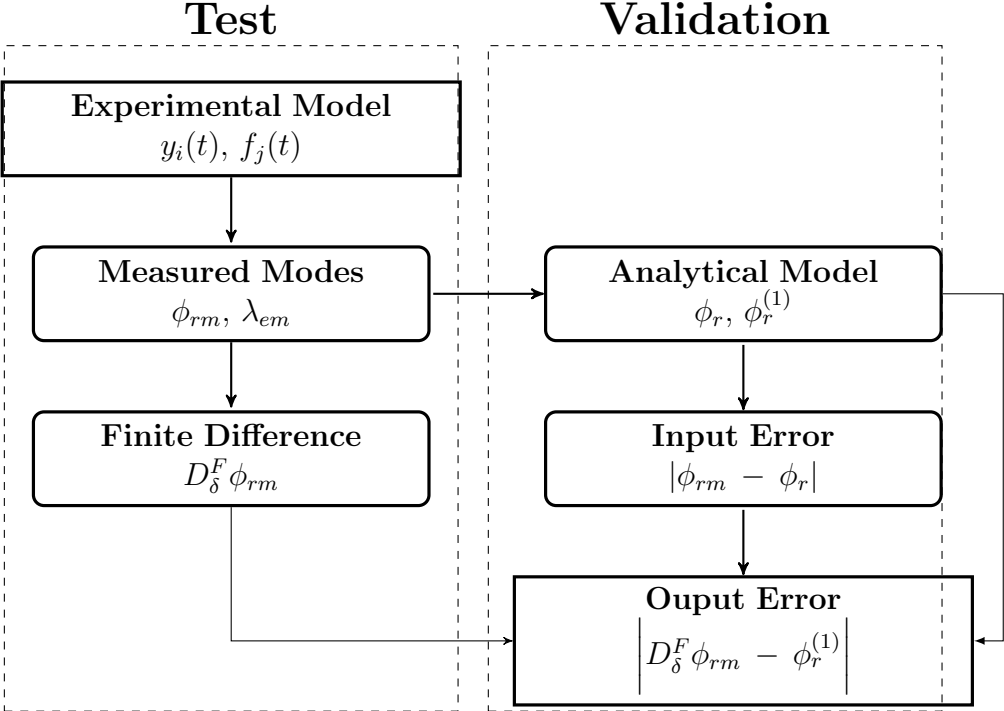


Figure 9.10: Flow chart detailing the process used to experimentally validate error analysis

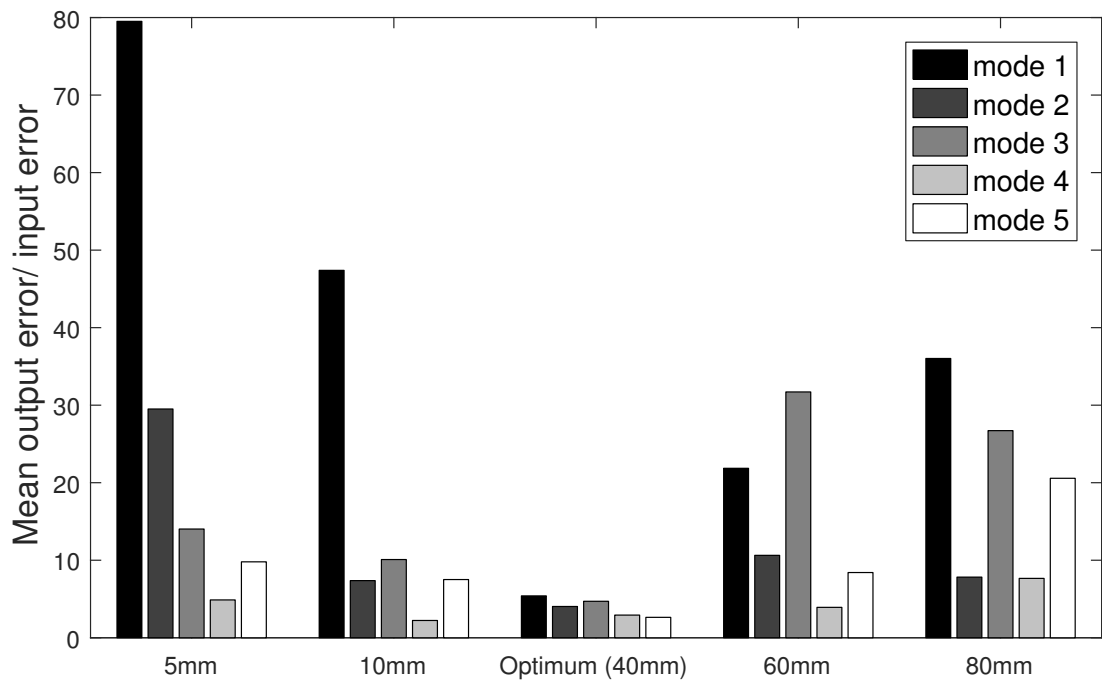


Figure 9.11: Bar chart comparing errors from experimental validation of error analysis at five spacings

Of all the results plotted in Fig. 9.11, there is only one scenario (Mode 4, 0.01m spacing) where the performance was better than that for the optimum spacing. This may be because the correct spacing for this mode was actually calculated to be 0.032 m, or it is also possible that, due to statistical variation in the data, the error for this mode in the 0.01 m spacing experiment was significantly lower than in the others.

9.7 Summary

The initial contribution of this chapter is a generalised error analysis of the finite difference method for rotational degree of freedom synthesis with non-exact data, which, to the author's knowledge, is the first of its kind. By finding bounds on both the truncation error and the propagation error from the perturbed data, it

was shown that as the spacing between data points is reduced the propagation error tends to infinity, whilst as the spacing is increased the truncation error tends to infinity, therefore making the method unstable. Using the error analysis result, the most significant contribution of this chapter was proposed. By balancing the two error terms, a new optimised spacing was proposed to reduce the total error of the method, for both forward/backward and central differences.

For the special case of the $n=3$ forward/backward difference scheme, the optimum spacing can be calculated exactly, assuming perfect knowledge of the mode shapes; whilst for all other finite difference equations, a good approximation can be found, without making any assumptions on the boundary conditions of the beam. Both the exact and approximate optimised spacings were demonstrated in a numerical example (where a perfect modal model can be obtained) of a beam with arbitrary boundary conditions. The results validated the error analysis, showing spacing that for values below the optimum, a propagation error perturbs the solution, whilst above the optimum, it is a truncation error that affects the solution.

The drawback of the proposed method when applied experimentally is that the user has no knowledge of the perfect modes; however, it was shown that by collecting a small set of measurements the measurement accuracy of the finite difference method may be optimised.

As a simple extension to this thesis, the new optimised finite difference method could be applied with the structural modification of tool holder geometry in place of the curve fitting method used throughout this thesis. It has the potential to significantly improve upon the results achieved in this project.

The contribution to knowledge from this chapter stretches beyond the scope of this project. One immediately obvious application of the above method would be to receptance coupling substructure analysis; which, similarly to this project, uses the finite difference method to approximate the rotational degrees of freedom of a

machine tool. Beyond this there are several areas of research within the dynamics field, in which the method could be applied to significantly improve the accuracy of the results.

Chapter 10

Conclusions

10.1 Thesis summary

Chapter 2: Literature Review The first chapter reviewed some of the published literature relevant to this project. Themes such as milling dynamics (and the prediction of milling stability), chatter avoidance methods, and dynamic substructuring were covered.

Chapter 3 : Background

In chapter 3 a brief overview of relevant theory was presented concentrating on structural and machining dynamics, chatter prediction methods (including the average tooth angle and Fourier series approach), as well as structural modification theory.

Chapter 4 : The Effect of Tool Holder Geometry

The observations that inspired this project were validated in chapter 4 . It had been observed in an industrial environment that tool holders from a leading manufacturer were significantly less chatter prone than that of their competitors which had been attributed to the difference in their masses. A set of tool tip frequency response functions were presented that highlighted the substantial effect of tool holder geometry. The ability of tool holder geometry as a chatter avoidance method was verified by comparison to tool stickout length – a variable that has

already been successfully used to avoid chatter.

Chapter 5 : The Effect of Tool Holder Stiffness

Modifying the geometry of a structure results in a change in its mass and stiffness; chapter 5 discussed the individual contributions of these factors when the tool holder geometry is varied. Using a numerical model, the effect of pure mass was compared to that of real mass and it was found that the contribution from the change in stiffness must be included in any modelling or optimisation of tool holder geometry.

Chapter 6 : Structural Modification of Tool Holder Geometry

In chapter 6 the structural modification (SM) method was applied to machining dynamics in order to model and optimise tool holder geometry. The direct SM method was used to successfully model how changes in tool holder diameter effect the tool tip dynamics, and thus the stability of the milling operation. This allows the user to select the most appropriate tool holder from the available selection, using only a single set of data. The inverse SM method was also applied to the same problem. It was shown that, despite the stability of a machining operation being dependent on the dynamics in both x - and y -directions, tool holder geometry may be optimised by applying inverse SM in a single direction.

Chapter 7 :

chapter 7.

Chapter 8 : Cutting Trials

The industrial capability of the prototype tunable tool holder was investigated in chapter 8. To begin, the cutting force model was calibrated with the correct tool

geometry and workpiece material, allowing for accurate stability lobe diagrams (from the mass modification data and standard impact test data) to be calculated. Then, cutting trials were performed to determine the experimental stability of the holder in various configurations. Predictions from the mass modification method were compared to the experimental stability results to show that: firstly, the mass modification method could be used to accurately predict the stability of the prototype in an industrial environment, and secondly, the prototype was capable of shifting the stability lobes to significantly lower spindle speeds.

Chapter 9 : Rotational Degree of Freedom Synthesis

With the potential of tool holder geometry as a chatter avoidance method established, the requirement for highly accurate rotational degree of freedom information becomes apparent. The finite difference method for rotational degree of freedom synthesis is well recognised in the research community, however, a lack of analytical error analysis has limited the methods practicality. Therefore, by performing an error analysis a new optimum spacing was proposed, which balances the two errors inherent in the method, thus limiting the instability of the method when applied to experimental data. The optimised method was then verified using both numerical and experimental data. This method is proposed as a potential improvement on the structural modification of tool holder geometry for chatter avoidance.

10.2 Contributions to knowledge

- This thesis was the first to consider the effect of tool holder geometry on tool tip dynamics. A set of experimental data was presented that showed not only that tool holder diameter has a significant effect on the tool tip FRF, but that its effect is comparable to that of tool stickout length. Therefore one of the contributions to knowledge is the evidence that tool holder geometry may be used as a chatter control method if the correct modelling procedure is developed. This could have significant financial benefits for

the manufacturing industry.

- One of the obstacles in developing such a modelling procedure is the understanding of why a change in geometry at the tool holder can have such a significant effect on the dynamics at the tool tip. The individual contributions of mass and stiffness were compared and it was found that the effect of tool holder geometry is attributable to both mass and stiffness; a contradiction to what had already been suggested by industry.
- Whilst the finite difference method relies on a small data set, the curve fitting method for rotational degree of freedom synthesis used in chapters 6-8 carries the advantage that the resultant mode shapes are continuous in the spatial domain. Therefore, the rotational FRFs may be extracted at any point along the length of the structure. This is particularly beneficial when using the prototype tunable tool holder.
- Direct structural modification theory for the selection of optimum tool holder geometry is a new method of chatter avoidance, which allows the user to select the best tool holder geometry from the available set. The capability of the new method is similar to that of receptance coupling substructure analysis with one important advantage it is not necessary to measure or model the contact parameters that occur at the tool/tool holder interface.
- Inverse structural modification theory for the selection of optimum tool holder geometry is also a new method of chatter avoidance, which allows the user to reassign resonance based on tool holder diameter alone. The user is able to calculate the tool holder geometry that will produce stability lobes at their desired spindle speeds. Therefore allowing the user to maximise the mass removal rate of a given operation by solving a single polynomial. Importantly, it is also unnecessary to measure the interface dynamics and the optimisation can be performed with the inclusion of damping. The simplicity of this method gives it the potential to be a much more efficient method of chatter avoidance than any previously proposed in the published literature.

- [REDACTED]
- Experimental rotational degree of freedom measurement has applications throughout the field of dynamics and beyond. The finite difference method has received particular attention as it does not rely on expensive experimental equipment; however, achieving accurate results can be difficult. A new optimised method has been presented, allowing the user to calculate a measurement spacing which balances the truncation and propagation errors. An experimental investigation showed the potential increase in accuracy when the optimum spacing is applied. The new optimised method has the potential to improve the results presented in this thesis.

10.3 Limitations and future research

Due to the industrial interest in the project, the research presented in this thesis has concentrated on tool holders with the HSKA63 spindle interface and in particular those that use the heat shrink tool clamping technology. Whilst these holders are becoming commonplace in high speed milling, this is a limited subset of the commercial tool holders available to the manufacturing industry. Moreover, within the HSK range, there are a vast array of tool holder geometries, of which a very small set has been considered. A simple, yet important, extension to this work is to demonstrate the ability of tool holder geometry as a chatter avoidance method on a wider variety of commercial tool holders and spindle interfaces. Such holders will always have similar (and most importantly simple) geometries that

are well within the capabilities of the structural modification method.

The method of chatter avoidance by structural modification theory of tool holder geometry has a simple drawback in that the length of the tool holders in consideration must be identical. This limits its effectiveness as the range of holders available to the user are likely to have varying lengths. Any dynamic substructuring method that was used to model or optimise tool holder length, would suffer the same difficulty as the receptance coupling substructure analysis method, in that the properties of the interface between tool and tool holder must be known. Whilst there is no obvious solution at the time of writing, the ability to optimise tool holder length (without measuring the interface properties) may bring with it the ability to optimise tool stickout length, a valuable instrument for the manufacturing community.

[REDACTED]

[REDACTED] chapter 7. [REDACTED]

[REDACTED]

[REDACTED]

chapter 5, [REDACTED]

[REDACTED] chapter 6 [REDACTED]

[REDACTED]

[REDACTED]

[REDACTED]

[REDACTED]

[REDACTED]

[REDACTED]

In chapter 4 the effect of tool holder geometry was shown to be independent of tool stickout length. In the later chapters, the length of the tool was minimised to produce a structure with a single dominant mode. Therefore the structural modification (SM) theory presented in chapter 6 looks at modelling and optimising tool holder geometry with respect to a single mode at around 1000 Hz. As the

tool length is increased, the higher frequency bending modes will become more dominant and must also be accurately predicted by the SM method. It is possible that the truncated numerical models of the modification (\mathbf{B}) (usually with 2 or three nodes) do not consider enough modes for this to be successful. There are two solutions to this problem. Either, include more nodes in both the experimental (\mathbf{H}_A) and numerical(\mathbf{B}) models, which will inherently include more error in the solution. Or, use model reduction methods (such as the Guyan reduction method [127]) to reduce the size of a larger numerical model so that the effect of higher frequency modes may be included.

As touched upon above, one of the long term goals in the machining dynamics field (and the wider engineering domain) is that of automated chatter detection and avoidance methods. A large part of this is the advancement of robotic machining. Robotic milling structures suffer from considerably lower stiffness than traditional milling machines, resulting in highly flexible low frequency modes dominating the tool tip dynamics. It has been shown that the prototype tool holder is capable of significantly reducing the natural frequency of the dominant mode of a milling machine. If a similar technology were applied to robotic milling, it may be possible to shift the frequency of these modes such that they no longer effect the dynamics of high speed milling operations.

The optimised finite difference method for rotational degree of freedom synthesis presented in chapter 9 is applicable in the modal domain only. Modal domain application has the advantage of accuracy; however, the method is not time effective due to requirement for experimental modal analysis. Actually, to produce accurate results experimental modal analysis requires some level of user input, and as the engineering community looks towards fully automated systems, the modal domain application becomes ineffective. As discussed previously, the method has also been applied in the frequency domain, which has the benefit of speed. Therefore optimisation of the frequency domain finite difference method could form a small but valuable future research project.

On a similar note, the optimised method is only applicable to beam and beam-like structures, due to the requirement of analytical knowledge of the mode shapes. The assumptions that underpin the optimised method are also met by Warburton's solution for the mode shapes of rectangular plates [128]. Therefore it is reasonable to suggest that the optimised finite difference method may be extended to include plates (and possibly shells), thus broadening the possible impact of this research.

Appendix A

Finite Element Model

A one dimensional finite element model of an exemplar milling spindle (based on partial knowledge of the Starrag ZT-1000 and Cincinnati FTV5 machines) was constructed using the SDTools finite element toolbox for MATLAB [129]. The geometry of the spindle is given in Table. A.1. The model was then constrained to two degree-of-freedom motion to include one translation and one rotation. The material used in the model includes standard steel (density $\rho = 7750 \text{ kg m}^{-3}$, Young's Modulus $E = 200 \text{ GPa}$) for the spindle and tool holder and tungsten carbide (density $\rho = 15630 \text{ kg m}^{-3}$, Young's Modulus $E = 55 \text{ GPa}$) for the tool. A beam element, called p_{beam} , was used throughout the whole length of the structure, the dynamics of which are based on the Euler-Bernoulli beam solution [105]. A viscous damping model was used with a damping ratio of 0.03 for all modes.

The spindle was supported by four bearings, two near the front and two near the back. Bearing stiffness was introduced using longitudinal spring elements applied at the relevant locations. A simple bearing model was used that considers only the applied preload (the force applied to the bearing to remove axial clearance) as stated in the manufacturer's guidelines. Since the FE model is static, thermal softening effects can be ignored [130] along with any variable preload system [131, 89]. Therefore the following relationship between bearing preload and axial

APPENDIX A. FINITE ELEMENT MODEL

Element No.	Length (mm)	Diameter	Material
1	18	9.6	1
2	18	11.4	1
3	24	12	1
4	25.5	24	2
5	40	24	3
6	28.5	24	3
7	40	24	2
8	4.7	63	3
9	7.2	55	3
10	14.1	63	3
11	16	64.95	3
12	40.5	64.95	3
13	26	64.95	3
14	9	64.95	3
15	7.77	75	3
16	6.11	65.36	3
17	6.11	55.72	3
18	213	46.08	3
19	7.5	40.01	3
20	30	40.01	3
21	17.5	40.01	3
22	22.5	38	3
23	20	30	3
24	7.5	27	3

Table A.1: Geometry of exemplar finite element model spindle/holder/tool structure. Material key: 1= Tungsten Carbide, 2= Effective Material, 3= Steel.

and radial stiffness (as outlined in [132] and further updated in [133]) is used:

$$\begin{aligned}k_a &= c_a \times 10^6 P_a^{1/3} B^{2/3} \sin^{5/3}(\beta) D^{1/3} && (\text{N/mm}) \\k_r &= 0.64 k_a \cot(\beta) && (\text{N/mm})\end{aligned}\tag{A.1}$$

where k_a is the axial stiffness, k_r is the radial stiffness, c_a is an empirically determined constant (specified by the bearing manufacturer), P_a is the axial preload (N), B is the number of balls, β is the contact angle, and D is the ball diameter (mm). This gave values of $k_a = 84 \times 10^5$, $k_r = 169 \times 10^5$ for the front two bearings and $k_a = 14 \times 10^6$, $k_r = 28 \times 10^6$ for the back two bearings.

Then a modal analysis can be performed using the Lanczos numerical solver [134]. A convergence study was performed by dividing the course mesh into ever finer elements until the natural frequency solution converged. Once an accurate modal model had been found, it was converted into the frequency domain as discussed in chapter 3, to find the tool tip FRF.

The MATLAB script used to generate the finite element model is given below.

MATLAB script

1D Finite Element Model

This file imports the geometry of the exemplar spindle as well as tool holder and tool and exports the tool-tip FRF

```
freq=(0:0.1:5000); % frequency in Hz
fil=[0 0 0];
dir=[1 0 0];

% Load geometry from xls file
% [length(mm) Node1(m) Node 2(m) Diameter (mm) Radius (m) Mat]
geom=xlsread('filename');
```

Generate Basic Mesh

Using imported geometry of spindle, tool holder, and tool generate a sparse mesh that captures changes in diameter along length of structure

```
model.Node=[(1:size(geom,1)+1)' zeros(size(geom,1)+1,3) ...  
[geom(:,5);geom(end,6)] zeros(size(geom,1)+1,2)];  
  
model.Elt=[Inf abs('beam1') 0 ; (1:size(geom,1))' ...  
(2:size(geom,1)+1)' geom(:,7) (1:size(geom,1))' ...  
ones(size(geom,1),1) zeros(size(geom,1),2)];  
  
model=fe_case(model,'FixDof','2-D motion',[.01 .03 .04 .05]');
```

Define Material Properties

Add material properties material 1= Tungsten Carbide 2= effective material 3=steel

```
model.pl=[3 fe_mat('m_elastic','SI',1) 5.5e11 0.22 15630 2.43E11;  
2 fe_mat('m_elastic','SI',1) 3.1200e+11 0.28 1.033e+04 1.33e+11;  
1 fe_mat('m_elastic','SI',1) 1.93e11 0.3 7800 0];
```

Define Element Type and Geometry

Input the various beam diameters from geom file to the p_beam element. The p_beam element is based on Euler-Bernoulli beam solution

```
for i=4:length(geom)  
    beam_probs=['dbval ',num2str(i),' circle ',num2str(geom(i,4)/2)];  
    model.il=p_beam(model.il,beam_probs);  
end
```

Define Boundary Conditions (Bearings)

Front bearings at nodes 7 and 10 ($k_a=84e5$, $k_r=169e5$) Back bearings at nodes 15 and 18 ($k_a=140e5$, $k_r=280e5$)

```

model=feutil('AddElt',model,'celas', ...
    [7 0 23 0 100 0 0; 7 0 12 0 101 0 0;7 0 13 0 101 0 0]);
model=feutil('AddElt',model,'celas', ...
    [10 0 23 0 100 0 0; 10 0 12 0 101 0 0;10 0 13 0 101 0 0]);
model=feutil('AddElt',model,'celas', ...
    [15 0 23 0 200 0 0; 15 0 12 0 201 0 0;15 0 13 0 201 0 0]);
model=feutil('AddElt',model,'celas', ...
    [18 0 23 0 200 0 0; 18 0 12 0 201 0 0;18 0 13 0 201 0 0]);
model.il=p_spring(model.il,'dbval 101 ...
    169e5','dbval 100 84e5','dbval 201 280e5','dbval 200 140e5');

```

Create Fine Mesh

Divide the sparse mesh to create fine mesh based on results of convergence study

```
model=feutil('Divide 5',model);
```

Perform Modal Analysis

solve for modal model using the Lanczos solver which allows for specification of frequency band of interest (in Hz)

```

InDof=1.02;OutDof=1.02';
model=fe_case(model,'DofLoad','Force',InDof,'SensDof','Sensors',OutDof);
model=stack_set(model,'info','Freq',freq);
modal_model=fe_eig(model,[2 15 1e3 0 1e-5]);

```

Convert Modal Modal into Frequency Domain

```
tooltip_frf=nor2xf(modal_model,model,'dis Hz');
```


Appendix B

Finite Difference Tables

n=1	Formula	Accuracy	$\sum a_k $	T
Backward	$\frac{\phi(x) - \phi(x-\delta)}{\delta}$	$O(\delta)$	2	1/2
Forward	$\frac{\phi(x+\delta) - \phi(x)}{\delta}$	$O(\delta)$	2	1/2
Central	$\frac{\phi(x+\delta) - \phi(x-\delta)}{2\delta}$	$O(\delta^2)$	1	1/6

Table B.1: Finite difference formulae with coefficients for optimisation for $n = 1$ points

n=2	Formula	Accuracy	$\sum a_k $	T
Backward	$\frac{3\phi(x) - 4\phi(x-\delta) + \phi(x-2\delta)}{2\delta}$	$O(\delta^2)$	4	1/3
Forward	$\frac{-3\phi(x) + 4\phi(x+\delta) - \phi(x+2\delta)}{2\delta}$	$O(\delta^2)$	4	1/3
Central	$\frac{-\phi(x+2\delta) + 8\phi(x+\delta) - 8\phi(x-\delta) + \phi(x-2\delta)}{12\delta}$	$O(\delta^4)$	3/2	1/30

Table B.2: Finite difference formulae with coefficients for optimisation for $n = 2$ points

n=3	Formula	Accuracy	$\sum a_k $	T
Backward	$\frac{11\phi(x)-18\phi(x-\delta)+9\phi(x-2\delta)-2\phi(x-3\delta)}{6\delta}$	$O(\delta^3)$	20/3	1/4
Forward	$\frac{-11\phi(x)+18\phi(x+\delta)-9\phi(x+2\delta)+2\phi(x+3\delta)}{6\delta}$	$O(\delta^3)$	20/3	1/4
Central	(\star)	$O(\delta^6)$	5/3	1/150

Table B.3: Finite difference formulae with coefficients for optimisation for $n = 3$ points

$$(\star) \frac{\phi(x + 3\delta) - 9\phi(x + 2\delta) + 45\phi(x + \delta) - 45\phi(x - \delta) + 9\phi(x - 2\delta) - \phi(x - 3\delta)}{60\delta}$$

Appendix C

Experimental Sheet

Experiment Sheet



Advanced Manufacturing Research Centre



Project No:	AE006	Operator:	TBC
Start Date:	19.10.2016	End Date:	25.10.2016
Document Number:	AE006-AMRC-160725-01	Associated Documents:	N/A

Aims and Objectives of the Experiment:

- Experimental validation of tuneable tool holder
- Experimental validation of structural modification theory
- Cutting Coefficient identification tests (mechanistic model)
- Stability verification using stair-case workpiece machining

Machine(s) and/or Equipment:	Material(s):
<p>Cincinnati FTV5 (21,000rpm) Kistler 9255B large plate dynamometer (KTC Green Kit) Haimer tool balancer Haimer Balancing Rings/Screws IDC Impact Test Kit D12 Short tool (Sandvik 2P121-1200-NC H10F)</p> <ul style="list-style-type: none"> • http://www.sandvik.coromant.com/en-gb/products/Pages/productdetails.aspx?c=2p121-1200-nc+h10f <p>Prototype tuneable tool holder + collars Sandvik D20 milling tool – For surface preparation 2P120-2000-NC H10F Bilz D20 Shrink fit holder (TH14 – Dynamic inventory)</p>	<p>AL6082 blocks (machined to fit on Kistler 9255B) x1 Block to be machined as stair case feature on FTV5</p>

Method:

All tests will be repeated for selected tools

Selected tools for the test:

D12 Short tool (Sandvik 2P121-1200-NC H10F)

I. Balancing of the tools (completed 19/09/2016)

- a. Mount the tools to the shrink fit tuneable tool holder – with longest possible overhang (check with short tool)
- b. Measure the tool run-out after mounting tools; IF run-out is high (>10um), reattach the tool in a different orientation until desired low run-out is achieved (FTV5 spindle measures high runout)
- c. Balance the tools on the Haimer balancer (in FOF) using balancing screws and/or rings
 - Maximum allowable residual unbalance for G2.5 grade holders is ~1.6um for 16,000rpm (Appendix □)

II. Mode shape measurement (completed 19/09/2016)

Nomenclature

G_{ij} | Transfer function measured by hitting at the j^{th} point and output measured from i^{th} point

- a. Measure G_{15-Gx5} where point 1 is located at the tool tip, point 5 at the tip of the tool holder, and x is number of locations required to fully capture the mode shapes (10mm spacing).
- b. Experimental modal analysis (curve fitting) using sdttools structural dynamics toolbox in MATLAB, extraction of mode shapes.

III. Rotational FRF synthesis/ Structural Modification (completed 19/09/2016)

- a. Fit 3rd order polynomials to measured translational mode shapes in MATLAB

Issue	Date	Author	Quality Review	Technical Authorisation	Reason for Change
1	25.07				Draft 02

Experiment Sheet

Project No:	AE006	Operator:	TBC
Start Date:	19.10.2016	End Date:	25.10.2016
Document Number:	AE006-AMRC-160725-01	Associated Documents:	N/A



Advanced Manufacturing Research Centre



- b. Differentiate polynomials to get rotational mode shapes
- c. Construct rotational FRFs using experimental modal data
- d. Apply structural modification theory to measured data to predict tool tip FRFs for holder with various collar setups

IV. Stability diagram generation (completed 19/09/2016)

- a. Generate the stability diagram in CutPro for the selected tool using FRF measurements
 - Half immersion milling up milling (6mm width)
 - Meet to discuss the results and decide on process to be tested
- b. Identify the absolute stability limit and maximum stable speed/depth
- c. Adjust the stair case feature CAD (step height, step count, step length and starting depth) according to the SLD
- d. Decide on the spindle speed range and increments to be tested

V. Check FRF measurements

- a. Double check tool-tip FRF measurements on day of cutting

VI. Preparation of the staircase block & cutting test

- a. Mount the dynamometer to the machine tool tomb stone
- b. Clock the dynamometer to achieve <100um/250mm parallelism
- c. Mount the workpiece using 6x M8 bolts
- d. Establish connection of the large plate dynamometer according to **Appendix B**
- e. Update the NX CAM according to (III)
 - CAM file: "K:\machining_dynamics\1_ACTIVE PROJECTS\ADG195 - Rotating FRF measurements\Drawings\StairCase"
 - D20 Sandvik tool will be used for the preparation
 - 12000PRM, 0.075mm/tooth (1800mmrpm)
 - Coolant on (M08)
 - ~32 minute machining time (for 15 steps, 17.33mm length, 1mm height)
- f. Post-process the operation with AMRC Post Master (install from *K:\common\Post Master*)
- g. Put D20 Sandvik tool mounted on Bilz shrink fit to the magazine
- h. Machine the part to stair case form

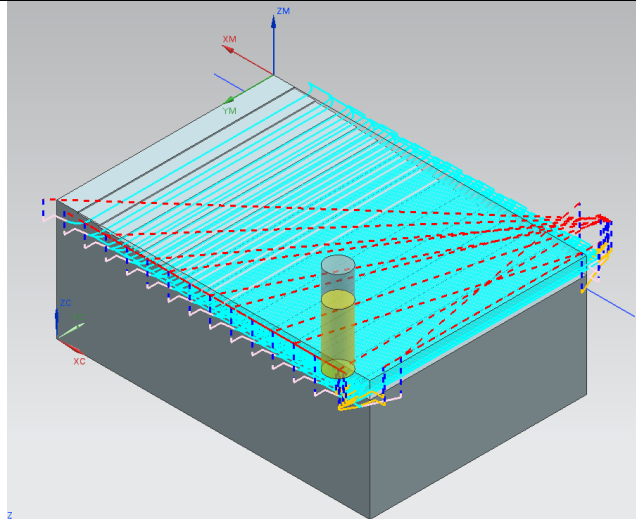
Issue	Date	Author	Quality Review	Technical Authorisation	Reason for Change
1	25.07				Draft 02

Experiment Sheet

Project No:	AE006	Operator:	TBC
Start Date:	19.10.2016	End Date:	25.10.2016
Document Number:	AE006-AMRC-160725-01	Associated Documents:	N/A

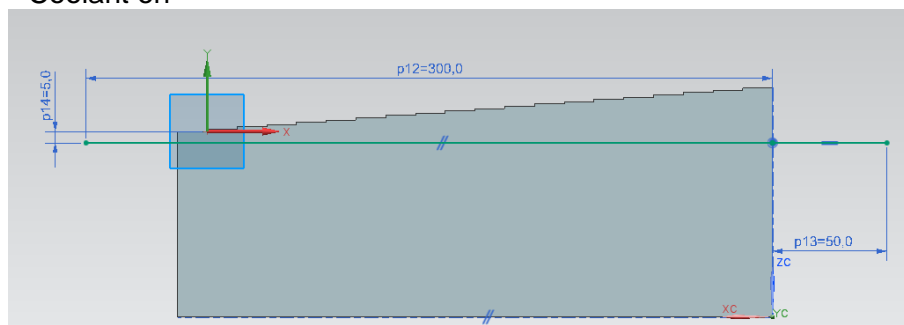


Advanced Manufacturing Research Centre



VII. Stability cutting tests

- Prepare a test table for the test where following will be recorded
 - $a_{p\text{start}}$ (starting depth), $a_{p\text{max}}$ (maximum depth at the end), a_e (radial depth) =6mm
 - Feed/tooth 0.05mm/tooth
 - Spindle speed 5000 rpm – 15000rpm
 - Feed 500-1500 mm/min
 - Process audio response peak frequency (Hz) & magnitude (Pa)
 - Tooth pass frequency (Hz)
 - F_x and F_y maximum cutting forces (N)
 - Force peak frequency with FFT analysis in KistlerDynoware
 - Surface assessment (stable OR chatter)
- (IF POSSIBLE)** Attach the PCB discretional microphone to an articulated arm on magnetic base and mount the assembly to the machine side wall
- Load the single line tool path program to the NC
 - 50mm start/end extension with respect to the part
 - 5mm depth start as default
 - Coolant on



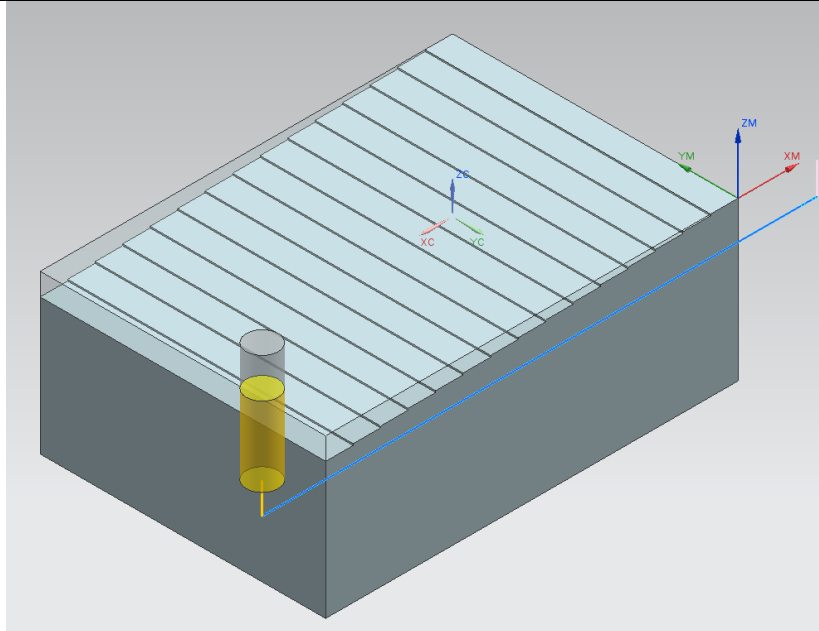
Issue	Date	Author	Quality Review	Technical Authorisation	Reason for Change
1	25.07				Draft 02

Experiment Sheet

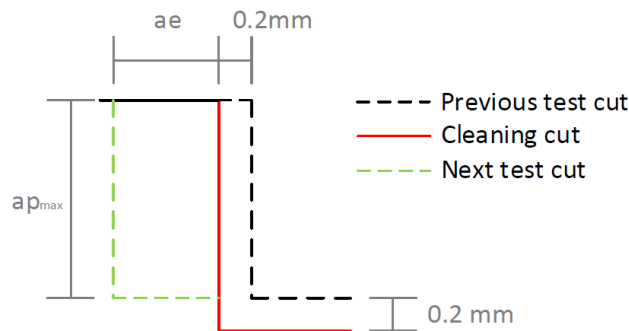
Project No:	AE006	Operator:	TBC
Start Date:	19.10.2016	End Date:	25.10.2016
Document Number:	AE006-AMRC-160725-01	Associated Documents:	N/A



Advanced Manufacturing Research Centre



- d. Put required Z (to change axial depth) and X (to change radial depth and cut start location) on the NC window – NC program will not be altered
- e. Record data during cutting
 - Cutting force (Kistler Dynoware software)
 - Audio output data (CutPro MALDAQ module)
- f. Take picture of the machine surface to distinguish step where chatter starts (exemplary picture below – chatter occurred at 15mm DoC)
- g. “Cleaning cut”: Machine the test surface using D20 Sandvik tool by removing +0.2 radial depth and +0.2 axial depth, as demonstrated below.
 - 12000 rpm, 0.15 mm/tooth (3600mmpm)



Issue	Date	Author	Quality Review	Technical Authorisation	Reason for Change
1	25.07				Draft 02

Experiment Sheet

Project No:	AE006	Operator:	TBC
Start Date:	19.10.2016	End Date:	25.10.2016
Document Number:	AE006-AMRC-160725-01	Associated Documents:	N/A

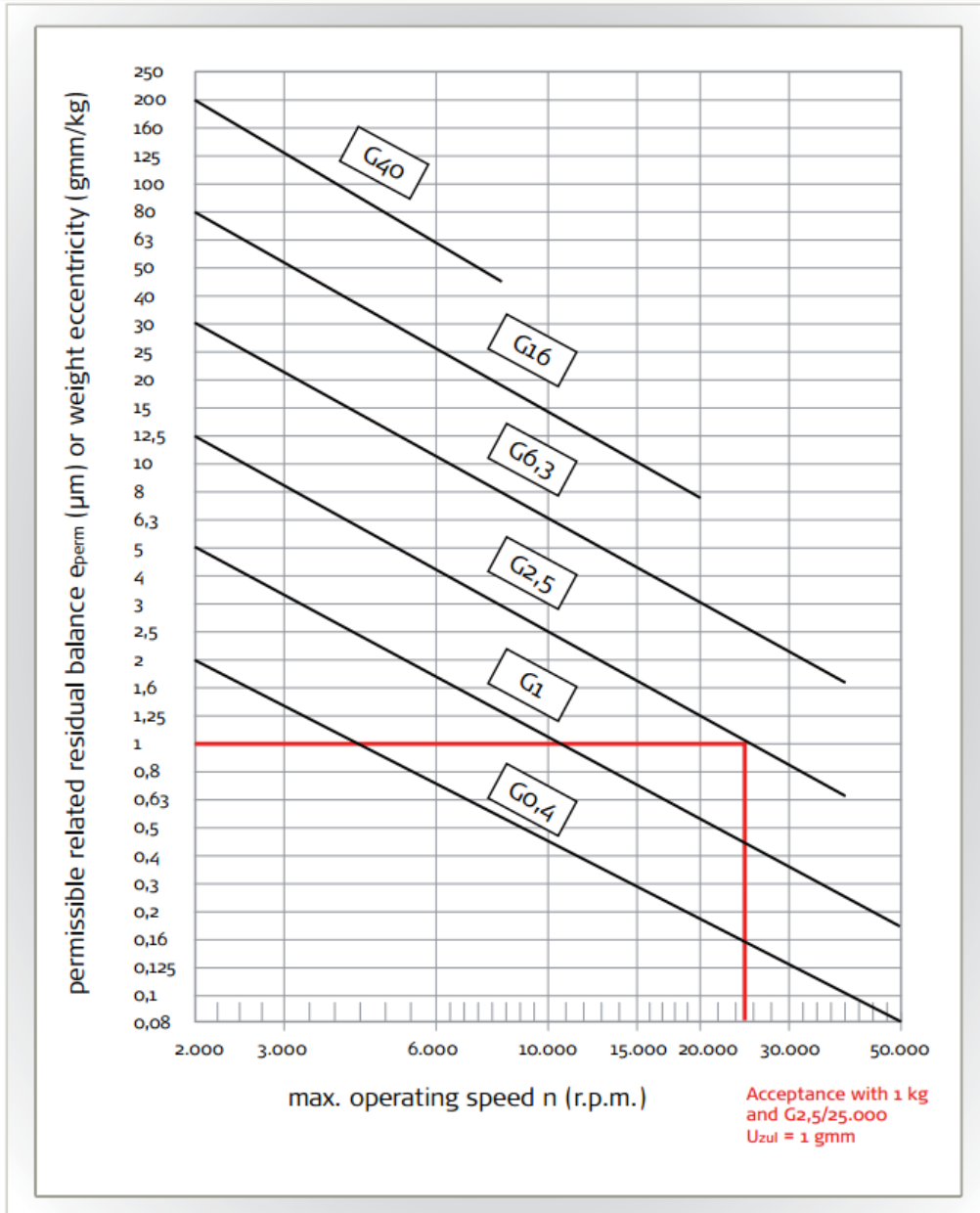


Advanced Manufacturing Research Centre



Appendix A – Maximum permissible residual unbalance

http://www.hornusa.com/fileadmin/user_upload/usa/PDF/Other-Catalogs/KFAHRIONUS - Technical Info - 2015.pdf



Issue	Date	Author	Quality Review	Technical Authorisation	Reason for Change
1	25.07				Draft 02

Experiment Sheet

Project No:	AE006	Operator:	TBC
Start Date:	19.10.2016	End Date:	25.10.2016
Document Number:	AE006-AMRC-160725-01	Associated Documents:	N/A



Advanced Manufacturing Research Centre



Appendix B – Kistler 9255B Dynamometer connection and software setup

- a. Connect the dynamometer cable to the 8 channel charge amplifier (Kistler Type 5070Ax11xx).
- b. Connect the charge amplifier to the Kistler DAQ system using RS232 and serial cable.
- c. Launch Kistler DynoWare software, click on *Hardware*, adjust:
 - i. Hardware – 5070
 - ii. 5070 version – 8 channel
 - iii. Sensitivities of the channels – Check, dynamometer calibration document
 - iv. Ranges of the channels – 2000N each (estimated, may be changed during test)
 - v. RS232C Setup – Set COM3 as default, check.
 - vi. Force & Moment calculation > Multi Component Mode – Type 1a for 8 channel Amplifier
- d. Under *Hardware* window, send adjusted parameters to the charge amplifier. Check for command to go through the charge amplifier screen.
- e. In Kistler DynoWare software, click *Edit*, adjust:
 - i. Sampling Rate = $RPS * 100$
 - ii. Measure time = $(LengthOfCut / Feed) * SamplingRate$
 - iii. Save
- f. Record a sample measurement by tapping on the dynamometer with soft hammer at each direction one by one (2 times in X, 3 times in Y, 4 times in Z and push in Z). Check for correct signal recording.

Issue	Date	Author	Quality Review	Technical Authorisation	Reason for Change
1	25.07				Draft 02

Bibliography

- [1] J. E. Mottershead and Y. M. Ram, “Inverse eigenvalue problems in vibration absorption: Passive modification and active control,” *Mechanical Systems and Signal Processing*, vol. 20, no. 1, pp. 5 – 44, 2006.
- [2] S. S. Sattinger, “A Method for Experimentally Determining Rotational Mobilities,” *The Journal of the Acoustical Society of America*, vol. 64, no. 6, pp. 1734–1764, 1978.
- [3] J. Tlustý and M. Polaceki, “The stability of machine tools against self-excited vibration in machining,” *International research in production engineering, ASME*, pp. 465–474, 1963.
- [4] S. A. Tobias and W. Fiswick, “Theory of regenerative machine tool chatter,” *The Engineer*, 1958.
- [5] Y. Altintas and M. Weck, “Chatter stability of metal cutting and grinding,” *CIRP Annals-Manufacturing Technology*, vol. 53, no. 2, pp. 619–642, 2004.
- [6] G. Quintana and J. Ciurana, “Chatter in machining processes: A review,” *International Journal of Machine Tools and Manufacture*, vol. 51, no. 5, pp. 363–376, 2011.
- [7] J. Tlustý, *Manufacturing Processes and Equipment*. Prentice Hall, 2000.
- [8] R. Sridhar, R. E. Hohn, and G. W. Long, “A stability algorithm for the general milling process,” *Journal of Engineering for Industry*, vol. 90, pp. 330–334, 1968.

BIBLIOGRAPHY

- [9] J. Tlusty, W. Zaton, and F. Ismail, “Stability lobes in milling,” *CIRP Annals – Manufacturing Technology*, vol. 32, pp. 309 – 313, 1983.
- [10] S. Smith and J. Tlusty, “Update on high-speed milling dynamics,” *Journal for Engineering for Industry*, vol. 112, no. 2, pp. 142–149, 1990.
- [11] S. Smith and J. Tlusty, “An overview of modeling and simulation of the milling process,” *Journal of engineering for industry*, vol. 113, no. 2, pp. 169–175, 1991.
- [12] I. Minis and B. Yanushevsky, “A new theoretical approach for the prediction of machine tool chatter in milling,” *Journal of engineering for industry*, vol. 115, p. 1, 1993.
- [13] Y. Altıntaş and E. Budak, “Analytical prediction of stability lobes in milling,” *CIRP Annals-Manufacturing Technology*, vol. 44, pp. 357–362, 1995.
- [14] Y. Altintas and E. Budak, “Analytical prediction of chatter stability in millingpart I: general formulation,” *Journal of Dynamic Systems, Measurement, and Control*, vol. 120, no. 1, pp. 25–31, 1998.
- [15] Y. Altintas and E. Budak, “Analytical prediction of chatter stability in millingpart II: application of the general formulation to common milling systems,” *Journal of Dynamic Systems, Measurement, and Control*, vol. 120, no. 1, pp. 31–36, 1998.
- [16] T. Insperger, “Full-discretization and semi-discretization for milling stability prediction: Some comments,” *International Journal of Machine Tools and Manufacture*, vol. 50, no. 7, pp. 658–662, 2010.
- [17] T. Insperger and G. Stépán, “Semi-discretization method for delayed systems,” *International Journal for numerical methods in engineering*, vol. 55, no. 5, pp. 503–518, 2002.
- [18] T. Insperger and G. Stépán, “Updated semi-discretization method for periodic delay-differential equations with discrete delay,” *International Journal for Numerical Methods in Engineering*, vol. 61, no. 1, pp. 117–141, 2004.

- [19] T. Insperger, G. Stépán, P. Bayly, and B. Mann, “Multiple chatter frequencies in milling processes,” *Journal of Sound and Vibration*, vol. 262, no. 2, pp. 333–345, 2003.
- [20] J. Wang and K. Lee, “Suppression of chatter vibration of a CNC machine centre—an example,” *Mechanical Systems and Signal Processing*, vol. 10, no. 5, pp. 551–560, 1996.
- [21] E. Marui, S. Ema, M. Hashimoto, and Y. Wakasawa, “Plate insertion as a means to improve the damping capacity of a cutting tool system,” *International Journal of Machine Tools and Manufacture*, vol. 38, no. 10, pp. 1209–1220, 1998.
- [22] S. Semercigil and L. Chen, “Preliminary computations for chatter control in end milling,” *Journal of Sound and vibration*, vol. 249, no. 3, pp. 622–633, 2002.
- [23] N. H. Kim, D. Won, and J. C. Ziegert, “Numerical analysis and parameter study of a mechanical damper for use in long slender endmills,” *International Journal of Machine Tools and Manufacture*, vol. 46, no. 5, pp. 500–507, 2006.
- [24] N. D. Sims, “Vibration absorbers for chatter suppression: A new analytical tuning methodology,” *Journal of Sound and Vibration*, vol. 301, no. 35, pp. 592 – 607, 2007.
- [25] C. Anderson, S. Semercigil, and F. Turan, “A passive adaptor to enhance chatter stability for end mills,” *International Journal of Machine Tools and Manufacture*, vol. 47, no. 11, pp. 1777 – 1785, 2007.
- [26] Y. Altintas, S. Engin, and E. Budak, “Analytical stability prediction and design of variable pitch cutters,” *Journal of Manufacturing Science and Engineering*, vol. 121, no. 2, pp. 173–178, 1999.
- [27] E. Budak, “An analytical design method for milling cutters with nonconstant pitch to increase stability, part I: theory,” *Journal of manufacturing science and engineering*, vol. 125, no. 1, pp. 29–34, 2003.

- [28] E. Budak, “An analytical design method for milling cutters with nonconstant pitch to increase stability, part IIS: application,” *Journal of manufacturing science and engineering*, vol. 125, no. 1, pp. 35–38, 2003.
- [29] S. Turner, D. Merdol, Y. Altintas, and K. Ridgway, “Modelling of the stability of variable helix end mills,” *International Journal of Machine Tools and Manufacture*, vol. 47, no. 9, pp. 1410–1416, 2007.
- [30] A. R. Yusoff and N. D. Sims, “Optimisation of variable helix tool geometry for regenerative chatter mitigation,” *International Journal of Machine Tools and Manufacture*, vol. 51, no. 2, pp. 133–141, 2011.
- [31] A. Ertürk, E. Budak, and H. Özgüven, “Selection of design and operational parameters in spindle–holder–tool assemblies for maximum chatter stability by using a new analytical model,” *International Journal of Machine Tools and Manufacture*, vol. 47, pp. 1401–1409, 2007.
- [32] A. Ertürk, H. Özgüven, and E. Budak, “Effect analysis of bearing and interface dynamics on tool point FRF for chatter stability in machine tools by using a new analytical model for spindle tool assemblies,” *International Journal of Machine Tools and Manufacture*, vol. 47, pp. 23–32, 2007.
- [33] S. Park, Y. Altintas, and M. Movahhedy, “Receptance coupling for end mills,” *International journal of machine tools and manufacture*, vol. 43, pp. 889–896, 2003.
- [34] I. Bucher and S. Braun, “The structural modification inverse problem: an exact solution,” *Mechanical Systems and Signal Processing*, vol. 7, no. 3, pp. 217–238, 1993.
- [35] D. de Klerk, D. J. Rixen, and S. Voormeeren, “General framework for dynamic substructuring: history, review and classification of techniques,” *AIAA Journal*, vol. 46, no. 5, pp. 1169–1181, 2008.
- [36] P. Ragnarsson, B. Pluymers, S. Donders, and W. Desmet, “Subcomponent modelling of input parameters for statistical energy analysis by using a

- wave-based boundary condition,” *Journal of Sound and Vibration*, vol. 329, no. 1, pp. 96–108, 2010.
- [37] M. L. M. Duarte and D. J. Ewins, “Some insights into the importance of rotational degrees-of-freedom and residual terms in coupled structure analysis,” in *Proceedings of the Thirteenth International Modal Analysis Conference*, 1995.
- [38] W. Duncan, “The admittance method for obtaining the natural frequencies of systems,” *Philosophical Magazine*, vol. 32, no. 214, pp. 401–409, 1941.
- [39] J. Crowley, A. Klosterman, G. Rocklin, and H. Vold, “Direct Structural Modification Using Frequency Response Functions,” in *Proceedings of the International Modal Analysis Conference & Exhibit*, vol. 1, pp. 58–65, 1984.
- [40] B. Jetmundsen, R. L. Bielawa, and W. G. Flannelly, “Generalized Frequency Domain Substructure Synthesis,” *Journal of the American Helicopter Society*, vol. 33, no. 1, pp. 55–64, 1988.
- [41] J. Gordis, R. Bielawa, and W. Flannelly, “A general theory for frequency domain structural synthesis,” *Journal of Sound and Vibration*, vol. 150, no. 1, pp. 139–158, 1991.
- [42] J. Gordis, “Structural synthesis in the frequency domain: a general formulation,” in *Proceedings of the Thwelth International Modal Analysis Conference*, pp. 587–581, 1994.
- [43] Y. Ren and C. Beards, “On substructure synthesis with FRF data,” *Journal of Sound and Vibration*, vol. 185, no. 5, pp. 845–866, 1995.
- [44] J. T. Weissenburger, “Effect of Local Modifications on the Vibration Characteristics of Linear Systems,” *Journal of Applied Mechanics*, vol. 35, no. 2, p. 327, 1968.
- [45] R. Pomazal and V. Snyder, “Local Modifications of Damped Linear Systems,” *AIAA Journal*, vol. 9, no. 11, pp. 2216–2221, 1971.

BIBLIOGRAPHY

- [46] J. Hallquist and S. V., “Synthesis of two discrete vibratory systems using eigenvalue modification,” *AIAA journal*, vol. 11, no. 2, pp. 247–249, 1973.
- [47] O’Callahan, J. C. and Chou, C. M., “Structural dynamics modification using generalized beam mass and stiffness,” in *Proceedings of the 3rd International Conference on Noise and Vibration Engineering*, pp. 447–482, 1985.
- [48] A. Kyprianou, J. E. Mottershead, and H. Ouyang, “Assignment of natural frequencies by an added mass and one or more springs,” *Mechanical Systems and Signal Processing*, vol. 18, no. 2, pp. 263–289, 2004.
- [49] H. N. Özgüven, “Structural modifications using frequency response functions,” *Mechanical Systems and Signal Processing*, vol. 4, no. 1, pp. 53–63, 1990.
- [50] J. V. Ferreira and D. J. Ewins, “Multi-harmonic nonlinear receptance coupling approach,” in *Proceedings of the Fifteenth International Modal Analysis Conference*, pp. 27–33, 1997.
- [51] D. Ewins, *Modal testing: theory, practice, and application*. Mechanical engineering research studies: Engineering dynamics series, Research Studies Press, 2000.
- [52] D. Poole, *Linear Algebra: A Modern Introduction*. Thomson Brooks/Cole, 2006.
- [53] M. Imregun and D. Robb, “Structural modification via FRF coupling using measured data,” in *Proceedings of the tenth international modal analysis conference*, pp. 1095–1099, 1992.
- [54] T. Carne and C. Dohrmann, “Improving experimental frequency response function matrices for admittance modeling,” in *Proceedings of the Nineteenth International Modal Analysis Conference*, 2006.
- [55] R. L. Mayes and E. C. Stasiunas, “Combining Lightly Damped Experimental Substructures with Analytical Substructures,” in *Proceedings of the Twentyfifth International Modal Analysis Conference*, 2007.

- [56] M. L. M. Duarte and D. J. Ewins, “High-frequency pseudo-mode approximation for the high-frequency residual terms,” in *proceedings of the fourteenth international modal analysis conference*, pp. 261–266, 1996.
- [57] M. L. M. Duarte and D. J. Ewins, “Improved experimental component mode synthesis with residual compensation based purely on experimental results,” in *proceedings of the fourteenth international modal analysis conference*, 1996.
- [58] M. L. M. Duarte and D. J. Ewins, “Rotational degrees of freedom for structural coupling analysis via finite-difference technique with residual compensation,” *Mechanical Systems and Signal Processing*, vol. 14, no. 2, pp. 205–227, 2000.
- [59] T. R. Licht, “Angular vibration measurements transducers and their configuration,” in *Proceedings of the Fourth International Modal Analysis Conference*, pp. 503–506, 1985.
- [60] R. A. L. Rorrer, A. L. Wicks, and J. Williams, “Angular acceleration measurements of a freefree beam ,” in *Proceedings of the Seventh International Modal Analysis Conference*, pp. 1300–1304, 1989.
- [61] B. Bill and A. Wicks, “Measuring simultaneously translational and angular acceleration with the new translational-angular-piezobeam (tap) system,” *Sensors and Actuators A: Physical*, vol. 21, no. 1, pp. 282 – 284, 1990.
- [62] D. R. Laughlin, A. Ardaman, and H. R. Sebesta, “Inertial angular rate sensors: theory and applications,” *Sensors*, pp. 20–24, 1992.
- [63] M. A. Stebbins, J. R. Blough, S. J. Shelley, and D. L. Brown, “Measuring and including the effects of moments and rotations for the accurate modeling of transmitted forces,” in *Proceedings of the fourteenth International Modal Analysis Conference*, pp. 429–436, 1996.
- [64] M. Bello, M. Sestieri, W. D’Ambrogio, and F. L. A. Gala, “Development of a rotational transducer based on bimorph PZTs,” *Mechanical Systems and Signal Processing*, vol. 17, no. 5, pp. 1069 – 1081, 2003.

BIBLIOGRAPHY

- [65] D. Oliver, “Non-contact vibration imager for wide range of component sizes and displacement amplitudes,” in *Proceedings of the Sixth International Modal Analysis Conference*, pp. 629–638, 1988.
- [66] J. Cafeo, M. Trethewey, J. Rieker, and H. Sommer, “Application of a three degree of freedom laser vibrometer for experimental modal analysis,” in *Proceedings of the Ninth International Modal Analysis Conference*, pp. 1161–1167, 1993.
- [67] E. H. Bockelberg, J. Trethewey, H. Sommer, and C. H. Chu, “Simultaneous measurement of six coordinate vibration: three translations and three rotations ,” in *Proceedings of the Eleventh International Modal Analysis Conference*, pp. 552–562, 1993.
- [68] M. Trethewey, H. Sommer, and J. Cafeo, “A dual beam laser vibrometer for measurement of dynamic structural rotations and displacements,” *Journal of Sound and Vibration*, pp. 67–84, 1993.
- [69] M. Ratcliffe and N. Lieven, “Measuring rotations using a laser Doppler vibrometer,” in *Proceedings of the Twentieth-Fourth International Modal Analysis Conference*, pp. 1002–1008, 1996.
- [70] J. Bell and S. Rothberg, “Rotational vibration measurements using laser Doppler vibrometry: comprehensive theory and practical application,” *Journal of Sound and Vibration*, pp. 673–690, 2000.
- [71] S. Rothberg and J. Bell, “On the application of laser vibrometry to translational and rotational vibration measurements on rotating shafts,” *Measurement*, pp. 201–210, 2004.
- [72] P. Giuliani, D. Di Maio, C. Schwingshackl, M. Martarelli, and D. Ewins, “Six degrees of freedom measurement with continuous scanning laser doppler vibrometer,” *Mechanical Systems and Signal Processing*, vol. 38, no. 2, pp. 367–383, 2013.

- [73] L. Bregant and M. Sanderson, “Rotational degrees of freedom: a historical overview on techniques and methods,” in *Proceedings of the 25th International Conference on Noise and Vibration Engineering*, pp. 995–1002, 2000. cited By 6.
- [74] D. Montalvão, A. M. R. Ribeiro, N. M. M. Maia, and J. M. M. Silva, “Estimation of the rotational terms of the dynamic response matrix,” *Shock and Vibration*, vol. 11, no. 3-4, pp. 333–350, 2004.
- [75] T. Schmitz and R. Donalson, “Predicting High-Speed Machining Dynamics by Substructure Analysis,” *CIRP Annals - Manufacturing Technology*, vol. 49, no. 1, pp. 303–308, 2000.
- [76] T. L. Schmitz and T. J. Burns, “Tool Point Frequency Response Prediction for High-Speed Machining by RCSA,” *Journal of Manufacturing Science and Engineering*, vol. 123, no. 4, pp. 700–707, 2001.
- [77] T. Schmitz, M. Davies, K. Medicus, and J. Snyder, “Improving High-Speed Machining Material Removal Rates by Rapid Dynamic Analysis,” *CIRP Annals - Manufacturing Technology*, vol. 50, no. 1, pp. 263–268, 2001.
- [78] T. L. Schmitz and T. J. Burns, “Receptance coupling for high-speed machining dynamics prediction,” in *Proceedings of the Twenty-First International Modal Analysis Conference*, pp. 1–12, 2003.
- [79] T. L. Schmitz, K. Powell, D. Won, G. S. Duncan, W. G. Sawyer, and J. C. Ziegert, “Shrink fit tool holder connection stiffness/damping modeling for frequency response prediction in milling,” *International Journal of Machine Tools and Manufacture*, vol. 47, no. 9, pp. 1368–1380, 2007.
- [80] M. Mehrpouya, E. Graham, and S. Park, “Identification of multiple joint dynamics using the inverse receptance coupling method,” *Journal of vibration and control*, vol. 1, pp. 3431–3449, 2014.
- [81] E. B. Kivanc and E. Budak, “Structural modeling of end mills for form error and stability analysis,” *International Journal of Machine Tools and Manufacture*, vol. 44, no. 11, pp. 1151–1161, 2004.

BIBLIOGRAPHY

- [82] G. S. Duncan and T. L. Schmitz, “An Improved RCSA Model for Tool Point Frequency Response Prediction,” in *Proceedings of the Twenty-First International Modal Analysis Conference*, pp. 26–36, 2003.
- [83] T. L. Schmitz and G. S. Duncan, “Three-component receptance coupling substructure analysis for tool point dynamics prediction,” *Journal of Manufacturing Science and Engineering*, vol. 127, no. 4, pp. 781–790, 2005.
- [84] A. Ertürk, H. Özgüven, and E. Budak, “Analytical modeling of spindle-tool dynamics on machine tools using timoshenko beam model and receptance coupling for the prediction of tool point FRF,” *International Journal of Machine Tools and Manufacture*, vol. 46, no. 15, pp. 1901 – 1912, 2006.
- [85] O. Ozsahin, H. Ozguven, and E. Budak, “Analytical modeling of asymmetric multi-segment rotor-bearing system with Timishenko beam model including gyroscopic moments,” *Computers and Structures*, vol. 144, pp. 119–126, 2014.
- [86] A. Jeffrey, *Mathematics for Engineers and Scientists, 5th Edition*. Taylor & Francis, 1996.
- [87] E. Budak, Y. Altintas, and E. Armarego, “Prediction of milling force coefficients from orthogonal cutting data,” *Journal of Manufacturing Science and Engineering*, vol. 118, no. 2, pp. 216–224, 1996.
- [88] E. Ozturk, O. Ozkirimli, T. Gibbons, M. Saibi, and S. Turner, “Prediction of effect of helix angle on cutting force coefficients for design of new tools,” *CIRP Annals - Manufacturing Technology*, vol. 65, no. 1, pp. 125 – 128, 2016.
- [89] E. Öztürk, U. Kumar, S. Turner, and T. Schmitz, “Investigation of spindle bearing preload on dynamics and stability limit in milling,” *CIRP Annals – Manufacturing Technology*, vol. 61, pp. 343–346, 2012.
- [90] N. Grossi, L. Sallese, A. Scippa, and G. Campatelli, “Chatter stability prediction in milling using speed-varying cutting force coefficients,” *Procedia CIRP*, vol. 14, pp. 170 – 175, 2014.

- [91] Y. Altıntaş and E. Budak, “Analytical prediction of stability lobes in milling,” *CIRP Annals-Manufacturing Technology*, vol. 44, no. 1, pp. 357–362, 1995.
- [92] Y. Altıntaş, *Manufacturing automation: metal cutting mechanics, machine tool vibrations, and CNC design*. Cambridge university press, 2012.
- [93] G. H. Golub and C. F. Van Loan, *Matrix computations*, vol. 3. JHU Press, 2012.
- [94] A. Kyprianou, J. E. Mottershead, and H. Ouyang, “Structural modification. part 2: assignment of natural frequencies and antiresonances by an added beam,” *Journal of Sound and Vibration*, vol. 284, no. 12, pp. 267 – 281, 2005.
- [95] “BS ISO 12164-1:2001 : Hollow taper interface with flange contact surface – Part 1 : Shanks – Dimensions,” tech. rep., International Organization for Standardization, 2001.
- [96] “BS ISO 12164-1:2001 : Hollow taper interface with flange contact surface – Part 2 : Receivers – Dimensions,” tech. rep., International Organization for Standardization, 2001.
- [97] R. Blevins, *Formulas for Natural Frequency and Mode Shape*. Krieger Publishing Company, 2001.
- [98] T. Insperger and G. Stépán, “Updated semi-discretization method for periodic delay-differential equations with discrete delay,” *International Journal for Numerical Methods in Engineering*, vol. 61, pp. 117–141, 2004.
- [99] H. S. Kim and T. L. Schmitz, “Bivariate uncertainty analysis for impact testing,” *Measurement Science and Technology*, vol. 18, no. 11, pp. 3565–3571, 2007.
- [100] N. D. Sims, P. V. Bayly, and K. A. Young, “Piezoelectric sensors and actuators for milling tool stability lobes,” *Journal of sound and Vibration*, vol. 281, pp. 743–762, 2005.

BIBLIOGRAPHY

- [101] E. Balmès, “Frequency domain identification of structural dynamics using the pole/residue parametrization,” *Office national d etudes et de recherches aérospatiales onera*, 1996.
- [102] Z. Shi and S. Law, “Structural damage localization from modal strain energy change,” *Journal of Sound and Vibration*, vol. 218, pp. 825–844, 1998.
- [103] A. Delgado, E. Ozturk, and N. Sims, “Analysis of non-linear machine tool dynamic behavior,” *Procedia Engineering*, vol. 63, pp. 761 – 770, 2013.
- [104] C. To, “A linearly tapered beam finite element incorporating shear deformation and rotary inertia for vibration analysis,” *Journal of Sound and Vibration*, vol. 78, no. 4, pp. 475 – 484, 1981.
- [105] D. Thomas, J. Wilson, and R. Wilson, “Timoshenko beam finite elements,” *Journal of Sound and Vibration*, vol. 31, no. 3, pp. 315–330, 1973.
- [106] E. Berger, “Friction modeling for dynamic system simulation,” *Applied Mechanics Reviews*, vol. 55, no. 6, pp. 535–577, 2002.
- [107] D. J. Segalman, “Modelling joint friction in structural dynamics,” *Structural Control and Health Monitoring*, vol. 13, no. 1, pp. 430–453, 2006.
- [108] J. Mottershead, C. Mares, and S. James, “Fictitious modifications for the separation of close modes,” *Mechanical Systems and Signal Processing*, vol. 16, no. 5, pp. 741–755, 2002.
- [109] T. Schmitz and K. Smith, *Machining Dynamics: Frequency Response to Improved Productivity*. Springer US, 2008.
- [110] “Operating Manual – Thermogrip Induction unit ISG3200WK-400V / 480V,” standard, Bilz.
- [111] “BS ISO 1940-1:2003 : Mechanical Vibration – Balance quality requirements for rotors in a constant (rigid) state – Part 1: Specification and verification of balance tolerances,” tech. rep., International Organization for Standardization, 2001.

- [112] “BS ISO 261:1998 : ISO general purpose Metric screw threads,” tech. rep., International Organization for Standardization, 1998.
- [113] S. Rao, *Mechanical Vibrations*. Pearson Education, 2016.
- [114] R. Blevins, *Formulas for Natural Frequency and Mode Shape*. Krieger Publishing Company, 2001.
- [115] A. Bayoumi, G. Yucesan, and L. Kendall, “An analytic mechanistic cutting force model for milling operations: a theory and methodology,” *Transactions-American Society of Mechanical Engineers Journal of Engineering for Industry*, vol. 116, pp. 324–324, 1994.
- [116] J. Williams, *Engineering Tribology*. Engineering Tribology, Cambridge University Press, 1994.
- [117] T. Insperger, G. Stépán, P. Bayly, and B. Mann, “Multiple chatter frequencies in milling processes,” *Journal of Sound and Vibration*, vol. 262, no. 2, pp. 333 – 345, 2003.
- [118] T. L. Schmitz, J. Couey, E. Marsh, N. Mauntler, and D. Hughes, “Runout effects in milling: Surface finish, surface location error, and stability,” *International Journal of Machine Tools and Manufacture*, vol. 47, no. 5, pp. 841 – 851, 2007.
- [119] T. Insperger, B. P. Mann, T. Surmann, and G. Stépán, “On the chatter frequencies of milling processes with runout,” *International Journal of Machine Tools and Manufacture*, vol. 48, no. 10, pp. 1081 – 1089, 2008.
- [120] T. Schmitz and R. Donalson, “Predicting High-Speed Machining Dynamics by Substructure Analysis,” *CIRP Annals - Manufacturing Technology*, vol. 49, no. 1, pp. 303–308, 2000.
- [121] A. Moorhouse, A. Elliott, and T. Evans, “In situ measurement of the blocked force of structure-borne sound sources,” *Journal of Sound and Vibration*, vol. 325, no. 4, pp. 679–685, 2009.

BIBLIOGRAPHY

- [122] A. Sestieri, P. Salvini, and W. D'Ambrogio, "Reducing scatter from derived rotational data to determine the frequency response function of connected structures," *Mechanical Systems and Signal Processing*, vol. 5, no. 1, pp. 25–44, 1991.
- [123] A. Elliott and A. T. Moorhouse, "Characterisation of structure borne sound sources from measurement in-situ," *Journal of the Acoustical Society of America*, vol. 123, no. 5, p. 3176, 2008.
- [124] A. Elliott, A. Moorhouse, and G. Pavić, "Moment excitation and the measurement of moment mobilities," *Journal of Sound and Vibration*, vol. 331, no. 11, pp. 2499–2519, 2012.
- [125] J. Stewart, *Calculus: Early Transcendentals*. Cengage Learning, 2015.
- [126] S. Lu and S. Pereverzev, *Regularization Theory for Ill-posed Problems: Selected Topics*. De Gruyter, 2013.
- [127] R. J. Guyan, "Reduction of stiffness and mass matrices," *AIAA journal*, vol. 3, no. 2, pp. 380–380, 1965.
- [128] G. B. Warburton, "The vibration of rectangular plates," *Proceedings of the Institution of Mechanical Engineers*, vol. 168, no. 1, pp. 371–384, 1954.
- [129] "Structural dynamics toolbox." <http://sdtools.com/help/sdt.pdf>.
- [130] Y. Li, W. Zhao, S. Lan, J. Ni, W. Wu, and B. Lu, "A review on spindle thermal error compensation in machine tools," *International Journal of Machine Tools and Manufacture*, vol. 95, pp. 20–38, 2015.
- [131] L. Xiaohu, L. Huanfeng, Z. Yanfei, and H. Jun, "Investigation of non-uniform preload on the static and rotational performances for spindle bearing system," *International Journal of Machine Tools and Manufacture*, vol. 106, pp. 11–21, 2016.
- [132] F. Wardle, S. Lacey, and S. Poon, "Dynamic and static characteristics of a wide speed range machine tool spindle," *Journal of Precision Engineering*, vol. 5, pp. 175–183, 1983.

- [133] C. Lin and J. Tu, “Model-based design of motorized spindle systems to improve dynamic performance at high speeds,” *Journal of Manufacturing Processes*, vol. 9, pp. 94–183, 2007.
- [134] G. Strang and G. J. Fix, *An analysis of the finite element method*, vol. 212. Prentice-hall Englewood Cliffs, NJ, 1973.